NORTHWESTERN UNIVERSITY

Mechanics of Rock-Cutter Interactions during Rock Shearing Processes

A DISSERTATION

SUBMITTED TO THE GRADUATE SCHOOL
IN PARTIAL FULFILLMENT OF THE REQUIREMENTS

for the degree

DOCTOR OF PHILOSOPHY

Field of Mechanical Engineering

By

Demeng Che

EVANSTON, ILLINOIS

September 2016

Abstract

Mechanics of Rock-Cutter Interactions during Rock Shearing Processes

Demeng Che

Shearing processes in which a single or multiple cutting elements (i.e., cutters) are driven to fracture and remove a rock formation layer-by-layer following a specific tool path, has been widely used in man-made rock opening practices such as oil well drilling, coal mining, and bulldozing. Rock shearing has been regarded as one of the most energy-efficient rock removal mechanisms due to its capability of generating very intensive interactions at the rock-cutter interfaces. Oil well drilling performed with polycrystalline diamond compact (PDC) cutters has become one of the major global shearing practices in the modern world since the 1970s. The intensive interactions between the rock and the cutter in shearing, although they have led to high rock removal rates and better cutting efficiency, make the PDC cutters intrinsically sensitive to the rock's physical properties. Hence, catastrophic damage is commonly encountered in drilling of not only extremely hard and abrasive but also highly inhomogeneous rock formations. Unfortunately, the complex material properties of rock, such as its inhomogeneity, dilatancy, pressure-dependent failure behaviors, random pores and defects, etc. and the lack of sensing and monitoring technologies at the rock-cutter interface are still limiting further advances in rock cutting performed with PDC cutters.

In response to the aforementioned challenges, the goal of this thesis is to enhance the fundamental understanding of the cutting mechanics and failure mechanisms governing the rock-cutter interactions in shearing processes, in particular as performed by PDC cutters. To seek a

comprehensive explanation on how the rock and cutter interact in typical shearing processes, three core technical methods, i.e., experimental investigation, analytical/numerical modeling, and dynamical/statistical analysis, have been exploited in several interrelated tasks so that a theoretical synergy can be achieved.

The thesis starts with the experimental investigation of rock shearing in face turning and linear cutting configurations based on the development of two rock cutting testbeds. The cutter's cutting performance is evaluated by monitoring and analyzing the force and temperature responses which are then theoretically related to the relevant process parameters and the rock's properties through analytical/numerical modeling of the rock shearing process. Finally, the dynamic failure behavior of rock in shearing is explored from a statistical point of view. The findings reveal that the rock's failure behavior in shearing is governed by a scale-free stochastic mechanism.

The understanding and results from this thesis could lay the essential foundation for the advanced development of PDC cutters and the efficient optimization and control of the corresponding processes. The obtained knowledge can also be simply extended to rock shearing processes performed with other types of tools in other applications without substantial changes.

Acknowledgments

I would like to thank my Ph.D. advisor, Professor Kornel F. Ehmann, for supporting me during these past five years. Professor Ehmann is someone you will instantly love and never forget once you meet him. He is the most humorous advisor and one of the smartest people I have ever known. I remember he used to say something like "you are always good at learning new stuff very quickly" to encourage me to read hundreds of research articles to keep myself updated. Ever since, he has been constantly supportive and instrumental in helping me come up with the thesis topic and providing me brilliant insights into various problems. And, during the most difficult times when pursuing my research goals, he gave me the moral support and the freedom I needed to move on.

I am equally grateful to Professor Jian Cao, as the co-advisor of my Ph.D. thesis, for her academic advice and scientific knowledge and many insightful discussions and valuable suggestions on my research work. I would also like to thank my Ph.D. committee members, Professors John W. Rudnicki and Xiaochun Li for their instrumental advice and suggestions during my Ph.D. career.

Many people have taught, helped and supported me at Northwestern University. I'd like to thank Robert Taglia and Scott Simpson for helping me prepare the experimental components of the rock cutting testbeds. I would like to thank Dr. Peidong Han, Dr. Ishan Saxena and Dr. Ping Guo for helping me compose the technology review articles on the machining of rock and carbon fiber reinforced plastics and answering my numerous academic and career problems. Thanks are due to Dr. Jake Smith, Dr. Jifeng Zhao, Huaqing Ren, and Weizhao Zhang for their insightful advice on the finite element modeling of rock cutting processes. And, also to Dr. Zhiwei Zhu for

providing me the original idea of self-organized criticality in rock cutting, Dr. Wule Zhu for many valuable discussions on the cutting theory in two-dimension rock cutting, Dr. Xiaoli Wang for teaching me how to use the white light interferometer and optical microscopies in our laboratory, and Michael Beltran for providing the CNC milling center for the linear rock cutting tests. I also thank Ebot Ndip-Agbor, Satyabrata Monhanty, and He Zhao for their proofreading and grammatical editing of my papers. I am also thankful to David Pritchet, Macro Giovannini, Newell Moser, Sarah Wolff, Man Kwan Ng, and Tim Velasquez for their constant support and help throughout my Ph.D. career.

The work to be presented in this thesis has been supported by a National Science Foundation collaborative research grant (CMMI#1301127).

Dedication

In dedication to my family and my wife, Na

whose unyielding support, unconditional love and constant encouragement have enriched my soul and inspired me to pursue and complete this research.

I love you all dearly.

Table of Contents

List of Tables

List of Figures

Chapter 1

Introduction

1.1 Background and motivation

Shearing is the most widely exploited method to fracture and remove rock formations in many man-made rock opening activities. During shearing, rock breaks into chips due to the periodic nucleation, propagation, and coalescence of numerous micro-cracks. Shearing was first introduced to fracture rock formations in rotary drilling using fixed-cutter bits (or drag bits) around 1900 (Detournay et al., 2008). The intensive interactions between the tool and rock under the shearing action along with the poor wear/impact resistance of the tools limited the shearing process only to the drilling of very soft and shallow rock formations. Fortunately, the polycrystalline diamond compact (PDC) cutters, first introduced by General Electric in 1973 (Warren, 1994), have led to a revolution in modern rock drilling technology in the past 40 years. As shown in Fig. 1.1 (a), PDC cutters are usually brazed onto a single drill bit body at an optimized spatial arrangement in real practice. Each PDC cutter advances along a spiral trajectory and shears the rock. In November, 1973, a field test using a drill bit with PDC cutters was conducted in Colorado and indicated a serious brazing problem due to the insufficient area of the small-diameter blanks (Kerr, 1988). In 1978, a PDC diamond layer was designed and attached to a tungsten carbide stud whose large enough blank area was brazed to the bit body. From then on, PDC cutters and bits with many technological advances take an important and growing share of the drilling bit market (2% of all

footage drilled in oil fields by 1982, 15% by late 1980s, 45% by late 1990s, 50% in 2003, and 65% in 2010 (Bellin et al., 2010; Menand and Gerbaud, 2005)).

Generally, PDC bits drill several times faster and are more energy-efficient than tri-cone bits (Brett et al., 1990), due to their shearing mechanism which is different from the conventional crushing mechanism. However, due to the intensive rock-cutter interactions during shearing, PDC bits are sensitive to the properties of the rock formation and can drill only relatively soft rock formations, e.g., shales, soft and unconsolidated sandstones, carbonates, etc., but they cannot effectively drill hard formations, e.g., granite, chert, pyrite, quartzite, conglomerate, etc. (Offenbacher et al., 1983). Figure 1.1(b) shows the approximate drillable zone of PDC bits in various rock formations (Che et al., 2012b).

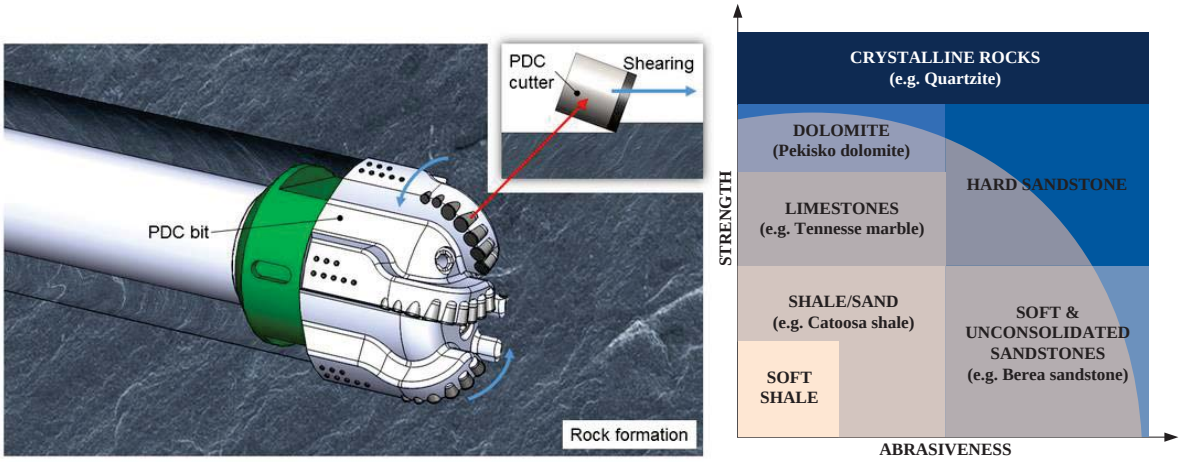

(a) (b)

Figure 1.1: PDC cutters and bits: (a) PDC bit in the field; (b) drillable zone of PDC bits.

As rock cutting/drilling demands push the limits of current technological capabilities it is increasingly becoming necessary to elevate the fundamental understanding of the underlying physical phenomena which is the key to process optimization and technology advancement in hard rock drilling processes. However, extreme challenges are still being faced in achieving these goals.

The reasons are threefold: (1) *Geometric complexity*: In commercial PDC drill bits, the cutters are brazed to several blades of a single bit body with a sophisticatedly designed profile aiming to improve their drilling efficiency and durability (Bruton et al., 2014). (2) *Environmental complexity*: During drilling, PDC drill bits bear complex dynamic vibrations due to the inhomogeneous properties and sudden breakage of the rock formations. Moreover, drilling fluids are commonly applied which also introduce complexities into the rock drilling system. (3) *Process complexity*: The PDC bits are controlled to drill along multiple directions, e.g., vertical and horizontal directions, at various penetration rates during different stages of the drilling process, which largely complicates rock-cutter interactions.

In fact, the revelation of the intrinsic cutting mechanisms in geological material cutting performed with PDC cutters is nearly impossible under realistic field conditions due to the aforementioned complexities. Therefore, rock cutting tests performed with single PDC cutters under carefully controlled laboratory conditions are highly recommended and used as a practical way to look for insights into the mechanics of the rock-cutter interactions (Che and Ehmann, 2014). The obtained knowledge can then be applied to describe the cutting mechanisms of the whole drill bit under realistic field conditions through spatial integration of various bit configurations (Glowka, 1986).

Numerous research topics, including rock material removal mechanisms (Goodrich, 1956; Guo et al., 1992; Mishnaevsky, 1995; Richard, 1999; Verhoef and Ockeloen, 1996; Yilmaz et al., 2007), loading response predictions (Fairhurst and Lacabanne, 1956; Nishimatsu, 1972; Richard et al., 2012; Warren and Sinor, 1989; Xue et al., 2009), heat transfer modeling (Cools, 1993; Freeman et al., 2012; Glowka, 1989a; Glowka and Stone, 1985; Loui and Karanam, 2005; Wilson and Vorono,

2003), and cutting dynamics (Harrell et al., 1997; Henneuse, 1992; Hutchinson et al., 1995) have received increased attention in both academia and industry. Yet both currently available analytical and numerical models for providing in-depth insights into the aforementioned research topics in the immediate contact region at the rock and cutter interfaces, as well as current measurement methods and testing technologies are lagging far behind in their ability to provide convincing and complete predictions and reliable measurements.

These limitations and challenges constitute the motivation for this thesis. Specifically, the science and technology base for the thorough understanding of the failure mechanisms of rock and the comprehensive explanation of the thermo-mechanical and dynamic behaviors of the PDC cutter in rock cutting constitute the focus of the investigations.

1.2 Scope and objectives

In light of the above, the objective of this thesis is to markedly enhance the fundamental understanding and performance of rock shearing process. Although this thesis focuses on rock shearing performed with PDC cutters because of their wide application in modern oil drilling practice, most of the obtained knowledge is also applicable for rock shearing performed with other tools.

Three interrelated tasks have been undertaken: (1) design and development of rock cutting process testbeds, (2) formulation and experimental verification of the cutting mechanics in rock cutting, and (3) exploration and analysis of the rock's failure behaviors in rock cutting.

Task (1) aims to provide experimental proof for model formulation and validation for the various aspects of the mechanical/thermal behaviors under well-controlled process conditions. In

this task, two rock cutting testbeds, namely rock face turning testbed (RFTT) and linear rock cutting testbed (LRCT) will be developed to generate rotational and simplified linear cutting motions between the rock and the PDC cutter respectively at the laboratorial level. Force, temperature, and vibration measurement sensors will be used to capture the in-situ mechanical, thermal, and dynamic responses of the PDC cutter during rock cutting. A high-speed camera system will be exploited to visualize the rock's failure behaviors.

Task (2) focuses on the formulation of efficient theoretical models to predict the loading force and temperature responses at the rock-cutter interfaces during rock cutting processes. The analytical modeling and numerical simulation methods, along with the experimental evidence provided by the testbeds developed in Task (1) will be utilized to achieve accurate and efficient predictions of the mechanical and thermal responses in rock cutting.

Task (3) is devoted to the physical explanation of the rock's intrinsic failure behaviors during various cutting motions performed by the PDC cutter. In this task, the experimental observation of the chip formation process will be analyzed and statistically characterized aiming to reveal the rock removal mechanisms.

1.3 Thesis outline

The thesis is organized as follows:

Chapter 2 provides a comprehensive review of the literature on the study of rock-cutter interactions during rock cutting processes based on the shearing mechanisms mainly performed with PDC cutters. This chapter first presents investigations and findings on the rock's failure behaviors, followed by the review of modeling research on loading forces and temperature as two

significant factors in rock cutting. The general measurement and testing methods in evaluating the rock's material properties and validating rock cutting theories will be presented at the end of this chapter.

Chapter 3 introduces the development of a rock face turning testbed which achieves a well-controlled and in-situ monitored rotational cutting motion between the rock and the PDC cutter. From the physical point of view, a phenomenological model of loading force responses will be developed based on a full factorial design of experiments performed on this testbed.

Chapter 4 develops a linear rock cutting testbed to further simplify the cutting conditions and obtain deeper insights into the intrinsic mechanisms which drive the complex rock cutting processes. A force compensation algorithm will be presented to avoid environmental and dynamical noise and achieve an accurate acquisition of the force responses. Moreover, the chip formation phenomena will be visualized by a high speed camera system to provide experimental evidence of the rock's failure behaviors.

Chapter 5 proposes a new cutting theory to explain the cutting mechanics involved in the orthogonal cutting of rock. The force data and chip formation videos obtained from the previous chapter will be exploited to frame and support the cutting theory including a force model and an explanation of the rock removal process. It will be shown that the predictions given by the force model are in good agreement with the experimental data.

Chapter 6 gives two numerical studies on rock cutting processes using the finite element method. Using the two different testbeds developed in Chapters 3 and 4, the first study is conducted to simulate the force responses and chip formation phenomena in the two-dimensional orthogonal

cutting of rock, while the second study formulates a simulation model for three-dimensional face turning of rock.

Chapter 7 focuses on the thermal responses in the PDC cutter during rock cutting. An analytical model will be developed to predict the temperature and heat flux contours in the PDC cutter under two-dimensional orthogonal cutting conditions. The temperature data derived from Chapter 3 will be adopted to calibrate and validate the model. In addition, the model will be further evaluated through simulations performed by a corresponding numerical model.

Chapter 8 illustrates the rock's scale-free fragmentation behaviors in rock shearing from a statistical point of view. The dynamical force responses captured in Chapter 4 will be further analyzed and shown to provide evidence of a power-law distribution of the power spectrum density in the frequency domain. The tuned criticality, as a widely-observed phenomenon in nature will be adopted to explain the dynamical failure behavior of rock in the shearing process.

Chapter 9 summarizes the work done in this thesis and illustrates the potential directions for future work on this topic.

Chapter 2

Literature Review

This chapter provides a comprehensive review of the literature that deals with issues surrounding the PDC cutter/rock interface in rock shearing processes. Most of the shearing processes discussed in this chapter are performed with PDC cutters. However, the general principles can be also applied to the shearing practices conducted by other tools such as drag tools, coal picks, or even bulldozer blades. This chapter addresses five significant issues. These are: rock removal mechanisms, loading force predictions, temperature predictions, numerical modeling of rock-cutter interactions, and experimental investigations in this field. Experimental, analytical and numerical methods are all included into the investigation of the above-mentioned five issues. Relevant concepts from metal cutting, micromachining and other machining processes are also introduced to provide important insights and draw parallels between these interrelated fields. A more comprehensive review on rock-cutter interactions during cutting processes can be found in the author's earlier publications (Che et al., 2012a, b).

2.1 Rock removal mechanisms

The interactions between the rock and cutters in coal mining and rock drilling processes have been extensively studied over the past half century. Referring to the literature, many man-made rock opening processes have been used to fragment rock formations, include shearing (also called dragging, wedging, or scraping) (Hood and Alehossein, 2000; Liu et al., 2009b), percussion or

crushing (Hustrulid and Fairhurst, 1972), indentation (Kou et al., 2004), grinding (Xu and Huang, 2003), erosion by fluid jet action (Crow, 1973; Leach et al., 1966), and torsion or twisting (Bourgoyne et al., 1986). Among them, rock shearing, also called rock cutting, rock ploughing, rock dragging, etc., is the most widely used method to fracture rock formations in the modern world.

In a typical rock shearing process (Fig. 2.1), a cutter (also called a drag tool or blade) is pre-set to a level lower than the rock formation, i.e., at a given depth of cut and then dragged to fracture the rock along a specific trajectory. During rock shearing, rock chips will be fragmented and removed from the virgin rock layer by layer. Rock shearing offers very intensive interactions between the rock and the tool, which highly improves the rock removal rate and process efficiency. Hence, people have adopted the rock shearing method in many man-made rock opening activities over the past century. Rock shearing was reported to be first exploited in drilling soft rock formations in the early 1900s (Detournay et al., 2008). Later on, people started to use similar processes to fracture coal and other geological materials in the mining industry (Evans, 1962). The advances in synthetic diamond technology, developed by General Electric in 1973 (Warren, 1994), have largely widened the application range of rock shearing in drilling hard and aggressive rock formations. Rock shearing has obtained a rapid growth in the share of the global oil well drilling footage from 2% in 1982 to 65% in 2010 (Bellin et al., 2010; Menand and Gerbaud, 2005). Moreover, due to its high energy efficiency, rock shearing has also been implemented in construction and underground excavation machinery, e.g., hydraulic/mechanical excavators and bulldozers (Goktan and Yilmaz, 2005; Qinsen and Shuren, 1994; Tsuji et al., 2012). On the other hand, the shearing action makes the cutters intrinsically sensitive to the material properties of the

drilled rock formations. Catastrophic damage commonly exists in drilling of extremely hard and abrasive rock formations. However, there is still a lack of a comprehensive understanding of the rock-cutter interactions to offer basic guidelines in applying promising technologies for improving the cutting performance of the cutters. The reasons are threefold: (1) rock cutting is usually considered as a brittle failure process with extremely fast chip formation phenomena, which is very difficult to model by either analytical or numerical methods; (2) the complex material properties of the rock, such as its inhomogeneity, dilatancy, pressure-dependent failure behavior, random pores and defects, etc., bring further difficulties into characterizing the failure behavior of rock; and (3) the lack of measuring and sensing technologies at the rock-cutter interface in the hostile down-hole conditions limits the experimental observations of rock-cutter interactions. To this end, people have put in tremendous efforts to obtain insights into the rock-cutter interaction problems in carefully defined laboratory tests. Their findings and advances are reviewed next.

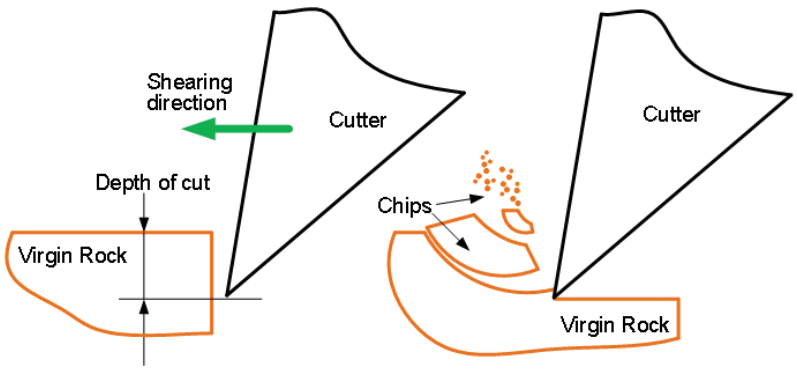

Figure 2.1: Schematic of a typical rock shearing process.

Merchant (Merchant, 1944, 1945) developed a model for material removal processes with emphasis on metallic and other ductile materials. This model was then subsequently suggested to

explain shearing in the cutting of some geological materials with plastic properties such as coal and wet chalk (Nishimatsu, 1993). In Merchant's model, the chip is assumed to be sheared off along a shear plane inclined under an angle with respect to the cutting velocity vector.

Based on Merchant's model, Fairhurst and Lacabanne (Fairhurst and Lacabanne, 1957) found that a flat is developed at the bottom of the cutting edge as a drag bit drills the rock and suggested that fracture occurs at some specific angle, λ_f, with respect to the resultant force (Fig. 2.2). They firstly proposed that two mechanisms are simultaneously acting: cutting of the rock and frictional contact underneath the cutter (Detournay and Defourny, 1992).

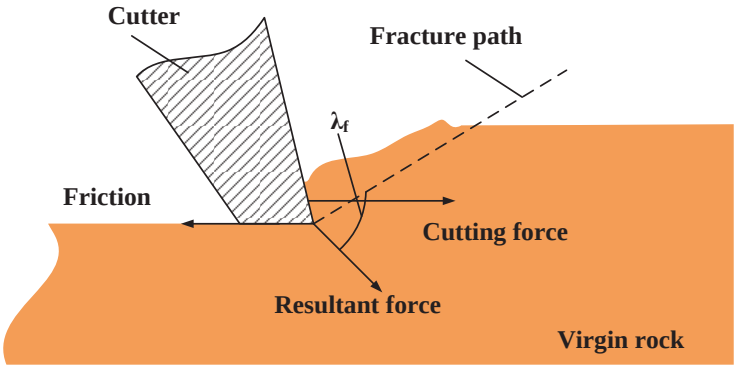

Figure 2.2: Force components in Fairhurst and Lacabanne's model adapted from (Fairhurst and Lacabanne, 1957).

Goodrich (Goodrich, 1956) conducted a series of linear cutting tests to simulate cutting by rotary bits and observed the chip formation process using a customized visualization system as shown in Fig. 2.3. Fine particles and large chips were found to be alternatively produced, which made him conclude that the rock fails in a crushing-chipping hybrid mode as shown in Fig. 2.4. Maurer (Maurer, 1966) proposed that the cutting action of a drag bit is a discontinuous process.

After a major chip is formed, the bit moves forward to form several small chips by crushing the rock until these small chips accumulate and become large enough to form another major chip (Maurer, 1966) as shown in Fig. 2.5. Zeuch and Finger (Zeuch and Finger, 1985) modified a milling machine to achieve linear cutting of three types of rock materials. Typical chips were collected and analyzed. An apparent crushed and powdery zone was found at the trailing edge of the chips, as seen in Fig. 2.6, which indicated that crushing and chipping both worked in the chip formation process. More specifically, it was concluded that the initial crushing phase is responsible for the subsequent chipping process.

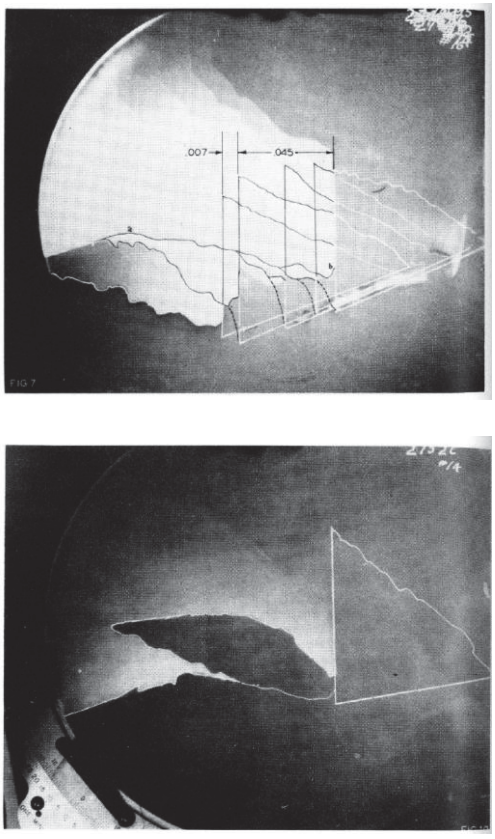

Figure 2.3: Photos taken by a Jones and Lamson comparator (Goodrich, 1956).

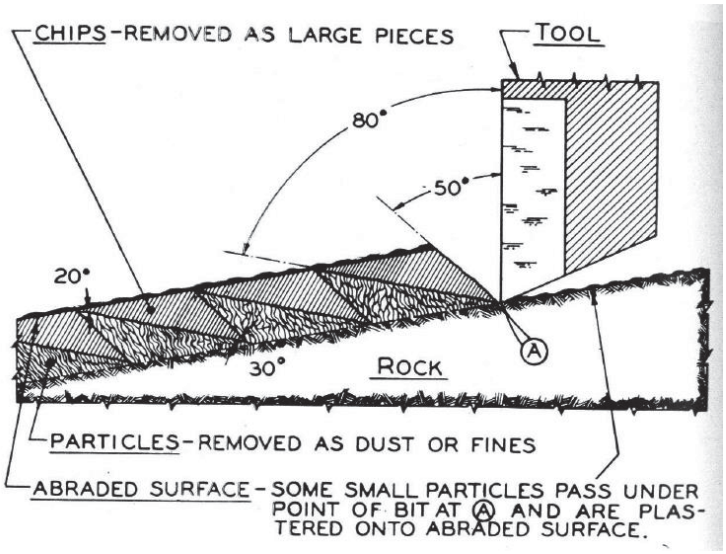

Figure 2.4: Periodic rock removing mechanism (Goodrich, 1956).

Verhoef and Ockeloen (Verhoef and Ockeloen, 1996) proposed a cataclastic ductile failure mode of rock cutting when very high compressive stresses occur in the vicinity of the cutter/rock interface. However, no explicit criterion is put forward to determine the start point of the "brittle-ductile" transition in rock cutting.

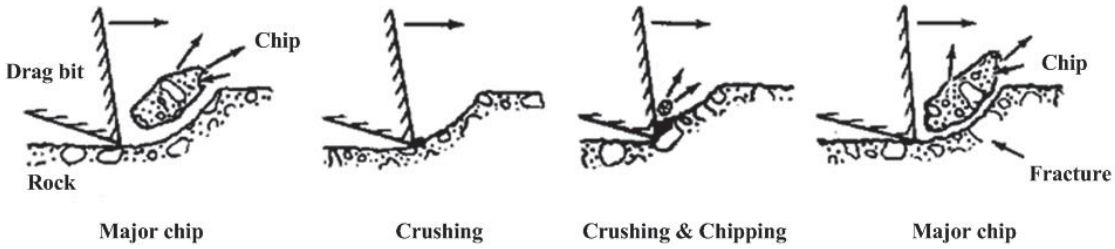

Figure 2.5: Periodic rock removal process in shearing (Maurer, 1966).

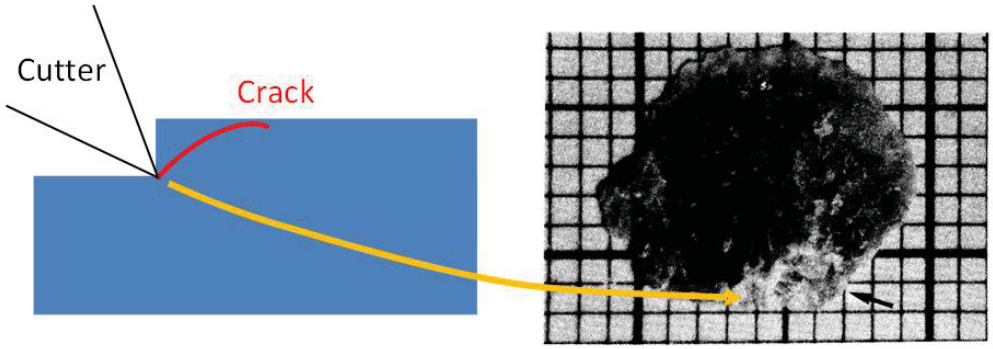

Figure 2.6: Crushed zone at trailing edge of the rock chip (Zeuch and Finger, 1985).

Mishnaevsky reviewed the work of others' (Mishnaevsky, 1995) and defined a crushed zone, namely the destruction kernel, beneath the cutter's tip (Mishnaevsky, 1994). The cracks were believed to be initiated from the destruction kernel and then propagating to form a chip segment as shown in Fig. 2.7. Similar material removal mechanisms were also mentioned in some other researchers' work (Guo et al., 1992; Richard, 1999; Yilmaz et al., 2007).

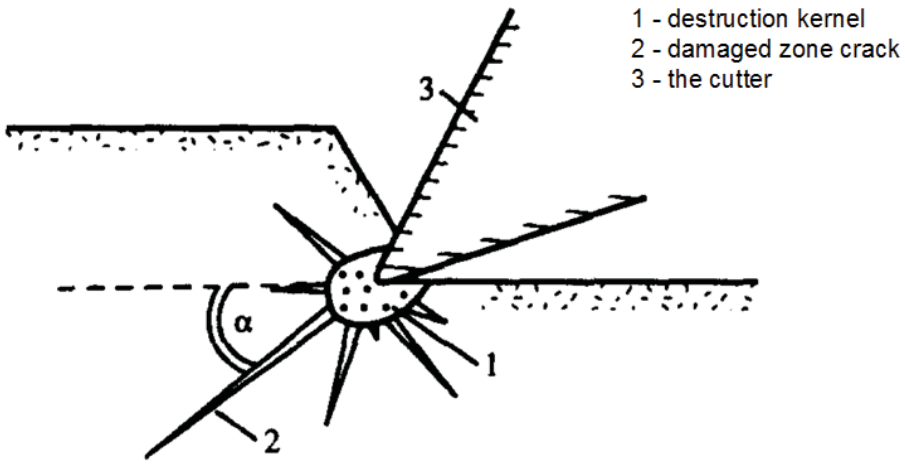

Figure 2.7: Crack systems formed in rock cutting (Mishnaevsky, 1994).

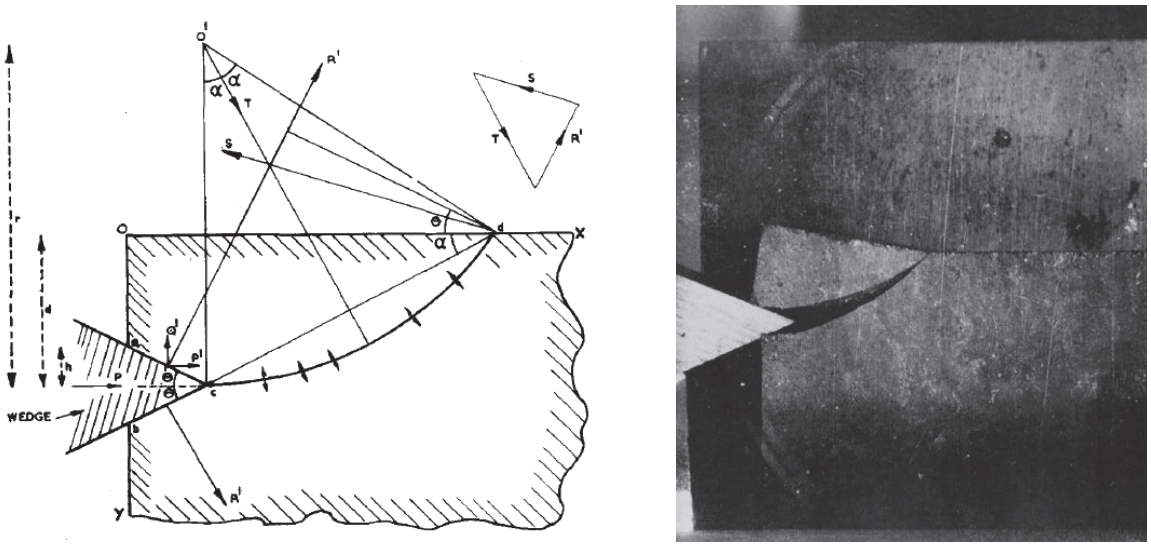

Figure 2.8: Tensile breakage of rock in shearing (Evans, 1965).

Although rock removal mechanisms can vary from case to case, there are two major failure modes widely considered to be involved in the cutting processes, i.e., the crushing and chipping modes. The crushing mode creates highly fractured and inelastically deformed rock, while the chipping mode initiates and propagates cracks to form big chips (Mishnaevsky, 1995). Although some researchers have proposed that rock fails in a single failure mode (Evans, 1962; Hood and Alehossein, 2000), a crushing-chipping hybrid failure mode has been widely accepted.

No consensus has, however, been reached so far in regard to the explanation of the chipping mode failure mechanism for the past five decades (Mishnaevsky, 1995). Some researchers proposed that chipping is caused by tensile breakage while others believed that the actions of the shear stresses are the intrinsic reasons for chipping. Evan (Evans, 1962), for the first time, assumed that crack initiation can be attributed to tensile breakage from the cutter's tip and then propagating to form chip segments as shown in Fig. 2.8. Based on the tensile failure assumption, he was able to derive an analytical expression for the force responses by equating the moments applied to a

single chip segment with respect to a specific location. Although Evan's model was only limited to simple coal ploughing applications, his assumptions on the tensile failure of rock in chipping have been accepted by many other researchers (Goktan and Yilmaz, 2005; Hood and Alehossein, 2000; Liu et al., 2007).

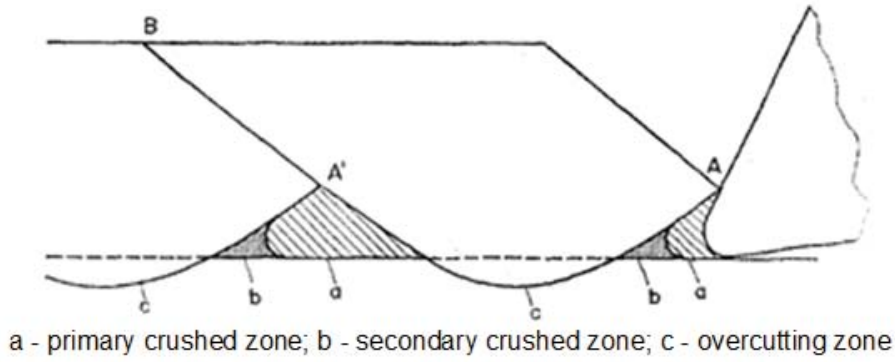

Figure 2.9: Rock removal mechanism in Nishimatsu's model. (Nishimatsu, 1972).

On the other hand, Nishimatsu (Nishimatsu, 1972; Nishimatsu, 1993) persisted in looking for a similarity between rock and metal cutting processes and recommended that chipping was induced by shear stresses. He suggested that the rock failure process in rock cutting is a cyclic and discontinuous brittle fracture failure mode. He separated the failure process into three zones, including a primary crushed zone where a "built-up edge" of crushed rock is created, a secondary crushed zone where the macroscopic fracture crack is crushed to fine cutting chips, and an overcutting zone where no substantial resistance exists due to the absence of coarse chips, as shown in Fig. 2.9. Kadiu (Kadiu, 1994) proposed yet another brittle mode rock cutting mechanism which is very similar as Nishimatsu's but focusing on the force variation during the rock removal process.

In short, all the above-mentioned rock removal mechanisms can only qualitatively explain a very limited range of rock cutting phenomena under quite unrealistic assumptions. No complete mechanism is developed to accurately predict rock failure behavior with respect to various rock properties and process parameters. These questions constitute a very big challenge in rock cutting.

2.2 Loading force predictions

Force responses have been considered to be consistent with the rock removal process (Zeuch and Finger, 1985). An increase of the total force exerted by the cutter can indicate an increase of the affected rock crushing zone at the rock-cutter interface while a quick drop of it can reveal the formation of a chip segment. Since force data is always very easy to collect and record, force responses are commonly used to indicate the cutter's performance and evaluate the accuracy of rock cutting theories.

Starting from the first analytical cutting theory for metal cutting processes developed by Merchant (Merchant, 1944, 1945), many cutting theories have been proposed to predict the loading forces at the tool/rock interface during rock cutting. Some of them emphasize the effects of stress distribution and failure criteria on loading force variations (Detournay and Atkinson, 2000; Evans, 1984; Hurt and Evans, 1981; Nishimatsu, 1972). Some of them focus on the relation between geometrical parameters and the loading forces (Clayton et al., 2005; Evans, 1965; Evans, 1984; Gerbaud et al., 2006; Glowka, 1989b; Hibbs and Flom, 1978; Maurer, 1966; Rånman, 1985), others deal with the loading forces from the viewpoint of energy distributions (Detournay and Defourny, 1992; Detournay et al., 2008; Rånman, 1985). Several experimental methods were also exploited to figure out the relation between the loading forces and other process parameters during

rock cutting processes (Coudyzer and Richard, 2005; Liu et al., 2009a; Quickelberghe et al., 2006). This section reviews several significant works done that are related to loading force prediction issues.

Merchant (Merchant, 1944) put forward the first cutting theory in metal cutting, which was used in rock cutting processes with plastic material properties. Based on Coulomb's criterion and the shear plane assumption (Merchant, 1944, 1945), Merchant's cutting force equation can be expressed by (Boothroyd and Knight, 1989):

$$F_c = \tau_s A_c \frac{\cos(\beta - \gamma)}{\sin\varphi \cos(\varphi + \beta - \gamma)} \tag{2.1}$$

where τ_s is the shear strength of the work material on the shear plane, β is the mean angle of friction between the chip and tool, φ is the shear angle, γ is the working normal rake angle (or back rake angle in rock cutting), and A_c is the cross-sectional area of uncut chip as shown in Fig. 2.10. In Merchant's model, φ can be derived based on the assumption of minimum cutting force, i.e.:

$$\varphi + \beta - \gamma = \frac{\pi}{2} \tag{2.2}$$

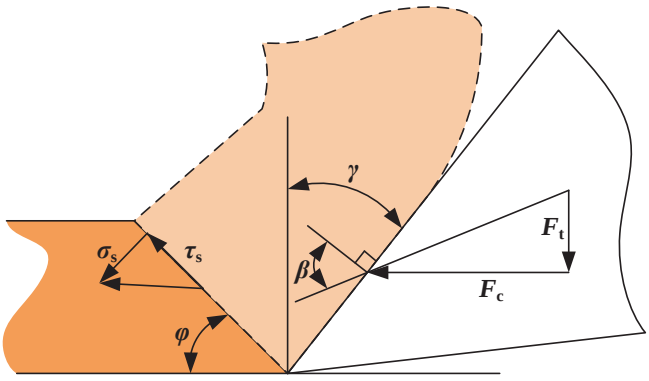

Figure 2.10: Schematic of Merchant and Nishimatsu's cutting models.

Considering the wear phenomena of the drag bit, Fairhurst and Lacabanne proposed that the forces on a drag bit along the wearflat can be expressed by (Fairhurst and Lacabanne, 1956):

$$F_t = pA_f \tag{2.3}$$

$$F_c = F_{cr} + \mu pA_f \tag{2.4}$$

where F_t and F_c are the vertical and horizontal components of the resultant force, F_c is the cutting force exerted by the diamond/rock interface, A_f is the area of the flat, p is the contact pressure under the bit, and μ is the coefficient of friction at the wearflat of the cutter/rock interface (Fig. 2.11). Based on Mohr's criterion of failure and the specific stress distribution assumption, Nishimatsu proposed a formula for the cutting force in rock cutting by a wedge-shaped tool, which can be described by (Nishimatsu, 1972):

$$F_c = \frac{2}{n+1} \cdot \tau_s A_c \cdot \frac{\cos k_f}{1-\sin(k-\gamma+\beta)} \cdot \cos(\beta-\gamma) \tag{2.5}$$

where n is the stress distribution factor and k_f is the angle of internal friction (Fig. 2.10). The methodology was developed to determine the parameters in the formula by comparing the test results with the proposed theory. Although it is similar as Merchant's, Nishimatsu's model is more realistic for the description of rock cutting processes due to its brittle mode failure criterion. Nishimatsu's model is used to describe the discontinuous cutting process with chips that are periodically formed and sheared off. However, the model fails to accurately predict the cutting forces under continuous cutting process conditions with inhomogeneous rock properties.

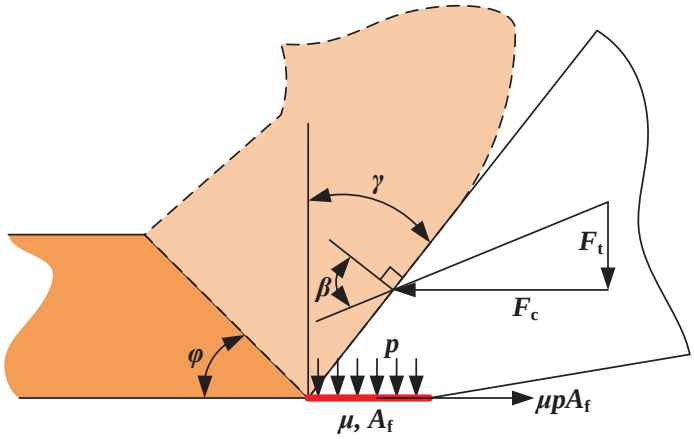

Figure 2.11: Force responses in Fairhurst and Lacabanne's rock cutting model.

Based on an empirical fit to laboratory drilling data, Warren et al. (Warren and Sinor, 1989) proposed a PDC cutter force model that introduces a bit factor to combine the performance of individual cutters and of the full scale bit. The penetrating force, i.e., thrust force was given by:

$$F_t = c_1 \frac{\cos(\beta - \gamma)}{1 - \sin(\beta - \gamma)} B_F S_R A_c + c_2 S_R A_w \tag{2.6}$$

where B_F is a bit factor to account for unexplained effects for a particular bit, S_R is a relative rock strength calculated from drilling data that is roughly proportional to the compressive strength of the rock, and c_1 and c_2 are constants obtained from drilling data. The cutting force is considered to be dependent on both the friction at the cutter/rock interface and the force required for the fracture the rock, i.e.:

$$F_c = c_3 \frac{\sin(\beta - \gamma)}{1 - \sin(\beta - \gamma)} S_R A_c + c_4 F_t \tag{2.7}$$

where c_3 and c_4 are constants calculated from drilling data. This model has been confirmed in laboratory tests with Carthage Marble, Berea sandstone, and Catoosa shale.

Glowka (Glowka, 1989b) developed a practical conceptual model of the rock cutting process to provide a mathematical description of the thrust and cutting forces applied during the process. The primary parameters affecting the thrust and cutting forces were studied including the rock type, cutter design, wear state, position on the bit, cutter interaction effect, cutting speed, rock stress state, and fluid environment. Significant experimental results showed that the thrust force over the wearflat area of the worn cutter has a power relationship with the depth of cut. Moreover, the drag coefficient K_d, defined as the ratio of the cutting force to the resultant force, i.e.:

$$K_d = \frac{F_c}{F} \tag{2.8}$$

varies with rock type but is relatively independent of the depth of cut and wearflat area. The drag coefficient also reduces quite significantly under jet-assisted, non-interacting cutting tests, compared with dry cutting tests. This observation is explained by the lubricating effect of water (Glowka, 1987) and indicates the effect of friction at the wearflat on the cutting force.

Detournay et al. (Detournay and Defourny, 1992) adopted the force response mechanisms of a drag bit, firstly developed by Fairhurst et al. (Fairhurst and Lacabanne, 1956) and experimentally verified by Glowka (Glowka, 1987), to build cutting force models (D-D model) for both sharp and worn cutters by introducing three characteristic constants: the intrinsic specific energy ε, the ratio of the vertical to horizontal force at cutter/rock interface ζ, and a coefficient of friction μ. For sharp cutters, the cutting and thrust forces can be expressed by:

$$F_c = \varepsilon A_c \tag{2.9}$$

$$F_t = \zeta \varepsilon A_c \tag{2.10}$$

For worn cutters, the friction force acting across the wearflat should also be considered, i.e.:

$$F_c = (1 - \mu\zeta)\varepsilon A_c + \mu F_t \tag{2.11}$$

Figure 2.12 shows the force response in the D-D model. Since all the characteristic constants can be completely determined through regular experimental results, the D-D model provides a convenient way to predict the force response at the cutter/rock interface. However, the D-D model can only describe the cutting process under the plastic mode of rock failure, i.e., when the rock fails like a plastic material (Adachi et al., 1996). This limits its applicability in predicting force responses under brittle modes of rock failure, i.e., when the rock fails as a brittle material. In fact, the plastic mode can be observed in sedimentary rocks only if the depth of cut is very small while the brittle mode is more commonly observed where the forces oscillate periodically due to the brittle failure mechanism.

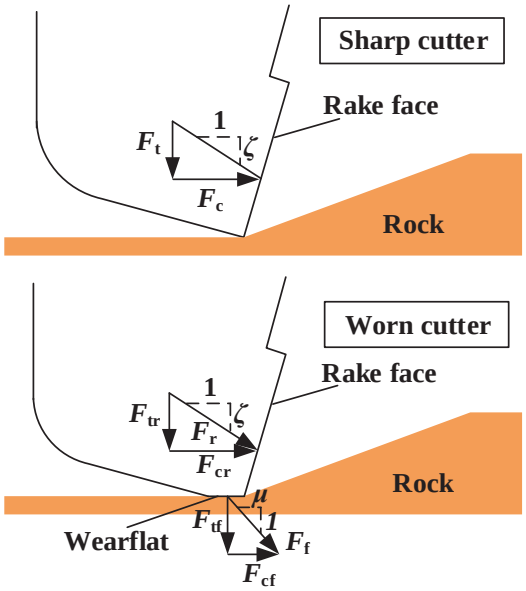

Figure 2.12: Force components in the D-D model (Detournay and Defourny, 1992).

Guo et al. (Guo et al., 1992) developed a cutting theory to describe the chipping of rock based on linear elastic fracture mechanics. Only cracks due to tensile stresses were modeled based on a displacement discontinuity method (Guo et al., 1990). A more realistic model was given by Yan (Yan, 1997) who assumed that the whole cutting process included indentation and fragmentation and used a linear elastic material model to derive the stress distribution at the rock-cutter interface. A force model was given based on the equilibrium of forces on the chip. However, Yan's model can only predict the force used for chipping the rock.

Xue et al. (Xue et al., 2009) provided a new method to combine the crushing and chipping processes. They assumed a small crushing zone beneath the cutter which initiates a crack and finally forms a chip. From the physical point of view, their model was in good agreement with the above-mentioned chipping-crushing hybrid failure mode. However, changes in the cutting and thrust forces exerted on the rake face of the cutter with respect to the rake angle cannot be well captured in their model due to the fixed shape of the crushed rock zone at the rock-cutter interface, which, in fact, has been observed in many other papers (Che and Ehmann, 2014; Che et al., 2015b; Huang et al., 2013). Moreover, their model can only predict the chipping process that initiates from the bottom of the crushed rock zone, which is not always true in real cutting practice.

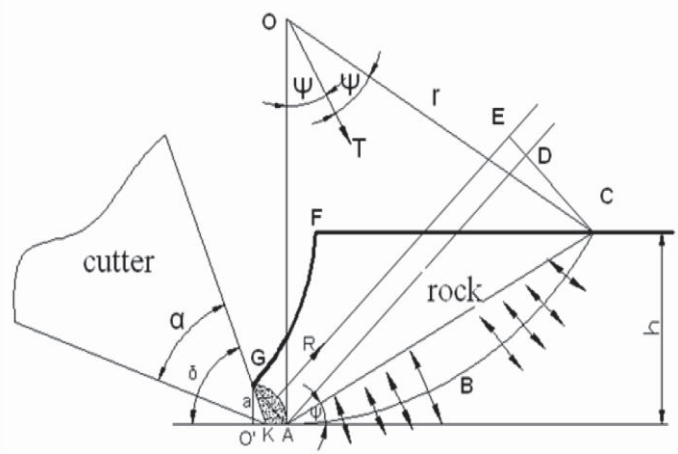

Figure 2.13: Crushing and chipping in Xue et al.'s model (Xue et al., 2009).

Recently, it has been shown that forming a noticeable annular chamfer on the cutting edge of the PDC cutter's diamond layer can enhance durability of the diamond layer, reduce spalling and fracture tendency during the initial stages of the drilling process (Beuershausen, 2004). In order to consider the significant effects of chamfered geometry on bit rate of penetration (ROP) and weight on bit (WOB)/torque on bit (TOB) relationship, Clayton et al. (Clayton et al., 2005) proposed a new cutter/rock interaction model to predict the applied forces during the cutting process. They divided the cutting edge of the cutter into three surfaces, namely, cutting face surface, chamfer surface and cylinder surface, responding to three forces including cutting force, axial force and radial force on each of them as shown in Fig. 2.14. Similarly, Gerbaud et al. (Gerbaud et al., 2006) suggested a new cutter/rock interaction model to include the effects of chamfer, side and back rake angles of the cutter. They introduced the built-up edge of crushed materials on the cutting face that was observed by Zijsling (Zijsling, 1984) and Chaput (Adachi et al., 1996) to provide a very good evaluation of the back and side rake angle effects on PDC forces. The introduction of the back

cutter forces also provides a way to evaluate cutter forces and to optimize process parameters. Figure 2.15 shows the resultant force in Gerbaud's model decomposed into three components:

$$F = F^{c} + F^{ch} + F^{b} \tag{2.12}$$

where F^{c}, F^{ch}, and F^{b} denote forces acting on the cutting face surface, chamfer surface and back cutter surface, respectively.

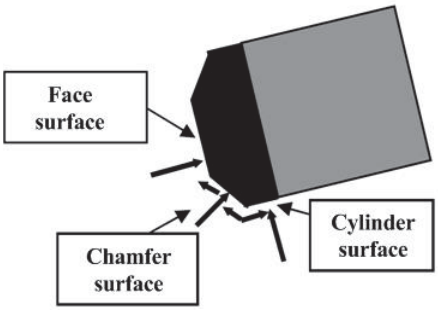

Figure 2.14: Characteristic surfaces in Clayton's model (Clayton et al., 2005).

Some laboratory and field tests have been conducted to explore the cutting force response with respect to various design and process parameters. Hibbs and Flom reported that the forces necessary to cut the rock are minimized with negative cutter back rake angels between -10 and -20 degrees independent of cutting speed and depth of cut (Hibbs and Flom, 1978). However, no direct relation between rock cutting force and cutting speed was found in their designed tests. They did not discuss the effect of the rake angle on the inclination of the cutting force vector, which was experimentally studied by Coudyzer and Richard (Coudyzer and Richard, 2005). They found that force inclination was strongly affected by the back rake and side rake angles corresponding to two specific planes. Besides, the specific energy and force magnitude increase with the increase of the back rake angle. The force response variation of the worn PDC bits, as it evolves with time, was

investigated by Quickelberghe et al. (Quickelberghe et al., 2006). They separated the force response into two distinct regimes: In the first regime, where the depth of cut is shallow, the evolution of drilling forces with respect to the depth of cut is controlled by the frictional process over the wearflat. In the second regime, where the maximal forces admissible on the wearflats are mobilized, the evolution of the drilling forces is governed by the cutting process over the cutting face. Moreover, Detournay et al. (Detournay et al., 2008) found another regime of the force response in the very late phase of the drilling process where the force response turns dependent on the loading path due to poor cleaning in the borehole.

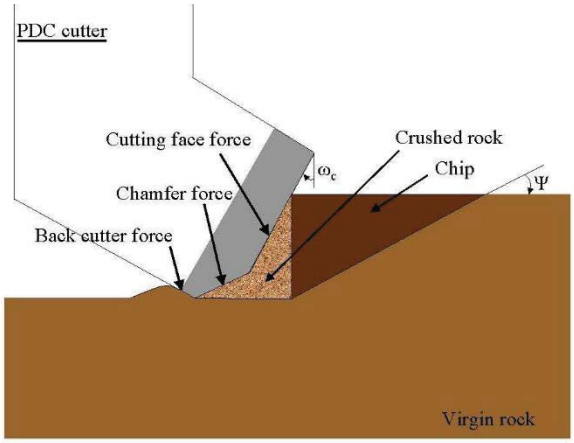

Figure 2.15: Characteristic forces in Gerbaud's model (Gerbaud et al., 2006).

Although all the above-mentioned cutting force analytical models provide quite effective ways to predict loading under quasi-static conditions and plastic or brittle rock failure modes, they fail to accurately predict the dynamic response of the cutter/rock interface where plastic and brittle rock failure modes are simultaneously happening during realistic drilling processes. Moreover, although the effects of design and process parameters were investigated in

various ways, no analytical models were put forward to exactly describe the effects of these parameters on the rock cutting force response. This probably results from the limitation of a commonly used standard to classify each aspect of the designs of the cutter geometry and rock cutting processes into specific categories. For instance, the chamfer style and the governing parameters should be standardized.

2.3 Temperature predictions

In rock cutting processes, the temperature at the cutter/rock interface significantly affects the PDC cutter's performance including its wear rate, drillability, and impact resistance under field conditions. The WC/Co bond at the diamond-stud interface was reported to damage very quickly when the temperature goes beyond 700°C (Feenstra, 1988). Based on experimental results, a more restrictive temperature limit was later on proposed with the value of 350°C (Glowka and Stone, 1985; Ortega and Glowka, 1984).

Glowka and Stone (Glowka and Stone, 1985) built a finite element thermal model of single PDC cutters to predict the average wearflat temperature under steady-state and transient downhole conditions which demonstrates the obvious adverse effects of wearflat temperatures on cutter wear rates. The fraction of the frictional heat created during the sliding along the cutter-rock interface assumed to flow into the cutter was expressed by (Glowka, 1989a):

$$\alpha_c = \left[1 + \frac{3\sqrt{\pi} k_r}{4} \left(\frac{V_c}{\chi L} \right)^{1/2} f \right]^{-1} \tag{2.13}$$

where k_r is the rock's thermal conductivity, χ is the rock's thermal diffusivity, L is the cutter wearflat length parallel to the cutting direction (Fig. 2.16), f is defined as the cutter thermal

response function which can be determined with two-dimensional numerical models, and V_c is the cutting speed as shown in Fig. 2.16. Therefore, the mean temperature between the rock and the cutter along the wearflat can be expressed by (Glowka, 1989a):

$$\overline{T}_r = \overline{T}_w = T_f + \frac{\alpha_c \mu F_t V_c}{A_w} f \tag{2.14}$$

where $\overline{T}_r$ and $\overline{T}_w$ denote the mean temperatures of the rock and the cutter separately, T_f is the initial rock formation temperature prior to frictional heating, F_t is the thrust force shown in Fig. 2.16, μ is the friction coefficient between the cutter and the rock which can be experimentally measured, and A_w is the wearflat area.

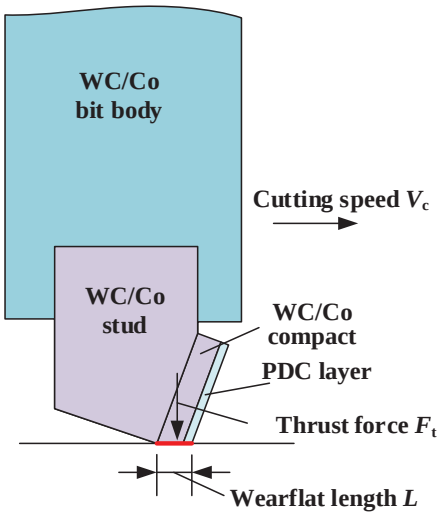

Figure 2.16: Configuration of the cutter/rock interface in Glowka's model.

Based on experimental results, a more restrictive temperature limit was proposed with the value of 350°C, rather than the 750°C limit assumed before (Glowka and Stone, 1985; Ortega and Glowka, 1984). The increase of WOB significantly increases the temperature of the wearflat and in turn exacerbates cutter wear, which indicates a tradeoff between ROP and bit life. Moreover,

the friction at the cutter/rock interface was found to significantly elevate the interface temperature, which determines the wear rate of PDC cutters (Glowka, 1989a).

Zijsling (Zijsling, 1984) developed a theoretical thermal model similar to Glowka's (Glowka, 1989a) to predict the temperature distribution in PDC cutters mounted on a bit under quasi-static drilling conditions. He found that the maximal temperature occurs at the PDC cutters' cutting edge and can be alleviated by reducing ROP and diamond layer thickness, or increasing the number of cutters on a bit. In metal cutting and micro-machining processes, a stable built-up edge, also called stagnant region, has been reported to be formed under specific process conditions by many researchers (Abdelmoneim and Scrutton, 1974; Liu et al., 2004; Ohbuchi and Obikawa, 2003; Waldorf et al., 1998). Similarly, the built-up edge is also observed to form under the cutting edge of the PDC cutter during rock cutting processes (Zijsling, 1984). This built-up edge was found to resist heat conduction and can be eliminated by cleaning and cooling with a drilling fluid.

All of the above investigations indicate the significant effect of the cutter temperature on the cutter's wear rate. However, Glowka's and Zijsling's models are both built on the heating model of a sliding, square heat source proposed by Jaeger (Jaeger, 1942) which can only predict the mean temperature rise of the total or a part of the wearflat rather than the temperature distribution all over the wearflat. In addition, the cutter/rock interaction is generally too intense to approach quasi-static drilling conditions. For these reasons, their models fail to accurately predict thermal effects on the cutter's performance. In 1993, the first direct experimental measurement of the temperature and the wear rate of the cutter given by Appl et al. (Appl et al., 1993) has shown that the wear rate of the cutter is not constant as the average wearflat temperature is constant, which indicates that a modification should be done to the previous thermal models.

In fact, the accurate measurement of the temperature and heat flux responses on the PDC cutters is still a big challenge. A widely-used method is to attach commercial thermocouples on PDC cutters. In this way, the temperature responses at specific spots on or beneath the cutter's surface can be captured during rock cutting processes. The work done with this method can be found in (Cools, 1993; Freeman et al., 2012; Loui and Karanam, 2005; Wilson and Vorono, 2003). However, the large dimensions and applicable attaching methods result in low sensitivity, low response speed, and difficult attachment of commercial thermocouples.

2.4 Numerical modeling of rock-cutter interactions

Recently, numerical methods, e.g., the finite element method (FEM) (Jaime et al., 2010; Liu et al., 2002b; Mendoza et al., 2011; Saouma and Kleinosky, 1984), the discrete element method (DEM) (Akbari et al., 2011; Block and Jin, 2009; Huang et al., 1999; Mendoza et al., 2010; Rojek et al., 2011) and the continuum method, e.g., FLAC (Cai et al., 2007; Tulu and Heasley, 2009), have gradually become the most promising methods for investigating the intrinsic mechanisms involved in rock cutting processes due to the ever increasing computational capabilities. Numerical methods generally outperform traditional analytical methods owing to their robust capability of solving highly non-linear problems associated with the phenomena at the rock-cutter interface. Moreover, the numerical methods can also provide predictions and visualizations of the stress/strain field, temperature gradients, and heat flux contours which are currently quite difficult to ascertain by regular analytical and experimental methods.

As an essential part of the numerical methods, the modeling of the rock material poses an extremely complex challenge due to the complexity of the physical characteristics and phenomena

involved, including the inhomogeneity and dilatancy of the rock, elastic-plastic deformation, crack initialization and propagation, complex contact/friction conditions, chip formation mechanism, and thermo-mechanical coupling.

Yu (Yu, 2005) modeled rock as an elastic material before failure and exploited the tensile and shear failure criteria to govern the failure of the rock material in a commercial FEM code. Liu (Liu, 2002) applied integrated image analysis and a numerical modeling method to fully on-line simulate the fracture behavior of a granite specimen as shown in Fig. 2.17. In his method, integrated image analysis was applied to simulate the microscopic elements of the rock sample, Weibull's (Weibull, 1939) and Freudenthal's (Freudenthal, 1968) statistical theories were used to simulate the failure of the heterogeneous material, and the Monte Carlo method was used to provide the random conditions. Later on, Liu et al. (Liu et al., 2002a) developed a rock and tool interaction code, namely, R-T^{2D}, to simulate the fracture process in cutting heterogeneous brittle materials (Fig. 2.18). The effects of back rake angle on stress distribution and cutting efficiency were investigated based on the R-T^{2D} code.

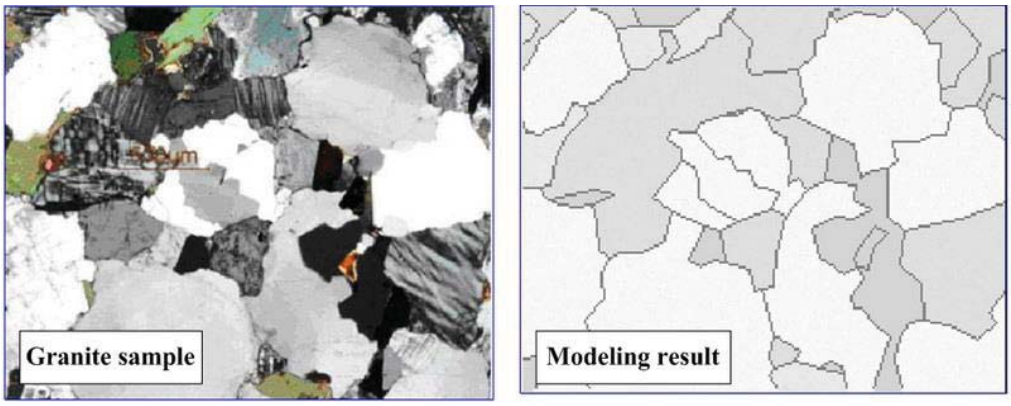

Figure 2.17: Modeling of rock using the R-T^{2D} method (Liu, 2002).

To obtain accurate predictions of force responses and rock's failure behavior, Jaime et al. (Jaime et al., 2010) used a very complex concrete damage model to model chip formation during rock cutting with the commercial FEM code LS-DYNA. More than 20 parameters without straightforward physical meanings had to be carefully calibrated based on experimental data and curve fitting techniques. Similarly, Wilt and Chowdhury (Wilt and Chowdhury, 2011) used the same material model but very different parameters to simulate the failure response of concrete structures due to large impact. In a large body of literature, sophisticated methods for parameter calibration are given to enable the capability of material models to accurately represent rock properties. A series of calibration tests have to be conducted again and again when different rock formations are involved.

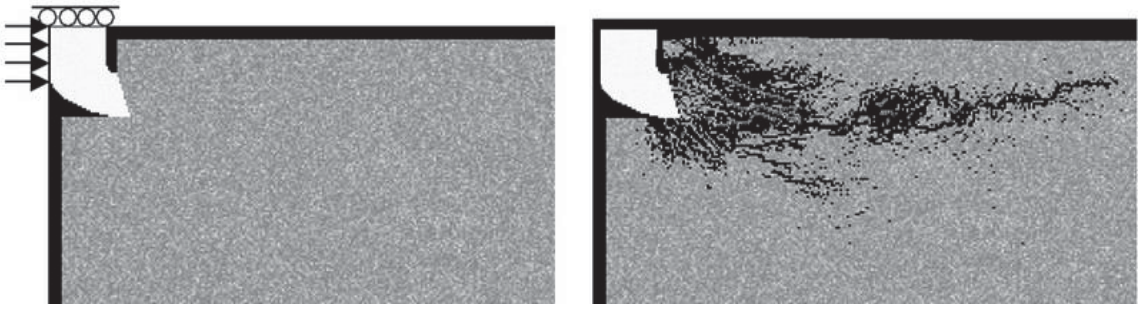

Figure 2.18: Rock cutting modeling using R-T^{2D} code (Liu, 2002).

Bilgesu et al. (Bilgesu et al., 2008) developed a parametric FLAC3D (Fast Lagrange Analysis of Continuum 3D) model to simulate the natural rock properties and failure processes. They generated a parametric grid of the rock specimen along the vertical and radial directions with consistent element sizes and varied grid density. The initial elastic and subsequent plastic behaviors of the rock were described by the strain-softening Mohr-Coulomb model.

Tulu and Heasley (Tulu and Heasley, 2009) proposed the use of the FLAC3D code to simulate the cutter-rock interaction. The model parameters were calibrated and compared to single cutter laboratory tests of the average thrust and cutting forces on the cutter. The rock model is built based on a sophisticated parametric grid generation method. The propagation of the crack is simulated by the failure of the element zones according to the Mohr-Coulomb criterion.

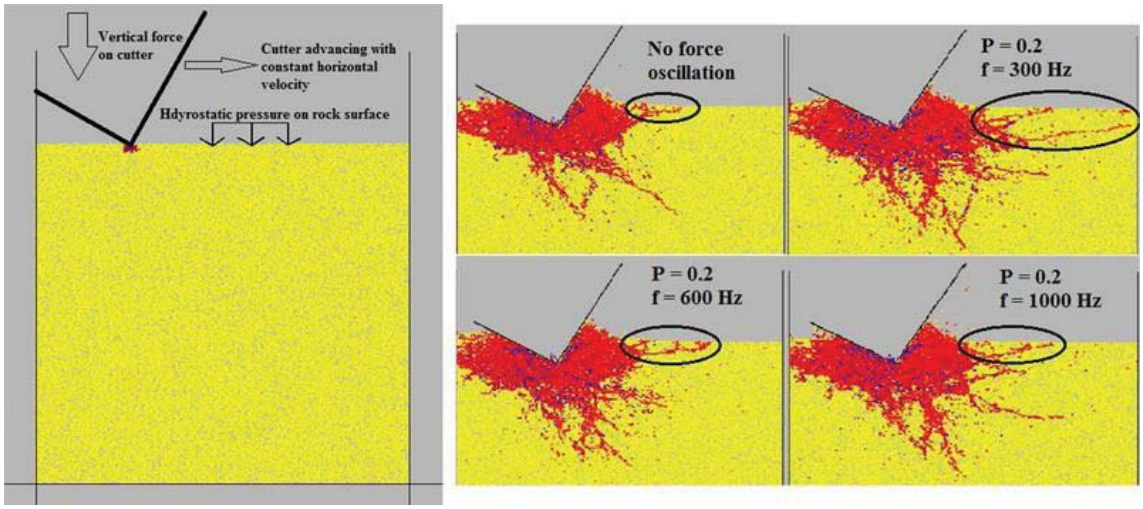

Figure 2.19: Boundary condition setup and simulation results of rock cutting processes (Akbari et al., 2011).

Akbari et al. (Akbari et al., 2011) exploited the DEM to study the bit-rock interactions and failure and penetration mechanisms. In this model, the rock sample was generated based on a material genesis function library of PFC developed by ITASCA International Inc. The loading conditions (thrust force and hydrostatic pressure), contact properties (friction coefficient), and boundary conditions were given to simulate realistic borehole conditions. They found that oscillations in magnitude of WOB can increase ROP under lower bottom-hole pressure which

indicates that axial-vibration-assisted PDC bit rotary drilling shows better performance than the conventional PDC bit drilling process with constant WOB, as shown in Fig. 2.19.

Block and Jin (Block and Jin, 2009) used a commercial 2D discrete element method code PFC^{2D} (two-dimensional particle flow code) to model shale cutting dynamics using a single PDC cutter. A Mohr-Coulomb criterion based linear failure envelope was used to characterize the brittle failure of the shale, as well as a semi-elliptical cap initiated at the brittle-ductile transition was used to describe the ductile failure of the shale. Results indicate a predominant relationship between rock failure modes (brittle to ductile) and chip morphology (chip-like to ribbon-like), as shown in Fig. 2.20. Su and Ali Akcin (Su and Ali Akcin, 2011) adopted statistical and regression methods to simulate rock behavior in an approximate way by using a computer program named particle flow code in 3 dimensions (PFC^{3D}), as shown in Fig. 2.21.

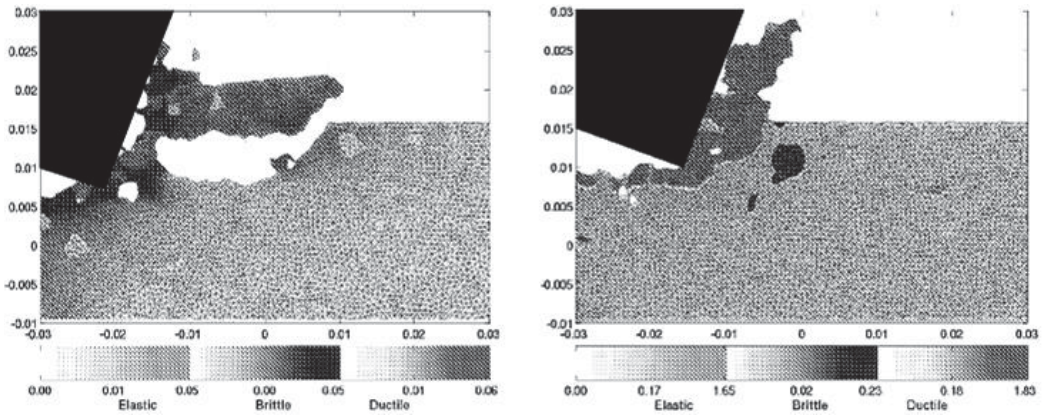

Figure 2.20: The results of rock cutting modeling using the PFC^{2D} code (Block and Jin, 2009).

Although they offer very good pictures of the whole process consisting of crushing, shearing, and cracking for given conditions, most of these models can only provide qualitative predictions of the rock cutting process with extremely sophisticated calibrations and experimental evaluations.

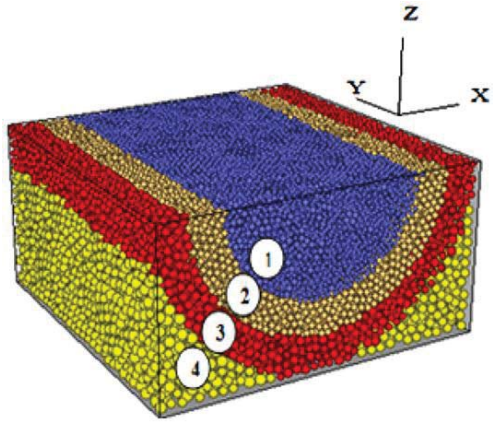

Figure 2.21: Modeling of rock using the PFC^{3D} method (Su and Ali Akcin, 2011).

2.5 Experimental investigations in rock cutting

The in-situ sensing and measurement of temperature and force at the tool-workpiece interface is extremely important to clarify the mechanisms in various cutting processes and to provide empirical information for the formulation of thermo-mechanical coupled cutting theories. Moreover, various testing methods are exploited to explore the properties of rock since they are essential for providing the fundamental knowledge required for explaining cutter/rock interactions. These measuring and testing methods enable the experimental investigation in the rock cutting area. In this section, several testing technologies for the measurement of force/temperature responses and of the rock's properties will be briefly introduced, followed by a review on the experimental investigation done in rock cutting.

2.5.1 Force measurement

Force measurement is an extremely essential element not only in the formulation and verification of cutting theories but also in the monitoring and controlling of the industrial level processes. A series of dynamometers are used to sense the characteristic force components in metal

cutting based on various principles of measurement such as strain-gauge dynamometers, electric transducers, piezoelectric dynamometers, etc. Comprehensive reviews of various force measurement methods are given by Shaw (Shaw, 2005) and Byrne et al. (Byrne et al., 1995). Similar technologies are also used to measure forces and torques in rock cutting/drilling processes. Wilson and Vorono (Wilson and Vorono, 2003) experimentally measured the cutting forces of a single PDC cutter during granite turning experiments, using a Lebow strain-gauge dynamometer. Similar experiments were conducted by Kaitkay and Lei (Kaitkay and Lei, 2005) using a Kistler 3-component pieozoelectric dynamometer. Moreover, Leseultre et al. (Leseultre et al., 1998) installed accelerometers, strain gauges and contact sensors to produce direct measurements of down-hole WOB and TOB. Several other works related to instrumentation setup on PDC bits to measure and monitor forces can be found in (Sullivan et al., 2003; Zaleski and Schmidt, 1998; Zhang et al., 2003). Limitations of the above-mentioned methods still exist, for example commercial dynamometers are unsuitable for force-based monitoring due to the absence of overload protection and their high costs (Byrne et al., 1995). Moreover, leakage effects of piezoelectric dynamometer may cause errors during the measurement of static forces (Shaw, 2005). All in all, more efficient and robust technologies with a higher frequency bandwidth are still desired due to the hostile working environment in which rock cutting/drilling processes are performed.

2.5.2 Temperature measurement

There are a number of direct or indirect sensing and measurement methods to experimentally investigate temperature evolutions at the tool-workpiece interface. Some of them can only measure

the average temperature at the specific area, while others can be used to determine the temperature distribution near the cutting edge.

Thermocouple techniques (e.g., work-tool, embedded thermocouple, thin film and dynamic thermocouples) are commonly used in metal machining processes to study cutting temperatures based on thermoelectric effect of various thermocouples. Some researchers have exploited thermocouple techniques to monitor the temperature change during rock cutting processes (Cools, 1993; Loui and Karanam, 2005; Ortega and Glowka, 1984; Wilson and Vorono, 2003)). Although it can directly determine the average temperature in a specific area near the cutting edge, this technique is limited due to its inability to indicate temperature distributions. Therefore radiation methods including infrared radiation pyrometers and infrared photography were exploited to determine the temperature distribution at the tool-workpiece interface. Relevant research can be found in (Lin, 1995; Prins, 1971; Ueda et al., 1985).

Up to now, temperature measurements are still facing numerous difficulties and limitations during rock cutting processes. For instance, traditional temperature measurements in the vicinity of the interface were obtained by using relatively large sensors, which were either destructively inserted into the tool or surface-mounted far away from the interface to avoid sensor damage (Appl et al., 1993; Martin and Fowell, 1997). Moreover, infrared methods always have a relatively low signal-to-noise ratio and are sensitive to vibrations and mists (Stephenson, 1993).

Very recently, in response to the above-listed barriers and needs, embedded micro thin film thermocouples (μ-TFESs) which can provide unprecedented capabilities for sensing temperature data very close to tool-workpiece interface during machining (i.e., 75-450 μm from the tool's rake face and 100-500 μm from tool's flank face) were developed as shown in Fig. 2.22. The embedded

sensor array characterized by sensor junctions of 5 μm × 5 μm was able to sense both the steady and the transient cutting temperature fields. The μ-TFESs, fabricated by MEMS techniques, were embedded into PCBN tools through diffusion bonding techniques. The same technology, if suitably extended, can be exploited in rock cutting/drilling processes performed by PDC cutters/bits as well. This could provide accurate in-situ information, a few hundred micrometers away, from the rock/PCD cutter interface and shed more light on the mechanics and dynamics of rock cutting.

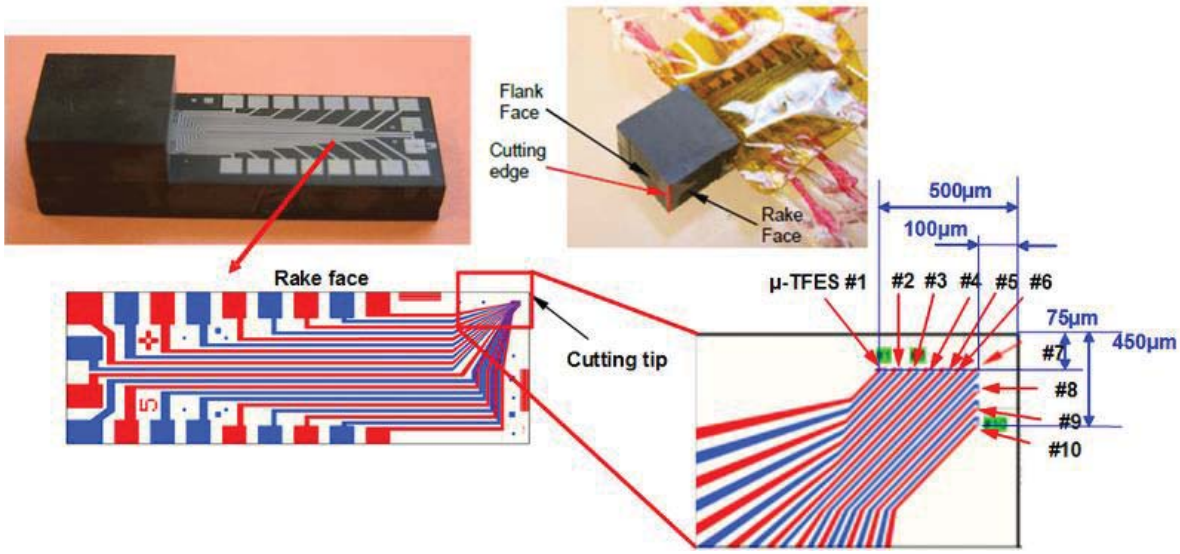

Figure 2.22: Micro thin film embedded sensors on a PCBN cutting tool adapted from (Werschmoeller et al., 2011; Werschmoeller and Li, 2011).

2.5.3 Rock property testing methods

The types of rock met in PDC bit drilling processes include shale, limestone, marble, granite, etc. Testing methods are needed to explore the properties of rock since they are essential for providing the necessary fundamental knowledge required for explaining cutter/rock interaction. Among many complex rock properties, the basic ones of concern in PDC bit rock cutting

experiments are compressive strength, hardness, grain size, composition, and availability (i.e., the level of difficulty to find it in nature) (Hibbs and Flom, 1978).

These are grouped into two categories: (1) static methods that include uniaxial compression (Eberhardt et al., 1999; Wawersik and Fairhurst, 1970), triaxial compression (Hallbauer et al., 1973; Lenoir et al., 2007; Sulem and Vardoulakis, 1990), multiaxial compression (Amadei and Robison, 1986), diametral compression (Brazilian test) (Guo et al., 1993; Jaeger and Hoskins, 1966), hollow cylinder test (Lee et al., 1999; Santarelli and Brown, 1989), torsion and bending (Nara and Kaneko, 2005; Paterson and Olgaard, 2000), and nondestructive test methods (Hardy, 1971; Lockner, 1993; Withjack, 1988), and (2) dynamic methods that include the resonant bar method (Guyer et al., 1998; Johnson et al., 1993; Lucet et al., 1991) and the ultrasonic pulse method (Rao and Ramana, 1992; Thill and Bur, 1969).

Among the above-mentioned static methods, none of them can measure rock mechanical properties in-situ. On the other hand, although the dynamics methods can measure the elastic behavior and failure behavior of the rock in-situ, most of the testing results are not straightforward enough to reflect the mechanical properties of the rock. Recently, Richard et al. (Richard et al., 2012) developed an experimental methodology to directly extract in-situ rock strength information from results of cutting tests. In their methodology, the internal friction and the uniaxial compressive strength of the rock can be monitored on-site which reflects variations of rock properties, based on the aforementioned D-D rock cutting model (Detournay and Defourny, 1992). However, more experiments with various types of rock are still required to quantitatively validate their method.

2.5.4 Rock cutting tests on single PDC cutters

Complex down-hole conditions are occurring at the interface between PDC bits and rock formations in oil/gas well drilling processes. These conditions are difficult to be fully repeated under laboratory conditions. Moreover, PDC cutters are always brazed to a drill bit body in a complex spatial arrangement. This makes it difficult to extract information of the force responses on an individual cutter from that of the resultant force responses of the whole bit.

In order to simplify the interaction between the PDC cutter and rock and simultaneously maintain a meaningful representation of the down-hole conditions, many different testing methods have been developed to advance the understanding of the cutting mechanics involved in rock drilling and qualify/evaluate the cutting performance of various types of PDC cutters. Most of them only focus on the study of a single PDC cutter's performance during rock cutting. In fact, the study of the performance of single PDC cutters can help to provide deeper insights into the mechanism of rock drilling processes using PDC bits. Since it only concerns a single cutter rather than all the cutters on a bit that are subjected to complex cutting and cleaning conditions, single PDC cutter studies are more effective in interpreting the intrinsic mechanisms during rock cutting/drilling processes than full-scale bit studies (Zijsling, 1987).

According to the cutting motions between rock and cutters, the testing methods used in rock cutting tests can be divided into four categories, i.e., rotational cutting (Bellin et al., 2010; Che et al., 2015b; Durrand et al.), linear cutting (Aluko and Seig, 2000; Che et al., 2014a; Copur, 2010), impacting (Franca, 2011; Li et al., 2010) and hybrid cutting (Balci, 2009; Li et al., 2001). During each test, mechanical responses, e.g., force (Che and Ehmann, 2013; Geoffroy and Minh, 1997) and torque (Hamade et al., 2010; Rao et al., 2002) and thermal responses, e.g., temperature (Appl

et al., 1993; Che et al., 2015a; Che et al., 2014c; Wilson and Vorono, 2003) are captured and analyzed based on the techniques introduced in the previous sections.

Among all these testing methods, linear cutting of rock is the most straightforward and convenient candidate to reveal the intrinsic mechanisms of rock-cutter interactions due to its simplicity offered by the linear motions.

In regard to linear rock cutting tests Cheatham and Daniels (Cheatham and Daniels, 1979) conducted a series of tests to investigate the influences of cutter configurations, rock properties and drilling fluid pressures on the drillability of shales. They recommended negative rake angles to improve the cutting efficiency and found that cutter shapes did not affect the cutting force responses in drilling of shale. However, the rock-cutter interactions were not discussed in detail. Later on, Finger and Glowka (Finger and Glowka, 1989) developed a rock cutting testbed to explore the cutting mechanisms involved in the linear rock cutting process. The failure of rock was proposed to take place due to crushing and tensile fracture in hard rock cutting while due to shearing action in soft rock cutting. On the other hand, crushing and tensile breakage was recently suggested to take place in soft rock cutting instead of shearing by Xue et al. (Xue et al., 2009).

Kaitkay and Lei (Kaitkay and Lei, 2005) applied external hydrostatic pressure on Carthage marble samples during linear cutting conducted with a single PDC cutter. Chip formation was found to transit from the brittle to the plastic failure mode at a certain confining pressure. Their findings are in accord with earlier experimental results mentioned in Verhoef and Ockeloen's paper (Verhoef and Ockeloen, 1996). However, the effect of the rock's mechanical properties, as an essential factor in the chip formation phenomena, was not investigated in their work. Tiryaki and Dikmen (Tiryaki and Dikmen, 2006) used data from linear cutting tests performed by standard

chisel picks to statistically correlate the specific cutting energy with the rock's mechanical properties such as Poisson's ratio, Brazilian tensile strength, and uniaxial compressive strength (UCS). The Poisson's ratio was found to be the most relevant parameter in linear rock cutting from the statistical point of view. A similar correlation between the specific cutting energy and the rock's mechanical properties was subsequently found to be consistent in both full- and small-scale linear rock cutting tests (Balci and Bilgin, 2007).

It should be noted that the cutters applied in the above-mentioned linear cutting tests generally have a curved cutting edge aiming to avoid stress concentrations during cutting. Although the tangent to a given curved cutting edge at specific locations can be set to be perpendicular to the cutting speed direction in rock cutting tests, the overall cutting process belongs to an oblique cutting rather than to an orthogonal cutting configuration. On the other hand, Richard et al. (Richard et al., 2012) exploited a cutter with a straight cutting edge to linearly scratch rock samples. The average cutting force and the rock's USC were found to be correlated with each other. They proposed that the scratch tests, i.e., the linear rock cutting tests can be used to determine the rock's strength in a very short time. However, the discrepancies between the rock's USC and its prediction were quite obvious in many cases.

Another extremely important testing method is the face turning of rock samples on a lathe. The face turning of rock is capable of simulating an ideal interaction between the rock and the cutter in rock drilling by providing a well-controlled rotational motion between them. To this end, this method has been widely used both in academia and industry. For companies, the face turning of rock is usually achieved on a vertical turret lathe (VTL) with the capability of force and temperature measurements to evaluate the high-temperature thermal stability, cutting efficiency,

and wear resistance of cutters, as shown in Fig. 2.23 (Bellin et al., 2010). Therefore, the testing methods in the face turning configuration are also known as the VTL tests.

Figure 2.23: Face turning of rock with a single PDC cutter on a VTL (Bellin et al., 2010).

Other experimental studies on the cutting performance of single PDC cutters are given next:

In the investigation of the cutter geometry affecting cutter performance, Glowka and Stone (Glowka and Stone, 1985) suggested that a larger thickness leads to longer lives of PDC cutters since the diamond layer composes a larger fraction of the wearflat. However, Zijsling (Zijsling, 1984) found that a thin diamond layer can improve heat conduction and reduce the maximal cutting edge temperature. Therefore, a tradeoff exists between the cutting and thermal performances of the cutter, in terms of the diamond thickness.

Wise et al. (Wise et al., 2002) exploited two in-house test facilities to evaluate PDC cutter performance from the viewpoint of cutter loads (e.g., thrust, cutting and side forces), wear state (e.g., G ratio), and durability (e.g., abrasion and impact resistance). They found quite a large variation in PDC performance with different parameter specifications. The G ratio of the best sample was 10 times that of the worst sample. Although they tried to assess sample performances with various parameter specifications, in terms of drilling, abrasion and impact performance

ranking, no comprehensive criterion was developed to give accurate assessments for all the cutters used under field conditions.

Some researchers draw attention to the evaluation of PDC cutter performance using energy approaches. The concept of mechanical specific energy (MSE) used by Simon (Simon, 1963) and Teale (Teale, 1965) is the amount of mechanical energy required to remove a unit volume of rock with a unit of N/m^2 or psi (Rafatian et al., 2010). In fact, specific energy concepts have been used in metal cutting aiming to analyze the material removal and deformation mechanisms (Shaw, 1993). However, in rock cutting, MSE and cutting efficiency in terms of MSE were exploited to analyze the wear of cutting elements and, thereby, evaluate the drilling response of the worn cutters under experimental conditions (Quickelberghe et al., 2006). Rafatian et al. (Rafatian et al., 2010) analyzed the cutter-rock interaction from an energy point of view by experimentally studying MSE of single PDC cutters interacting with rock under high pressure conditions. Their experimental results show that the frictional forces involved in the cutter-rock interface primarily influence the MSE and the efficiency of the cutting process. However, more in-depth studies are still required to provide further evidence for the better understanding of the cutter/rock interface under pressurized conditions.

Chapter 3

Experimental Investigation of Rock Turning

This chapter presents an experimental study and investigation of force responses in the three-dimensional (3D) oblique face turning of rock performed with PDC cutters. Since the depths of cut to be used, compared to the cutter's diameter and the feedrates, are very small, the 3D oblique cutting configuration will be assumed to be a two-dimensional (2D) quasi-orthogonal cutting configuration. Therefore, the measured force data (i.e., cutting, thrust and feed forces) in the oblique face turning process configuration will be suitably transformed to derive models for the cutting force (nominal cutting force) and thrust force (nominal thrust force) in the quasi-orthogonal cutting configuration. In this way, the complex oblique cutting configuration will be approximated by an orthogonal cutting configuration. The phenomenological force response model developed under this assumption establishes a relationship between the force responses and the rake angle, feedrate, and depth of cut. In addition, the force response of the PDC cutters will be considered not only at the rake face, in terms of the friction and compression forces, but also at the cutting edge in terms of the ploughing force and at the flank face in terms of the friction and lateral interaction forces to be defined in Section 3.4.

The chapter is arranged as follows: Section 3.1 introduces the rock turning testbed for turning operations performed with single PDC cutters that will be used, followed by the detailed experimental procedures described in Section 3.2. An analysis of the experimental data derived from a 7×3×3 full factorial design of experiments in rock turning is given in Section 3.3. Section

3.4 presents a new phenomenological model of the force response for 2D orthogonal cutting in a second order polynomial form with respect to feedrate and depth of cut. The physical meaning of each term in the new model will then be discussed. Section 3.5 draws conclusions and gives a short summary of the work done.

3.1 Rock face turning testbed

A rock face turning testbed (RFTT) was developed on an OKUMA CNC turning center whose general arrangement can be seen in Fig. 3.1. The experimental apparatus includes a three component Kistler dynamometer (KISTLER 9256), a triaxial accelerometer (KISTLER 8692C5M1) and dual-mode charge amplifiers (KISTLER 5004) to measure and record cutting forces and vibrations. Signal acquisition is realized through LabVIEW® with a National Instruments data acquisition (DAQ) system (NI PCI-6259). Temperature measurements are performed with conventional K-type thermocouples attached to the rake face of the PDC cutter at approximately 2 mm from the cutting edge through a signal conditioner (OMEGA iDRN-TC). The spindle speeds in the testbed can range from 75 to 4,200 rpm. The dynamometer can measure three dimensional forces up to 10 kN, while the accelerometer can detect accelerations ranging from -5 g to 5 g (g = 9.8 m/s^2). The thermocouple can measure temperatures up to 1,200°C which is far more than the thermal response of diamond tools.

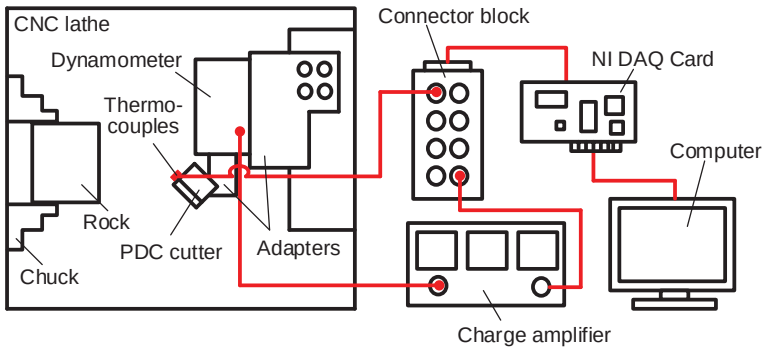

(a)

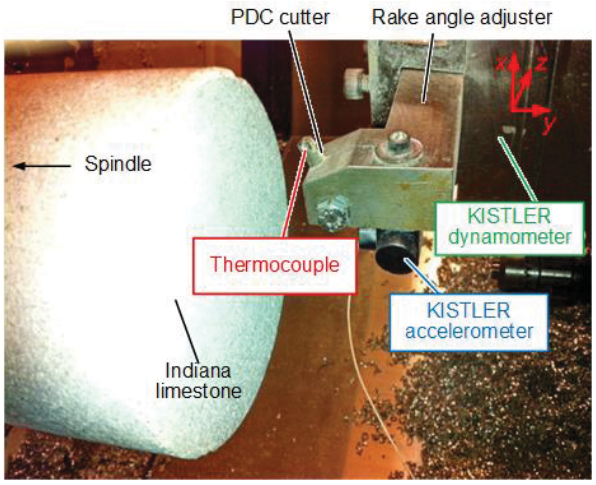

(b)

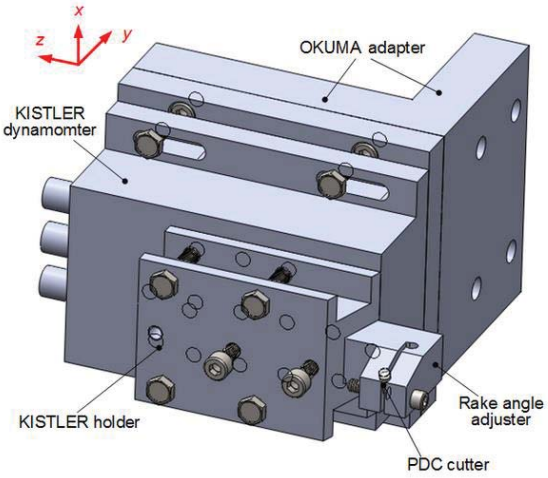

(c)

Figure 3.1: Experimental setup of RFTT: (a) system configuration; (b) photo of RFTT; (c) tool holding system.

The PDC cutters used in this testbed are clamped by a tool holder system shown in Fig. 3.1(c). The rake angle of the cutter in the turning process can be changed by replacing the rake angle adjuster depicted in Fig. 3.1(c). In the present case, the rake angle can be set to 10°, 12°, 15°, 17°, 20°, 22° and 25° by seven different rake angle adjusters. As shown in Fig. 3.2(a), the PDC cutters with a diameter of 5.6 mm provided by Diamond Innovations, Inc. have a 3 mm diamond layer on

a 10 mm high tungsten carbide (WC) stud. The rock samples used in the turning tests are Indiana limestone cylinders with a 101.6 mm diameter and 101.6 mm length, as shown in Fig. 3.2(b).

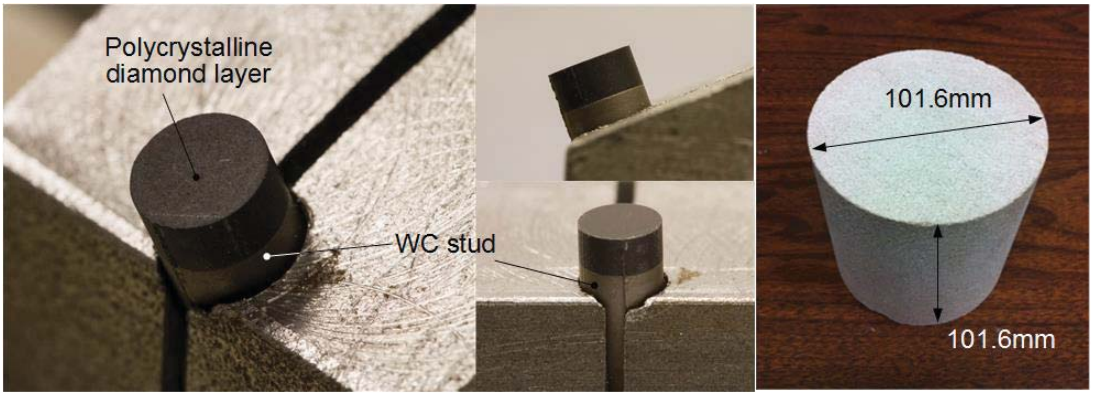

(a) (b)

Figure 3.2: PDC cutter and limestone sample used in the tests: (a) PDC cutter held at a 25º rake angle; (b) cylindrical Indiana limestone sample.

3.2 Experimental procedures

As shown in Fig. 3.1(b) and (c), the *x*-direction denotes the cutting speed direction, the *y*-direction the thrust direction, and the *z*-direction the feed direction, respectively. When the turning tests are conducted, the PDC cutter, mounted on the machine's turret, will move along the feed direction with a specific feedrate. The cutting speed, along the *x*-direction, is provided by the rotation of the rock sample. During the turning tests, all the instruments (i.e., dynamometer, accelerometer and thermocouple) measure the desired thermal/mechanical responses and send them to the computer through the DAQ system. Complex control of the turning process variables (e.g., feedrate, cutting speed, spindle speed, etc.) can be accomplished by G-code programming.

Face cutting was performed with 5.6 mm diameter PDC cutters in 101.6 mm diameter Indiana limestone cylindrical samples. Under field conditions the cutting speed of the PDC cutters ranges

from 1.6 to 4 m/s obtained by bit rotation speeds ranging from 60 to 250 rpm depending on bit dimension, hardness of the rock formation and cooling mode (Che and Ehmann, 2014). To achieve these speeds on the developed testbed, given the sample specimen size, spindle speeds ranging from 300 to 800 rpm are suitable to simulate the cutting speeds used under field conditions. Given that the force responses are, in general, independent of cutting speed due to the brittle failure mode of rock cutting (Nishimatsu, 1972), the dry turning experiments were performed under a constant spindle speed (i.e., 300 rpm) but different levels of the rake angle, depth of cut, and feedrate, aiming to investigate their effects on the force responses under specific processing conditions. Three orthogonal force components were measured during all the tests, including the cutting force along the *x*-direction, the thrust force along the *y*-direction, and the feed force along the *z*-direction. The results will be discussed in detail in the following section.

3.3 Experimental results

In this section, two aspects of the work are discussed: (a) the design of experiments for PDC cutter-based turning of limestone on the testbed introduced in Section 3.2, and (b) the obtained experimental results.

3.3.1 Design of experiments

The independent variables in the performed rock turning experiments are the rake angle, the depth of cut and feedrate. In the 7×3×3 full factorial design of experiments, the factor – rake angle has seven levels, i.e., 10, 12 15, 17, 20, 22 and 25 degrees, the factor – depth of cut has three levels, i.e., 0.254, 0.508 and 1.016 mm, and the factor – feedrate has three levels as well, i.e., 0.16, 0.4

and 0.8 mm/rev. The spindle speed for all 63 tests is the same, i.e., 300 rpm. The geometrical representation of the 7×3×3 factorial design is shown in Fig. 3.3 while the test configurations are given in Table A1 in Appendix A. All of the 63 tests are separated into 7 sets. For each set of tests, the rake angle is the same while the feedrate and depth of cut vary within each set of tests.

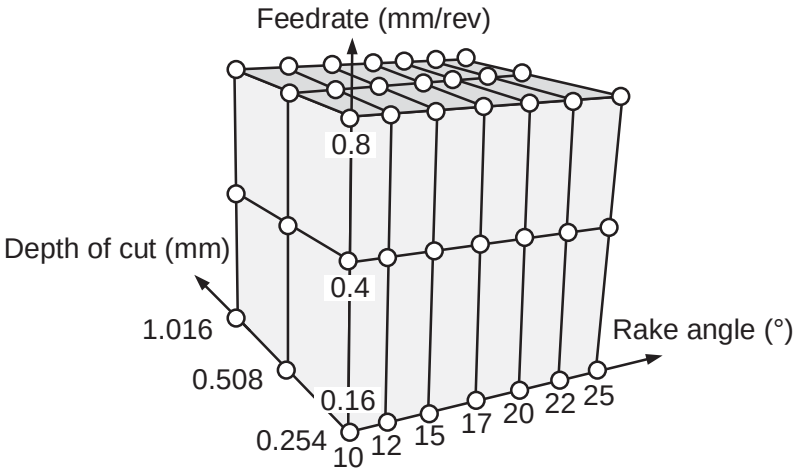

Figure 3.3: Geometrical representation of the 7x3x3 full factorial design of experiments.

3.3.2 Results

In each of the 63 tests, the depth of cut, the feedrate and rake angle were changed to different levels. The cutting, thrust and feed forces exerted on the PDC cutters were measured at a 20 kHz sampling rate. Due to the noisy environment during turning, the raw data shown in Fig. 3.4(a) were filtered by a low pass digital filter with a cut-off frequency of 10 Hz, as shown in Fig. 3.4(b). As a function of time, all the force components (i.e., cutting, thrust and feed forces) exhibit similar trends in different phases, i.e., start, stable and unstable phases shown in Fig. 3.4(c). After the cutter contacts the rock cylinder at the start point, the force components increase rapidly during the starting phase and then reach a relatively stable phase lasting for quite a long time period, i.e.,

during the stable phase. When the cutter is approaching the centerline of the rock cylinder (i.e., unstable phase), the force components experience a brief rapid increase followed by a drop-off after all the material is removed. The obvious oscillation phenomona in all the measured force components can be attributed to two main reasons, i.e., the brittle failure characteristics of rock (Verhoef and Ockeloen, 1996) and the inhomogenous microstructure of the sample (Yan, 1997). Actually, several analytical models were formulated to calculate the mean value of the force oscillations based on the brittle failure characteristics of rock (Evans, 1984; Nishimatsu, 1972; Nishimatsu, 1993), while the inhomogeneity of the rock was dealt with using statistical techniques (Bazant et al., 1991; Bazant and Xi, 1991; Weibull, 1939).

It should be noted that since the spindle speed is kept constant in the performed tests, the cutting speed linearly decreases when the cutter is feeding towards to the center of the cylindrical workpiece. However, as shown in Fig. 3.4(b), the force responses oscillate around a nearly constant value during a stable phase, i.e., from 5~25s in Test 5. This indicates that the rock is exhibiting a brittle failure mode during which the force responses are, to a considerable extent, independent of cutting speed.

In each of the 63 test given in Table A1, the cutting, thrust and feed forces during the stable phase were averaged to represent the force responses with respect to the different levels of the rake angle, depth of cut and feedrate, namely average cutting, thrust and feed forces given in Table A1.

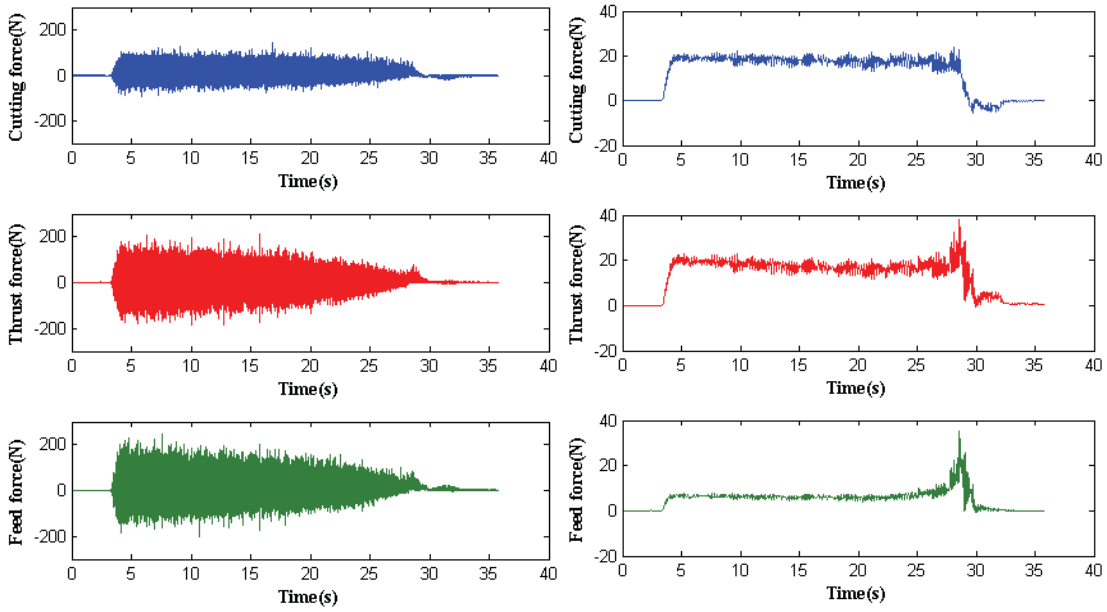

(a) (b)

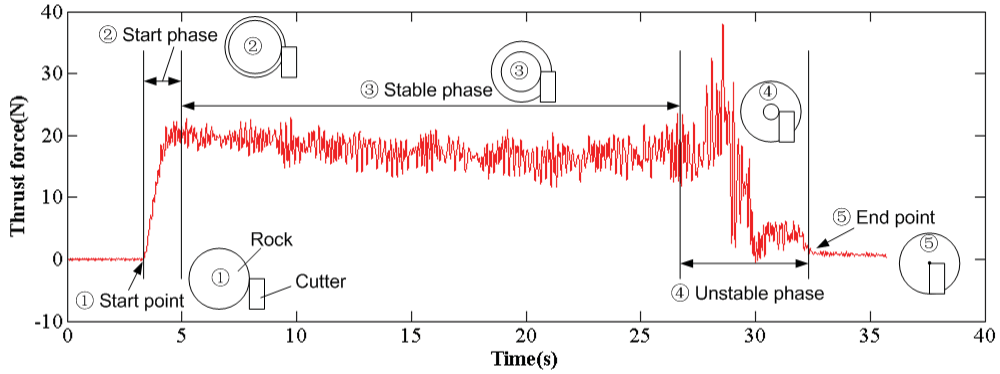

(c)

Figure 3.4: The experimental data of force responses with respect to time in Test 5: (a) raw data; (b) filtered data; (c) filtered thrust force response.

3.4 Discussion on force responses

In this section, the experimental data obtained in Section 3.3 will be analyzed and discussed to formulate a phenomenological force model.

3.4.1 Design of experiments

In a large body of literature dealing with force response modeling in rock cutting, modeling of the cutting and thrust force components under orthogonal cutting conditions draws most of the attention due to the simple geometry and interaction between the rock and the cutter that easily reveals the intrinsic mechanicsms involved.

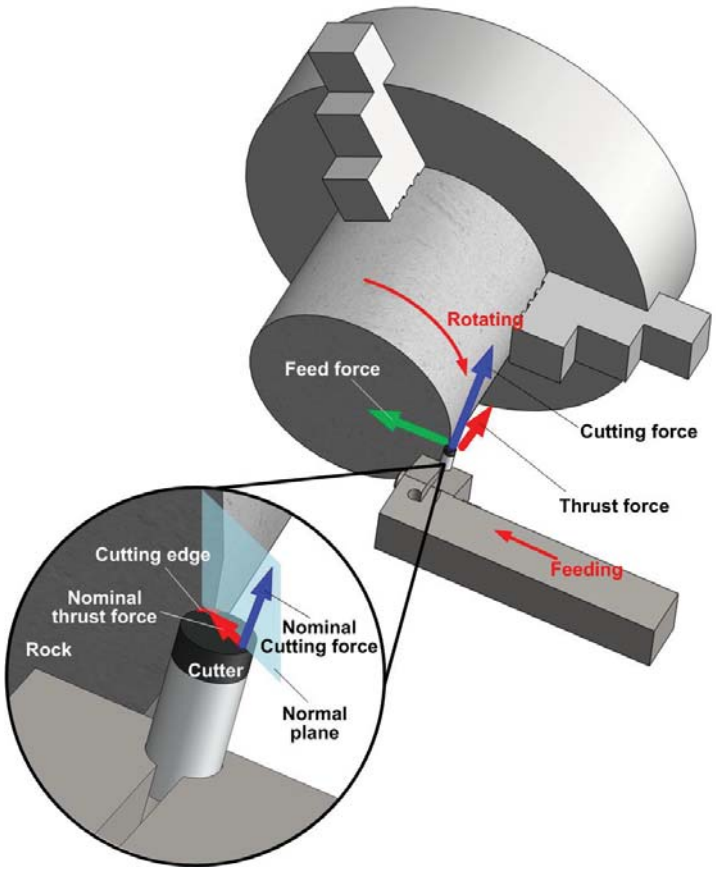

Figure 3.5: Mapping of force components from 3D face turning to 2D orthogonal cutting.

However, ideal orthogonal cutting conditions are very difficult to achieve in rock cutting under laboratory conditions. Some of the techniques used to simulate orthogonal cutting in metal cutting cannot be simply introduced in rock cutting. For example, a thin disk shaped workpiece made of AISI-O2 used in a turning configuraion by Li et al. (Li et al., 2012) cannot be used in rock cutting.

The customary orthogonal cutting of tubular workpieces is also not applicable. The reason being is that in rock cutting tests, rock is too brittle to be machined in the form of a disk or tube. To this end, this section will discuss the methodology to extract force responses under orthogonal cutting conditions from a 3D oblique turning configuration.

Face turning, illustrated in Fig. 3.5, is achieved by feeding the tool and rotating the rock sample simulatenously, that clearly represents 3D oblique cutting conditions. In the mechanics of oblique cutting, the force response during face turning can be decomposed into three components, i.e., cutting, thrust and feed forces. In the performed tests in this work, the feedrates are very small compared to the average cutting speed. Moreover, the depth of cut is much smaller than the cutter's diameter. Therefore, the oblique cutting condition can be approximated by a quasi-orthogonal cutting condition. Since the cutting force is always pointing in the direction of the cutting speed and the thrust and feed forces are normal to the cutting speed direction due to the cutter's feed motion, as shown in Fig. 3.5, the cutting force component can be assumed as the nominal cutting force in the normal plane which is normal to the equivalent cutting edge in the quasi-orthogonal cutting configuration, while the resultant of the thrust and feed forces can be assumed to be the nominal thrust force in the normal plane, i.e.:

$$F_{nc} = F_c \tag{3.1}$$

$$F_{nt} = \sqrt{F_t^{\,2} + F_s^{\,2}} \tag{3.2}$$

$$\alpha = \arccos \frac{F_t}{F_{nt}} \tag{3.3}$$

where F_{nc} and F_{nt} denote the nominal cutting and thrust forces in the quasi-orthogonal cutting configuration respectively, F_c, F_t and F_s denote the cutting, thrust and feed force components in

the face turning configuration respectively, and the olique angle α denotes the angle between the thrust force and the nominal thrust force. In this way, oblique cutting during 3D face turning can be approximated by an orthognal cutting configuration in the normal plane. The nominal thrust forces in the tests were calucated based on the averaged measured thrust and feed forces as listed in Table A1.

3.4.2 A phenomenological force model

In this section, a phenomenological force model will be given based on the experimental data obtained from the above-mentioned tests. The physcial meaning of all the terms in the force model will be discussed.

In each set of tests indicated in Table A1, 9 tests with different levels of depth of cut, D_c, and feedrate, f_r, but the same level of the rake angle, γ, were analyzed to extract the information on the effects of these parameters. For the turing tests with the same material properties of the rock and the same rake angle, the cutting and thrust forces are proposed to be represented by a second order polynomial form, i.e.:

$$F_c(N) = C_0 + C_1 f_r(\text{mm/rev}) + C_2 D_c(\text{mm}) + C_3 f_r D_c \tag{3.4}$$

$$F_{nt}(\text{N}) = B_0 + B_1 f_r(\text{mm/rev}) + B_2 D_c(\text{mm}) + B_3 f_r D_c \tag{3.5}$$

where F_c is the cutting force, F_{nt} is the nominal thrust force, C_i and B_i (i = 0, 1, 2, and 3) are constants. Based on the force responses (i.e., average cutting and nominal thrust forces) shown in Table A1, the constants for each set of tests can be determined using polynomial least square regression techinques. The evaluated constants are given in Table 3.1. Figure 3.6 shows the

prediction surface and experimental data of the force responses. As it can be seen in Fig. 3.6(a) and (b), for a constant rake angle, both the cutting and thrust forces tend to increase linearly with an increase in the depth of cut for a constant feedrate rate and, also, they tend to increase linearly with an increase in the feedrate rate under the same levels of depth of cut, which can be accurately predicted by Eqs. (3.4-3.5).

Table 3.1: Derived constants for the analytical expressions of the force responses.

Set No.	C_0	C_1	C_2	C_3	B_0	B_1	B_2	B_3
1	3.5442	15.8670	5.9974	25.8466	5.2503	20.7443	5.4659	14.3111
2	3.0491	14.0464	6.2013	29.3656	4.1225	17.7594	5.5955	18.2750
3	2.8519	14.8603	5.9965	30.9240	3.4897	18.8774	5.7856	19.4634
4	2.9426	15.0394	7.5108	32.3027	3.9965	16.3953	6.9831	22.4645
5	4.2858	14.7530	5.9102	33.1070	5.7158	16.6837	4.8828	21.8266
6	3.1245	15.4555	7.5338	38.0114	4.2673	16.2509	7.0504	29.2240
7	4.1976	12.3153	4.1767	55.8418	6.0325	15.3514	4.3592	45.1124

The nature of the obtained nominal cutting and thrust force responses can be explained by the existence of four force components at the cutting edge and the flank face respectively, i.e., frictional, ploughing, lateral interaction, and shearing components.

The first terms in Eqs. (3.4-3.5), i.e., C_0 and B_0, represent the force component due to the friction effect at the flank surface independent of the depth of cut and feedrate, which can be related by:

$$F_0 = B_0 \tag{3.6}$$

$$F_f = C_0 = \mu F_0 \tag{3.7}$$

where μ is the friction coefficient between the rock and the flank face of the cutter. It is assumed to be constant and is determined by the material properties of the rock and the cutter but is independent of the process parameters (i.e., feedrate, depth of cut, and rake angle), F_0 is the initial thrust force as a constant component of the thrust force at the flank face, and F_f is the friction force as a component of the cutting force at the flank face.

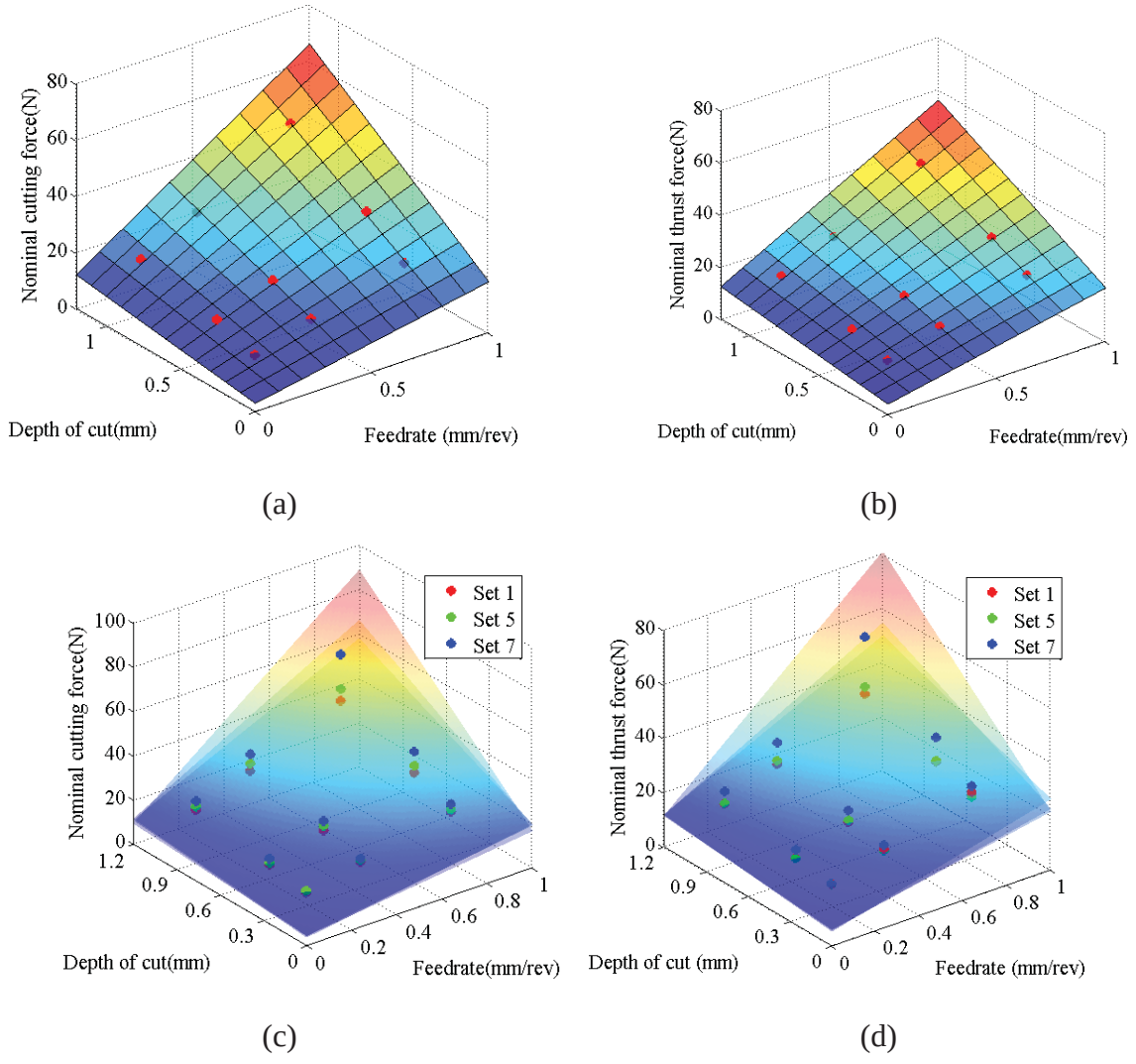

Figure 3.6: Nominal cutting and thrust force responses for different sets of tests: nominal cutting force (a) and nominal thrust force (b) for the 4th set; nominal cutting force (c) and nominal thrust force (d) response comparisons for the 1st, 5th and 7th sets.

The ploughing force exerted on the tool's cutting edge which was reported to be proportional to the cutting width (Waldorf, 2006) but insignificantly affected by the depth of cut (Albrecht, 1960) in metal cutting. Therefore, the second terms in Eqs. (3.4-3.5), i.e., $C_1 f_r$ and $B_1 f_r$, are independent of the depth of cut but linearly related to the feedrate in face turning affecting the cutting width under orthogonal cutting condition, which represent the force component due to the ploughing effect, i.e.:

$$F_{cp} = C_1 f_r \tag{3.8}$$

$$F_{tp} = B_1 f_r \tag{3.9}$$

where F_{cp} and F_{tp} are the components of the ploughing force which contribute to the cutting and thrust forces at the cutting edge respectively, and C_1 and B_1 are constants determined by the material properties of the rock and the cutter but independent of process parameters.

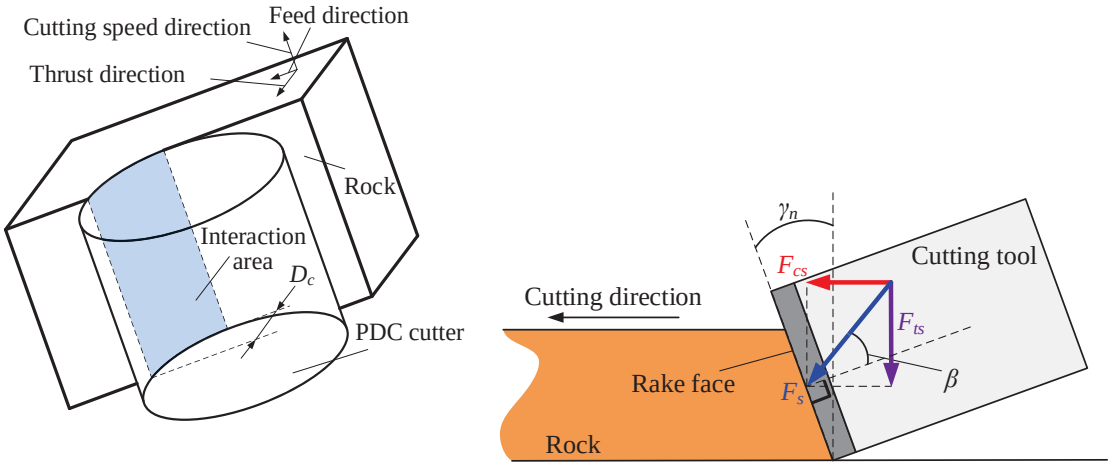

Figure 3.7: Illustration of the interaction area and mean friction angle: (a) interaction area in face turning; (b) mean friction angle in orthogonal cutting.

Moreover, the intense interaction between the rock and the flank surface of the PDC cutters due to rock dilatancy, chip residues and the coarse interface between the rock and the cutter is assumed to create an interaction zone as shown in Fig. 3.7(a). A so-called lateral force is defined to represent the contribution of the interaction zone to the force responses. It is assumed proportional to the interaction area at the flank face. Since the depth of cut is approximately proportional to the interaction area at the flank face, the third terms in Eqs. (3.4-3.5), i.e., C_2D_c and B_2D_c, linearly related to depth of cut, account for the lateral force component, i.e.:

$$F_{cl} = C_2 D_c \tag{3.10}$$

$$F_{tl} = B_2 D_c \tag{3.11}$$

where F_{cl} and F_{tl} are the components of the lateral force contributing to the cutting and thrust forces respectively, and C_2 and B_2 are constants.

Based on many analytical and mechanistic models in the literature, the force components used to shear the chips out of the virgin workpiece are proportional to the cutting area which is the projection of the cutter profile on the plane normal to the cutting speed direction (Boothroyd and Knight, 1989; Che et al., 2014b; Nishimatsu, 1993). In the above-metioned tests, the cutting area is proportional to the product of feedrate and depth of cut. Therefore, the last terms in Eqs. (3.4-3.5), i.e., $C_3f_rD_c$ and $B_3f_rD_c$, can accout for the force components due to the shearing effect, i.e.:

$$F_{cs} = C_3 f_r D_c \tag{3.12}$$

$$F_{ts} = B_3 f_r D_c \tag{3.13}$$

where F_{cs} and F_{ts} are the components of the shearing force applied at the rake face of the PDC cutter. As shown in Fig. 3.7(b), the mean friction angle, defined as the inclination angle of the total shearing force F_s with respect to the normal to the cutter's rake face, namely β, can be expressed by (Huang et al., 2013):

$$\beta = \arctan\left(\frac{F_{ts}}{F_{cs}}\right) - \gamma_n \tag{3.14}$$

where F_{cs} and F_{ts} are the components of the shearing force contributing to the cutting and thrust forces respectively, and γ_n is the nominal rake angle.

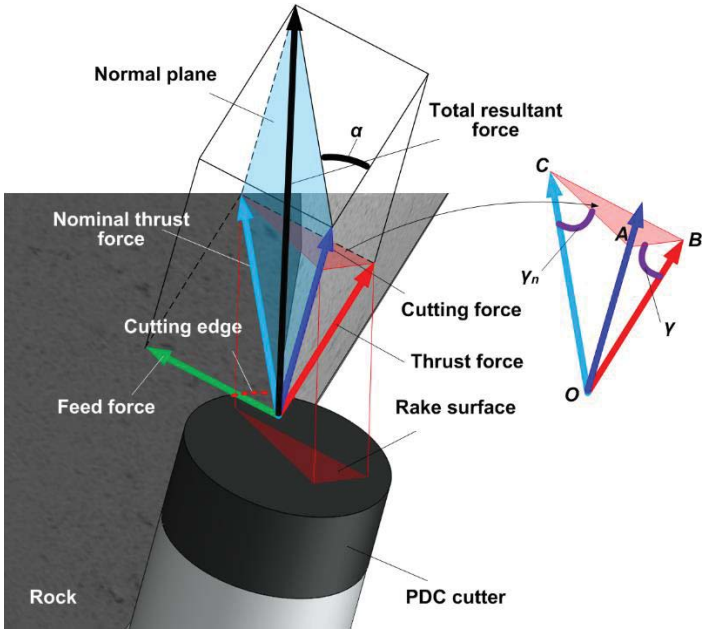

Figure 3.8: Force components in 3D face turning of rock.

In addition to the effects of the feedrate and depth of cut on force responses, as shown in Fig. 3.6(c) and (d), the prediction surfaces for both the cutting and thrust force responses tend to raise

along the force response axes, which indicates that the rake angle also affects the force responses that will be evaluated in the next section.

3.4.3 Model discussion

In this section, the process parameters (α, γ_n, μ, β, B_i and C_i, i = 0, 1, 2, and 3) required to determine the cutting and thrust force responses will be discussed by comparing the force model developed in Section 3.4.2 with the results of the experimental analyses done in Section 3.4.1.

a) Oblique angle and nominal rake angle

As mentioned in Section 3.4.1, the 3D oblique cutting configuration during face turning was approximated by a 2D orthogonal cutting configuration. Figure 3.8 shows the geometrical relations between all force components in face turning of rock. The three force components, i.e., cutting, thrust and feed forces, in the 3D oblique cutting configuration are transformed into two components in the normal plane, i.e., the nominal cutting and the nominal thrust forces in the resulting 2D orthogonal configuration. The oblique angle between the thrust and the nominal thrust forces α is the measure of how far away the thrust force in face turning is from the nominal thrust force in ideal orthogonal cutting and characterizes the transformation from the 3D to the 2D configuration. For example, if α is equal to zero, the thrust force can completely represent the nominal thrust force, while if α is equal to 90º, the thrust force is infinitely far away from the nominal thrust force. According to Eq. (3.3), the oblique angle was calculated for each test and is shown in Fig. 3.9(a). The oblique angle determines the chip flow direction. When α is equal to zero, the chips flow along the rake face in the *xy* plane generated by the cutting and thrust force

directions. However, when α is larger than zero, the chips flow along the rake face in the normal plane. As shown in Figure 3.9(a), seven horizontal groups indicate seven sets of tests with different levels of rake angle. Each group includes nine tests with various levels of the feedrate and depth of cut. The oblique angle significantly increases with depth of cut and feedrate but changes only slightly with rake angle.

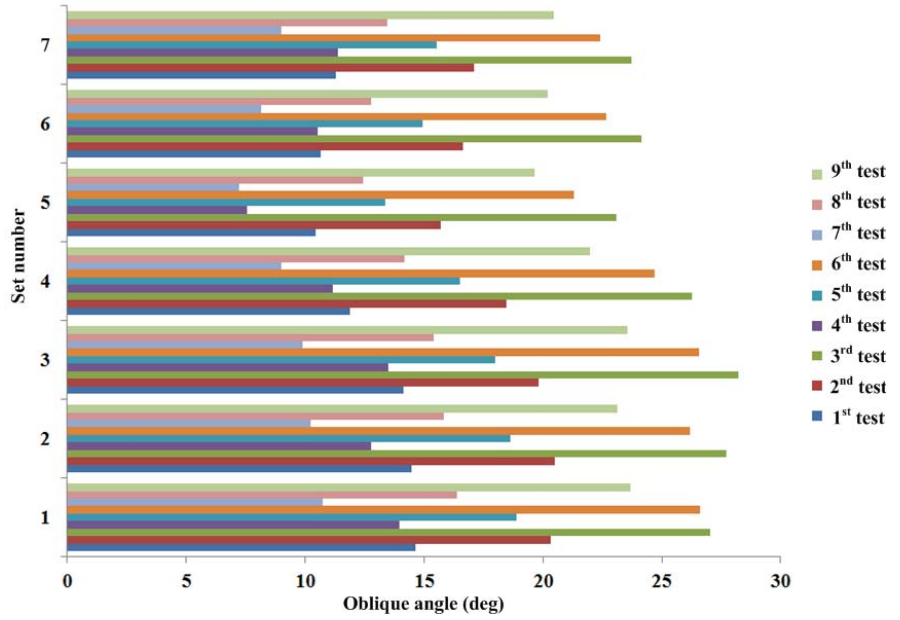

(a)

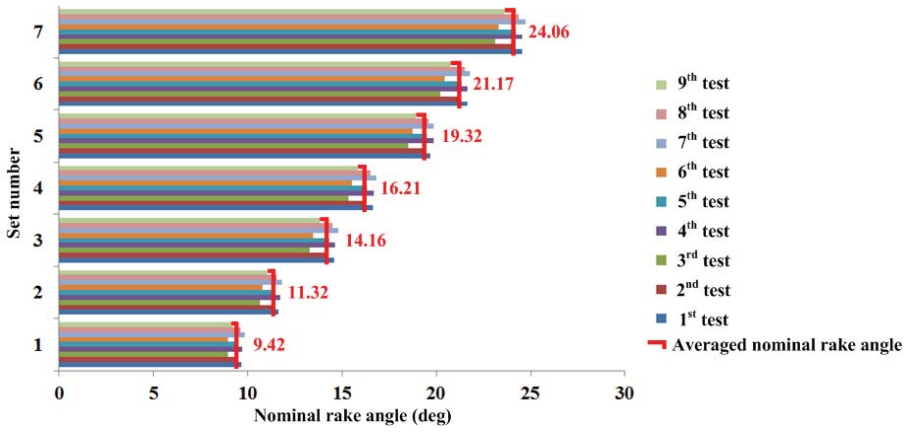

(b)

Figure 3.9: Characteristic angles in the experiments: (a) oblique angle; (b) rake angle.

The rake angle γ, defined in the face turning of rock, is the inclination angle of the rake surface with respect to the plane normal to the cutting speed direction, as shown in Fig. 3.8. However, the rake angle used in the orthogonal cutting approximation, namely the nominal rake angle γ_n is not the same as the defined rake angle γ, which can be calculated as follows:

$$\gamma_n = \arctan\left(\frac{\left\|\overline{AO}\right\|}{\left\|\overline{CO}\right\|}\right) = \arctan\left(\tan\gamma\cos\alpha\right) \tag{3.15}$$

where α is the oblique angle between the thrust and nominal thrust forces, $\left\|\overline{AO}\right\|$ and $\left\|\overline{CO}\right\|$ are the lengths of segments AO and CO respectively. The nominal rake angles for all the tests are listed in Fig. 3.9(b). The nominal rake angle slightly varies with depth of cut and feedrate, however it is, to the largest extent, influenced by the rake angle. Therefore, for each rake angle set, the nominal rake angles were averaged as listed in Fig. 3.9(b). Since a constant value of the rake angle for each set of experiments has to be given to determine the other process parameters and coefficients of the force model, the averaged nominal rake angels (indicated in red in Fig. 3.9(b)) will be used for the performed experiments in the following sections.

b) Friction coefficient and initial thrust force

Based on Eqs. (3.6-3.7), the initial thrust force F_0 can be considered equal to the constant term B_0, while the corresponding friction force, F_f, can be considered equal to the constant term C_0. Therefore, the friction coefficient between the rock surface and the cutter's flank face, μ, can be derived from:

$$\mu = \frac{F_f}{F_0} = \frac{C_0}{B_0} \tag{3.16}$$

As shown in Fig. 3.10(a), the initial thrust force, F_0, is approximately independent of the rake angle, depth of cut and federate and, as such, can be averaged as follows:

$$F_0 = \frac{\sum_{i=1}^{7} B_{0i}}{7} = 4.6964(\mathrm{N}) \tag{3.17}$$

where *i* denotes the set number ranging from 1 to 7.

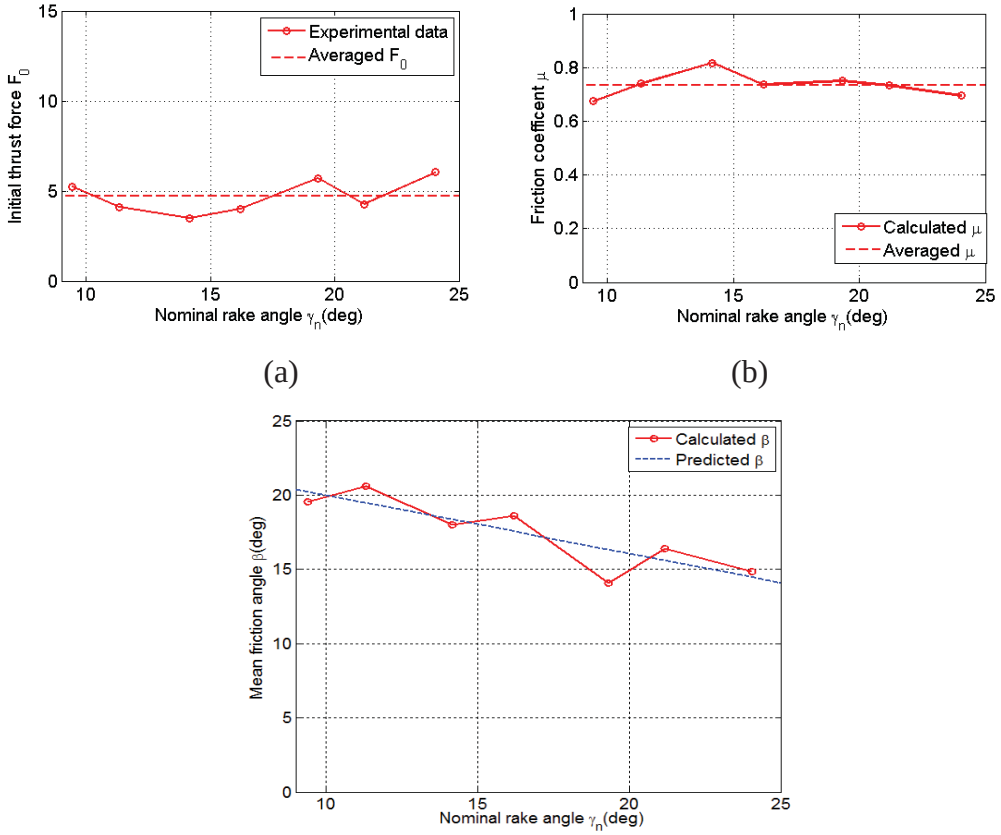

Figure 3.10: Process parameters vs. nominal rake angle: (a) initial thrust force; (b) friction coefficient; (c) mean friction angle.

According to the data in Table 3.1, the friction coefficient in different sets of tests can be calculated from Eq. (3.16) as shown in Fig. 3.10(b), which is approximately independent of the rake angle, depth of cut and feedrate as assumed in the preceding section. Therefore, the friction coefficient, μ, can be averaged as follows:

$$\mu = \frac{\sum_{i=1}^{7} \frac{B_{0i}}{C_{0i}}}{7} = 0.7351 \tag{3.18}$$

where i denotes the set number ranging from 1 to 7.

c) Coefficients of ploughing and lateral interaction effects

The coefficients for the ploughing effects, i.e., C_1 and B_1, and lateral interaction effects, i.e., C_2 and B_2 in Eqs. (3.8-3.11) can be evaluated based on Table 3.1.

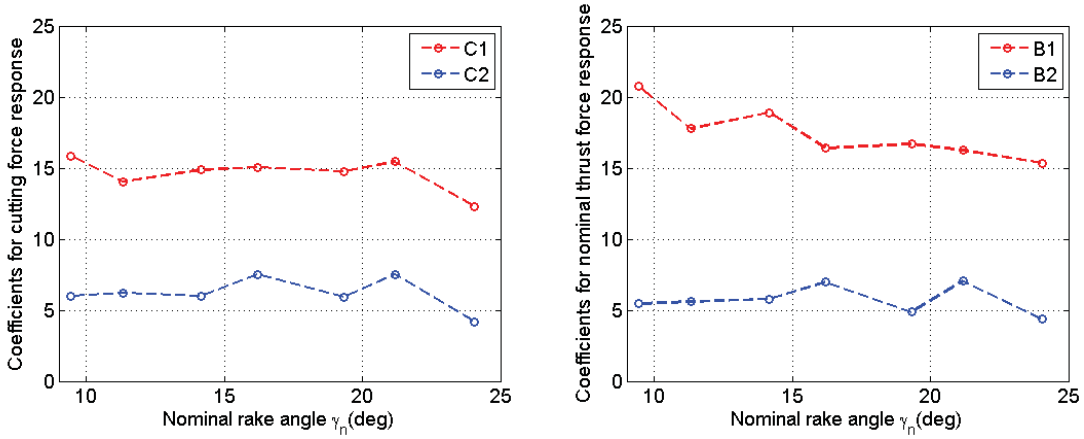

(a) (b)

Figure 3.11: Evolution of the coefficients of ploughing and lateral interaction effects with respect to rake angle: (a) for the cutting force response; (b) for the thrust force response.

Figure 3.11 shows the evolution of these coefficients with no significant changes with respect to the rake angle. Therefore, these coefficients can be determined by averaging the calculated values at different rake angle as summarized as follows. For the plowing effect, $C_1 = 14.6196$, and $B_1 = 17.4375$. For the lateral interaction effects, $C_2 = 6.1895$, and $B_2 = 5.7319$.

3.5 Conclusions

In this chapter an experimental study for the evaluation of the force responses in the three-dimensional face turning process of rock performed with PDC cutters was conducted. The following conclusions can be drawn:

(1) A rock face turning testbed (RFTT) was developed on a CNC turning center with the core capability of measuring thermal and mechanical responses during rock cutting. The tools used were polycrystalline diamond compact cutters while the workpiece was a sedimentary rock, i.e., Indiana limestone.

(2) A 7×3×3 full factorial design of experiments of face turning tests was designed and conducted with 7 levels of rake angles, 3 levels of depths of cut, and 3 levels of feedrate, aiming to investigate the effects of the rake angle, depth of cut and feedrate on the force responses of the cutter. The experimental results indicate that a 2nd order polynomial in terms of feedrate and depth of cut can accurately represent their effects on the force responses, while the effect of the rake angle on the force responses is highly non-linear.

(3) The obtained force responses in the 3D face turning configuration were approximated by force responses in 2D orthogonal cutting by mapping the 3D force data into the normal plane which is normal to the cutting edge.

(4) A phenomenological force response model was developed to decompose the force response into four categories, i.e., frictional effect, ploughing effect, lateral interaction effect, and shearing effect. The frictional effect represents the friction occurring at interface between the virgin rock and the cutter's flank face, the ploughing effect accounts for the force components at the cutting edge, the lateral interaction effect represents the complex interaction between the rock and the lateral surface of the cutter, and the shearing effect denotes the force used to shear chips out of the virgin rock.

(5) All the parameters required to define the force response model were discussed from the physical point of view, including the oblique angle between the thrust and nominal thrust forces α, the nominal rake angle γ_n, the friction coefficient between the flank face and the rock, μ, the initial thrust force, F_0, the mean friction angle, β, and coefficients for ploughing and lateral interaction effects at the cutting edge and the flank face respectively, C_1, B_1, C_2, and B_2. Among them, μ, F_0, C_1, B_1, C_2, and B_2 were found to be independent of the rake angle, depth of cut, and feedrate, while β was found to be exclusively linearly affected by the rake angle which is in close agreement with previous studies.

Chapter 4

Experimental Investigation of Linear Rock Cutting

In order to obtain a better understanding of rock-cutter interactions, this chapter presents an experimental investigation to illustrate the influences of various parameters, e.g., the depth of cut, rake angle, cutting speed, and rock properties on the cutter's cutting performance and the rock's failure behavior during linear rock cutting processes. A series of cutting tests on three types of rock samples with multiple levels of rake angles, depths of cut and cutting speeds were performed on a newly developed linear rock cutting facility. The force responses and chip formation phenomena were captured and recorded by a force measuring system and a high speed camera respectively. The influences of selected parameters on the force responses and chip formation phenomena were then investigated based on the acquired testing results. To simplify the rock-cutter interactions, a customized PDC cutter with a straight cutting edge was used to realize an orthogonal cutting configuration.

This chapter is organized as follows: An introduction of the testbed and the design of experiments for this work are given in Sections 4.1 and 4.2 respectively. Section 4.3 presents the detailed procedures for force signal processing aiming to accurately capture the desired force components during linear rock cutting. The investigation of chip formation phenomena will be discussed in Section 4.4, followed by the discussion of the change of force responses with respect to process parameters given in Section 4.5. Lastly, Section 4.6 summarizes the work and draws conclusions.

4.1 Linear rock cutting testbed

The testbed used in this work, namely the linear rock cutting testbed (LRCT), was built based on a CNC milling machine (Cincinnati Milacron EV-750) illustrated in Fig 4.1.

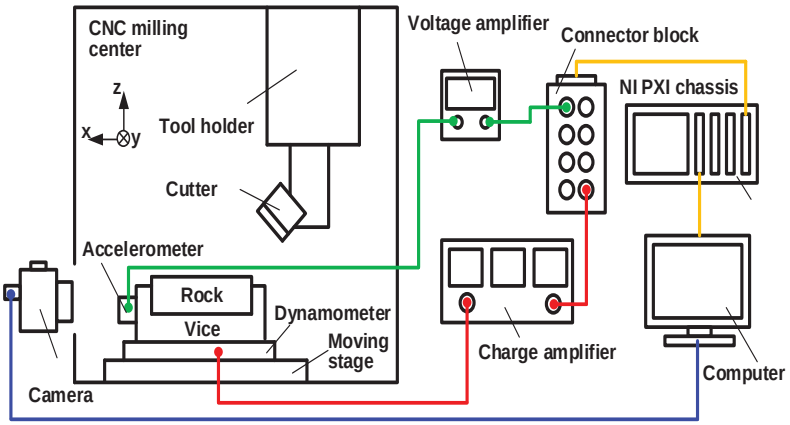

(a)

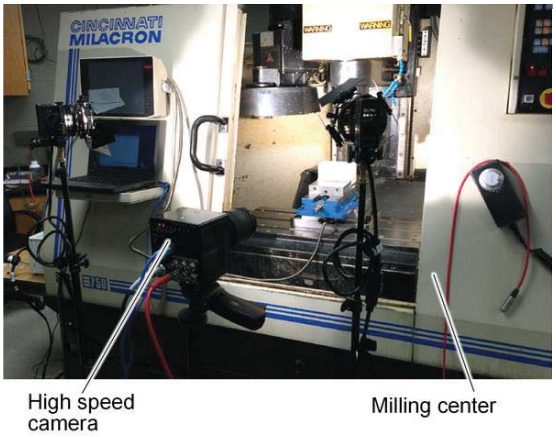

(b)

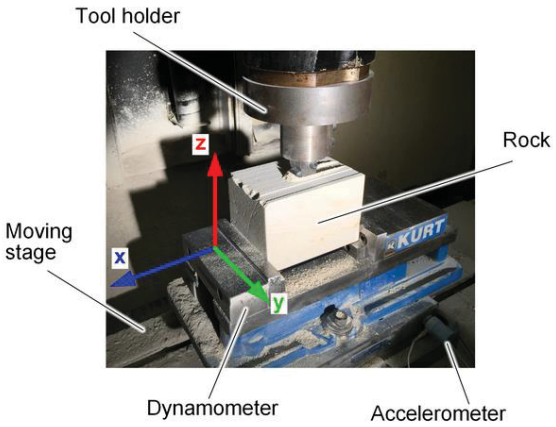

(c)

Figure 4.1: Linear rock cutting testbed: (a) system configuration; (b) outside view; (c) inside view.

As shown in Fig. 4.1(a), the LRCT includes the moving stage, tool adapter, PDC cutter, rock sample, vice, camera, dynamometer, accelerometers and data acquisition (DAQ) system. The moving stage of the milling center was utilized to achieve the linear cutting motions at cutting speeds ranging from 3 to 12,000 mm/min. The travel ranges in the *x*-, *y*-, and *z*-directions are 762, 381, and 508 mm respectively. A tool holder was manufactured to fix the PDC cutters onto the milling center's top structure with five levels of negative rake angles, i.e., 10˚, 15˚, 20˚, 25˚, and 30˚. A rock block was fixed on a vice fastened on the top surface of the moving stage. The cutter used is a polycrystalline diamond compact cutter consisting of two layers, i.e., a diamond layer and a tungsten carbide layer. The cutting edge, as indicated in red in Fig. 4.2, was ground to a nearly straight shape with an approximately 19 mm width in order to ensure a simple orthogonal cutting condition in which the cutting edge is always perpendicular to the cutting speed direction. The cutter's side edges are curved to avoid stress concentration.

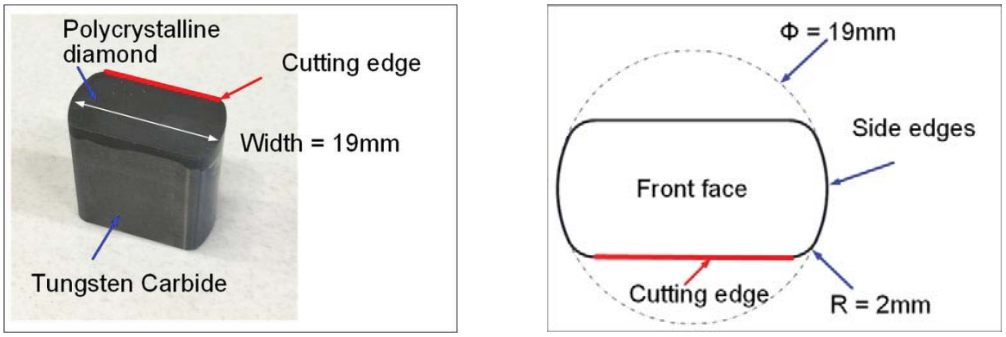

(a) (b)

Figure 4.2: Polycrystalline diamond compact cutter used in the reported tests: (a) picture of the cutter; (b) top view of the cutter.

The testbed has a fully equipped force measuring system, including a 3-component piezoelectric dynamometer (Kislter 9255A), three unidirectional accelerometers (PCB 308B15), and a data acquisition (DAQ) unit. The dynamometer can measure three dimensional forces up to 20 kN, while the accelerometer can detect accelerations ranging from -50 g to 50 g (g = 9.8 m/s^2). The DAQ unit consists of two voltage amplifiers (PCB 480C02 and KISTLER 5112), a 3-channel charge amplifier (KISTLER 5010), a DAQ module (NI PXI-6123) and a remote controller module (NI PXI-8360) inserted in a NI PXI chassis (NI PXI-1036), a connector block (NI BNC-2120), and a computer. A high speed camera (Photron Fastcam Mini UX100) with a 1280x1024 resolution and up to 4,000 fps was used to visualize and record the chip formation phenomena during linear cutting.

Table 4.1: Process parameters used in linear rock cutting tests.

Test Set	Cutting speed (mm/s)	Depth of cut (mm)	Rake angle (°)	Rock type
1	63.5	0.2, 0.4, 0.6, 0.8, 1, 1.2, 1.4, 1.6, 1.8, 2, 2.4, 2.8, 3	10, 15, 20, 25, 30	Indiana limestone
2	63.5	0.4, 0.8, 1.2, 1.6, 1.8, 2, 2.2, 2.4, 2.6, 2.8, 3	10, 15, 20, 25, 30	Austin chalk
3	63.5	0.4, 0.5, 0.6, 0.7, 0.8, 1, 1.2, 1.4	10, 15, 20, 25, 30	Berea sandstone
4	4.2, 21.2, 42.3, 63.5, 84.7, 127, 169.3	0.6, 1.4	15, 25	Indiana limestone
5	4.2, 21.2, 42.3, 63.5, 84.7, 127, 169.3	0.8, 2.4	15, 25	Austin chalk

Table 4.2: Mechanical properties of the sedimentary rocks used in the tests.

Rock type	UCS (MPa)	ISRM Grade	ISRM description
Austin chalk	20.7	R2	Weak
Indiana limestone	27.6~34.5	R3	Medium strong
Berea sandstone	44.8~55.2	R4	Strong

4.2 Design of experiments

The ultimate goal of this work is to explore how the cutter interacts with the rock in linear rock cutting from two aspects, i.e., the rock's failure behavior and the cutter's cutting performance. Hence, a series of cutting tests were designed and performed based on the aforementioned testbed to ascertain the effect of process parameters and rock's mechanical properties on the rock removal process and force responses. The studied process parameters are the rake angle, cutting speed, and depth of cut, while the rock's mechanical properties are limited to the rock's UCS and the strength grade provided by the International Society of Rock Mechanics (ISRM).

Five sets of tests are conducted as shown in Table 4.1. Three types of sedimentary rock blocks, e.g., Indiana limestone, Austin chalk, and Berea sandstone are selected in this work as seen in Fig. 4.3. According to (Goodman, 1989; Hill, 2015; KocurekIndustries, 2015), the rock properties are listed in Table 4.2. Austin chalk, Indiana limestone, and Berea sandstone belong to weak, medium strong, and strong rocks respectively.

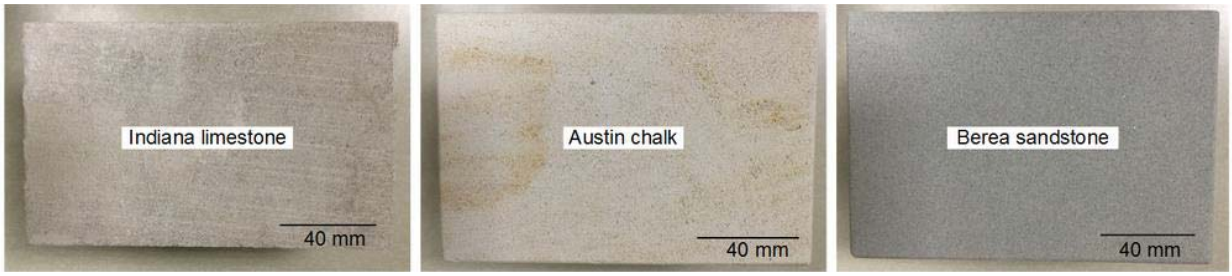

Figure 4.3: Three types of sedimentary rock used in the tests.

As shown in Table 4.1, each of the first three sets can be used to explore how the depth of cut and rake angle affect the chip formation and force responses, while the effect of the rock's UCS can be investigated by comparing the data among these three sets. Test sets 1, 2, and 3 all have

five levels of rake angles, i.e., 10˚, 15˚, 20˚, 25˚, and 30˚ but different levels of depths of cut in order to avoid tool wear due to different rock strengths. Test sets 4 and 5 were performed to investigate whether the cutting speed has a significant effect on chip formation and force responses. Each of these two test sets has 7 levels of cutting speeds, i.e., 4.2, 21.2, 42.3, 63.5, 84.7, 127, and 169.3 mm/s.

For each combination of the rake angle, cutting speed, depth of cut, and rock type in the aforementioned five sets of experiments, the tests were replicated three times to reduce experimental errors. Before each test, the cutter was mounted into the tool holder with a specific rake angle and then moved vertically (i.e., along the *z*-direction as illustrated in Fig. 4.1(a) and (c)) to set the desired cutting depth. Then the rock was fed towards the cutter in the *x*- direction at a constant cutting speed with a user-defined value while the cutter was kept stationary. In this way, the linear cutting motion was achieved. For each test, three force components, i.e., the cutting, side and thrust forces along the *x*- *y*- and *z*-directions respectively were acquired by the force measuring system, while the chip formation phenomena were recorded by the high speed camera. It should be noted that a pre-cutting procedure was conducted to flatten the top surface of the rock before each test.

4.3 Force signal processing

The filtering and signal processing procedures used to eliminate the undesired noise in the captured force signals, along with the algorithm used to evaluate and average the dynamic force responses will be addressed in this section.

4.3.1 Inertia force compensation

As shown in Fig. 4.4, there are force readings when moving the stage at 84.7 mm/s with zero depth of cut. In fact, non-zero force readings are usually observed in all the tests no matter what cutting speed is specified. The higher the cutting speed is, the larger the force values are. The two major reasons for the undesired noise include: (1) environmental noise introduced by the moving stage and (2) inertia forces created due to the sudden move and stop of the stage. The noise due to the first reason can be suppressed by a digital low-pass filter while the inertia forces have to be compensated in a more sophisticated way.

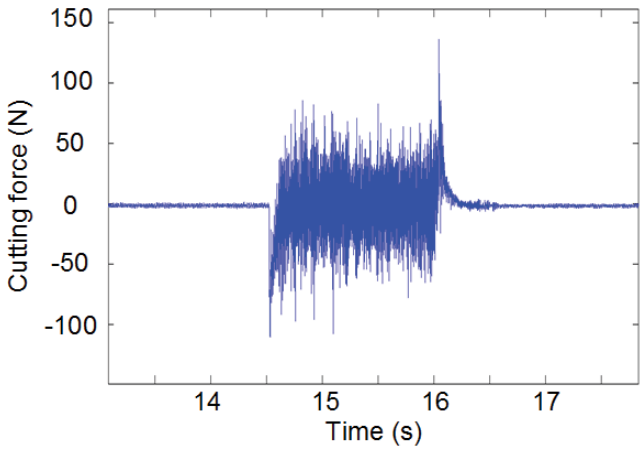

Figure 4.4: Non-zero force readings when the stage is moving without cutting.

The cause of the inertia forces is illustrated in Fig. 4.5. When a cutting test is performed at a constant cutting speed, the PDC cutter will apply a cutting force, i.e., F_c on the rock block. However, there is an inertia acceleration, i.e., a_{inertia} applied to all the components such as the rock, vice and the dynamometer fixed to the moving stage when the stage starts to move and is in motion. According to Newton's second law, the following equation can be drawn:

$$F_c = F_{\text{dyno}} - \sum_{i=1}^{4} M_i \times a_{\text{inertia}} \tag{4.1}$$

where F_{dyno} is the force reading along the x-direction derived from the dynamometer, M_1, M_2, M_3, and M_4 are the masses of the rock, vice, the top part of the dynamometer, i.e., the dynamometer table and the accelerometer attached on the dynamometer table.

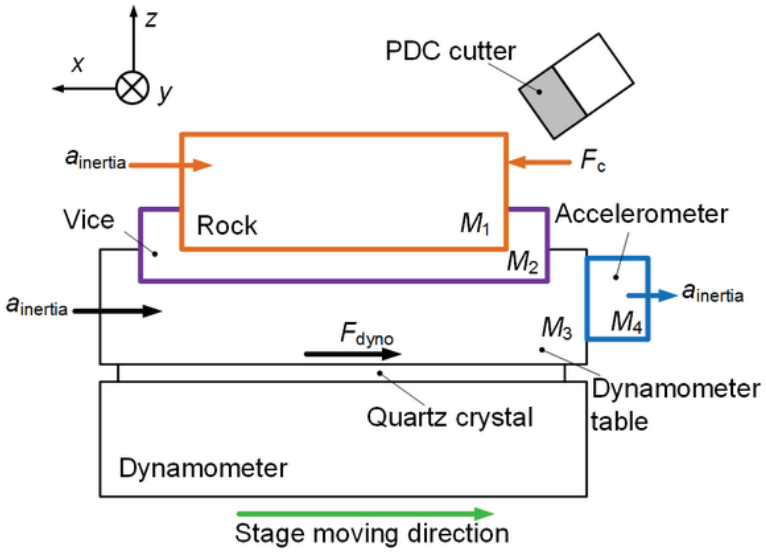

Figure 4.5: Sketch of inertia force compensation.

According to Eq. (4.1), the actual cutting forces are not equal to the dynamometer's force signal as long as there is an inertial acceleration in this dynamic system. Therefore, the inertia force term has to be compensated. The inertial acceleration can be captured by the accelerometer attached on the dynamometer table as shown in Fig. 4.5, i.e.:

$$a_{\text{acc}} = a_{\text{inertia}} \tag{4.2}$$

where a_{acc} is the accelerometer's signal. Substituting a_{inertia} from Eq. (4.2) into Eq. (4.1) yields:

$$F_c = F_{\text{dyno}} - \sum_{i=1}^{4} M_i \times a_{\text{acc}} \tag{4.3}$$

According to Eq. (4.3), inertia force compensation can be achieved by adding the accelerometer's signal multiplied by a factor to the dynamometer's signal:

$$F_{\text{c-comp}} = F_{\text{dyno}} + \beta_c a_{\text{acc}} \tag{4.4}$$

where $F_{\text{c-comp}}$ is the cutting force from compensation, β_c is the compensation constant for the cutting force which can be calibrated by a test with zero depth of cut at an arbitrary cutting speed. By comparing Eqs. (4.3) and (4.4), β_c is exclusively related to the total mass of the dynamic system. Moreover, the rock mass is far smaller than the dynamometer table mass. Therefore, once β_c is determined, the change in the mass of the rock samples will not affect the value of β_c. The calibration procedures are presented next.

As shown in Fig. 4.6, the signals from the dynamometer and accelerometer are captured at a 20 kHz sampling rate during a non-cutting test at a cutting speed of 84.7 mm/s. Then the signals are filtered through a digital low-pass filter as illustrated in Fig. 4.7. The cut-off frequency of the filter is set to 300 Hz. Since the cutting depth of the non-cutting test is zero, the realistic cutting force is zero accordingly. Based on Eq. (4.4), β_c can be determined to minimize $F_{\text{c-comp}}$. Figure 4.8 shows the comparison between the raw cutting force signal derived from the dynamometer and the force signal compensated in the aforementioned way. Moreover, the other two force components, i.e., the thrust and side forces are both compensated in a similar way. In this work, the data from all the tests are filtered and compensated using the above-mentioned method to ensure noise-free force responses.

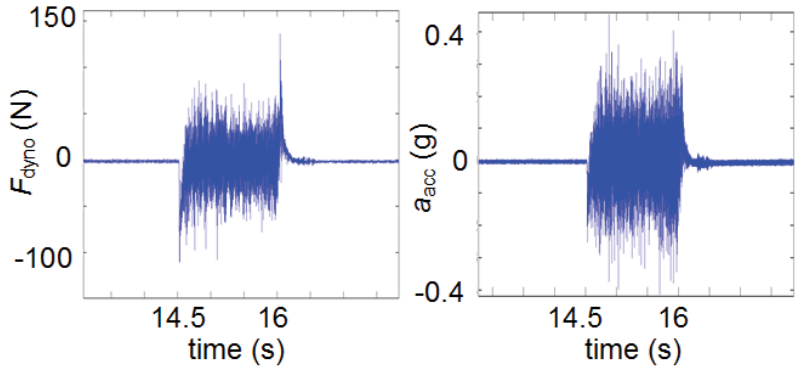

Figure 4.6: Raw data when the stage is moving without cutting.

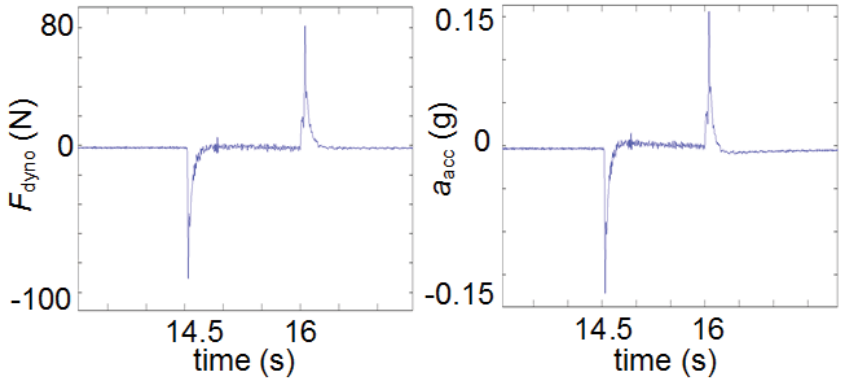

Figure 4.7: Filtered data when the stage is moving without cutting.

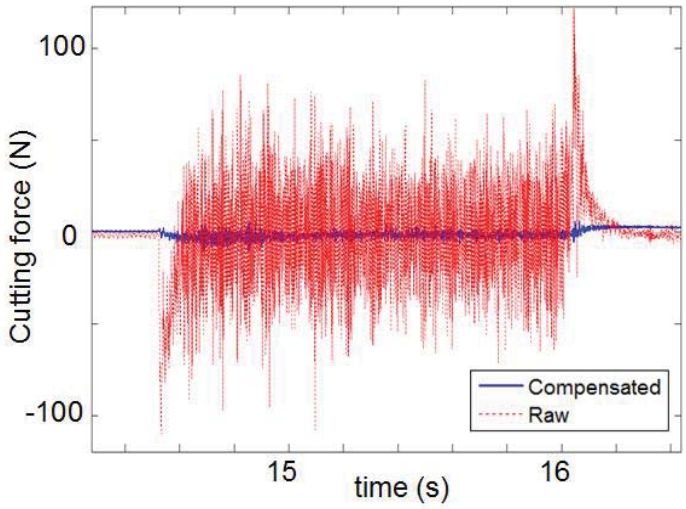

Figure 4.8: Comparison between raw and compensated force data in a non-cutting test.

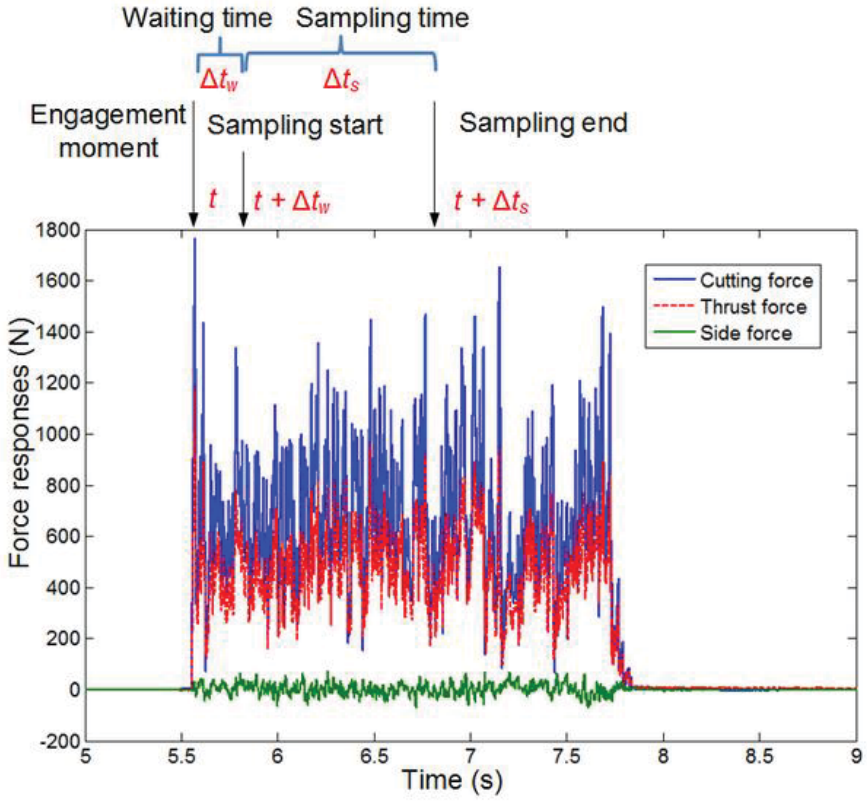

Figure 4.9: Illustration of the force averaging algorithm in linear cutting of Indiana limestone with 1.6 mm depth of cut, 20º rake angle, and 63.5 mm/s cutting speed.

4.3.2 Force averaging algorithm

The dynamic force responses, i.e., the force oscillation data with respect to time which include sufficient information on the rock cutting process, are indeed important for a complete perspective of the process. However, the inhomogeneity of the rock material and the brittle failure nature of the process cause big difficulties to accurately characterize the dynamic force responses in a simple way. Therefore, many researchers purpose the use of average force responses within a certain period of time or travel distance and then study the change of the average forces with respect to various process parameters (Che and Ehmann, 2014; Kaitkay and Lei, 2005; Richard et al., 2012; Wise et al., 2002). In this way, the force responses are characterized from an average point of view.

In fact, time-averaged force values are considered to be a good representative for the dynamic force responses in rock cutting. To this end, change in the time-averaged force responses were investigated with respect to process parameters and rock material properties.

Figure 4.9 shows the principle of averaging the dynamic force responses on the example of cutting Indiana limestone with a 1.6 mm depth of cut and a 20º rake angle at a 63.5 mm/s cutting speed. The moment when the cutter starts to engage the rock is recorded as t. After a waiting time Δt_w, the force data begins to be acquired and averaged within a sampling time interval of Δt_s. For test sets 1, 2, and 3, Δt_w and Δt_s were set to 0.3 s and 1 s respectively. However, since the cutting speed changes between tests in test sets 4 and 5, Δt_w and Δt_s were determined such as to ensure that the rock's traveling distances within both the waiting time and sampling time are the same as those in the first three test sets, i.e.:

$$\Delta t_w = 0.3(\mathrm{s}) \times \frac{63.5(\mathrm{mm/s})}{v_c} \tag{4.5}$$

$$\Delta t_s = 1.0(\mathrm{s}) \times \frac{63.5(\mathrm{mm/s})}{v_c} \tag{4.6}$$

where v_c is the cutting speed in an arbitrary test of test sets 4 and 5. In such a way, three average force components, i.e., the average cutting, thrust and side forces can be obtained from all the cutting tests.

4.4 Chip formation phenomena

This section presents the chip formation phenomena observed in linear cutting of rock by using a high speed camera. The high speed camera was set up to record chip formation from the view

pointing in the *y*-direction, as shown in Fig. 4.10. The focus of the camera was fixed at the interface between the rock and cutter for the whole cutting period.

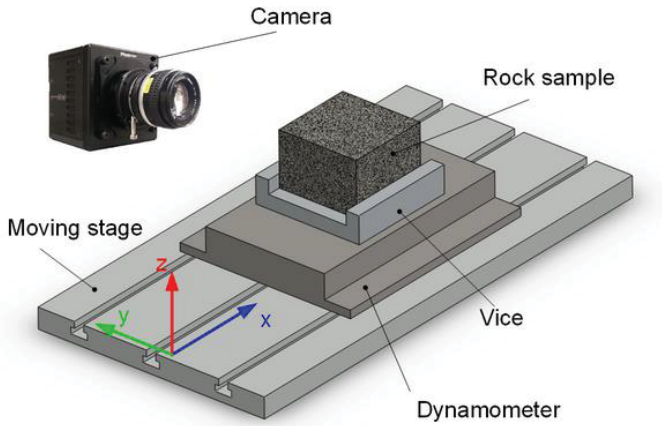

Figure 4.10: Spatial setup of the high speed camera.

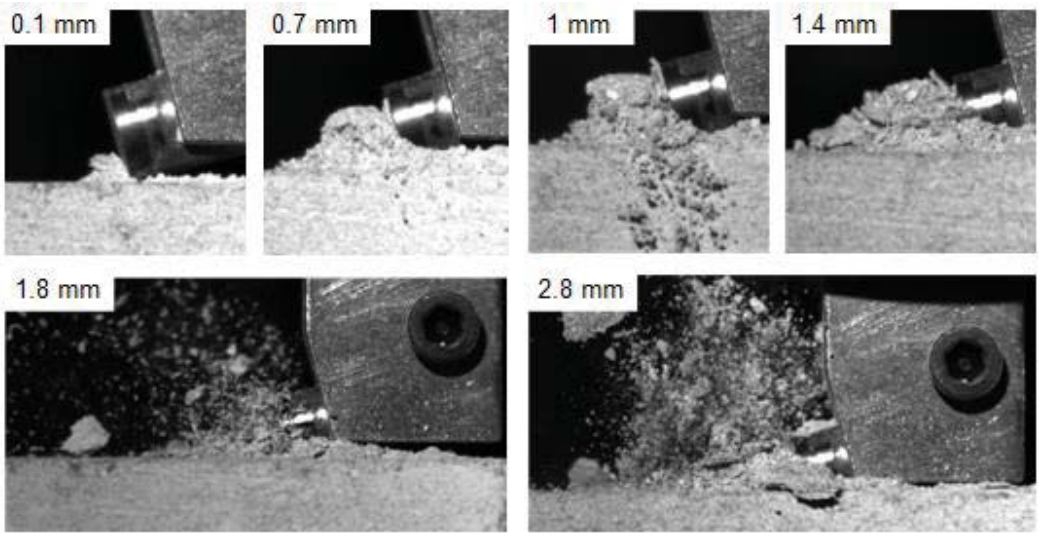

Figure 4.11: Chip formation vs. depth of cut in cutting of Indiana limestone.

Figure 4.11 shows the chip formation phenomena in cutting of Indiana limestone at a 63.5 mm/s cutting speed with a 15º rake angle and 6 levels of depths of cut, i.e., 0.1, 0.7, 1, 1.4, 1.8,

and 2.8 mm. The chips are formed as powders when the depth of cut is below 1 mm, while they become bigger and more chunk-like at depths of cut larger than 1 mm. In other words, the chip size increases when the depth of cut increases. Moreover, the rock fails mildly in shallow cuts but aggressively in deep cuts. As shown in Fig. 4.11, mini-explosions of the rock are found to occur beneath the cutter's rake face at deep cuts, i.e., when the depth of cut is larger than 1.8 mm. In fact, there are two major types of failure in rock cutting, i.e., crushing and chipping (Mishnaevsky, 1995). As observed in Fig. 4.11, the highly fractured and powder-like chips are formed due to crushing, while big chips due to chipping. The chipping mode becomes more and more obvious with the increase of the depth of cut.

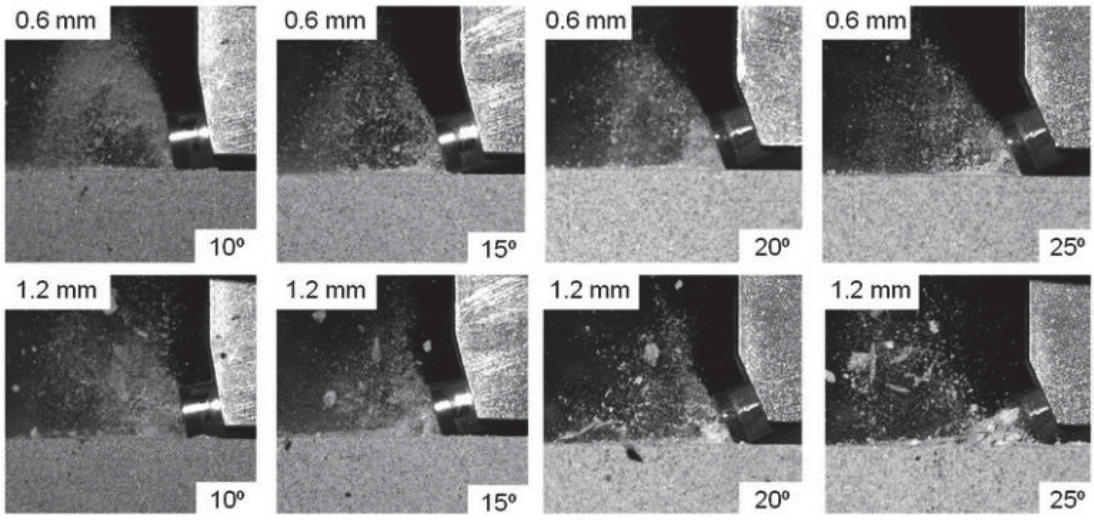

Figure 4.12: Chip formation vs. rake angle in cutting of Berea sandstone.

From the aspect of the rake angle, the chip formation pictures are compared between different rake angles in cutting of Berea sandstone, as illustrated in Fig. 4.12. The depth of cut for the top row is 0.6 mm while 1.2 mm for the bottom row. In fact, for any given depth of cut, the change of

the rake angle does not have an obvious effect on the rock removal process. Similar independence can also be observed in the investigations of the cutting speed's effect on the chip formation process. As shown in Fig. 4.13, the rake angle and depth of cut are set to be 15º and 0.8 mm for the top row while 15º and 1.4 mm for the bottom row. Two types of rocks, i.e., Austin chalk and Indiana limestone are selected for the comparison. The cutting speed has very minor effect on the rock removal process.

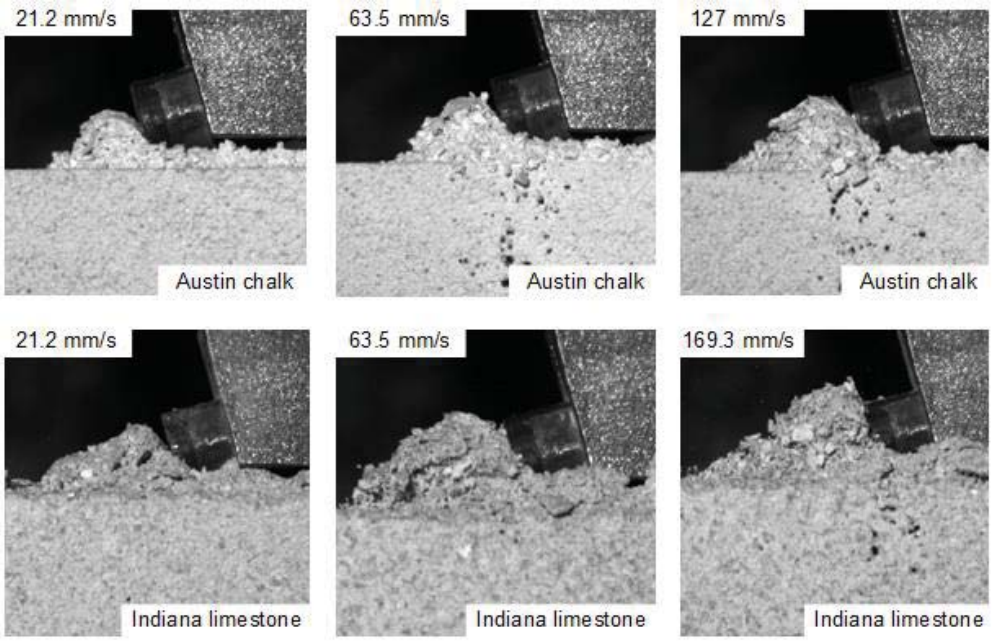

Figure 4.13: Chip formation vs. cutting speed.

The effect of the rock properties on chip formation is shown in Fig. 4.14. Three tests were conducted with a 0.8 mm depth of cut and a 20º rake angle with three types of rocks, i.e., Austin chalk, Indiana limestone, Berea sandstone. As shown in Fig. 4.14, the biggest chips were observed in cutting of Berea sandstone while the smallest chips are observed in cutting of Austin chalk. According to Table 4.2, Berea sandstone is considered as the strongest rock with the highest UCS among the three selected rock types while Austin chalk is the weakest rock with the lowest UCS.

Therefore, it can be concluded that the stronger rock with the higher UCS will lead to larger chips, i.e., a more noticeable chipping failure mode, during linear rock cutting.

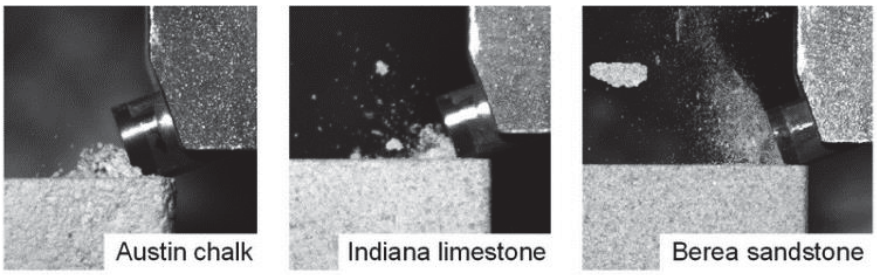

Figure 4.14: Chip formation vs. rock type.

In summary, the depth of cut is the only process parameter which has obvious influence on how the chips are formed according to the above-mentioned experimental observations. The increase of the depth of cut will magnify the chipping of rock. In addition, the strength of the rock also plays a significant role in the chip formation process. Higher rock strengths lead to more intensive chipping and bigger chips.

4.5 Force responses

Chip formation described in Section 4.4 has exhibited the characteristics of rock cutting processes. However, it is difficult to quantitatively relate the process parameters with the chip formation phenomena. Moreover, the characterization of chip formation requires complex image processing technology, which brings even more challenges to clearly illustrate the cutting mechanisms. On the other hand, force responses, as another important indicator of the rock cutting processes, are capable of revealing the intrinsic mechanisms of rock cutting in a quantitative way.

This section will discuss the relationships between the time-averaged force responses, defined in Section 4.3, and the various process parameters.

4.5.1 Influence of process parameters on force responses

In this work, numerous cutting tests have been conducted with three types of rock and multiple levels of process parameters, i.e., the depth of cut, cutting speed, and rake angle, as shown in Table 4.1. For simplicity, only one portion of the experimental results will be selected and compared in this subsection, with the aim of revealing the general relationships between force responses and process parameters.

As shown in Fig. 4.15, the three time-averaged force components, i.e., the cutting, thrust and side forces are plotted at different depths of cut and rake angles. The cutting and thrust forces increase with increasing depths of cut and rake angles, while the side forces oscillate around the zero value due to the orthogonal cutting condition.

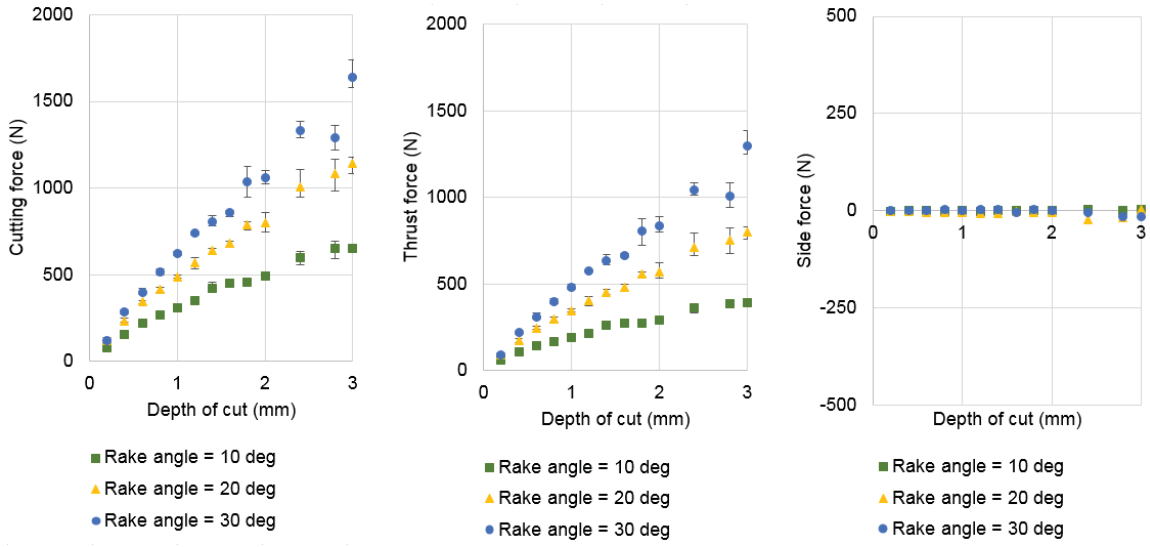

Figure 4.15: Force responses in cutting of Indiana limestone.

For a constant rake angle, the cutting and thrust forces do not linearly increase with the increase of the depth of cut. As mentioned in Section 4.4, both crushing and chipping are involved in rock cutting. Crushing creates highly deformed/damaged rock powders while chipping propagates cracks to form big rock fragments. According to its nature, crushing requires more energy than chipping does. Hence, an increase of the depth of cut requires a larger increase in the cutting force in the crushing mode than that in the chipping mode. As shown in Figs. 4.11 and 4.12, the chipping failure becomes more obvious with larger depths of cut. Therefore, the cutting force is increasing with the depth of cut following a concave downward curve rather than a linear trend. In other words, the non-linearity of the time-averaged force responses can be attributed to the transition of the rock failure mode from crushing to chipping. However, both the cutting and thrust forces can be approximated to be linearly related to the depth of cut when the crushing mode dominates the rock's failure behavior, i.e., the depth of cut is below 1 mm, as illustrated in Fig. 4.15. This result agrees well with other researchers' findings (Jaime et al., 2010; Richard et al., 2012). Similar relationships are observed in cutting of all the three types of sedimentary rocks, i.e., Indiana limestone, Austin chalk, and Berea sandstone as seen in Figs. 4.15, 4.16 and 4.17.

Moreover, the force responses are dramatically fluctuating at large cutting depths due to the intensive coalescence and propagation of cracks under chipping. At small depths of cut, powder-like chips are continuously created by crushing. The chip size varies very little in the crushing mode. Therefore, the variations in the force responses are very small. However, at large depths of cut, chunk-like chips with random sizes are periodically formed due to chipping. The chip size

highly varies due to the inhomogeneity of the rock. Hence, large force variations are observed in tests with large depths of cut.

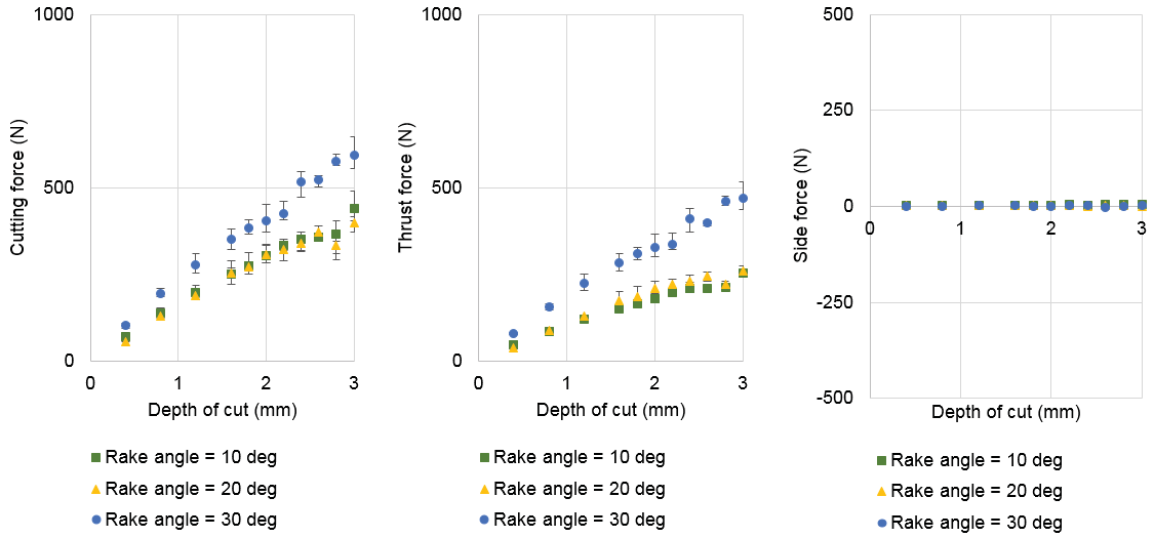

Figure 4.16: Force responses in cutting of Austin chalk.

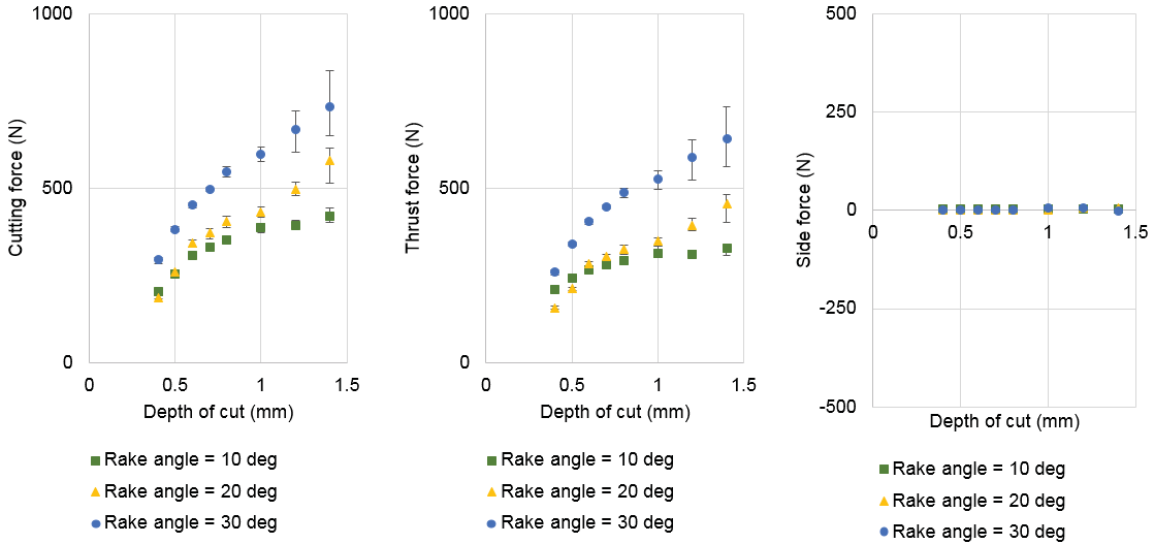

Figure 4.17: Force responses in cutting of Berea sandstone.

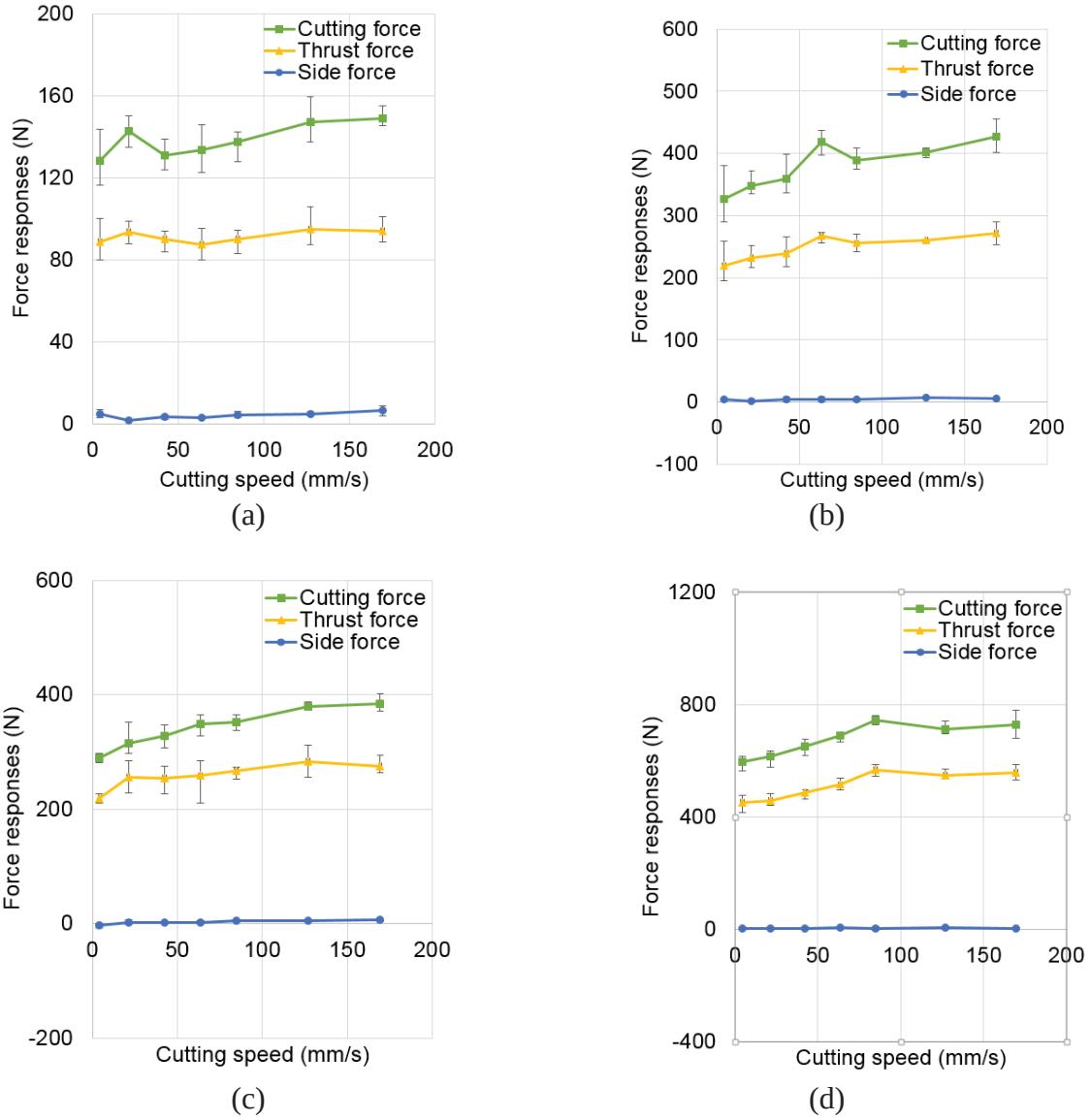

Figure 4.18: Force responses vs. cutting speed: (a) cutting of Austin chalk with 15º rake angle and 0.8 mm depth of cut; (b) cutting of Austin chalk with 15º rake angle and 2.4 mm depth of cut; (c) cutting of Indiana limestone with 25º rake angle and 0.6 mm depth of cut; (d) cutting of Indiana limestone with 25º rake angle and 1.4 mm depth of cut.

In addition to the above, the type of rock was also found to largely affect the force responses. According to Figs. 4.15, 4.16 and 4.17, given the same rake angle and depth of cut, the cutting and

thrust forces for the three types of rock are different. The highest force magnitudes are observed in cutting of Berea sandstone while the smallest ones in cutting of Austin chalk. Based on the rock's properties listed in Table 4.2, an increase in the rock's UCS can be concluded to cause the increase of the force magnitude.

Furthermore, Figure 4.18 indicates that the increase of cutting speed only slightly increases the force responses, no matter what type of rock and what levels of rake angles and depths of cut are specified. Therefore, the force responses can be considered to be independent of cutting speed, excluding the extreme low (i.e., 4.2 mm/s) and high (i.e., 169.3 mm/s) speeds. Similar conclusions were made in the work done by other researchers as well (Richard, 1999).

4.5.2 Relationship between cutting and thrust forces

The cutting and thrust forces exhibit similar responses with respect to various parameters as discussed in Section 4.5.1. As shown in Fig. 4.19, for each type of rock sample, the thrust force is actually proportional to the cutting force for a constant rake angle. In other words, the ratio of the thrust to cutting forces κ is constant for a given rake angle.

The mean friction angle between the cutter and rock on the cutter's rake face, namely the mean friction angle hereafter, has been defined to relate the cutting and thrust forces (Huang et al., 2013; Nishimatsu, 1972), as shown in Fig. 4.20, i.e.:

$$\varphi = \arctan\left(\frac{F_t}{F_c}\right) - \gamma = \arctan\kappa - \gamma \tag{4.7}$$

where F_c and F_t are the cutting and thrust forces, and γ is the rake angle.

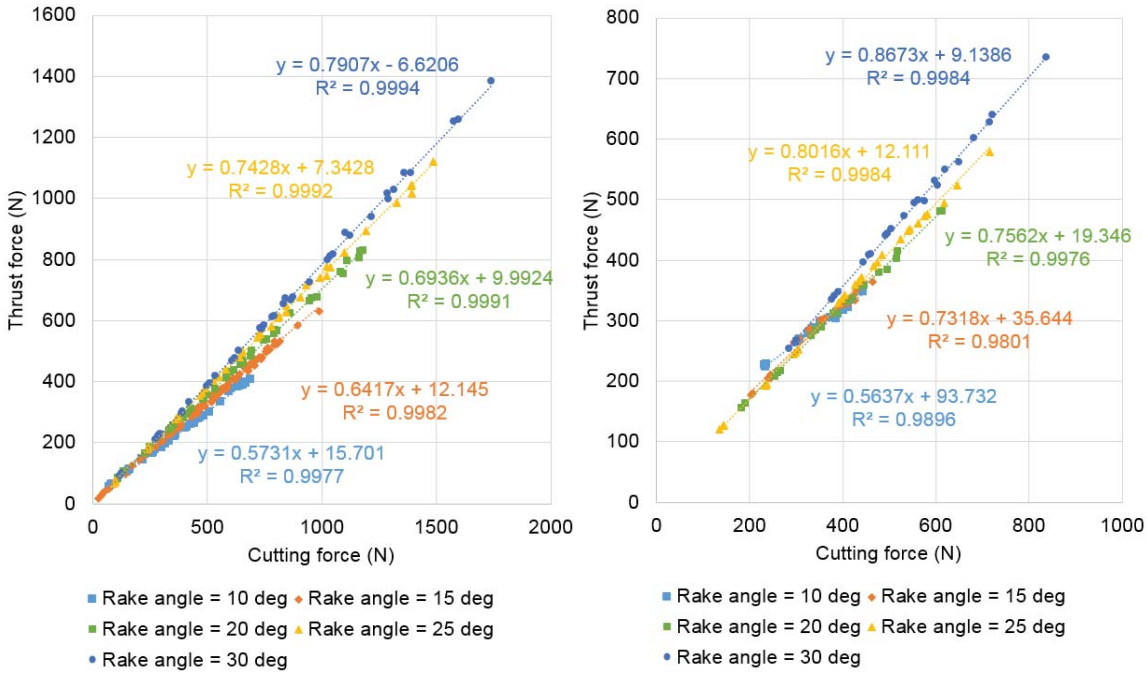

Figure 4.19: Cutting force vs. thrust force: (a) Indiana limestone; (b) Berea sandstone; (c) Austin chalk.

Based on Eq. (4.7) and the data plotted in Fig. 4.19, a linear relation between the friction angle φ and the rake angle γ can be obtained as shown in Fig. 4.21. In accordance with Eq. (4.7) and the linear trend shown in Fig. 4.21, it should be noted that κ is approximately constant for a given rake angle.

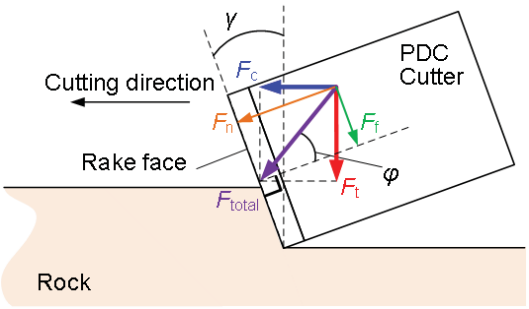

Figure 4.20: Schematic of force responses in orthogonal cutting of rock.

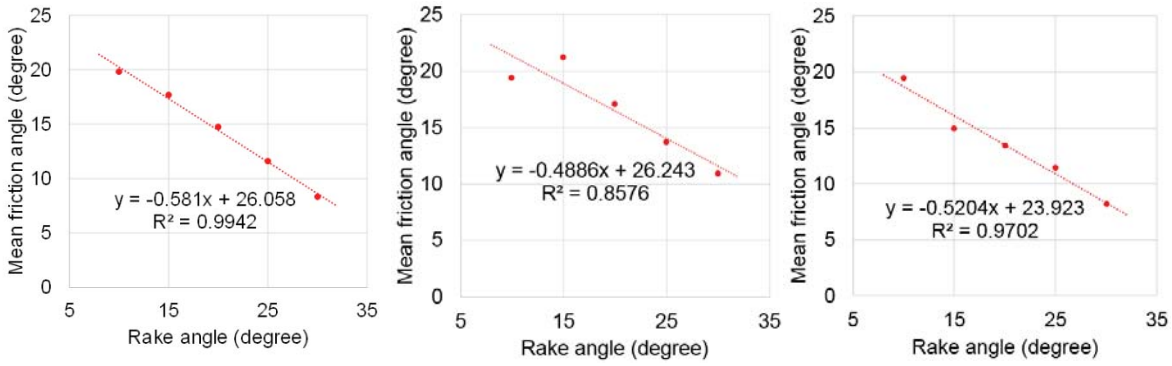

Figure 4.21: Linear relationship between rake and mean friction angle: (a) 1st test set; (b) 2nd test set; (c) 3rd test set.

The increase of the rake angle will increase the force component normal to the rake face, i.e., F_n but decrease the force component tangential to the rake face, i.e., F_f as illustrated in Fig. 4.20. From a physical perspective, F_n is generated due to the chip's impact on the cutter's rake face

while F_f is generated due to the frictional/impact action between the rock and the cutter at the cutter's rake face. In fact, the commercial PDC cutters that are used in oil drilling usually have a much higher impact resistance along the normal direction than the tangential direction, which indicates that a higher rake angle will improve the cutter's cutting performance and reduce the damage rate. On the other hand, the increase of the rake angle will obviously increase the magnitudes of the force responses as shown in Figs. 4.15-4.17, which results in a higher risk of cutter damage. To this end, the rake angle of PDC cutters has to be carefully selected to avoid catastrophic impact damage on the diamond layer of the PDC cutters in the oil drilling practice.

4.6 Conclusions

This chapter has presented an experimental study on linear cutting of sedimentary rocks. Conclusions are given as follows:

(1) Linear rock cutting, among all testing methods, avoids the geometrical complexity encountered in other types of cutting processes and offers the most straightforward way to reveal the intrinsic mechanisms of rock cutting processes.

(2) A linear rock cutting testbed has been developed to investigate the rock-cutter interactions in linear rock cutting, which is equipped with a piezoelectric dynamometer to measure the force responses and a high-speed camera to capture the chip formation phenomena. The orthogonal cutting configuration was ensured by using PDC cutters with customized shapes.

(3) A series of cutting tests were designed to explore the influences of significant parameters, i.e., depth of cut, rake angle, cutting speed and rock type on chip formation and force responses.

(4) The acquired force signals were filtered and compensated to minimize environmental noise and undesired dynamic behaviors that occur during the cutting tests.

(5) The effects of the process parameters and the rock's mechanical properties on the chip formation phenomena and force responses were discussed. Chipping failure is intensified, i.e., the chip size increases with the increase of the depth of cut and the rock's uniaxial compressive strength (UCS). Moreover, the magnitudes of the force responses increase with an increase in depth of cut, rake angle and the rock's UCS but they are independent of the cutting speed except for extremely high values.

(6) For all the tested rocks, the thrust force was found to be proportional to the cutting force with a constant rake angle. The mean frictional angle which relates the cutting and thrust forces was discussed and observed to linearly increase with an increase in the rake angle.

Chapter 5

Cutting Mechanics in Orthogonal Cutting of Rock

In the previous chapter, linear cutting tests have been conducted and their results have been analyzed in terms of chip formation and force response phenomena. This chapter aims to develop a cutting theory which can explain how the rock and cutter interact based on a more realistic rock removal mechanism and more accurate force predictions under ideal cutting conditions, i.e., the orthogonal cutting condition.

In order to achieve this goal, a crushing zone, namely the Tip Crushing Zone (TCZ) is defined right beneath the cutter's rake face with a specific stress distribution. A crack is assumed to initiate at an arbitrary location on the boundary of the TCZ and propagate towards the free surface of the virgin rock to form a chip. The force responses are then derived based on the equilibrium of moments applied to the chip and the minimum chipping energy principle. A series of linear rock cutting tests, presented in Chapter 4, will facilitate the calibration and feasibility assessment of the developed force model.

The organization of this chapter is given as follows: Section 5.1 develops the above-mentioned new cutting theory. In Section 5.2 the proposed cutting theory will be evaluated by comparing the force predictions with experimental measurements. Several characteristic parameters for this new theory will be discussed in Section 5.3, followed by the drawn conclusions in Section 5.4.

5.1 Theory

This section presents a new cutting theory which explains how rock fails in the linear rock cutting process and then provides predictions of the forces exerted by the PDC cutter onto the rock. The ultimate goal of this theory is to reveal the nature of rock failure and then formulate closed form expressions for the two orthogonal force components in rock cutting, namely the cutting and thrust forces, which are defined as force components along and perpendicular to the cutting direction respectively, as shown in Fig. 5.1.

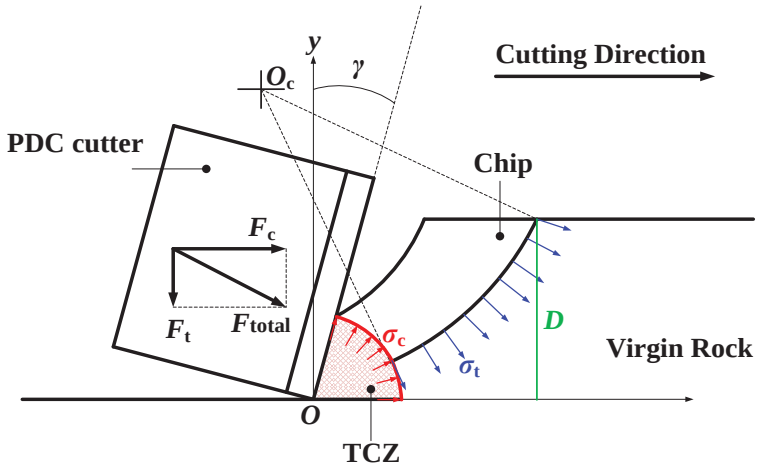

Figure 5.1: Schematic of the rock removal mechanism in the new cutting theory.

To achieve the set forth goal, necessary assumptions are made to simplify this problem in accordance with realistic cutting conditions, as summarized in Section 5.1.1. For a better understanding of the theory, Section 5.1.2 will discuss the derivation of a closed form expression of the cutting force for a simple case. Then, the cutting force model will be naturally extended to a more general case in Section 5.1.3 with intrinsic similarities to the simpler case. Based on the derived general cutting force model, a thrust force model will also be given by defining a new process parameter from a physical perspective, which will be discussed in Section 5.1.4.

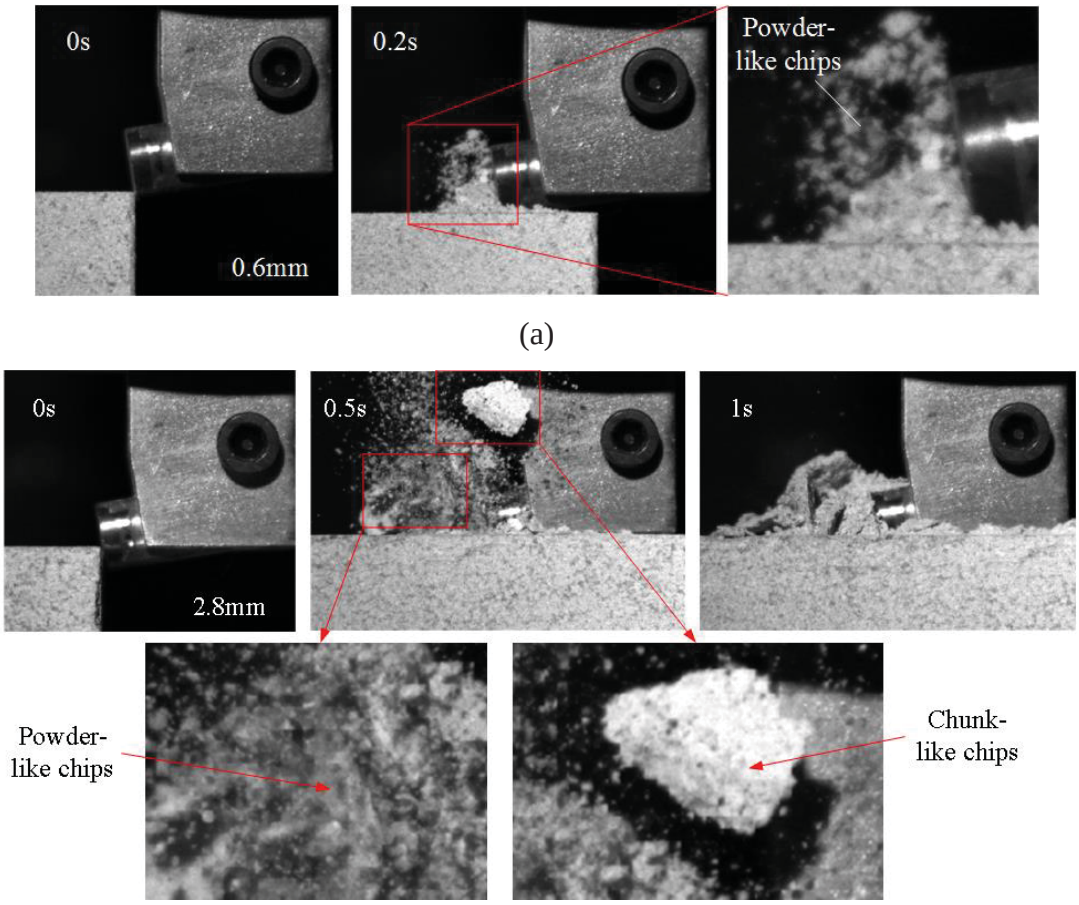

Figure 5.2: Linear cutting of Indiana limestone: (a) shallow cut with a depth of cut of 0.6 mm; (b) deep cut with a depth of cut of 2.8 mm.

5.1.1 Assumptions

Assumption (1): For simplicity, the two-dimensional orthogonal cutting condition is assumed in this cutting theory.

Assumption (2): Figure 5.2 shows a comparison of the chip formation phenomena between small and large depths of cut in the linear cutting of Indiana limestone. Powdery chips, attributed to the crushing failure mode, exist in both shallow and deep cutting tests but chunk-like chips,

attributed to the chipping failure mode, only exist in deep cutting tests. Therefore the theory assumes that chipping and crushing modes simultaneously exist during the cutting process.

Assumption (3): A rock crushing zone, i.e., the red and shaded area in Fig. 5.1, namely a Tip Crushing Zone (TCZ) is assumed to be formed beneath the cutter's rake face and close to the cutting edge. Since the TCZ is formed due to the crushing of rock, the TCZ boundary is assumed as an arc with a uniform stress distribution equal to the rock's uniaxial compressive strength, σ_c, from the physical point of view. During the cutting process, the TCZ moves further along the cutting speed direction and continuously forms a stable crushing zone beneath the cutter's rake face.

Assumption (4): The TCZ initiates the chipping of rock. Hence, the crack initiates on the TCZ boundary and propagates following an arc-shaped path towards the free surface of the virgin rock.

Assumption (5): The chip is assumed to be formed due to tensile stresses along the crack propagation path between the chip and the virgin rock, i.e., the crack is a Mode I crack defined in the theory of fracture mechanics. Since the chip is rapidly formed due to the high speed cutting process, the stress distribution along the arc-shaped crack propagation path right before the separation of the chip from the virgin rock, is assumed to be uniform with a value equal to the rock's tensile stress, σ_t, as shown in Fig. 5.1. Similar assumption has been made by other researchers (Evans, 1962; Evans, 1965; Xue et al., 2009; Yan, 1997).

Assumption (6): The resultant forces exerted from the TCZ and crack propagation path to the chip and their moments are assumed to remain in equilibrium.

Assumption (7): The energy used to form the chip, namely the chipping energy, is assumed to comply with the minimum energy principle proposed in (Boothroyd and Knight, 1989; Merchant,

1944; Nishimatsu, 1972), which is essential to quantitatively determine how the chip forms during the chipping mode.

Assumption (8): The cutting process is assumed to be performed by a sharp cutter, which indicates that all the force components applied by the cutter are from the rake face of the cutter. No friction on the flank face is considered in this theory.

Assumption (9): Due to the brittle failure behavior of the rock cutting processes, it is commonly assumed that the cutting speed has very little influence on the force responses (Nishimatsu, 1972; Yan, 1997).

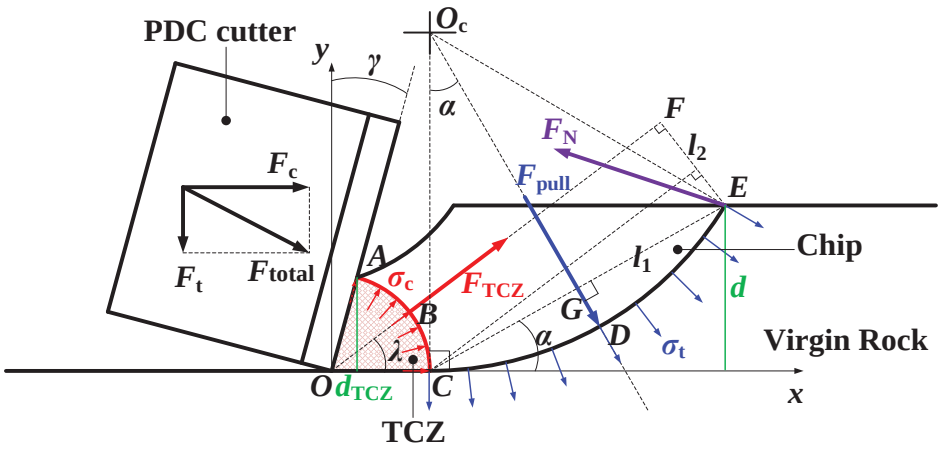

Figure 5.3: Schematic of crack initiated along the horizontal direction.

5.1.2 Cutting force in a simple case

For simplicity, in this section, the crack was first assumed to initiate at the bottom of the cutting area, which is regarded as a simple model. Crack initiating at arbitrary locations, considered as a general model, will be discussed in the next section. As shown in Fig. 5.3, the crack initiates at point *C* which is located at the same horizontal level as the cutter's cutting edge. Since the crack

is assumed to be a Mode I crack, due to tensile breakage according to Assumption (5), the crack has to initiate along the direction perpendicular to the maximum principal stress (Scheidegger, 1982), i.e., the horizontal direction.

According to Assumption (3), the rock in the TCZ is assumed to be crushed after engaging with the PDC cutter and the stress distribution on the boundary of the TCZ, shown in red, is assumed as a uniform compressive stress with a value equal to the rock's uniaxial compressive strength, σ_c. Assumption (8) indicates that the cutting and thrust forces are exclusively exerted by the cutter's rake face on the TCZ. Therefore, the horizontal component of the resultant force exerted by the TCZ on the chip, i.e., F_{TCZ}, as shown in Fig. 5.3, can be considered to be equal in magnitude to the cutting force F_c. F_{TCZ} has to be determined first in order to derive an expression for F_c. Based on the stress distribution on the boundary of the TCZ, F_{TCZ} can be expressed as:

$$\overrightarrow{F_{TCZ}} = w\int_0^{2\lambda} \vec{n}\cdot\sigma_c r\,d\theta = w\int_0^{2\lambda} (\cos\theta\,\vec{i} + \sin\theta\,\vec{j})\cdot\sigma_c r\,d\theta = w\sigma_c r[\vec{i}\sin 2\lambda - \vec{j}(\cos 2\lambda - 1)] \quad (5.1)$$

where $\overrightarrow{F_{TCZ}}$ is the resultant force exerted at the middle point of the arc *ABC*, i.e., point *B* and pointing upward in the direction normal to arc *ABC* at Point *B*. In Eq. (5.1) w is the cutter's width, $\vec{n}$ is the normal vector on arc *ABC*, λ is the half angle of the TCZ, r is the radius of the TCZ, $\vec{i}$ and $\vec{j}$ are the unit vectors along the horizontal and vertical directions respectively. According to process geometry, the following relations can be given:

$$2\lambda + \gamma = \frac{\pi}{2} \quad (5.2)$$

$$r = \frac{d_{TCZ}}{\sin 2\lambda} \quad (5.3)$$

where d_{TCZ} is defined as the depth of the TCZ. Substituting λ from Eqs. (5.2) and r from (5.3) into Eq. (5.1) yields:

$$F_{TCZ} = 2w\sigma_c \frac{d_{TCZ}}{\cos\gamma} \sin\left(\frac{\pi}{4} - \frac{\gamma}{2}\right) \tag{5.4}$$

where F_{TCZ} is the magnitude of the resultant force. According to Eq. (5.4), the only unknown parameter, i.e., d_{TCZ}, has to be determined in order to solve for F_{TCZ}. Hence, the ratio of d_{TCZ} to the depth of cut d, i.e., the tip crushing ratio, will be derived based on the equilibrium of moments exerted on the chip. Since d is directly given by the cutting conditions, d_{TCZ} can then be determined from the tip crushing ratio. To solve the equilibrium of moments, the resultant force exerted by the virgin rock onto the chip, i.e., F_{pull}, shown in Fig. 5.3, has to be determined first. According to Assumption (5), the crack propagation path is assumed as an arc, i.e., arc *CDE*, which is tangential to the horizontal direction at point *C*. Moreover, a uniform tensile stress distribution with the value equal to the rock's tensile strength, σ_t, is assumed to exist along the arc *CDE* at the moment right before the chip separates from the virgin rock. Therefore, the resultant force exerted by the virgin rock onto the chip can be given by:

$$\overrightarrow{F_{pull}} = w\int_0^{2\alpha} \vec{N}\cdot\sigma_t R\,d\theta = w\int_0^{2\alpha} (\sin\theta\,\vec{i} + \cos\theta\,\vec{j})\cdot\sigma_t R\,d\theta = w\sigma_t R[\vec{j}\cos 2\alpha - \vec{i}(\cos 2\alpha - 1)] \tag{5.5}$$

where $\overrightarrow{F_{pull}}$ is the resultant force exerted at the middle point of arc *CDE*, i.e., point *D* and pointing downward to the direction normal to arc *CDE* at point *D*, $\vec{N}$ is the normal vector at arc *CDE*, α is the crack initial angle equal to the half angle of arc *CDE*, *R* is the radius of arc *CDE*. The geometrical relationships in Fig. 5.3 can be expressed by:

$$\overline{CE} = \frac{d}{\sin\alpha} \tag{5.6}$$

$$R = \frac{\overline{CE}}{2} \times \frac{1}{\sin\alpha} \tag{5.7}$$

where $\overline{CE}$ is the length of segment *CE*, and *d* is the depth of cut. Substituting $\overline{CE}$ from Eq. (5.6) into Eq. (5.7) and then inserting *R* from Eq. (5.7) into Eq. (5.5) yields:

$$F_{\text{pull}} = \sigma_{\text{t}} \frac{d}{\sin\alpha} \tag{5.8}$$

Based on Assumption (6), the forces applied on the chip and their moments are assumed to be in equilibrium before the chip separates from the virgin rock. Therefore, a supporting force F_N, as shown in Fig. 5.3, is defined to equalize the other two forces, i.e., F_{TCZ} and F_{pull}. The equilibrium of moments about point *E* yields the following condition:

$$F_{\text{pull}} \times l_1 - F_{\text{TCZ}} \times l_2 = 0 \tag{5.9}$$

where l_1 is the length of segment *EG* and l_2 is the length of segment *EF* which can be expressed by:

$$l_1 = \frac{1}{2}\frac{d}{\sin\alpha} \tag{5.10}$$

$$l_2 = \frac{d}{\sin\alpha}\sin\left(\frac{\pi}{4} - \frac{\gamma}{2} - \alpha\right) + \frac{d_{\text{TCZ}}}{\cos\gamma}\sin\left(\frac{\pi}{4} - \frac{\gamma}{2}\right) \tag{5.11}$$

Substituting F_{TCZ} from Eq. (5.4), F_{pull} from Eq. (5.8), l_1 from Eq. (5.10), and l_2 from Eq. (5.11) into Eq. (5.9) gives:

$$\left(\frac{d_{TCZ}}{d}\right)^2 + \frac{d_{TCZ}}{d} \bullet \frac{\cos\gamma \sin\left(\frac{\pi}{4} - \frac{\gamma}{2} - \alpha\right)}{\sin\left(\frac{\pi}{4} - \frac{\gamma}{2}\right)\sin\alpha} - \frac{P\cos^2\gamma}{4\sin^2\alpha \sin^2\left(\frac{\pi}{4} - \frac{\gamma}{2}\right)} = 0 \tag{5.12}$$

where $\frac{d_{TCZ}}{d}$ is defined as the tip crushing ratio, while the tensile-compressive ratio, namely P, can be defined by:

$$P = \frac{\sigma_t}{\sigma_c} \tag{5.13}$$

Since $\frac{d_{TCZ}}{d}$ is always non-negative, from the physical point of view, the following equation can be drawn:

$$\frac{d_{TCZ}}{d} = \frac{-\frac{\cos\gamma \sin\left(\frac{\pi}{4} - \frac{\gamma}{2} - \alpha\right)}{\sin\left(\frac{\pi}{4} - \frac{\gamma}{2}\right)\sin\alpha} + \sqrt{\Delta}}{2} \tag{5.14}$$

where

$$\Delta = \frac{\cos^2\gamma\left[\sin^2\left(\frac{\pi}{4} - \frac{\gamma}{2} - \alpha\right) + P\right]}{\sin^2\alpha \sin^2\left(\frac{\pi}{4} - \frac{\gamma}{2}\right)} \tag{5.15}$$

Substitution of Δ from Eq. (5.15) into Eq. (5.14) yields:

$$\frac{d_{TCZ}}{d} = \frac{\cos\gamma}{2\sin\left(\frac{\pi}{4} - \frac{\gamma}{2}\right)} F \tag{5.16}$$

where

$$F = -\frac{\sin(\varepsilon-\alpha)}{\sin\alpha} + \sqrt{\frac{\sin^2(\varepsilon-\alpha)}{\sin^2\alpha} + P\csc^2\alpha} \\ = \cos\varepsilon - \sin\varepsilon\cot\alpha + \sqrt{(\sin^2\varepsilon + P)\cot^2\alpha - \sin 2\varepsilon\cot\alpha + P + \cos^2\varepsilon} \tag{5.17}$$

and where

$$\varepsilon = \frac{\pi}{4} - \frac{\gamma}{2} \tag{5.18}$$

As it can be seen, to evaluate the tip crushing ratio, given by Eq. (5.16), with reference to Eqs. (5.17) and (5.18), the rake angle γ, the tensile-compressive ratio P, and the crack initial angle α need to be known. The first two are known since they are defined by the given cutting conditions, while α needs to be determined. Its determination is addressed next.

Based on the minimum energy principle, mentioned under Assumption (7), the crack initial angle α can be determined by minimizing the chipping energy, E_c, i.e.:

$$\frac{\partial}{\partial\alpha}(E_c) = 0 \tag{5.19}$$

where

$$E_c = F_c \cdot L \tag{5.20}$$

and where L is the total distance that the cutter has moved. According to Eq. (5.1), the cutting force used to chip the rock can be determined by:

$$F_c = \vec{i} \cdot \overrightarrow{F_{TCZ}} = \sigma_c w r \sin 2\lambda = \sigma_c \left(\frac{d_{TCZ}}{d} \right) w d \tag{5.21}$$

Therefore, substituting F_c from Eq. (5.21) into Eq. (5.20) and then inserting E_c from Eq. (5.20) into Eq. (5.19) yields:

$$\frac{\partial}{\partial \alpha} \left(\frac{d_{TCZ}}{d} \right) = 0 \tag{5.22}$$

According to Eqs. (5.16), (5.17) and (5.22), $\frac{\partial F}{\partial \alpha}$ has to be zero and can be given by the following expression:

$$\frac{\partial F}{\partial \alpha} = \sin \varepsilon \csc^2 \alpha - \frac{2\left(\sin^2 \varepsilon + P\right)\cot \alpha - \sin 2\varepsilon}{2\sqrt{\left(\sin^2 \varepsilon + P\right)\cot^2 \alpha - \sin 2\varepsilon \cot \alpha + P + \cos^2 \varepsilon}} \csc^2 \alpha = 0 \tag{5.23}$$

Simplification of Eq. (5.23) yields:

$$4P\left(P + \sin^2 \varepsilon\right)\cot^2 \alpha - 4P \sin 2\varepsilon \cot \alpha - 4P \sin^2 \varepsilon = 0 \tag{5.24}$$

Since α is assumed to be positive, α can be solved from Eq. (5.24), i.e.:

$$\alpha = \arctan \frac{2\left(P + \sin^2 \varepsilon\right)}{\sin 2\varepsilon + \sqrt{\sin^2 2\varepsilon + 4\left(P + \sin^2 \varepsilon\right)\sin^2 \varepsilon}} \tag{5.25}$$

Substitution of P from Eq. (5.13) and ε from Eq. (5.18) into Eq. (5.25) yields:

$$\alpha = \arctan \frac{2\left(\frac{\sigma_t}{\sigma_c} + \sin^2\left(\frac{\pi}{4} - \frac{\gamma}{2}\right)\right)}{\cos\gamma + \sqrt{\cos^2\gamma + 4\frac{\sigma_t}{\sigma_c}\sin^2\left(\frac{\pi}{4} - \frac{\gamma}{2}\right) + 4\sin^4\left(\frac{\pi}{4} - \frac{\gamma}{2}\right)}} \tag{5.26}$$

Therefore, substituting α from Eq. (5.26) and F from Eq. (5.17) into Eq. (5.16) gives the closed form expression of the tip crushing ratio, i.e.:

$$\frac{d_{TCZ}}{d} = \cos\gamma\left[-\frac{\cos\gamma}{4\sin^2\left(\frac{\pi}{4} - \frac{\gamma}{2}\right) + 4\frac{\sigma_t}{\sigma_c}} - \frac{\sqrt{\cos^2\gamma + 4\frac{\sigma_t}{\sigma_c}\sin^2\left(\frac{\pi}{4} - \frac{\gamma}{2}\right) + 4\sin^4\left(\frac{\pi}{4} - \frac{\gamma}{2}\right)}}{4\sin^2\left(\frac{\pi}{4} - \frac{\gamma}{2}\right) + 4\frac{\sigma_t}{\sigma_c}}\right. \tag{5.27}$$
$$\left. + \frac{\sqrt{\frac{\sigma_t}{\sigma_c} + 1}}{2\sin\left(\frac{\pi}{4} - \frac{\gamma}{2}\right)} + \frac{1}{2}\cot\left(\frac{\pi}{4} - \frac{\gamma}{2}\right)\right]$$

Finally, substituting $\frac{d_{TCZ}}{d}$ from Eq. (5.27) into Eq. (5.21) yields the close form expression for the cutting force, i.e.:

$$F_c = w\sigma_c d\cos\gamma\left[-\frac{\cos\gamma}{4\sin^2\left(\frac{\pi}{4} - \frac{\gamma}{2}\right) + 4\frac{\sigma_t}{\sigma_c}}\right.$$
$$- \frac{\sqrt{\cos^2\gamma + 4\frac{\sigma_t}{\sigma_c}\sin^2\left(\frac{\pi}{4} - \frac{\gamma}{2}\right) + 4\sin^4\left(\frac{\pi}{4} - \frac{\gamma}{2}\right)}}{4\sin^2\left(\frac{\pi}{4} - \frac{\gamma}{2}\right) + 4\frac{\sigma_t}{\sigma_c}} + \frac{\sqrt{\frac{\sigma_t}{\sigma_c} + 1}}{2\sin\left(\frac{\pi}{4} - \frac{\gamma}{2}\right)} + \frac{1}{2}\cot\left(\frac{\pi}{4} - \frac{\gamma}{2}\right)\Bigg] \tag{5.28}$$

At this stage, the cutting force required to form a horizontal crack can be explicitly determined by Eq. (5.28) with the knowledge of the corresponding parameters. The required parameters

include process parameters, i.e., cutter's width w, depth of cut d, and rake angle γ, material parameters, i.e., the rock's uniaxial compressive strength σ_c and its tensile strength σ_t.

In reality, however, the crack usually initiates at a random location and propagates along an arbitrary direction rather than the horizontal direction. Therefore, a more general cutting force model has to be derived. This follows in the next section.

5.1.3 A general cutting force model

In reality, the crack does not necessarily initiate horizontally as it was assumed for simplicity in Section 2.3. Therefore, a more general cutting force model has to be formulated. As shown in Fig. 5.4, the crack is assumed to initiate at an arbitrary location C on the boundary of the TCZ. The crack propagation path is perpendicular to the boundary of TCZ at point C. In this way, the chip will be formed above line CK following a similar mechanism as for the simple case discussed in Section 5.1.2, while the rest of the rock below line CK will fail in a pure crushing mode. Hence, both chipping and crushing mechanisms are naturally included in this general force model. The total cutting force can be expressed by:

$$F_c = \vec{i}\cdot\left(\overrightarrow{F_{\text{TCZ-c}}} + \overrightarrow{F_{\text{TCZ-cr}}}\right) = \vec{i}\cdot w\int_0^{\frac{\pi}{2}-\gamma} \vec{n}\cdot\sigma_c \frac{D_{\text{TCZ}}}{\cos\gamma}\,d\theta = w\sigma_c D_{\text{TCZ}} \tag{5.29}$$

where $\overrightarrow{F_{\text{TCZ-c}}}$ and $\overrightarrow{F_{\text{TCZ-cr}}}$ are the resultant chipping and crushing forces respectively, w is the cutter's width, D_{TCZ} is the depth of the TCZ for the general case, $\vec{n}$ is the normal vector along the TCZ boundary, and $\vec{i}$ is the unit vector along the horizontal direction. According to Eq. (5.29),

D_{TCZ} has to be determined to fully predict F_c. Therefore, in a manner similar to the simpler case in Section 5.1.2, the tip crushing ratio, i.e., $\frac{D_{TCZ}}{D}$, has to be determined.

From the physical point of view, line *OCK*, shown in Fig. 5.4, divides the rock into two portions, i.e., the upper portion affected by the chipping action and the lower portion affected by the crushing action. Therefore, the upper portion is defined as the chipping affected zone, while the lower portion is defined as the crushing affected zone. The angle ω, namely the chipping-crushing transition angle, is defined to characterize the transition boundary between these two affected zones.

Similarities in the chipping action exist between the simple and the general cases described in Sections 5.1.2 and 5.1.3 respectively. As shown in Fig. 5.3, the chipping action occurs beneath the cutter's rake face but above the *x*-axis, i.e., line *OCx* which can be defined as the chipping affected zone in the simple case. Similarly, the chipping affected zone in the general case, shown in Fig. 5.4, is the rock beneath the cutter's rake face but above the *x'*-axis, i.e., line *OCK*. Therefore, by rotating the chipping affected zone in the simple case, shown in Fig. 5.3, by the angle ω, the chipping affected zone in the general case can be derived as shown in Fig. 5.4. In other words, as shown in Fig. 5.4, the coordinate system *x'Oy'* is defined by rotating the original coordinate system *xOy* by ω. Therefore, the chipping action for the general case with an equivalent rake angle Γ, equivalent depth of cut *d*, and equivalent depth of the TCZ d_{TCZ}, as observed in the coordinate system *x'Oy'*, as shown in Fig. 5.4, is completely equivalent to that in the simple case with a rake angle γ, depth of cut *d*, and depth of the TCZ d_{TCZ} observed in the original coordinate system *xOy* shown in Fig. 5.3.

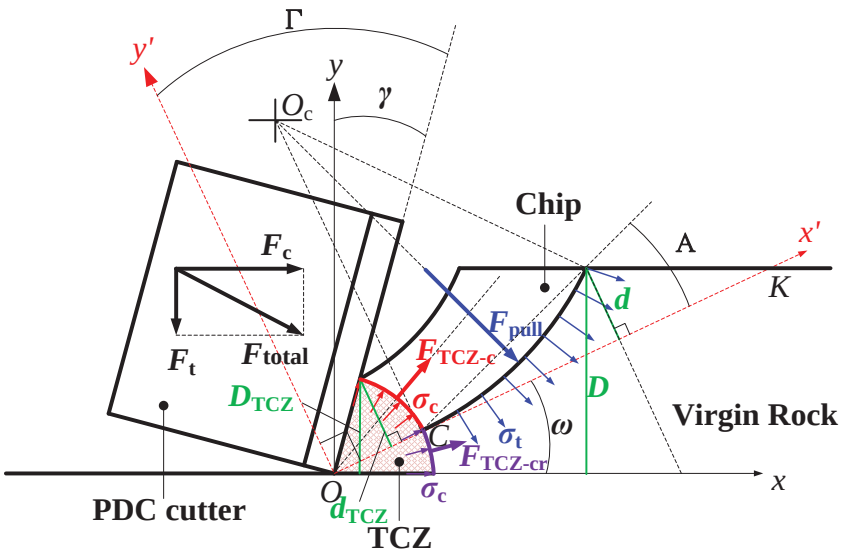

Figure 5.4: Schematic of the rock removal mechanism in the arbitrary chipping mode.

Therefore, based on the above-stated geometrical similarity, Γ can be used as the equivalent rake angle to derive the ratio of d_{TCZ} to d in the general case based on Eq. (5.27), i.e.:

$$m = \frac{d_{TCZ}}{d} = \cos\Gamma \times [-\frac{\cos\Gamma}{4\sin^2\left(\frac{\pi}{4}-\frac{\Gamma}{2}\right)+4\frac{\sigma_t}{\sigma_c}} - \frac{\sqrt{\cos^2\Gamma+4\frac{\sigma_t}{\sigma_c}\sin^2\left(\frac{\pi}{4}-\frac{\Gamma}{2}\right)+4\sin^4\left(\frac{\pi}{4}-\frac{\Gamma}{2}\right)}}{4\sin^2\left(\frac{\pi}{4}-\frac{\Gamma}{2}\right)+4\frac{\sigma_t}{\sigma_c}} + \frac{\sqrt{\frac{\sigma_t}{\sigma_c}+1}}{2\sin\left(\frac{\pi}{4}-\frac{\Gamma}{2}\right)} + \frac{1}{2}\cot\left(\frac{\pi}{4}-\frac{\Gamma}{2}\right)] \tag{5.30}$$

Since the coordinate system *x'Oy'* is derived by rotating the coordinate system *xOy* by ω, the relationship between Γ and γ is given by:

$$\Gamma = \gamma + \omega \tag{5.31}$$

According to the geometrical relationships shown in Fig. 5.4, the depth of cut D and depth of the TCZ D_{TCZ} can be expressed by:

$$D = \left[\left(\frac{d_{TCZ}}{\cos(\gamma+\omega)} + \frac{d}{\tan A}\right)\tan\omega + d\right]\cos\omega \tag{5.32}$$

$$\frac{D_{TCZ}}{\sin\left(\frac{\pi}{2}-\gamma\right)} = \frac{d_{TCZ}}{\sin\left(\frac{\pi}{2}-\gamma-\omega\right)} \tag{5.33}$$

Combining Eqs. (5.30), (5.31), (5.32) and (5.33) to derive the relationship between D_{TCZ} and D, one obtains:

$$M = \frac{D_{TCZ}}{D} = \frac{\sin\left(\frac{\pi}{2}-\gamma\right)}{\sin\left(\frac{\pi}{2}-\gamma-\omega\right)} \times \frac{m}{\frac{m\sin\omega}{\cos(\gamma+\omega)} + \frac{\sin\omega}{\tan A} + \cos\omega} \tag{5.34}$$

where M is the tip crushing ratio in the general case, and A is the equivalent crack initial angle. According to Eq. (5.26), A can be expressed as:

$$A = \arctan \frac{2\left(\frac{\sigma_t}{\sigma_c} + \sin^2\left(\frac{\pi}{4}-\frac{\Gamma}{2}\right)\right)}{\cos\Gamma + \sqrt{\cos^2\Gamma + 4\frac{\sigma_t}{\sigma_c}\sin^2\left(\frac{\pi}{4}-\frac{\Gamma}{2}\right) + 4\sin^4\left(\frac{\pi}{4}-\frac{\Gamma}{2}\right)}} \tag{5.35}$$

Combining Eqs. (5.29), (5.31), (5.34) and (5.35), the cutting force for the general case can be expressed by:

$$F_c = w\sigma_c D \frac{\sin\left(\frac{\pi}{2}-\gamma\right)}{\sin\left(\frac{\pi}{2}-\gamma-\omega\right)} \times \frac{m}{\frac{m\sin\omega}{\cos(\gamma+\omega)} + \sin\omega \frac{\cos(\gamma+\omega)+\sqrt{\cos^2(\gamma+\omega)+4\frac{\sigma_t}{\sigma_c}\sin^2\left(\frac{\pi}{4}-\frac{\gamma+\omega}{2}\right)+4\sin^4\left(\frac{\pi}{4}-\frac{\gamma+\omega}{2}\right)}}{2\left(\frac{\sigma_t}{\sigma_c}+\sin^2\left(\frac{\pi}{4}-\frac{\gamma+\omega}{2}\right)\right)}} + \cos\omega \tag{5.36}$$

where

$$m = \cos(\gamma+\omega)\times\left[-\frac{\cos(\gamma+\omega)}{4\sin^2\left(\frac{\pi}{4}-\frac{\gamma+\omega}{2}\right)+4\frac{\sigma_t}{\sigma_c}} - \frac{\sqrt{\cos^2(\gamma+\omega)+4\frac{\sigma_t}{\sigma_c}\sin^2\left(\frac{\pi}{4}-\frac{\gamma+\omega}{2}\right)+4\sin^4\left(\frac{\pi}{4}-\frac{\gamma+\omega}{2}\right)}}{4\sin^2\left(\frac{\pi}{4}-\frac{\gamma+\omega}{2}\right)+4\frac{\sigma_t}{\sigma_c}} + \frac{\sqrt{\frac{\sigma_t}{\sigma_c}+1}}{2\sin\left(\frac{\pi}{4}-\frac{\gamma+\omega}{2}\right)} + \frac{1}{2}\cot\left(\frac{\pi}{4}-\frac{\gamma+\omega}{2}\right)\right] \tag{5.37}$$

In this way, the cutting force can be derived, based on Eq. (5.36), for the general case in which the crack initiates at an arbitrary location on the TCZ boundary. All the parameters required in Eqs. (5.36) and (5.37) for evaluating the cutting force are directly available except for the newly defined parameter ω which needs to be calibrated. According to definition, the increase of ω will decrease the size of the chipping affected zone as shown in Fig. 5.4 and, in turn, decrease the size

of the formed chips. Even though the physical meaning of ω is intuitive, the accurate value of ω is unknown without experimental calibration. In this work, ω has been found to change linearly with respect to depth of cut at a constant rake angle, which can be calibrated by using linear regression techniques. The calibration of ω will be presented in detail in Section 5.2.2.

5.1.4 Relationship between cutting and thrust forces

One of the two orthogonal components of the resultant force, i.e., the cutting force, has been derived in Section 5.1.3. In this section, the other component, i.e., the thrust force will be related to the cutting force in accordance with the physical interaction between the cutter and rock on the cutter's rake face.

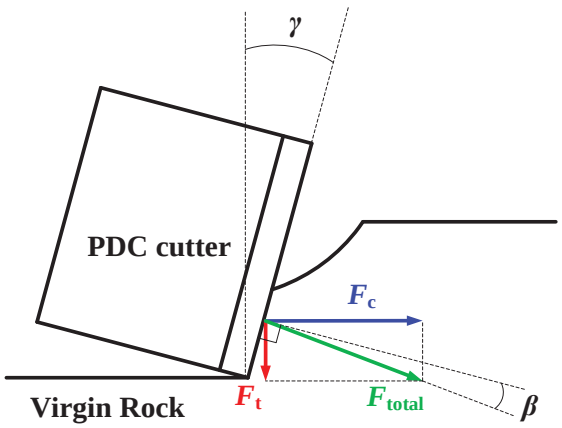

Figure 5.5: Relationship between the cutting and thrust forces.

Figure 5.5 shows the decomposition of the resultant force F_{total} exerted on the rake face of the PDC cutter into two orthogonal force components, i.e., cutting and thrust forces which can be related by:

$$\frac{F_t}{F_c} = \tan(\gamma + \beta) \tag{5.38}$$

where β is the mean friction angle between the rock and the cutter's rake face. β characterizes the frictional interaction between the cutter's rake face and the rock from an average point of view. The larger β is, the more likely the chip will stick to the rake face.

Replacing F_c in Eq. (5.38) with Eq. (5.36) yields:

$$F_t = \tan(\gamma+\beta)\, w\sigma_c D \frac{\sin\left(\frac{\pi}{2}-\gamma\right)}{\sin\left(\frac{\pi}{2}-\gamma-\omega\right)} \times \frac{m}{\frac{m\sin\omega}{\cos(\gamma+\omega)} + \sin\omega \frac{\cos(\gamma+\omega)+\sqrt{\cos^2(\gamma+\omega)+4\frac{\sigma_t}{\sigma_c}\sin^2\left(\frac{\pi}{4}-\frac{\gamma+\omega}{2}\right)+4\sin^4\left(\frac{\pi}{4}-\frac{\gamma+\omega}{2}\right)}}{2\left(\frac{\sigma_t}{\sigma_c}+\sin^2\left(\frac{\pi}{4}-\frac{\gamma+\omega}{2}\right)\right)}} + \cos\omega \tag{5.39}$$

As it has been shown, both the cutting and thrust forces can be determined based on Eqs. (5.36) and (5.39) respectively. It should be noted that all the parameters involved in the closed form expressions of the cutting and thrust forces, i.e., Eq. (5.36) and (5.39) are automatically determined as long as the cutting conditions are specified, except for two parameters, i.e., ω and β. According to Eqs. (5.36) and (5.39), ω has to be determined to evaluate the value of the cutting force, while β has to be determined to derive the thrust force as a function of the cutting force. As mentioned in Section 5.1.3, ω is linearly related to the depth of cut for a constant rake angle. Moreover, as it will be shown, β can be linearly related to the rake angle and is independent of the depth of cut. Therefore, given the available force data from preliminary tests, the linear change of ω with respect to the depth of cut and the linear trend of β with respect to the rake angle can be accurately

calibrated using linear regression techniques. In this way, both ω and β can be determined for different rake angles and depths of cut for future predictions. The detailed calibration procedures will be presented in the next section.

5.2 Model evaluations

This section will utilize the experimental data to calibrate the two parameters defined in the new force model, i.e., the chipping-crushing transition angle ω and the mean friction angle β. The calibrated ω and β will then be adopted to predict the cutting and thrust force responses, as discussed in Section 5.1.4.

5.2.1 Experiments

One portion of the linear rock cutting tests presented in Chapter 4 will be used to evaluate the theory. The selected rock sample is Indiana limestone, shown in Figs. 4.3 and Fig. 5.6, with a uniaxial compressive and tensile strength of 34.5 MPa and 3.45 MPa respectively. The cutting speed was set to a constant value of 63.5 mm/s. The PDC cutter is considered to be sharp for all the cutting tests conducted in this work. The experiments include 3 levels of rake angles, i.e., 10º, 20º, and 30º and 13 levels of depths of cut, i.e., 0.2, 0.4, 0.6, 0.8, 1, 1.2, 1.4, 1.6, 1.8, 2, 2.4, 2.8 and 3 mm. Since the selected depths of cut are much smaller than the cutter's width (i.e., 19 mm as shown in Fig. 4.2), the cutting process in this work can be assumed to remain two-dimensional orthogonal cutting. The data acquisition process and force averaging algorithm are identical to those described and used in Chapter 4. The average cutting force is pointing along the cutting speed direction while the average thrust force is vertical to the top surface of the rock. The average

side force is orthogonal to both the average cutting and thrust forces. The process parameters and corresponding force responses are listed in Table A2 in the Appendix A. As shown in Table A2, the average cutting and thrust forces increase as the depth of cut and rake angle increase, while the average side force remains a very small value satisfying the assumption on orthogonal cutting.

Figure 5.6: Indiana limestone sample after three repeated cutting tests.

5.2.2 Calibration of ω

According to Eqs. (5.36) and (5.37), for each test listed in Table A1, all the parameters except for the chipping-crushing transition angle ω are given/known based on the specific cutting conditions. Moreover, the average cutting force has also been experimentally derived. Therefore, ω is the only unknown parameter in Eq. (5.36) and can be determined numerically.

As shown in Fig. 5.7, ω is decreasing linearly with the increase of the depth of cut D. Therefore, for each rake angle, ω was calibrated using the linear regression function to yield:

$$\omega(^\circ) = -6.2696D(\text{mm}) + 58.634 \tag{5.40}$$

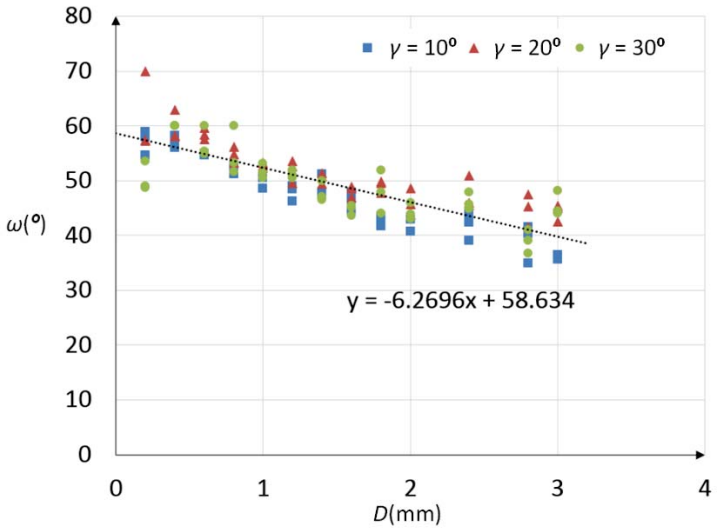

Figure 5.7: Linear trends of the chipping-crushing transition angle with respect to depth of cut.

5.2.3 Calibration of β and γ

Figure 5.8 shows the linear increase of the thrust force as the cutting force increases at a constant rake angle γ. According to Eq. (5.38), β can be solved by:

$$\beta = \arctan\left(\frac{F_t}{F_c}\right) - \gamma \tag{5.41}$$

where the ratios of the thrust to cutting forces can be derived based on the slopes of the three lines plotted in Fig. 5.8. The ratio of thrust to cutting forces remains constant at each level of the rake angle, as shown in Fig. 5.9. Hence β can be linearly related to γ by:

$$\beta(^\circ) = -0.5742\gamma(^\circ) + 25.782 \tag{5.42}$$

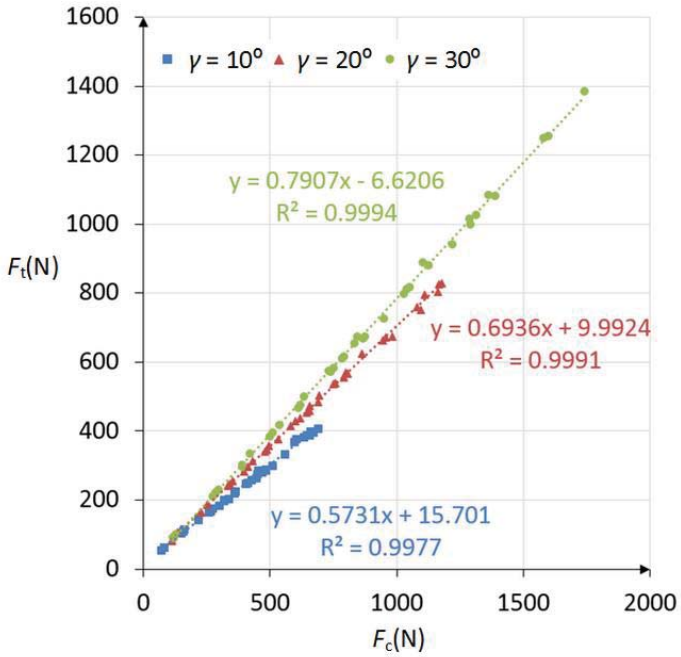

Figure 5.8: Relationship between the cutting and thrust forces with 3 levels of rake angles.

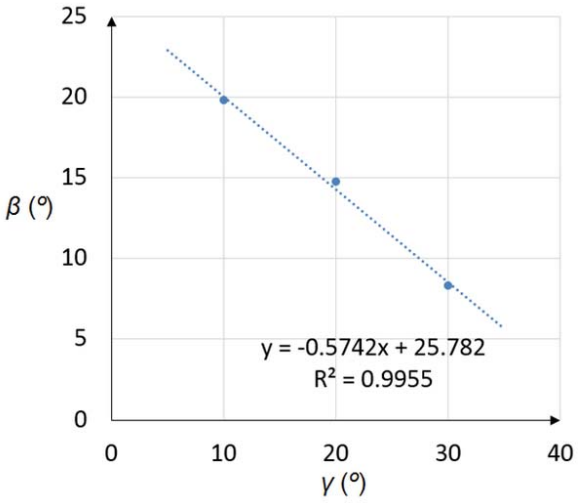

Figure 5.9: Linear relationship between the rake and mean friction angles.

5.2.4 Force predictions

As discussed above, given the depth of cut D and rake angle γ, ω and β can be determined by Eqs. (5.40) and (5.42). Substituting the calibrated values of ω and β and the pre-defined process

parameters w, D, γ, σ_t, and σ_c into Eqs. (5.36), (5.37) and (5.39) will give the predictions of the desired cutting and thrust forces. The predicted values and their prediction errors are listed in Table A1. The average prediction errors of the cutting and thrust forces for all the data points in Table A1 are about 5% and 8% respectively. Figure 5.10 compares the experimental results with the predictions.

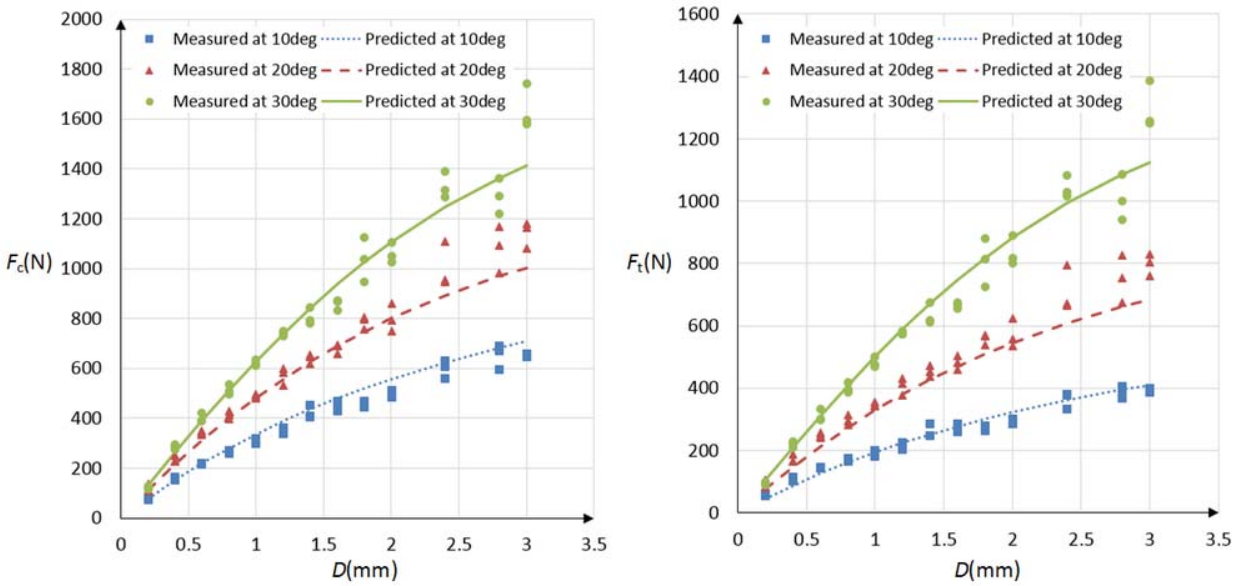

Figure 5.10: Comparison of measured and predicted cutting and thrust forces in linear cutting of Indiana limestone with three levels of rake angles: 10º in blue, 20º in red, and 30º in green.

5.3 Discussion

5.3.1 Force responses

As shown in Fig. 5.10, the average cutting and thrust forces increase non-linearly from very small (~0.2 mm) to quite large depths of cut (~3 mm) values. However, the increase of the average force responses can be approximated with a linear trend for depths of cut below 1 mm. This is in good agreement with other researchers' experimental findings (Jaime et al., 2010; Richard et al.,

2012). Above a 1 mm depth of cut, the chunk-like chips due to the chipping action become more and more noticeable. Since the chipping mode induces cracks to form chips, while the crushing mode has to smash the rock into powdery chips, the chipping mode requires less energy and force than the crushing mode. Therefore, the average force responses become concave downward with an increase in the depth of cut.

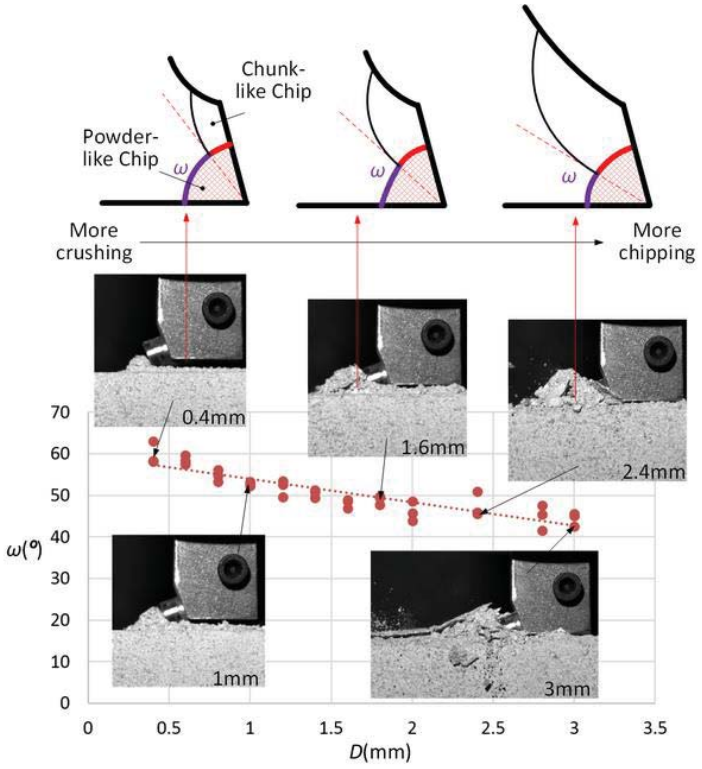

Figure 5.11: Effect of chipping-crushing transition angle on chip formation for a 20º rake angle.

5.3.2 Chipping-crushing transition angle

As defined in Section 5.1.3, the chipping-crushing transition angle ω will determine the portion of the TCZ which induces the chipping mode. The decrease of ω results in an increase of the chipping mode, which in turn, leads to an increase in the size of the chip. Figure 5.11 gives a better illustration of how ω relates to the chip formation phenomena in the linear rock cutting process. ω

was observed to decrease with the increase of the depth of cut, which means the chipping mode becomes more noticeable at deeper cuts.

As shown in Fig. 5.11, the rock fails with crushed and powdery chips for shallow cuts while both powdery chips and chunk-like chips are formed simultaneously for deep cuts. Moreover, the chip size increases with the increase of the depth of cut. As mentioned in Section 5.1.1, powdery and chunk-like chips are considered to be formed due to the crushing and chipping failure modes respectively. The above experimental observations indicate that the chipping mode becomes more and more obvious and dominant from small to big depths of cut. Therefore, the experimental observations are in good agreement with the physical meaning of ω.

5.3.3 Tip crushing ratio

Based on Eq. (5.34), the tip crushing ratio M can be expressed by:

$$M = \frac{D_{TCZ}}{D} \tag{5.43}$$

According to Eq. (5.29), the required cutting force can be obtained by:

$$F_c = \sigma_c w D M = \sigma_c A_c M \tag{5.44}$$

where A_c is the cross-section of the cutting area along the cutting speed direction. Based on Eq. (5.44), with predefined A_c and σ_c, M will be the only parameter which influences the cutting force. The increase of M will linearly increase the cutting force. Based on the geometrical relationships in Fig. 5.4 and the angle relationship in Eq. (5.31), the range of ω can be determined by:

$$0 \le \omega \le 90^{\circ} - \gamma \tag{5.45}$$

According to Eqs. (5.34), (5.35) and (5.45), the change of M with respect to the chipping-crushing transition angle ω can be shown by the plots in Fig. 5.12. As shown in Fig. 5.12, the increase of the rake angle γ decreases the maximal value of ω but increases the possible values of M. M was observed to approach 1 when ω reaches its maximal value. From the physical perspective, the increase of ω decreases the chipping action but increases the crushing action in the whole rock removal process, which, in turn, increases the required cutting force. According to Eq. (5.44), M is proportional to the cutting force. To this end, M increases as ω increases. Moreover, the increase of the rake angle will increase the cutting force as shown in Fig. 5.10, which will also increase M.

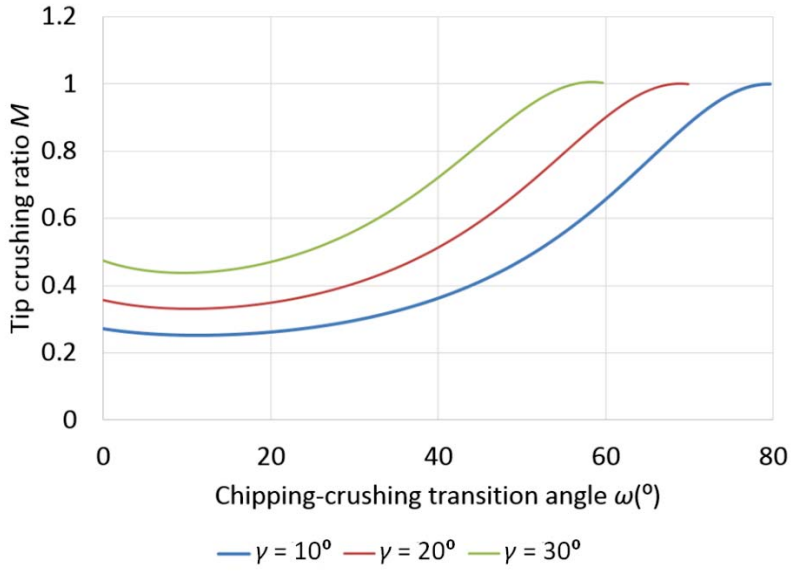

Figure 5.12: Relationship between the tip crushing ratio and chipping-crushing transition angle.

5.4 Conclusions

The following conclusions can be drawn from this work:

(1) The rock removal mechanism in the rock cutting process includes crushing and chipping failure modes. Crushed and powdery chips are attributed to the crushing mode while chunk-like chips are formed due to the chipping mode. Chipping of rock has been concluded to be caused by either tensile or shear stresses by different researchers. However, no agreement has been reached.

(2) This chapter has developed a new cutting theory to describe both the crushing and chipping failures involved in the linear rock cutting process. A rock crushing zone, namely the Tip Crushing Zone (TCZ) that is formed beneath the cutter's rake face was defined. Cracks were assumed to initiate on the boundary of the TCZ and propagate towards the free surface of the virgin rock in order to form a chip. The chipping failure was considered to be caused by tensile breakage of the rock. Based on the equilibrium of moments on the chip and the minimum chipping energy principle, an analytical expression of the force responses was derived.

(3) Several parameters were defined in the theory with clear physical meaning. The crack initial angle indicates the direction of the crack's propagation path; the chipping-crushing transition angle characterizes the transition boundary between the chipping and crushing affected zones; the tip crushing ratio reflects how deep the TCZ is compared to the defined depth of cut; and the mean friction angle between the rock and the cutter's rake face relates the cutting and thrust forces.

(4) A series of linear rock cutting tests conducted in the previous chapter were used to provide experimental evaluation of the theory. Indiana limestone was selected as the testing rock sample. Cutting tests include 3 levels of rake angles and 13 levels of depths of cut.

(5) Two characteristic parameters, i.e., the chipping-crushing transition angle and the mean friction angle between the rock and the cutter's rake face were calibrated based on experimental data. The chipping-crushing transition angle was found to be linear with respect to the depth of cut while the mean friction angle was found to be linear with respect to the rake angle.

(6) The predicted cutting and thrust forces have shown a non-linear relationship between the force responses and the depth of cut. The forces were approximately proportional to the depth of cut for shallow cutting tests, i.e., for depths of cut below 1 mm for Indiana limestone, which are in good agreement with others' work.

(7) The chip formation phenomena were found in good agreement with the theoretical predictions from the physical point of view.

Chapter 6

Finite Element Modeling of Rock Cutting Processes

This chapter describes a finite element (FE) study of rock cutting performed by PDC cutters under two-dimensional (2D) orthogonal cutting conditions. Particular emphasis will be placed on the chip formation phenomena and force response predictions based on the LS-DYNA platform. The ultimate goal is to simulate material properties using an as simple as possible material model with as few and easily derived as possible input parameters without losing similarity of the chip formation phenomena and prediction accuracy of the force responses in comparison to actual rock cutting processes. To this end, the rock will be modeled by the Drucker-Prager yield surface in combination with an element erosion criterion based on the maximal shear strain at failure. The Drucker-Prager model requires fewer than 10 input parameters which have clear physical meaning and can be easily obtained from industrial and academic literature sources. On the other hand, the PDC cutter will be modeled as a rigid body. In order to evaluate the accuracy of the FE study, rock cutting tests are performed on the LRCT described in Chapter 4.

After the comparison between the FE simulations and experimental data, it will be shown that the chip formation phenomena and the predicted force responses capture the major characteristics of the experimental data. After that, the FE model will be further extended to a three-dimensional (3D) case to simulate the rock face turning process based on another FE commercial code – ABAQUS/Explicit.

The chapter is arranged as follows: Section 6.1 presents the FE formulation of the 2D rock cutting process simulated by using LS-DYNA, followed by the evaluation of the validity of the FE simulations based on the data derived from the cutting tests in Section 6.2. Section 6.3 extends the FE model for 3D rock turning processes whose results are then compared with the experimental results in Section 6.4. Finally, Section 6.5 summarizes the findings.

6.1 Finite element formulation for 2D orthogonal cutting of rock

In this section, a FE model is formulated by using explicit Lagrangian integration in the commercial code LS-DYNA to simulate rock cutting under 2D orthogonal cutting conditions. The Drucker-Prager model will be used to simulate the elastic-plastic behavior of the rock material, while the PDC cutter will be modeled as a rigid body. Chip formation will be achieved by deleting the elements at the interface between the chip and the virgin rock when a specific shear strain is reached.

6.1.1 Process definition

The cutting process is modeled as a 2D orthogonal cutting process under plane strain deformation. This necessitates a suitable representation of the rock sample and of the PDC cutter respectively. The geometry of the rock and the cutter is shown in Fig. 6.1. The cutter is assumed to have a square shape with a 19 mm side length, while the rock is defined as a rectangle with a 100 mm length and a 30 mm height. A 5 mm chamfer is given on the rock geometry to eliminate the non-physical contact behavior/penetration of the cutter tip element into the rock elements at the interface. The depth of cut is set to 5 mm. The rock is fixed on 3 sides, while the cutter is

assumed to move along the *x*-direction at a constant speed of 100 mm/s. The rake angle of the cutter is -20^{o} which is the same as the rake angle used in the actual cutting tests.

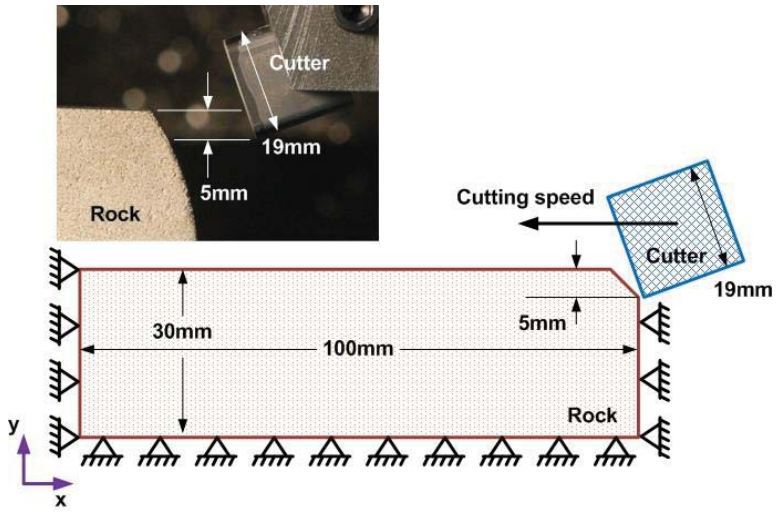

Figure 6.1: Geometry and boundary conditions for the 2D FE model.

2D linear quadrilateral solid elements are assigned under plane strain conditions to the rock and the cutter. A non-uniform mesh distribution is assumed for both the rock and cutter, as shown in Figs. 6.2 and 6.3. For the rock, the interaction area between the rock and the cutter, i.e., the top layer with the 5 mm thickness is defined and modeled by a finer mesh than the bottom area. Moreover, a bias sizing control is used with a 0.38 mm minimum size and a 0.5 mm maximum size in the top layer of the rock. The mesh size is defined to decrease when the element location approaches the cutter. In the bottom layer, a bigger mesh size (i.e., maximum size 1.9 mm) is applied since in this area no significant interaction between the rock and the cutter occurs. For the cutter, bias sizing control is also used with a 0.38 mm minimum size and a 1.9 mm maximum size. The mesh size is defined to decrease with the decrease of the distance between the element location and the rock.

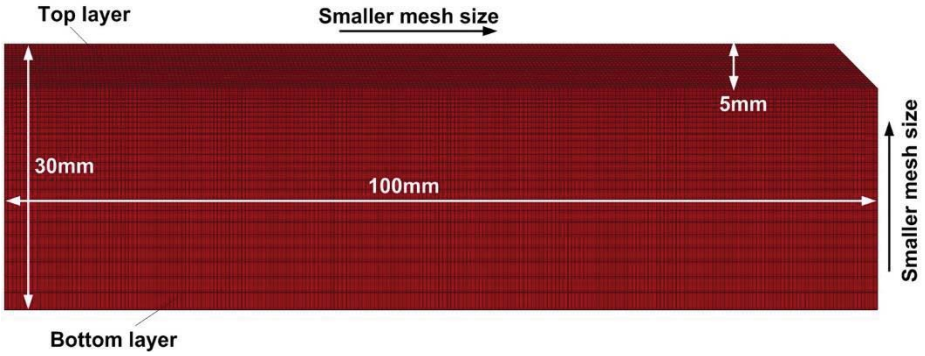

Figure 6.2: Mesh definition of rock for the 2D FE model.

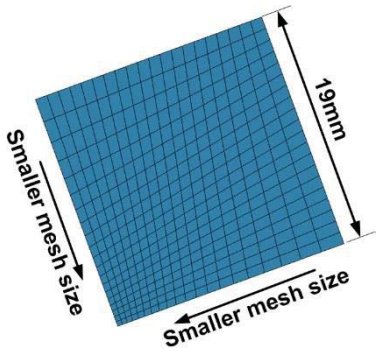

Figure 6.3: Mesh definition of cutter for the 2D FE model.

The contact between the rock and the cutter are defined as a 2D surface to surface contact (2D_AUTOMATIC_SURFACE_TO_SURFACE) in LS-DYNA. Moreover, in order to avoid the non-physical penetration of chips into virgin rock, a 2D_AUTOMATIC_SINGLE_SURFACE contact was defined in this model. The static and dynamic coefficients of friction were set to 0.3 for the above-mentioned two contact conditions.

6.1.2 Material model and failure criterion

Geo-materials like soil and rock are relatively difficult to model using finite element methods due to their complex properties such as brittleness, inhomogeneity, abrasiveness, and dilatancy. A

series of material models in LS-DYNA have been developed for geo-material modeling. Due to the complex properties of these materials, most of the models require a large number of input parameters which have to be calibrated under strict testing conditions, e.g., uniaxial, tri-axial, and pressure confined conditions. As mentioned above, since the ultimate goal is to simulate chip formation and to predict the force responses using an as simple as possible material model with as few parameters as possible, the Drucker-Prager (D-P) constitutive model will be exploited to represent the pressure-dependent yield which is significantly affected by frictional and dilatational effects.

The D-P model is actually a modified von Mises yield criterion that incorporates pressure effects into the yield surface expression (Belytschko et al., 2000), i.e.:

$$f = \sigma_{\text{eff}} + \alpha \boldsymbol{\sigma} : \mathbf{I} - Y = 0 \tag{6.1}$$

where σ_{eff} is the effective Cauchy stress, $\boldsymbol{\sigma}$ is the Cauchy stress tensor, $\mathbf{I}$ is the second order unit tensor, the constants α and Y are related to the material properties of geo-materials as:

$$\alpha = \frac{2\sin\phi}{3-\sin\phi} \tag{6.2}$$

$$Y = \frac{6c\cos\phi}{3-\sin\phi} \tag{6.3}$$

where ϕ represents the angle of friction and c represents the cohesion strength. As shown in Fig. 6.4, the D-P model is elastic when the stress state is below the yield surface but perfectly plastic when the stress state exceeds the yield surface (Resende and Martin, 1985).

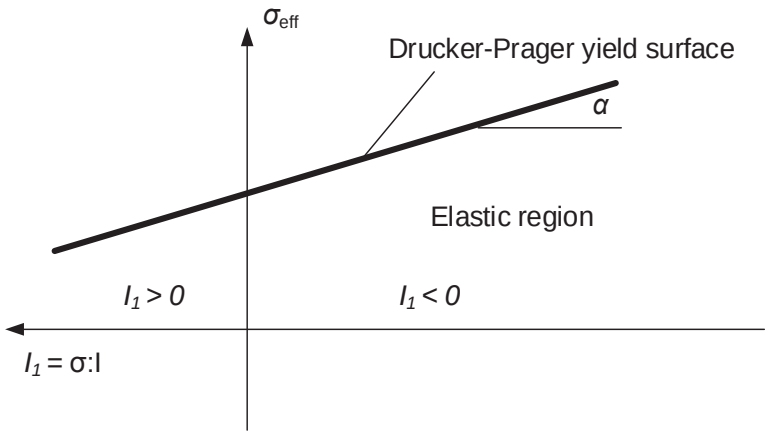

Figure 6.4: Mesh definition of cutter for the 2D FE model.

Since the D-P model is an elastic-plastic model without a damage criterion, chip formation cannot be simulated (i.e., no element deletion occurs) in the FE code when only the D-P model is used. In this study, the maximal shear strain criterion will be applied in conjunction with the D-P model with the aim of simulating chip formation phenomena. In LS-DYNA, the D-P model is developed in the material model - MAT_193_Drucker_Prager, and the maximal shear strain can be defined in the material model - MAT_000_ADD_EROSION.

6.2 Simulation results of 2D orthogonal cutting of rock

6.2.1 Simulation conditions

In the FE simulation, the PDC cutter is defined as a rigid body material while the rock sample is defined as a D-P material. The simulation parameters were assigned as shown in Table 6.1. According to the given simulation parameters, the linear rock cutting test was conducted with the process parameters and material properties listed in Table 6.2 and Table 6.3 respectively. The input parameters were specified in the following consistent units: length (mm), force (N), mass (tonne),

time (s), stress (MPa), energy (mJ), and density (tonne/mm^3). The maximal shear strain criterion is applied to accomplish element deletion during the simulations. The shear strain at failure can affect the chip size and force magnitude, which has to be calibrated based on the experimental tests.

Table 6.1: Simulation parameters for 2D FE model.

	Parameters	Symbols	Values
Process	Cutting speed	V_c	-100
	Rake angle	γ	-20°
	Depth of cut	D_c	5
Draker-Prager model	Density	RO	2.7e-9
	Elastic shear modulus	GMOD	1.015e4
	Poission's ratio	RNU	0.33
	Failure shape factor	RKF	1
	Angle of friction	PHI	0.61
	Dilation angle	PSI	0.087
	Cohesion value	CVAL	10

Table 6.2: Experimental parameters for 2D FE model evaluation.

Experimental parameters	Values
Cutting speed	100 mm/s
Rake angle	-20°
Clearance angle	20°
Depth of cut	5 mm
Tool radius	0.02 - 0.04 mm

In the current simulations, the failure shear strain has been calibrated in a manner to match the chip size and also the peak and valley magnitudes of force oscillations obtained from the

experimental tests described in Section 3. The smaller value of the failure shear strain will lead to a smaller peak and valley magnitudes in the force responses, and also result in a smaller chip dimension. The failure shear strain was set to a value of 0.3 in the current simulations.

Table 6.3: Material properties of Indiana limestone.

Material properties	Values
Young's modulus *E*	27800 MPa (Miller and Florence, 1991)
Poission's ratio *υ*	0.33 (Miller and Florence, 1991)
Density *ρ*	2.7e-9 tonne/mm^3 (GEOL615, 2009)
Angle of friction *ϕ*	35° (GEOL615, 2009)
Dilation angle *ψ*	5° (GEOL615, 2009)
Cohesion strength *c*	10 MPa (GEOL615, 2009)

6.2.2 Chip formation

Figure 6.5 shows the simulation results of the chip formation phenomena. The contour of the effective Green strain is plotted to indicate the crack propagation path. Chip separation is achieved by deleting the damaged elements at the interface between the chip and the virgin rock without considering the fracture mechanics involved in the cracking area. This is a simplified method to qualitatively simulate chip formation in the brittle failure cutting mode. As shown in Fig. 6.5, when the cutter is shearing rock at a constant depth of cut, a specific stress/strain field will be generated in the rock structure. When the maximal shear strain is exceeded along certain curved contours, elements along the contour will be deleted and then a big individual chip will be formed.

Since the deleted elements cannot be visualized in FE simulation animations, only big sheared chips and some relatively small crushed chips can be seen in Fig. 6.5. Elements tend to separate from virgin rock to form small or powder-like chips rather than being deleted directly when a

smaller mesh size is utilized. Therefore, more realistic depiction of chip formation phenomena can be expected with the use of a finer mesh.

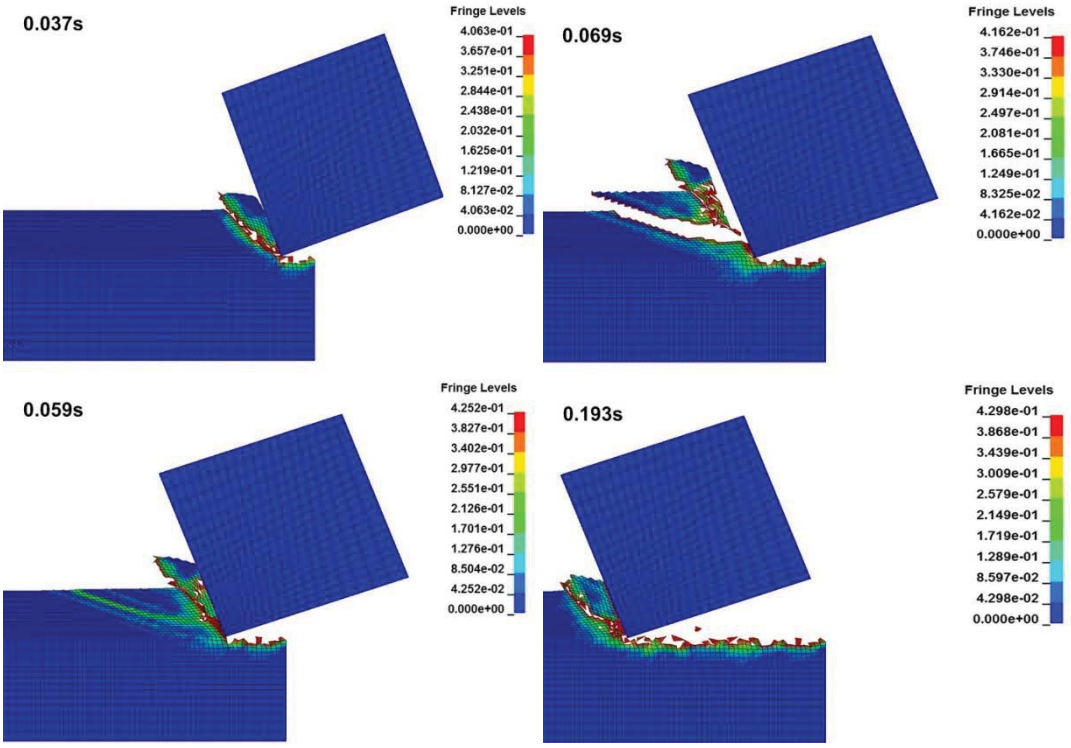

Figure 6.5: Contours of the effective Green strain during the 2D FE simulation.

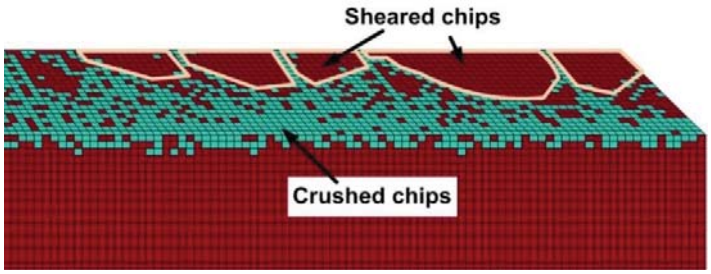

Figure 6.6: Illustration of sheared and crushed chips.

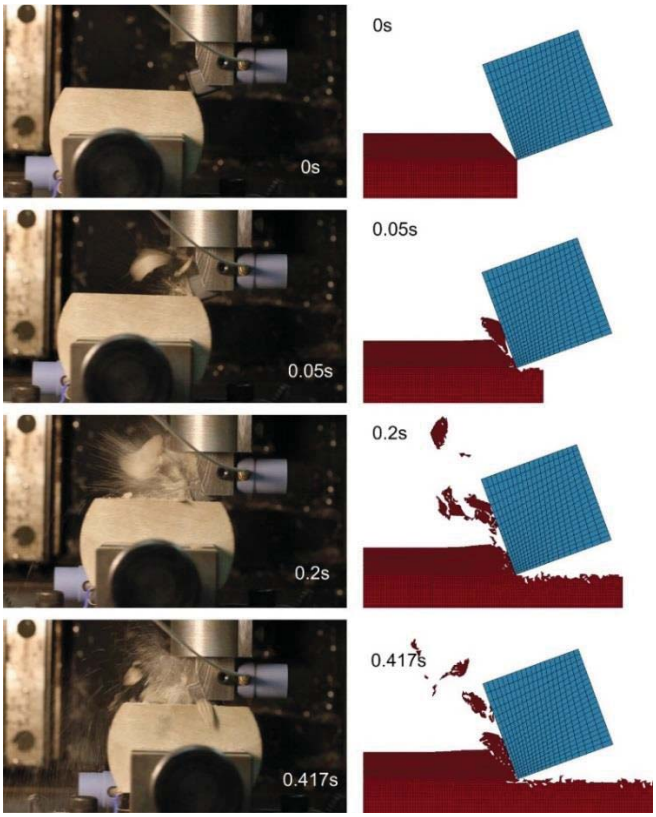

Figure 6.7: Comparison of chip formation between experiments and simulations.

As shown in Fig. 6.5, a big chip consisting of a group of elements was formed at 0.037 s in the simulation. The separation of this big chip from the virgin rock is due to the deletion of elements along the interface between the chip and virgin rock. Other groups of elements were also separated from the virgin rock to form additional big chips in a similar manner. On the other hand, a large number of elements were deleted based on the shear strain failure criterion. The deleted elements were considered to be damaged due to the above-mentioned crushing mechanism. In other words, the deleted elements can be considered to constitute the small and powder-like chips. As shown in Fig. 6.6, the groups of elements separated from the virgin rock were considered as chips formed due to the chipping (or shearing) mechanism, namely sheared chips, while the small individual

elements separated from the virgin rock and the deleted elements, marked in cyan, were considered as chips formed due to the crushing mechanism, namely crushed chips. The simulations indicate that crushed chips and sheared chips are formed in an alternating manner during the cutting process, which is in good agreement with the experimental tests and the cutting theory presented in Chapters 4 and 5 respectively. A more straightforward comparison of chip formation phenomena between the experimental tests and FE simulations can be found in Fig. 6.7.

6.2.3 Force responses

As observable in the simulations, due to the non-continuous chip formation phenomena, the force responses including the cutting and thrust forces exhibit a vibratory nature during the cutting process. As shown in Fig. 6.8, the cutting force response is oscillating during the simulation evolution, while the thrust force follows a similar trend albeit with a smaller magnitude. Figures 6.9 and 6.10 show the comparison of the cutting force and thrust force responses between the experimental tests and FE simulations respectively. Both cutting and thrust force responses qualitatively match with each other between the experimental tests and FE simulations. Moreover, the mean values of the cutting and thrust forces indicated by the dashed-lines are in good agreement between the experimental tests and FE simulations.

The difference in the mean cutting forces between the experimental tests and FE simulations is 205.7 N (i.e., 18.8% with respect to the mean cutting force obtained in the experiments) while the difference in the mean thrust forces is 98.0 N (i.e., 13.2% with respect to the mean thrust force in the experiments).

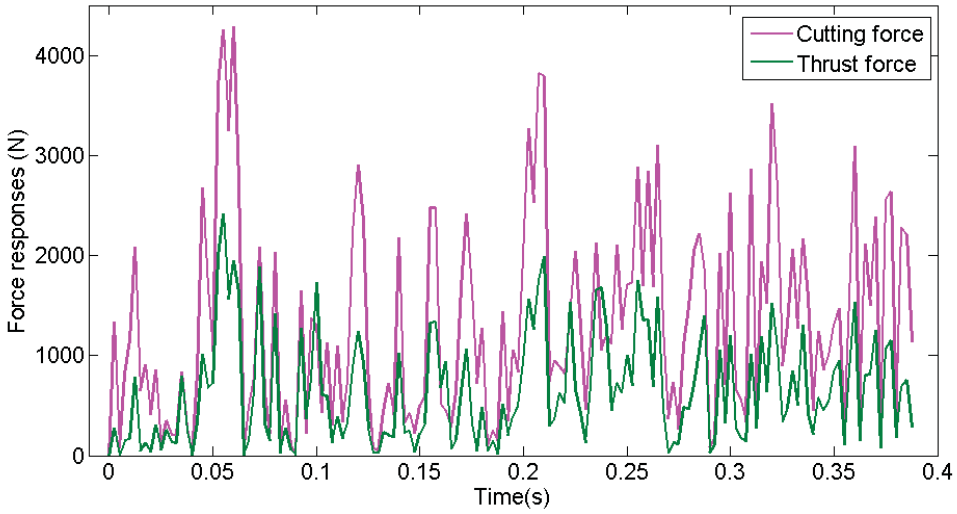

Figure 6.8: Force responses in FE simulation.

As indicated in Figs. 6.9 and 6.10, the cutting and thrust forces oscillations are more pronounced in the FE simulations than those in the experimental tests. For example, as shown in Fig. 6.9, there are 7 quick-drops of the cutting force with a magnitude larger than 1,000 N between 0.05s and 0.15s in the FE simulation. However, there are only 2 quick-drops with the similar magnitude in the experimental tests. Actually, a quick-drop in the force response indicates that a chip has separated from the virgin rock, i.e., a chip has been formed. The larger is the magnitude of the quick-drop in the force response, the larger is the chip being formed. The higher frequency of the large-magnitude quick-drops in the FE simulations indicates that chips are more often formed in the simulations. The observed discrepancy is considered to be caused by the following reasons: (1) the rock properties are too complex to be modeled by such a simple elastic-plastic model, i.e., the D-P model; (2) the maximal shear strain criterion is independent of the D-P model which leads to possibly inaccurate predictions of the stress/strain fields and in turn affects the prediction of the force responses; and (3) the large deformation and distortion of the elements due

to the extremely aggressive cutting of rock results in computational inaccuracy or even leads to a negative volume of elements which will terminate the whole simulation.

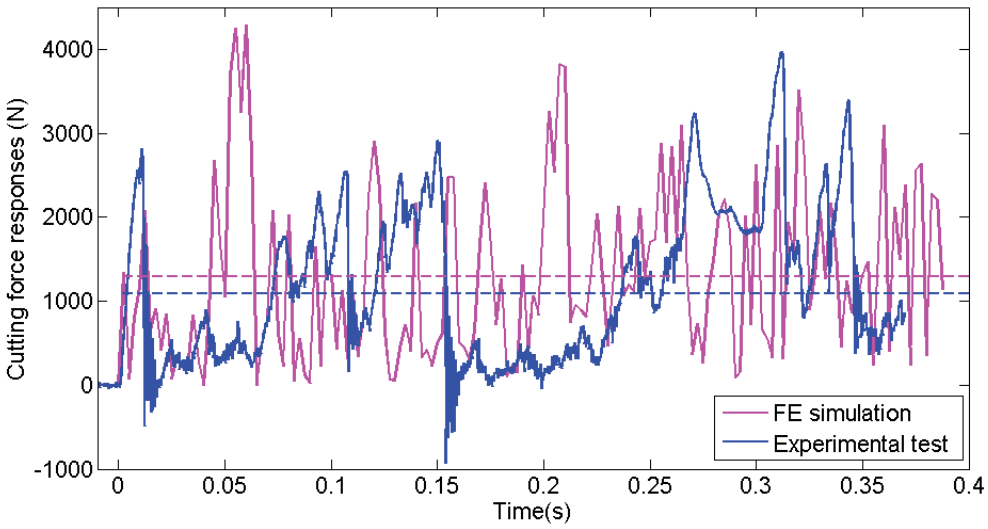

Figure 6.9: Cutting force response comparison.

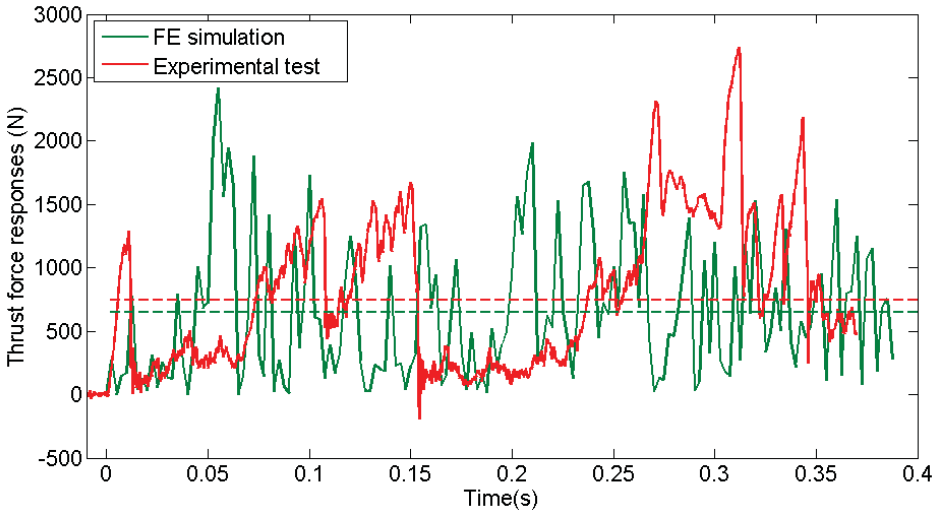

Figure 6.10: Thrust force response comparison.

6.2.4 Discussion

The advantage of the D-P model is that only a small number of input parameters are required and most of these parameters can be obtained from the literature without conducting complex laboratory tests. However, no damage criterion is included in the D-P model (i.e., MAT_193) in LS-DYNA, which means that perfectly plastic phenomena will last forever after the stress state exceeds the yield surface. Therefore, no chip formation can be observed in the simulations. In order to simulate chip formation, a failure shear strain criterion was introduced and integrated with the D-P model. Although chip formation and force response can be simulated quite similarly to the experimental test by adjusting the maximal shear strain at failure, the stress and strain fields cannot be expected to be accurate due to the lack of the capability of modeling crack initialization and propagation which actually weakens the rock structure and prompts chip separation during the cutting process. In the near future, the cracking phenomena will be taken into account and also a more realistic material model with a packed damage criterion will be implemented to accomplish more accurate prediction of stress and strain fields from the physical point of view.

6.3 Finite element formulation of 3D face turning of rock

As an extension of the 2D FE model, this section will present an FE formulation of rock cutting for a 3D face turning configuration by using another commercial FE code – ABAQUS/Explicit.

6.3.1 Geometry and mesh

Figure 6.11 shows the assembly layout of the model corresponding to the experimental setup mentioned in Chapter 3, including a cylindrical PDC cutter and a circular rock plate. The PDC

cutter has a 5.6 mm diameter and a 13 mm length, which is of the same size as the PDC cutter used in the rock turning test. In order to ensure efficient computation with a fine enough mesh size, the size of the rock plate was selected to be smaller than the actual rock sample, i.e., 30 mm in diameter and 6 mm in length. The cutter was positioned in space to give a specific rake angle (i.e., -20°) with respect to the rock plate.

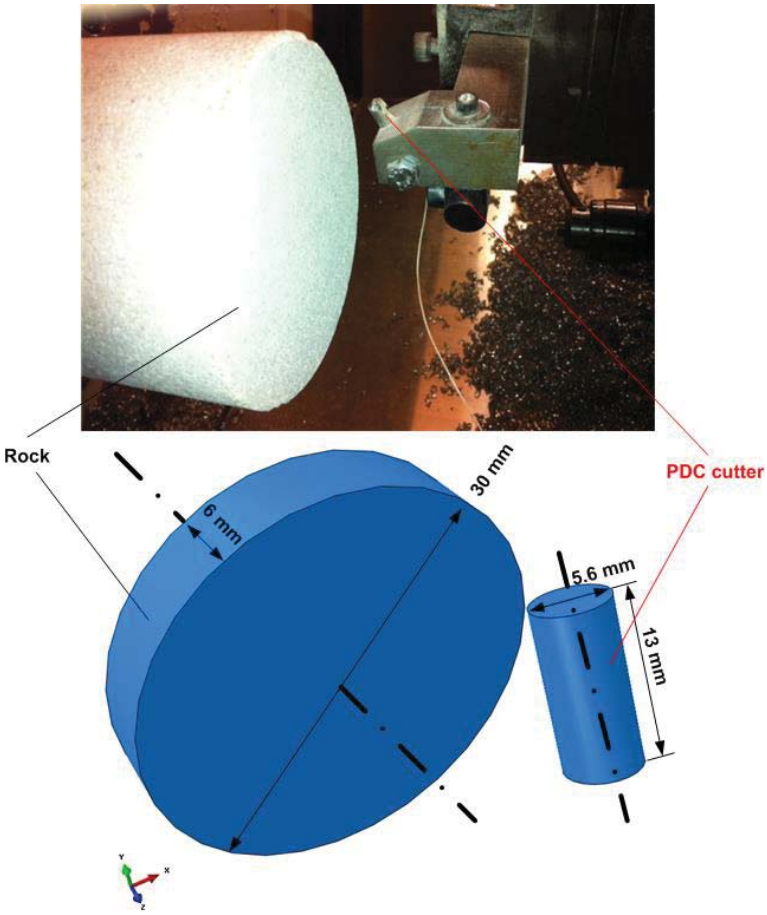

Figure 6.11: Geometric model of the finite element assembly.

Similar to the 2D FE model, the rock sample was defined as a 3D deformable part while the PDC cutter was defined as a 3D discrete rigid body. According to the definition of the body types

in ABAQUS, 3D linear hexahedron solid elements were assigned to the rock plate, while 2D linear quadrilateral shell elements were assigned to the PDC cutter.

Figure 6.12 shows the non-uniform meshing distributions defined on the cutter and rock respectively. The mesh size of the PDC cutter at the outer circle of the top surface, closest to the rock plate, was set to 0.5 mm. However, a single bias was assigned to the cutter along the direction of the centerline from 0.5 mm at the top surface to 3 mm at the bottom surface. As to the rock plate, a non-uniform mesh distribution was set along the radial direction from 0.2 mm at the outer circle to 5 mm at the center. Moreover, to further reduce the computational cost, two mesh zones were defined along the thickness direction of the rock plate. The fine mesh zone has a 0.2 mm mesh size while the coarse mesh zone has a 5 mm mesh size along the rock plate thickness direction.

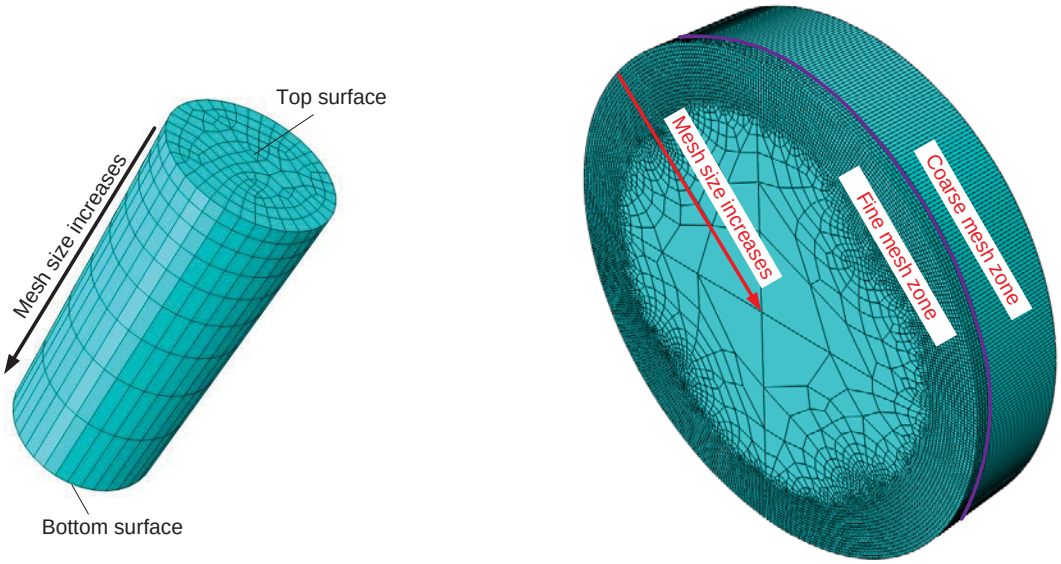

(a) (b)

Figure 6.12: Mesh definitions for the cutter and rock plate.

6.3.2 Definition of process, boundary and contact conditions

According to the face turning configuration, the rock was constrained to rotate along a reference point at its centerline at a constant spindle speed S of 300 rpm, while the cutter was defined to move towards the center of the rock plate along the radial direction at a constant feedrate f with a certain rake angle γ and depth of cut D_c. Table 6.4 summaries the process parameters in the formulated model.

Since the 3D solid elements assigned to the rock have only three translational degrees of freedom (DOFs) in ABAQUS, the rotational motion of the rock plate cannot be directly realized by constraining the elements with a certain angular velocity or displacement. In order to solve this problem, a reference point RF1 with 3 translational and 3 rotational DOFs was defined at the center of the back surface of the rock plate, as shown in Fig. 6.13. A kinematic coupling constraint was then defined with the control point as RF1 and the controlled surface as the back surface of the rock plate. The x-direction is the feed direction along the radial direction of the rock plate, the z-direction is along the thickness direction of the rock plate, and the y- direction is perpendicular to both x- and z-directions.

Table 6.4: Process parameters in the FE simulations.

Test No.	S (rpm)	f (mm/rev)	D_c (mm)	γ (°)
1	300	0.8	0.3	20
2	300	0.8	0.6	20
3	300	0.8	0.6	25
4	300	0.8	0.6	30
5	300	0.8	0.8	20
6	300	1.2	0.6	20
7	300	1.5	0.6	20

The cutter was defined as a rigid body whose motion was constrained at another reference point RF2 located at the bottom surface of the cutter. RF1 was constrained to rotate about the *z*-direction while RF2 was constrained to move along the *x*-direction. In addition, the back surface of the rock plate was also fixed along the *z*-direction.

A surface-to-surface contact (Explicit) was defined between the surfaces of the cutter and rock. The contact properties include the tangential behavior aimed to define the frictional effect between two surfaces and the normal behavior aimed at controlling the penetration of the cutter into the rock during the turning process. According to the experimental results presented in Chapter 3, a frictional coefficient of 0.7 was assigned to the tangential contact behavior under a penalty friction formulation, while a contact stiffness of 100 was assigned to the normal contact behavior under a linear pressure-overclosure mode.

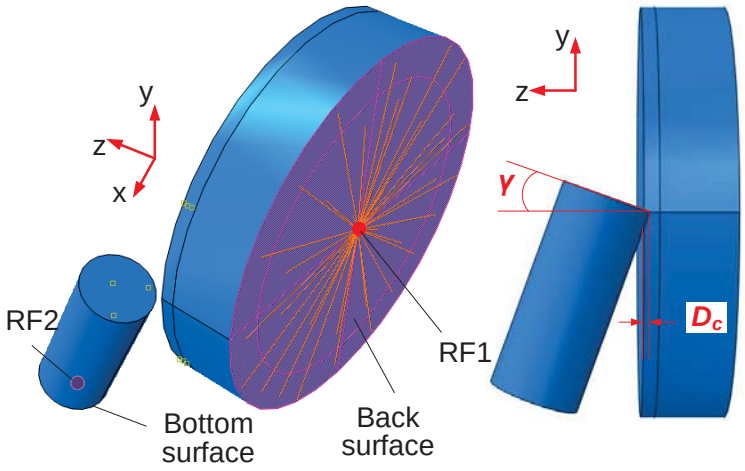

Figure 6.13: Process and boundary condition definitions.

In order to reduce the stable time increment in the explicit method and further increase the running speed of the simulation, the mass scaling technique was used with a target time increment

of 8e-7s. The internal and kinematic energies were tracked during the simulation to ensure the accuracy of the approximation by using mass scaling.

6.3.3 Material model and failure law

As in Section 6.1.1, the pressure-dependent linear Drucker-Prager (D-P) model is continuously used to model the elastic-plastic failure behavior of limestone in the 3D FE model, expressed in ABAQUS as follows:

$$F = t - p \tan \beta - d = 0 \tag{6.4}$$

where the variable t is equal to the Mises equivalent stress for the flow stress ratio $K = 1$, i.e.:

$$t = \sqrt{\frac{3}{2}(\mathbf{S} : \mathbf{S})} \tag{6.5}$$

and the equivalent pressure stress p is defined by:

$$p = -\frac{1}{3}\operatorname{trace}(\boldsymbol{\sigma}) \tag{6.6}$$

and d is the cohesive strength of the material. The constants β and d can be related to the material properties of geological materials by:

$$\tan \beta = \frac{2 \sin \phi}{3 - \sin \phi} \tag{6.7}$$

$$d = \frac{6c \cos \phi}{3 - \sin \phi} \tag{6.8}$$

Table 6.5: Material parameters of the 3D FE model.

Material properties	Values	Units
Density	2.7e-9	tonne/mm^3
Young's modulus	27800	MPa
Possion's ratio	0.33	1
Friction angle	25.21	°
Flow stress ratio	1	1
Dilation angle	5	°
Yield stress for DP hardening	20.26	MPa

The D-P hardening module with shear type of hardening behavior was used to define the hardening property in the above-mentioned linear D-P model. Unlike the maximal shear strain failure criterion used in the above-mentioned 2D FE model, the equivalent plastic strain (PEEQ) is exploited as a measure of the intensity of the rock's failure process in this wok. The elements of the rock were regarded to fail and be deleted when the PEEQ exceeds a specified value. The critical PEEQ can be determined by comparing the force responses of the cutter in the simulation with the experimental data.

In this work, the PEEQ was set to 0.8 in order to match the simulation results with the experiments in terms of force responses and material removal phenomena. Since the D-P model is too simple to represent all the physical behaviors of the rock, the very large critical equivalent plastic strain can only be considered as a factor indicating the intensive interaction between the rock and cutter without any realistic physical meaning. According to the material properties listed in Table 6.3, the parameters for the rock material model are summarized in Table 6.5.

6.4 Simulation results of 3D face turning of rock

6.4.1 Results

Figure 6.14 shows the rock removal phenomena during face turning of rock in Test 1. The PEEQ in the rock was extremely high at the interface between the cutter and rock but very small (~0) in the remaining areas of the rock. This corresponds to the intensive interaction at the rock-cutter interface but no obvious interaction in the remaining portions of the rock.

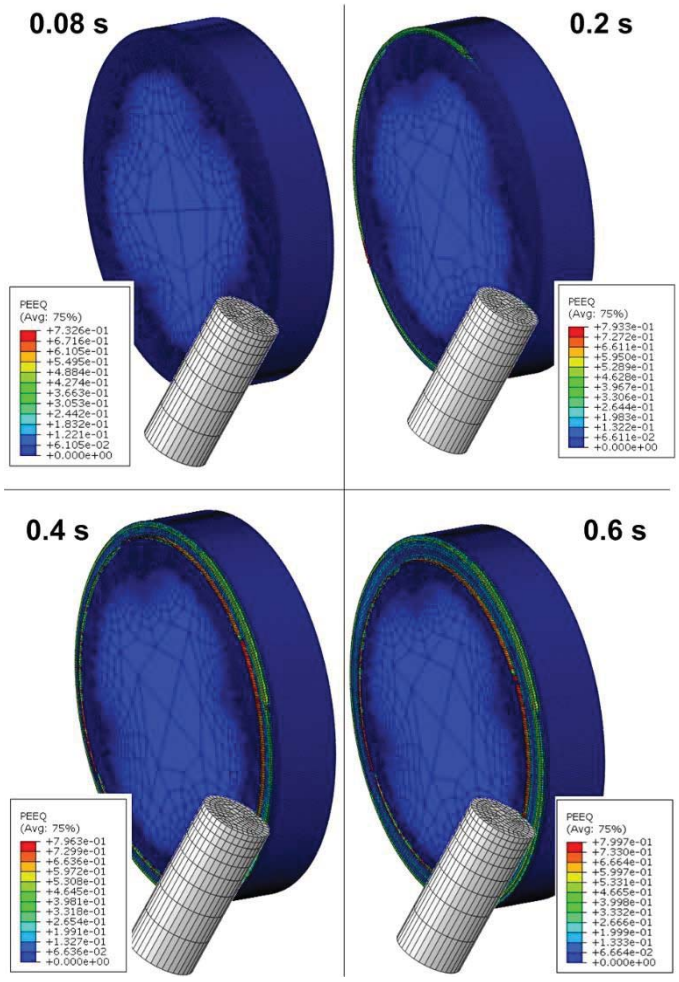

Figure 6.14: Element deletion phenomena in Test 1.

The reaction force components on the PDC cutter, i.e., cutting, thrust and feed forces, are shown in Fig. 6.15(a). The force components were close to zero before the contact between the PCD cutter and the rock plate and then rapidly increased towards a very large magnitude. Finally, the force components oscillated around a certain value, indicating that a stable phase was reached. Here also, as in the experiments, the three force components were found to exhibit similar trends but different magnitudes. The cutting force was leading the other two in magnitude. The feed force was the smallest among the three force components. According to Fig. 6.15, the trends of the force responses in the FE model are in good agreement with those in the experimental tests. However, the prediction given by the FE model underestimated the magnitude of three force components by approximately 50%, which is considered to be caused by the softer material behaviors of the D-P model compared to the realistic limestone samples.

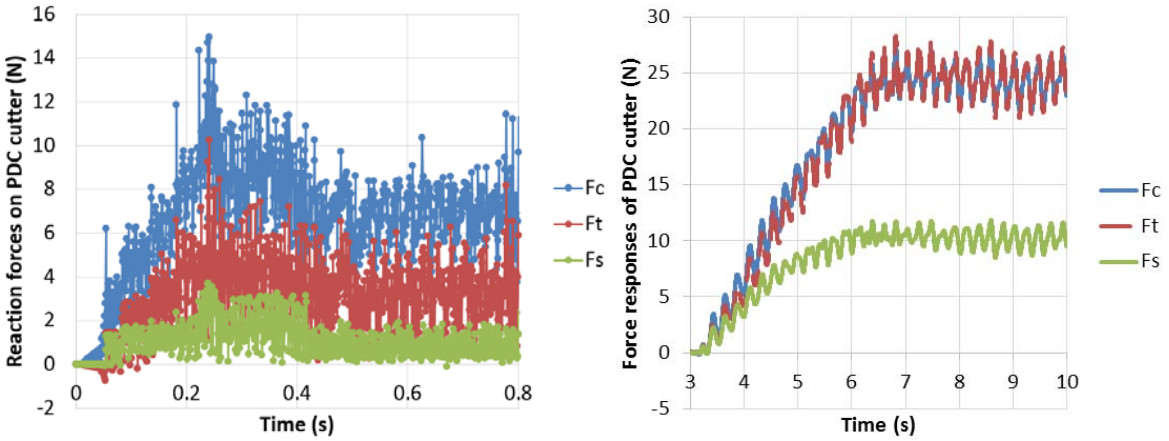

(a) (b)

Figure 6.15: Force responses in the simulation and experiment: (a) simulation results from Test 1; (b) experimental results.

6.4.2 Discussion

The satisfactory prediction of the trends in the force responses provides an efficient way to qualitatively analyze the effects of various process parameters, i.e., feedrate, depth of cut, and rake angle, on the response of the force components, i.e., cutting, thrust, and feed forces, during the rock turning process.

a) Feedrate

In order to investigate how the feedrate affects the response of the cutting force, a comparison was made between Tests 2, 6, and 7 with the same depth of cut and rake angle but three different levels of the feedrate as indicated in Table 6.4. As shown in Fig. 6.16, the increase of feedrate leads to an increase of the magnitude of the cutting force. Moreover, the tests with higher feedrate levels were found to have a quicker response of the cutting force. These findings are in good agreement with the experimental observations, which can be explained from the energy point of view. The increase of the feedrate will increase the rock removal rate and, in turn, increase the required total energy input in unit time. Therefore, a higher cutting force has to be applied to provide a higher material removal energy with the increase of the feedrate.

b) Depth of cut

The cutting force was found to proportionally increase with respect to the depth of cut in the face turning of rock, which has been discussed in detail in Chapter 3. This is again in good agreement with the comparison between Tests 1, 2, and 5. As shown in Fig. 6.17, the cutting forces exhibit a similar trend but with slightly different magnitudes between the three tests. The cutting

force was averaged from 0 to 0.8 s for the three tests. The average cutting forces are 6.63 N for D_c = 0.3 mm, 7.14 N for D_c = 0.6 mm, and 7.35 N for D_c = 0.8 mm respectively. The larger depths of cut result in higher cutting forces. This behavior, as above, can be similarly explained from the theory of material removal energy. That is to say, an increase in the depth of cut will lead to an increase in the energy required to remove the rock. Therefore, a higher cutting force will be required.

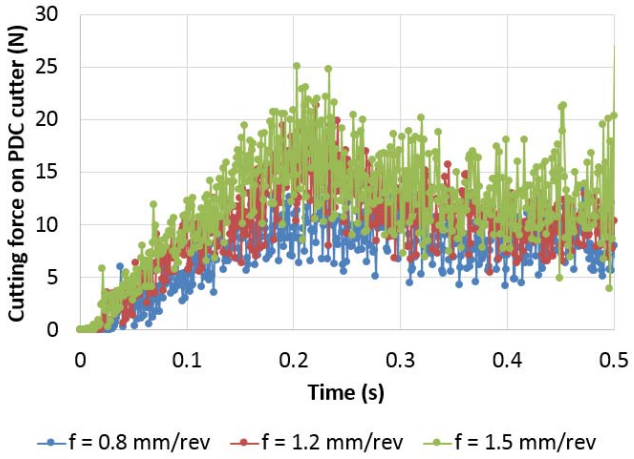

Figure 6.16: Cutting force vs. feedrate for Tests 2, 6 and 7.

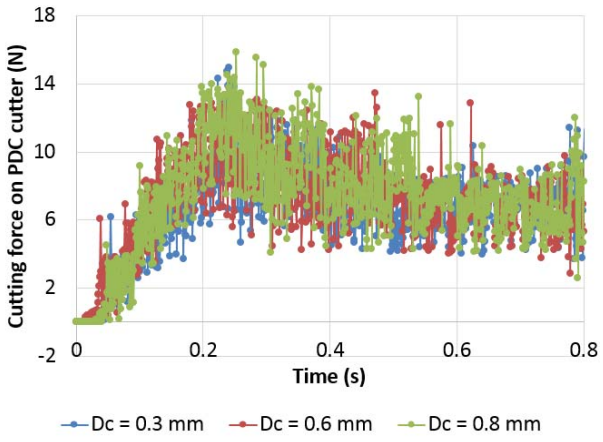

Figure 6.17: Cutting force vs. depth of cut for Tests 1, 2 and 5.

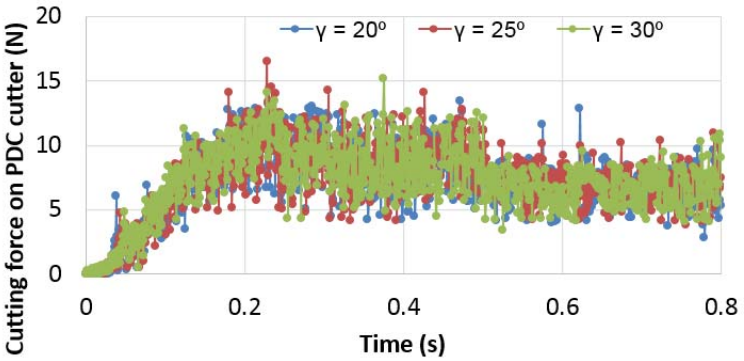

(a)

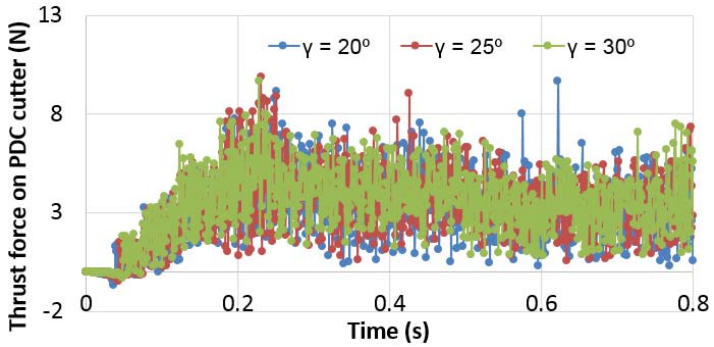

(b)

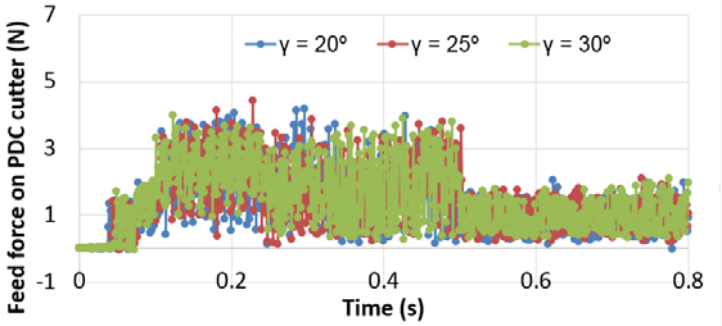

(c)

Figure 6.18: Force responses vs. rake angle for Tests 2, 3 and 4.

c) Rake angle

The effect of rake angle on the cutting, thrust, and feed forces was compared for three levels, i.e., 20° in Test 2, 25° in Test 3, and 30° in Test 4, as shown in Fig. 6.18. As it can be seen in Fig. 6.18, the force responses for the three rake angles are similar with each other. Moreover, the feed force is much smaller than the cutting and thrust forces due to the high ratio of the cutting speed to feedrate. Therefore, quasi-orthogonal cutting condition can be considered in the FE tests after the force components reach their stable phase, i.e., after 0.5 s. The feed forces were omitted in the following analysis. The force responses were averaged in the time interval between 0.5 s and 0.8 s, and summarized in Table 6.6.

Table 6.6: Time-averaged cutting and thrust forces.

Test No.	γ (°)	F_c (N)	F_t (N)
2	20	6.72	3.27
3	25	7.04	3.40
4	30	6.79	3.30

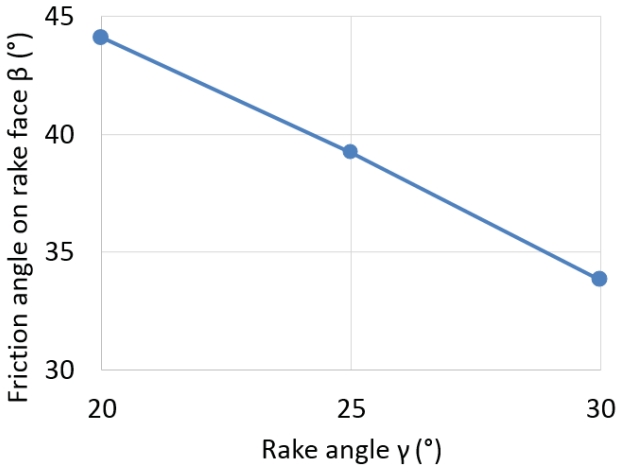

Figure 6.19: Linear relation between β and γ derived from the simulation.

Based on the relationship between thrust and cutting forces under the orthogonal cutting conditions mentioned in Section 5.1.4, the rake angles for each test can be derived and are listed in Table 6.6. The friction angles β can be then calculated based on Eq. (5.38) and are given in Table 6.6. The linear relation between β and γ is shown in Fig. 6.19, from which it is evident that a good match with the previous experimental and theoretical studies (Huang et al., 2013; Nishimatsu, 1972) exists.

6.5 Conclusions

This chapter presented an as simple as possible FE model to simulate chip formation and predict force responses in 2D orthogonal rock cutting where intensive interactions and complex cracking phenomena are involved. Furthermore, the FE model was then extended to a 3D model for 3D face turning of rock. Both models are capable of qualitatively capturing the rock removal process and force responses at a low computational cost. The following conclusions can be drawn:

(1) A 2D FE model was given to simulate the 2D orthogonal cutting of rock using the commercial code – LS-DYNA. The cutter was modeled as a rigid body while the rock sample was defined with the Drucker-Prager material model. The maximal shear strain failure criterion was applied to achieve element erosion during the simulations.

(2) Chip formation mechanisms, i.e., chipping and crushing, were discussed with a comparison of experiments and simulations. Two types of chips were defined, namely sheared and crushed chips, which were observed in both the experimental tests and the simulation results. The chip formation phenomena qualitatively matched well between the experimental tests and FE simulations.

(3) In both experimental tests and FE simulations, the cutting force was observed to largely oscillate due to the non-continuous chip formation phenomena and the brittle cutting mode, while the thrust force was observed to follow a similar trend but with a smaller magnitude than the cutting force. The differences in the predicted and measured mean cutting and thrust forces are 18.8% and 13.2% respectively. The cutting and thrust forces were observed to oscillate more intensively and frequently in FE simulations compared to experimental tests. The reasons of this discrepancy were discussed.

(4) A 3D FE model was then formulated to simulate the 3D face turning of rock based on ABAQUS/Explicit. The rock material model from the 2D model was directly adopted in the 3D model, while the failure law was changed with the maximal equivalent plastic strain criterion.

(5) Force responses were captured in the simulations. The trend in the force responses shows a good match with the experimental tests but the magnitudes were significantly underestimated in the simulations due to the use of a softer material model as compared to the realistic rock sample.

(6) The cutting mechanics involved in face turning of rock was discussed based on simulation results. The effects of process parameters on the force responses in simulations were found to qualitatively match the experimental tests. Increases in the feedrate and depth of cut lead to higher cutting forces. Moreover, a linear relation between the friction angle on rake face and the rake angle found in the previous experimental work was confirmed in the simulations.

Chapter 7

Heat Transfer Modeling in Rock Cutting

Heat transfer phenomena at the rock-cutter interface are extremely significant since they affect the polycrystalline diamond compact (PDC) cutter's performance in rock cutting/drilling processes. The understanding of how temperature and heat flux responses in the cutter influence the intrinsic mechanisms of the rock-cutter interactions is an essential prerequisite for providing insights to enhance the performance of PDC cutters and to optimize rock cutting/drilling processes. In this chapter, a mixed boundary value heat transfer problem was formulated to analytically describe the heat transfer phenomena in the PDC cutters during two-dimensional orthogonal rock cutting under steady state conditions. An analytical solution in the form of an infinite series was derived based on the method of separation of variables, the use of appropriate simplifications in the formulated problem and the separation of the thermal from the mechanical phenomena. A series of experimental tests were conducted on the rock cutting testbed introduced in Chapter 3 to calibrate the process parameters in the analytical solution and then to confirm the validity of the assumed boundary conditions. The comparison between the newly-derived analytical solution and the experimental data shows a good match in terms of temperature responses during rock cutting performed by PDC cutters.

This chapter is organized as follows: The general mathematical description of the heat transfer problem will be given in Section 7.1 with simplified geometry and boundary conditions defined from the physical point of view, followed by the general analytical solution of the formulated heat

transfer problem in Section 7.2. Section 7.3 will give the detailed description of the experimental conditions and test results to be used in evaluating the heat transfer problem formulated in Section 7.1. The calibration of the above-derived solutions and the evaluation of the formulated boundary value problem will be discussed in Section 7.4. In addition, a finite element model will be developed to numerically verify the derived analytical solution in Section 7.5. Finally, the work done will be concluded in Section 7.6.

7.1 Heat transfer problem formulation

The heat transfer problems associated with rock cutting performed with PDC cutters can be extremely complex due to the diversity of physical phenomena involved, e.g., complex contact/friction conditions, inhomogeneous material properties for both the cutter and rock formation, and thermal-mechanical coupling mechanisms. Therefore, numerical modeling of the thermal phenomena is commonly exploited by researchers to accurately capture the major aspects of the process. However, numerical modeling, according to its characteristics, usually requires sophisticated attempts on material modeling, boundary condition assignments, and mesh optimization. To this end, this section will formulate a heat transfer problem to describe the heat transfer phenomena in a PDC cutter during 2-dimensional (2D) (i.e., orthogonal) rock cutting processes without cutting fluids (i.e., under dry cutting condition) from the theoretical point of view, aiming to explore the intrinsic mechanisms associated with the thermal response of the cutters involved in rock cutting. The problem will be described mathematically under reasonable simplifications and separated from the mechanical responses like force, stress and strain, aiming at making the derivation of an accurate analytical solution possible.

As shown in Fig. 7.1, the formulation of a 2D heat transfer problem, i.e., of a 2D mixed boundary value problem, for the PDC cutter including the tungsten carbide stud (represented by the square shape *AEFO*) and the diamond layer (represented by the square shape *EBCF*) is being proposed. Even though there are many complex interface geometries in use for PDC cutters, a flat interface is generally used between the tungsten carbide (WC) stud and the diamond layer. Therefore, this model considers a flat interface between the tungsten carbide (WC) stud and the diamond layer, i.e., *EF*. Segment *AO* is the end of the PDC cutter fixed to the tool holder, segment *AB* is the flank face, segment *OC* is the back face, and segment *BC* is the rake face. Segment *BC* includes two segments *BS* and *SC*. During the rock cutting process, segment *BS* is in contact with the rock with a length equal to the depth of cut D_c while segment *SC* will be subjected to chip flow. In order to mathematically describe this problem, the following assumptions will be made:

Assumption (1): It will be assumed that steady state conditions are reached. The validity of this assumption will be confirmed in Section 7.3 based on experimental measurements of the temperature response of the cutter.

Assumption (2): Since *AO* is fixed to the tool holder in the testbed configuration given in Section 7.3, and is far away from the cutting edge *B*, a constant temperature is assumed along *AO*.

Assumption (3): Since the *AB* and *OC* boundaries are directly in contact with air, heat convection occurring at *AB* is assumed to be very small. In this case, heat insulation is assigned to the *AB* and *OC* boundaries.

Assumption (4): Chips are generated and then slide away along *BC*. Considerable heat will be generated at the interface due to friction and conducted into the diamond layer. Therefore, the *BC* boundary is assumed to be prescribed by a certain heat flux equation $q(y)$. In particular, the segment

BS, i.e., the depth of cut, indicating the contact length between the rock and the cutter is assumed to be prescribed by a constant heat flux going into the cutter, while the segment *SC* will be subjected to chip flow. Since the temperature of the chips is higher but the flowing speed of the chips is lower when chips are closer to the virgin rock, i.e., point *S*, the heat flux carried out of the cutter by chips on boundary *SC* decreases when the location is approaching *S*. In this case, the prescribed heat flux on *SC* is defined as a power function with specific factors.

Assumption (5): The interface *EF* between the diamond layer and the tungsten carbide stud is represented by a thermal contact resistance *R*. The larger *R* is, the larger is the difference between the temperatures of the diamond layer and tungsten carbide at the interface. For perfect contact (i.e., no temperature difference at the interface), $R = 0$.

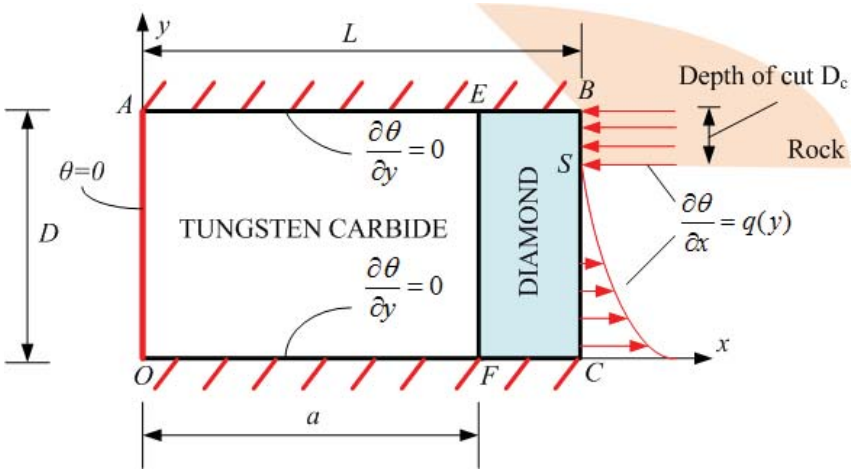

Figure 7.1: Boundary condition assignment on the PDC cutter.

According to assumption (1), the relative temperature at an arbitrary location (x, y) in the PDC cutter with respect to the temperature at boundary *AO*, $\theta_i(x, y)$ can be assumed to be governed by the Laplace's equation, i.e. (Carslaw and Jaeger, 1959):

$$\frac{\partial^2 \theta_i(x,y)}{\partial x^2} + \frac{\partial^2 \theta_i(x,y)}{\partial y^2} = 0 \tag{7.1}$$

where i = 1 and 2 denote the regions of the tungsten carbide stud and diamond layer respectively. The reference temperature is the temperature at the left boundary of the PDC cutter. Assumptions (2), (3) and (4) yield the following boundary conditions:

$$\theta_1 = 0,\ x = 0,\ 0 < y < D \tag{7.2}$$

$$\frac{\partial \theta_1}{\partial y} = 0,\ 0 < x < a,\ y = 0 \text{ and } D \tag{7.3}$$

$$\frac{\partial \theta_2}{\partial y} = 0,\ a < x < L,\ y = 0 \text{ and } D \tag{7.4}$$

$$\left.\frac{\partial \theta_2}{\partial x}\right|_{x=L} = q(y) \tag{7.5}$$

$$q(y) = \begin{cases} H_1, D - D_c \le y \le D \\ H_2 (y - D + D_c)^{H_3}, 0 \le y < D - D_c \end{cases} \tag{7.6}$$

where D is the cutter diameter, a is the length of the tungsten carbide stud, L is the cutter length, $q(y)$ is the temperature gradient at the rake face, and H_1, H_2, and H_3 are three constant factors governing $q(y)$. Assumption (5) yields the contact conditions at the interface which were depicted in the three-dimensional (3D) case by (Haji-Sheikh et al., 2003):

$$-k_1 \left.\frac{\partial \theta_1}{\partial x}\right|_{x=a} = -k_2 \left.\frac{\partial \theta_2}{\partial x}\right|_{x=a} \tag{7.7}$$

$$-k_1 \left.\frac{\partial \theta_1}{\partial x}\right|_{x=a} = \frac{\theta_1\big|_{x=a} - \theta_2\big|_{x=a}}{R} \tag{7.8}$$

where R is the contact resistance between the tungsten carbide stud and the diamond layer on a unit area, and k_1 and k_2 are the thermal conductivities of the tungsten carbide and polycrystalline diamond respectively.

The above-formulated problem is in general enough to represent a series of heat transfer phenomena in two-dimensional rock cutting under steady state conditions. For instance, the variation of the length of segment *BS* represents the variation of the depth of cut; the change of thermal contact resistance represents the change of contact conditions at the interface between the tungsten carbide stud and the diamond layer; the magnitude of the heat flux at the boundary *BS* indicates the intensity of the interaction between the rock and cutter, and the change of the power function governing the heat flux at the boundary *SC* denotes the magnitude of the interactions that occur between the cutter and the chips at the rake face.

In order to cast the above-described general form into a realistic problem, all the uncertain parameters have to be calibrated and determined. All the geometrical parameters, i.e., a, L, D and D_c in Eqs. (7.2-7.8) and material properties, i.e., k_1 and k_2 in Eqs. (7.7) and (7.8) can be determined based on the cutter geometry and material properties in real tests. The three heat flux factors, i.e., H_1, H_2 and H_3 and the thermal contact resistance at WC-diamond interface R have to be, in turn, calibrated based on experimental data of temperature responses derived during real tests. From the physical point of view, H_1 will determine how much heat is generated at the rock-cutter interface (i.e., segment *BS*), H_2 will determine how much of the heat is carried away by the chips along the cutter's rake face (i.e., segment *SC*) during rock cutting, and H_3 indicates how fast the heat flux is changing from the rock-cutter interface (i.e., point *S*) to the free end of the cutter (i.e., point *C*). Finally, R will affect the temperature difference between the diamond and WC layers at their

interface (i.e., segment *EF*). Therefore, the increase in H_1 but a decrease of H_2 will increase temperature levels over the whole cutter in rock cutting, the increase of H_3 will intensify the heat flux, i.e., the temperature gradient along the *x*-direction on the free side of the cutter (i.e., segment *SC*), and the increase of *R* will increase the temperature difference between the diamond and the WC layers. In this way, H_1, H_2, H_3, and *R* can be calibrated based on temperature responses at several sampling locations on the cutter obtained during experimental tests.

7.2 Analytical solution

This section provides an analytical solution of the 2D mixed boundary value problem formulated in Section 7.1 in the form of an infinite series.

The method of separation of variables has been commonly used for solving boundary value problems in Cartesian coordinate systems (Haji-Sheikh and Beck, 2002). Specifically, in the above-formulated problem, the method of separation of variables was exploited by assuming the desired solution of $\theta_i(x, y)$, where $i = 1$ and 2, can be expressed as a product of two functions, one of which only depends on *x* while the other depends on *y*. Therefore, the temperature response in the two layers can be expressed by:

$$\theta_1(x, y) = X_1(x)Y_1(y) \tag{7.9}$$

$$\theta_2(x, y) = X_2(x)Y_2(y) \tag{7.10}$$

where $i = 1$ and 2 denote the regions of the tungsten carbide stud and diamond layer respectively, X_i and Y_i represent mathematical functions independent of *y* and *x* respectively. Substituting Eqs. (7.9) and (7.10) into Eq. (7.1) yields:

$$-\frac{1}{X_1}\frac{d^2X_1}{dx^2}=\frac{1}{Y_1}\frac{d^2Y_1}{dy^2}=-\lambda^2 \tag{7.11}$$

$$-\frac{1}{X_2}\frac{d^2X_2}{dx^2}=\frac{1}{Y_2}\frac{d^2Y_2}{dy^2}=-\lambda^2 \tag{7.12}$$

where λ is a constant real number. Therefore, possible solutions, i.e., eigensolutions of Eqs. (7.11) and (7.12) can be found as:

$$X_e=\sinh\lambda x,\ \text{or}\ X_e=\cosh\lambda x \tag{7.13}$$

$$Y_e=\cos\lambda y,\ \text{or}\ Y_e=\sin\lambda y \tag{7.14}$$

where X_e is a possible form for X_1 and X_2, while Y_e is a possible form for Y_1 and Y_2. According to the boundary conditions described by Eqs. (7.3) and (7.4), a possible solution of Eq. (7.1) can be given by:

$$\theta_1(x,y)=\left(A_{1n}\sinh\frac{n\pi}{D}x+B_{1n}\cosh\frac{n\pi}{D}x\right)\cos\frac{n\pi}{D}y \tag{7.15}$$

$$\theta_1(x,y)=\left(A_{1n}\sinh\frac{n\pi}{D}x+B_{1n}\cosh\frac{n\pi}{D}x\right)\cos\frac{n\pi}{D}y \tag{7.16}$$

where n is an arbitrary integer. In order to determine the parameters (i.e., A_{in} and B_{in}, i = 1 and 2), the following equations can be obtained by replacing θ_1 and θ_2 in Eqs. (7.2), (7.7) and (7.8) with those in Eqs. (7.15) and (7.16):

$$\left(A_{1n}\sinh\frac{n\pi}{D}x+B_{1n}\cosh\frac{n\pi}{D}x\right)_{x=0}=0 \tag{7.17}$$

$$-k_1 \frac{n\pi}{D}\left(A_{1n} \cosh \frac{n\pi}{D} x + B_{1n} \sinh \frac{n\pi}{D} x \right)_{x=a} = -k_2 \frac{n\pi}{D}\left(A_{2n} \cosh \frac{n\pi}{D} x + B_{2n} \sinh \frac{n\pi}{D} x \right)_{x=a} \quad (7.18)$$

$$-k_1 \frac{n\pi}{D}\left(A_{1n} \cosh \frac{n\pi}{D} x + B_{1n} \sinh \frac{n\pi}{D} x \right)_{x=a} = \frac{\left(A_{1n} - A_{2n} \right) \sinh \frac{n\pi a}{D} + \left(B_{1n} - B_{2n} \right) \cosh \frac{n\pi a}{D}}{R} \quad (7.19)$$

According to Eq. (7.17), the factor B_{1n} can be determined by:

$$B_{1n} = 0 \quad (7.20)$$

Based on Eq. (7.20), Eqs. (7.18) and (7.19) reduce to:

$$A_{2n} = \left[\frac{k_1}{k_2} \cosh^2 (\frac{n\pi a}{D}) - \sinh^2 (\frac{n\pi a}{D}) - \frac{n\pi R k_1}{D} \sinh (\frac{n\pi a}{D}) \cosh (\frac{n\pi a}{D}) \right] A_{1n} \quad (7.21)$$

$$B_{2n} = \left[(1 - \frac{k_1}{k_2}) \sinh (\frac{n\pi a}{D}) \cosh (\frac{n\pi a}{D}) + \frac{n\pi R k_1}{D} \cosh^2 (\frac{n\pi a}{D}) \right] A_{1n} \quad (7.22)$$

Therefore, the temperature in the regions of the tungsten carbide stud and diamond layer can be expressed in the form of an infinite series, i.e.:

$$\theta_1 (x, y) = \sum_{n=1}^{\infty} A_{1n} \sinh \frac{n\pi}{D} x \cos \frac{n\pi}{D} y \quad (7.23)$$

$$\theta_2 (x, y) = \sum_{n=1}^{\infty} A_{1n} \left(G_{2n} \sinh \frac{n\pi}{D} x + G_{3n} \cosh \frac{n\pi}{D} x \right) \cos \frac{n\pi}{D} y \quad (7.24)$$

where G_{2n} and G_{3n} can be expressed by:

$$G_{2n} = \frac{k_1}{k_2} \cosh^2 (\frac{n\pi a}{D}) - \sinh^2 (\frac{n\pi a}{D}) - \frac{n\pi R k_1}{D} \sinh (\frac{n\pi a}{D}) \cosh (\frac{n\pi a}{D}) \quad (7.25)$$

$$G_{3n} = (1 - \frac{k_1}{k_2}) \sinh(\frac{n\pi a}{D}) \cosh(\frac{n\pi a}{D}) + \frac{n\pi R k_1}{D} \cosh^2(\frac{n\pi a}{D}) \tag{7.26}$$

Consequently, the temperature gradient along the *x*-direction can be derived as follows:

$$\frac{\partial \theta_1(x,y)}{\partial x} = \sum_{n=1}^{\infty} A_{1n} \frac{n\pi}{D} \cosh \frac{n\pi x}{D} \cos \frac{n\pi}{D} y \tag{7.27}$$

$$\frac{\partial \theta_2(x,y)}{\partial x} = \sum_{n=1}^{\infty} A_{1n} \frac{n\pi}{D} \left(G_{2n} \cosh \frac{n\pi x}{D} + G_{3n} \sinh \frac{n\pi x}{D} \right) \cos \frac{n\pi}{D} y \tag{7.28}$$

There is commonly a constant difference between the above expressions and the solutions satisfying the required boundary conditions on the right side which can be easily compensated for by a constant term:

$$\frac{\partial \theta_1(x,y)}{\partial x} = \sum_{n=1}^{\infty} A_{1n} \frac{n\pi}{D} \cosh \frac{n\pi x}{D} \cos \frac{n\pi}{D} y + C_1 \tag{7.29}$$

$$\frac{\partial \theta_2(x,y)}{\partial x} = \sum_{n=1}^{\infty} A_{1n} \frac{n\pi}{D} \left(G_{2n} \cosh \frac{n\pi x}{D} + G_{3n} \sinh \frac{n\pi x}{D} \right) \cos \frac{n\pi}{D} y + C_2 \tag{7.30}$$

where C_1 and C_2 are two constants. In this way, the temperature distribution can be expressed by:

$$\theta_1(x,y) = \sum_{n=1}^{\infty} A_{1n} \sinh \frac{n\pi}{D} x \cos \frac{n\pi}{D} y + C_1 x + C_3 \tag{7.31}$$

$$\theta_2(x,y) = \sum_{n=1}^{\infty} A_{1n} \left(G_{2n} \sinh \frac{n\pi}{D} x + G_{3n} \cosh \frac{n\pi}{D} x \right) \cos \frac{n\pi}{D} y + C_2 x + C_4 \tag{7.32}$$

where C_1, C_2, C_3, and C_4 are constants, which can be determined as described next.

By evaluating the temperature gradient in the diamond layer, $\partial\theta_2/\partial x$, at the boundary *BC*, i.e., $x = L$, Eq. (7.30) changes to:

$$\left.\frac{\partial \theta_2(x,y)}{\partial x}\right|_{x=L} = \sum_{n=1}^{\infty} A_{1n}\frac{n\pi}{D}\left(G_{2n}\cosh\frac{n\pi L}{D} + G_{3n}\sinh\frac{n\pi L}{D}\right)\cos\frac{n\pi}{D}y + C_2 \tag{7.33}$$

Comparing Eqs. (7.5) and (7.33) yields the expression for the temperature gradient at boundary *BC*, $q(x)$, i.e.:

$$q(y) = \sum_{n=1}^{\infty} A_{1n}\frac{n\pi}{D}\left(G_{2n}\cosh\frac{n\pi L}{D} + G_{3n}\sinh\frac{n\pi L}{D}\right)\cos\frac{n\pi}{D}y + C_2 \tag{7.34}$$

Multiplying both sides of Eq. (7.34) by $\cos(m\pi y/D)$, where m is an arbitrary non-negative integer, and then integrating the derived expression on both sides over the boundary *BC* (i.e., $x = L$) yields:

$$\begin{aligned}&\int_0^D q(y)\cos\frac{m\pi y}{D}dy \\ &= \sum_{n=1}^{\infty} A_{1n}\frac{n\pi}{D}\left(G_{2n}\cosh\frac{n\pi L}{D} + G_{3n}\sinh\frac{n\pi L}{D}\right)\int_0^D \cos\frac{n\pi y}{D}\cos\frac{m\pi y}{D}dy + C_2\int_0^D \cos\frac{m\pi y}{D}dy\end{aligned} \tag{7.35}$$

The orthogonality of functions $\cos(m\pi y/D)$ and $\cos(n\pi y/D)$ yields the following relations:

$$\int_0^D \cos\frac{m\pi}{D}y\cos\frac{n\pi}{D}ydy = \begin{cases} 0, & \text{n} \neq \text{m} \\ \dfrac{D}{2}, & \text{n} = \text{m} \end{cases} \tag{7.36}$$

For $m = n > 0$, based on Eqs. (7.35) and (7.36), an expression for the coefficient A_{1n} can be obtained, i.e.:

$$A_{1n} = \frac{2}{n\pi} \frac{\int_0^D q(y) \cos \frac{n\pi}{D} y dy}{G_{2n} \cosh(\frac{n\pi L}{D}) + G_{3n} \sinh(\frac{n\pi L}{D})} \tag{7.37}$$

For $m = 0$, Eq. (7.35) reduces to:

$$\int_0^D \left. \frac{\partial \theta(x, y)}{\partial x} \right|_{x=L} dy = C_2 \int_0^D 1 dy \tag{7.38}$$

which leads to the expression for the constant C_2:

$$C_2 = \frac{1}{D} \int_0^D q(y) dy \tag{7.39}$$

The next step is the determination of constants C_1, C_3 and C_4. Substitution of Eq. (7.31) into Eq. (7.2) yields:

$$C_3 = 0 \tag{7.40}$$

while replacing θ_1 and θ_2 in Eqs. (7.7) and (7.8) with those in Eqs. (7.31) and (7.32) yields:

$$-k_1 C_1 = -k_2 C_2 \tag{7.41}$$

$$-k_1 C_1 = \frac{(C_1 a + C_3) - (C_2 a + C_4)}{R} \tag{7.42}$$

Replacing C_2 and C_3, using Eqs. (7.39) and (7.40), C_1 and C_4 can be obtained from Eqs. (7.41) and (7.42), i.e.:

$$C_1 = \frac{k_2}{k_1 D}\int_0^D q(y)dy \tag{7.43}$$

$$C_4 = \frac{1}{D}\left[k_2 R + (\frac{k_2}{k_1} - 1)a\right]\int_0^D q(y)dy \tag{7.44}$$

Finally, the temperature distributions in the two distinct regions (WC and diamond) in the PDC cutter can be expressed by:

$$\theta_1(x,y) = \sum_{n=1}^{\infty} A_{1n} \sinh\frac{n\pi}{D}x \cos\frac{n\pi}{D}y + C_1 x \tag{7.45}$$

$$\theta_2(x,y) = \sum_{n=1}^{\infty} A_{1n}\left(G_{2n}\sinh\frac{n\pi}{D}x + G_{3n}\cosh\frac{n\pi}{D}x\right)\cos\frac{n\pi}{D}y + C_2 x + C_4 \tag{7.46}$$

where

$$A_{1n} = \frac{2}{n\pi}\frac{\int_0^D q(y)\cos\frac{n\pi}{D}ydy}{G_{2n}\cosh(\frac{n\pi L}{D}) + G_{3n}\sinh(\frac{n\pi L}{D})}$$

$$G_{2n} = \frac{k_1}{k_2}\cosh^2(\frac{n\pi a}{D}) - \sinh^2(\frac{n\pi a}{D}) - \frac{n\pi R k_1}{D}\sinh(\frac{n\pi a}{D})\cosh(\frac{n\pi a}{D})$$

$$G_{3n} = (1 - \frac{k_1}{k_2})\sinh(\frac{n\pi a}{D})\cosh(\frac{n\pi a}{D}) + \frac{n\pi R k_1}{D}\cosh^2(\frac{n\pi a}{D})$$

$$C_1 = \frac{k_2}{k_1 D}\int_0^D q(y)dy$$

$$C_2 = \frac{1}{D}\int_0^D q(y)dy$$

$$C_4 = \frac{1}{D}\left[k_2 R + (\frac{k_2}{k_1} - 1)a\right]\int_0^D q(y)dy$$

Moreover, the heat fluxes can be derived based on Fourier's law of heat conduction (Incropera and De Witt, 2011), i.e.:

$$q_{x1} = -k_1 \frac{\partial \theta_1(x,y)}{\partial x} = -k_1 \left[\sum_{n=1}^{\infty} A_{1n} \frac{n\pi}{D} \cosh \frac{n\pi}{D} x \cos \frac{n\pi}{D} y + C_1 \right] \tag{7.47}$$

$$q_{x2} = -k_2 \frac{\partial \theta_2(x,y)}{\partial x} = -k_2 \left[\sum_{n=1}^{\infty} A_{1n} \frac{n\pi}{D} \left(G_{2n} \cosh \frac{n\pi}{D} x + G_{3n} \sinh \frac{n\pi}{D} x \right) \cos \frac{n\pi}{D} y + C_2 \right] \tag{7.48}$$

$$q_{y1} = -k_1 \frac{\partial \theta_1(x,y)}{\partial y} = k_1 \sum_{n=1}^{\infty} A_{1n} \frac{n\pi}{D} \sinh \frac{n\pi}{D} x \sin \frac{n\pi}{D} y \tag{7.49}$$

$$q_{y2} = -k_2 \frac{\partial \theta_2(x,y)}{\partial y} = k_1 \sum_{n=1}^{\infty} A_{1n} \frac{n\pi}{D} \left(G_{2n} \sinh \frac{n\pi}{D} x + G_{3n} \cosh \frac{n\pi}{D} x \right) \sin \frac{n\pi}{D} y \tag{7.50}$$

Substituting the defined form of $q(y)$ in Eq. (7.6) into Eqs. (7.37), (7.39), (7.43) and (7.44) yields:

$$A_{1n} = \frac{2}{n\pi} \frac{\int_0^{D-D_s} H_2 (y - D + D_s)^{H_3} \cos \frac{n\pi}{D} y dy + \int_{D-D_s}^{D} H_1 \cos \frac{n\pi}{D} y dy}{G_{2n} \cosh(\frac{n\pi L}{D}) + G_{3n} \sinh(\frac{n\pi L}{D})} \tag{7.51}$$

$$C_1 = \frac{k_2}{k_1 D} \left[-\frac{H_2}{H_3 + 1} (D_s - D)^{H_3 + 1} + H_1 D_s \right] \tag{7.52}$$

$$C_2 = \frac{1}{D} \left[-\frac{H_2}{H_3 + 1} (D_s - D)^{H_3 + 1} + H_1 D_s \right] \tag{7.53}$$

$$C_4 = \frac{1}{D} \left[k_2 R + (\frac{k_2}{k_1} - 1) a \right] \left[-\frac{H_2}{H_3 + 1} (D_s - D)^{H_3 + 1} + H_1 D_s \right] \tag{7.54}$$

In this way, the thermal responses, i.e., temperature and heat flux, in the PDC cutter can be predicted exclusively based on geometrical parameters, i.e., a, L, D and D_c, material properties,

i.e., k_1 and k_2, and process parameters, *i.e.*, R, H_1, H_2, and H_3. In the next section, several rock cutting tests will be conducted to determine all the required parameters and evaluate the accuracy of the above-formulated heat transfer problem.

7.3 Experimental configurations

7.3.1 Temperature measurement

Rock cutting tests were performed on the RFTT described in Chapter 3. Five OMEGA K-type thermo-couples (OMEGA 5TC-GG-K-30-72), namely TC-I, II, III, IV and V, were attached to the center plane of the PDC cutter at specific locations to enable the capability of temperature measurements. As shown in Fig. 7.2, TC-I was attached to the flank face of the PDC cutter, TC-IV and TC-V were attached on the rake face of the cutter, and TC-II and TC-III were attached to the back face of the cutter. In the real cutting tests, the depth of cut was set to very small value, i.e., 5% of the PDC cutter's diameter, in order to approximate 2D orthogonal cutting conditions. Therefore, the temperature responses in the center plane at which all the thermocouples were attached were sufficient to represent the temperature responses at specific locations corresponding to a 2D problem. A photograph of the thermocouple-attached PDC cutter can be found in Fig. 7.3. A high temperature cement binder was deposited at the junctions of the thermocouples for electrical insulation purposes. Since welding cannot be used to attach thermocouples to polycrystalline diamond, epoxy glue was used to attach the thermocouples at specific locations on the surface of the PDC cutter. The large size of the commercial thermocouples, the insulation requirements, and the special material property of diamond make it very different to attach these thermocouples to the quite tiny PDC cutter neatly and accurately. Moreover, it should be also noted

that the attachment of the thermocouples will, to a certain extent, change the heat transfer mechanisms in the PDC cutter. However, given the lack of efficient temperature measuring techniques, the current experimental results can provide hints to qualitatively formulate the theoretical model of heat transfer involved in rock cutting.

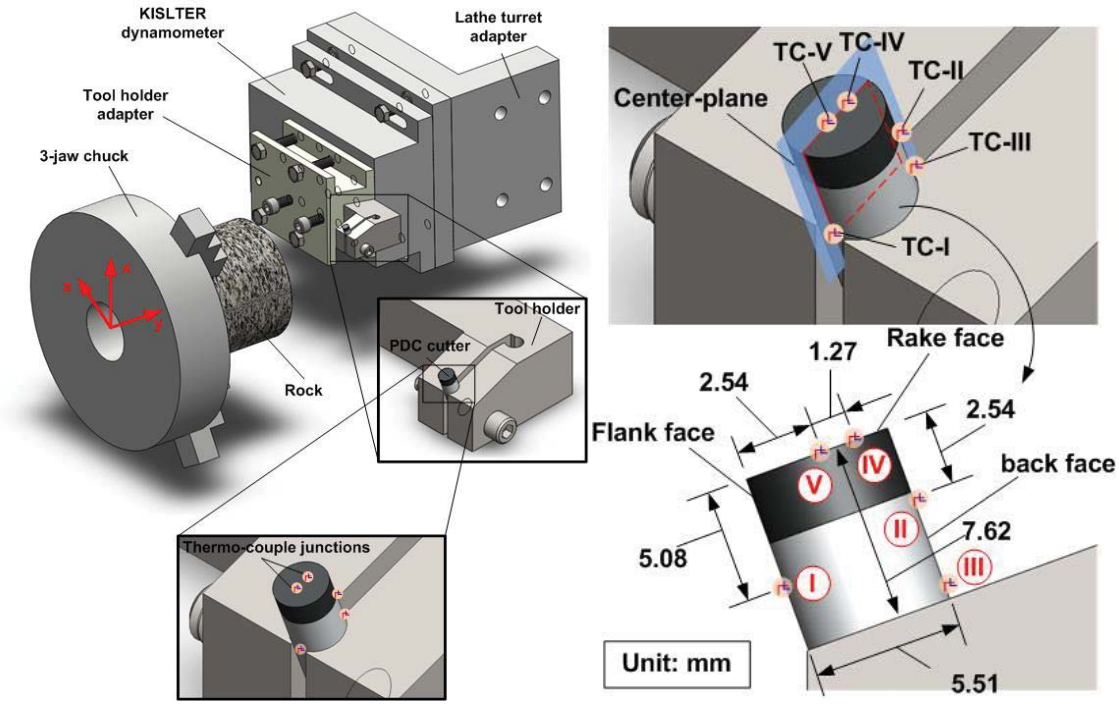

Figure 7.2: Temperature measurement in rock face turning tests: (a) testbed layout; (b) thermocouple attachment locations.

The temperature responses generated by the above-mentioned five thermocouples were captured by the NI DAQ card (NI PCI-6259) via a connector block (SCB-68). The maximal temperature measurement is up to 1,200 °C. More details about this testbed can be found in Chapter 3 and have been published in (Che and Ehmann, 2013, 2014). Using the testbed shown in

Fig. 7.2(a), a series of face turning tests were conducted to capture the thermal responses acting on the PDC cutter during rock cutting.

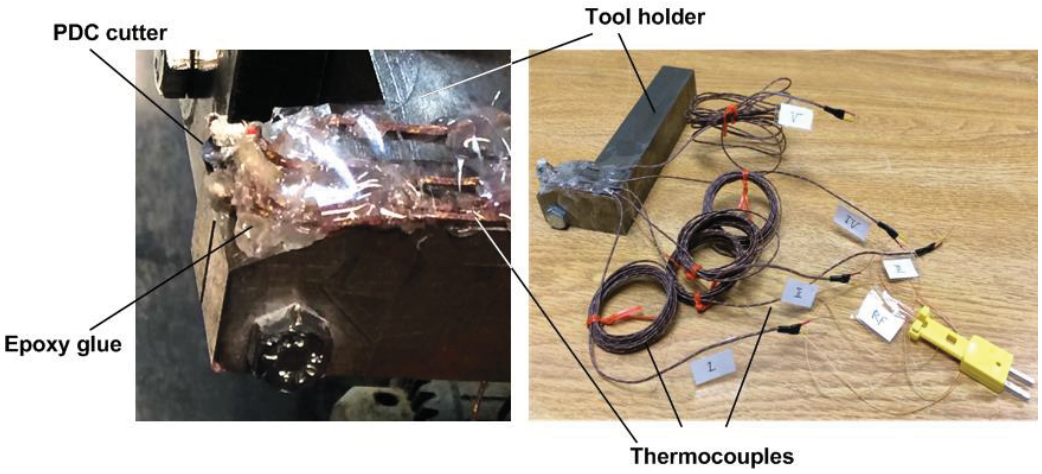

Figure 7.3: Photograph of the PDC cutter with thermocouples attached.

7.3.2 Experimental conditions

The ultimate goal of the series of tests performed is to capture the thermal responses of the PDC cutter. The process parameters used in the face turning tests are summarized in Table 7.1. No coolant or cutting fluid was applied during the performed rock cutting tests in order to simulate the dry cutting conditions assumed in the above-formulated problem. A very small depth of cut, i.e., 0.254 mm, was used to approximate 2-dimensional orthogonal cutting conditions. The spindle speed was selected to be 800 rpm which falls in the range of commonly used cutting speeds of PDC cutters under field conditions (i.e., 1.6 ~ 4m/s (Che et al., 2015a)). The data generated by the thermocouples were sampled at a 5 kHz sampling rate.

It needs to be noted, that during the face turning of the rock samples, the spindle speed was maintained at a constant value implying that when the cutter is fed at a constant feedrate towards the center of the rock cylinder a linear decrease in cutting speed occurs (i.e., the cutting speed

decreases gradually from 4.3 m/s to 0 m/s). Even though the cutting speed is changing during the cutting process, a steady state was found to be reached for each test which will be discussed in next section.

Table 7.1: Experimental conditions.

Parameters	Values
Spindle speed	800 rpm
Cutting speed	4.3 m/s
Rake angle	-25°
Clearance angle	25°
Feedrate	0.15 mm/rev
Depth of cut	0.254 mm

Since the signals derived from the five thermocouples were quite noisy due to the intensive interactions between the rock and the cutter as well as due to environmental noise, three repeated tests, i.e., tests 1, 2, and 3, under exactly the same process parameters were conducted and the results were averaged in order to obtain more valuable and accurate data.

7.3.3 Experimental results

The temperature responses of the cutter at the five thermocouple attachment locations in one of the three tests, i.e., Test 1, are shown in Fig. 7.4. The temperature responses at all the five locations reach a relatively flat phase, i.e., approximately between 20 and 25s, during face turning with a constant spindle speed. The flat phase is considered as the steady-state phase assumed in Section 7.1. Moreover, the temperature responses acquired by all the thermocouples and from other tests have similar trends but different magnitudes.

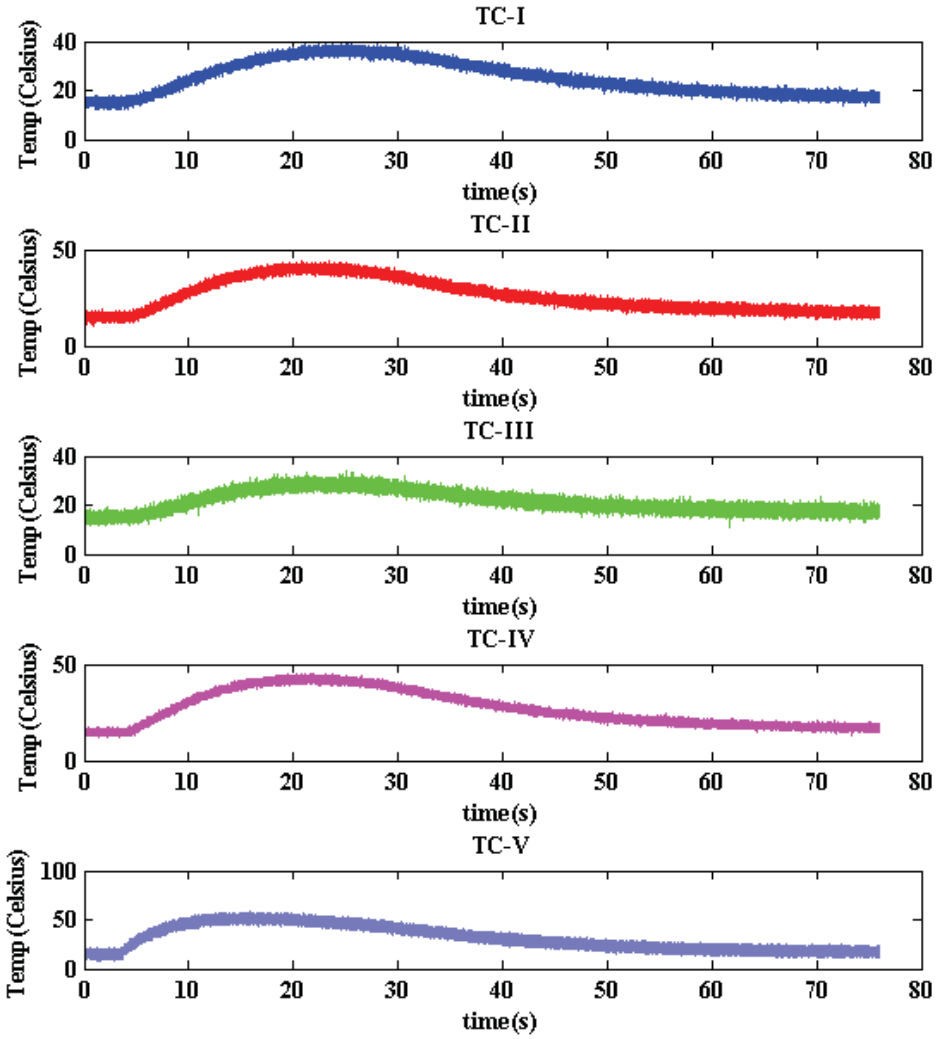

Figure 7.4: Temperature responses at five thermocouple attachment locations.

A series of temperature response phases obtained in the tests are depicted in Fig. 7.5. The intensity of the interactions between the rock and the PDC cutter, as it can be seen, significantly affects the temperature response of the cutter. At the start of the rock-cutter interaction, the temperature at location TC-IV starts to increase until it reaches the flat phase, i.e., steady state. With the decrease of the rock-cutter interaction at the end of the test, the temperature tends to decrease. Since a steady-state condition was assumed in the above-derived heat transfer problem

formulation, only the data during the flat phase (i.e., approximately from 20 to 25 s) will be selected and also averaged, to reduce the influence of noise, in the subsequent analyses.

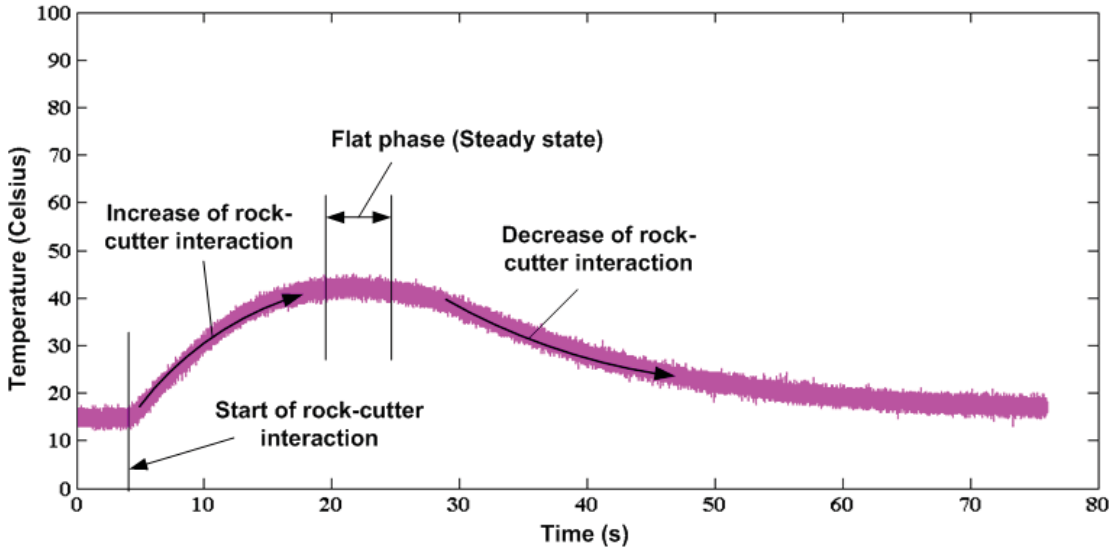

Figure 7.5: Temperature responses at five thermocouple attachment locations.

The tests were conducted under face turning conditions of a 101.6 mm diameter limestone cylinder mentioned in Section 3.1. According to the specified feedrate given in Table 7.1, it takes about 25 s for the PDC cutter to cut off one rock layer during the face turning process. Due to the relatively low response speed of commercial thermocouples, a long period of time (~20 s) is required by the thermocouples to reach a stable temperature. Therefore, the steady state temperature lasted only for a relatively short period of time (i.e., ~5 s).

The steady-state temperature, i.e., average temperature in the flat phase, at various locations is shown in Table 7.2. As expected, the highest temperatures are measured by the thermocouple closest to the cutting edge of the PDC cutter, i.e., the interface between the cutter and rock, while the lowest temperatures are obtained by the thermocouple farthest away from the cutting edge. The first three columns in Table 7.2 represent the steady-state temperatures for the three different tests,

while the last column represents the average of the steady-state temperatures at each thermocouple attachment location for the three tests. The steady-state temperatures in the last column in Table 7.2 will be used to calibrate the parameters governing the above-mentioned 2D mixed boundary value problem, which will be discussed in detail in next section.

Table 7.2: Steady-state temperatures with the unit of degree Celsius.

	Test 1	**Test 2**	**Test 3**	**Average**
TC-I	46.7	46.5	46.5	46.6
TC-II	51.0	51.5	51.8	51.4
TC-III	39.4	39.5	39.5	39.5
TC-IV	53.2	53.3	53.8	53.4
TC-V	59.2	59.4	60.0	59.5

7.4 Experimental evaluation of the analytical solution

In this section, the methodology for the determination and evaluation of the required parameters, i.e., R, H_1, H_2, and H_3 will be discussed, aiming to specify the above-defined boundary value problem for the description of the experiments done in this work. Moreover, the accuracy of the formulated boundary value problem will be evaluated based on the comparison between the predicted and experimental temperature responses at the five thermocouple locations.

7.4.1 Parameter calibration for the analytical solution

As it can be seen in Table 7.3, all the parameters in terms of geometry and material properties can be determined directly either from the experimental conditions or references. The thermal contact resistance of metallic interfaces under vacuum conditions and 10 MPa pressure is around 0.02~0.4 K·mm^2/mW (Che et al., 2015a). However, the thermal resistance of the WC-diamond interface under the diffusion bonding conditions (~50 MPa (Santos et al., 2004)) is considered to

be much smaller than that of metallic interfaces. Therefore, the defined thermal contact resistance R in the analytical solution was approximately set to 6e-4 K·mm^2/mW according to the temperature differences between the WC stud and diamond layer derived from the experiments.

Table 7.3: Parameters for the analytical solutions.

Parameters	Symbols	Values	Units
Cutter diameter	D	5.51	mm
WC layer thickness	a	5.08	mm
Cutter length	L	7.62	mm
Depth of cut	D_c	0.254	mm
Thermal conductivity of WC	k_1	84	mW/(mm·K)
Thermal conductivity of polycrystalline diamond	k_2	543	mW/(mm·K)
Thermal contact resistance at interface	R	6e-4	K·mm^2/mW
Heat flux factor 1	H_1	48.5488	K/mm
Heat flux factor 2	H_2	-5.15820e-8	K/mm^{13}
Heat flux factor 3	H_3	12	1

The heat flux factors, i.e., H_1, H_2, and H_3, were then calibrated based on experimental data. As the first trial test, H_1 is set to 1, and the relative temperatures at TC-V, TC-IV, and TC-II with respect to the reference temperature at location TC-III are found. Two ratios are defined as follows:

$$\delta_1 = \frac{\theta_{\text{TC-IV}}}{\theta_{\text{TC-V}}} \tag{7.55}$$

$$\delta_2 = \frac{\theta_{\text{TC-II}}}{\theta_{\text{TC-V}}} \tag{7.56}$$

$$\delta_{1e} = \frac{T_{IV} - T_{III}}{T_V - T_{III}} \tag{7.57}$$

$$\delta_{2e} = \frac{T_{II} - T_{III}}{T_V - T_{III}} \tag{7.58}$$

where $\theta_{TC\text{-}II}$, $\theta_{TC\text{-}IV}$, and $\theta_{TC\text{-}V}$ denote the relative temperature at locations TC-II, IV, and V respectively predicted by the analytical solution, while T_{II}, T_{III}, T_{IV}, and T_V are the absolute temperature responses at locations TC-II, III, IV, and V respectively measured by the thermocouples. According to Eqs. (7.55), (7.56), (7.57) and (7.58), a smaller error between δ_1 and δ_{1e} will result in a more accurate prediction of the relative temperature at location TC-VI, while a smaller error between δ_2 to δ_{2e} will result in a more accurate prediction of the relative temperature at location TC-II. In this work, the error between δ_1 and δ_{1e} and between δ_2 and δ_{2e} were limited to a specific range. Since H_2 determines how much heat will be carried away by the chips from the PDC cutter, the increase of H_2 will increase the temperature gradient on the boundary *BC*, i.e., decrease δ_1. Moreover, H_3 determines how fast the heat, carried by chips, changes along segment SC from the near end to the far end to the rock. The increase of H_3 will intensify the temperature gradient between TC-V and TC-II, i.e., decrease δ_2. Therefore, in order to obtain a more accurate prediction of the relative temperature at TC-VI, the error between δ_1 and δ_{1e} was set to 5%, i.e.:

$$\frac{\delta_1 - \delta_{1e}}{\delta_{1e}} \leq 5\% \tag{7.59}$$

Based on Eq. (7.59) and considering that increasing values of H_2 lead to a decrease of δ_1, an acceptable value of H_2, namely H_{2s}, can be determined. After H_2 is determined, the value of H_3 can be adjusted to minimize the error between δ_{2e} and δ_2, while the value of H_2 is fixed to H_{2s}. In

order to balance the accuracy and efficiency of parameter calibration, the error between δ_2 and δ_{2e} for the calibration of H_3 was set to 10%, i.e.:

$$\frac{\delta_2 - \delta_{2e}}{\delta_{2e}} \leq 10\% \tag{7.60}$$

As a consequence, the optimal value of H_3 can be determined accordingly, namely H_{3s}. The above-mentioned calibration of H_2 and H_3 under the assumption of $H_1 = 1$ ensures the accuracy of the predicted relative temperature ratios δ_1 and δ_2, i.e., $\theta_{\text{TC-IV}}/\theta_{\text{TC-V}}$ and $\theta_{\text{TC-II}}/\theta_{\text{TC-V}}$ respectively. The next step is to simultaneously adjust the parameters H_1, H_2, and H_3 to decrease the error between $\theta_{\text{TC-V}}$ and the experimental data without changing δ_1 and δ_2. If this step can be achieved, $\theta_{\text{TC-V}}$, $\theta_{\text{TC-IV}}/\theta_{\text{TC-V}}$ and $\theta_{\text{TC-II}}/\theta_{\text{TC-V}}$ (*i.e.*, $\theta_{\text{TC-II}}$, $\theta_{\text{TC-IV}}$, and $\theta_{\text{TC-V}}$) will match the experimental data very well.

Since the above-defined boundary value problem is linear, the scaling of the three factors H_1, H_2 and H_3 by the same value will only scale the predictions of the temperature and heat flux but maintain similar contours. In order words, if the following equations are satisfied:

$$H_{11} = \alpha_s H_1,\ H_{22} = \alpha_s H_2 \text{ and } H_{33} = \alpha_s H_3,$$

then the temperature and heat flux contours for H_1, H_2 and H_3 and H_{11}, H_{22} and H_{33} are similar but the temperature and heat flux values between these two sets differ by the scale factor α_s. Therefore, a scale factor α_s was determined to ensure that the predicted temperature at location TC-V, i.e., $\theta_{\text{TC-V}}$, matches the experimental data without changing the relative temperature ratios δ_1 and δ_2, i.e.:

$$\alpha_s = 1 \times \frac{T_V - T_{III}}{\theta_{TC\text{-}V}} \tag{7.61}$$

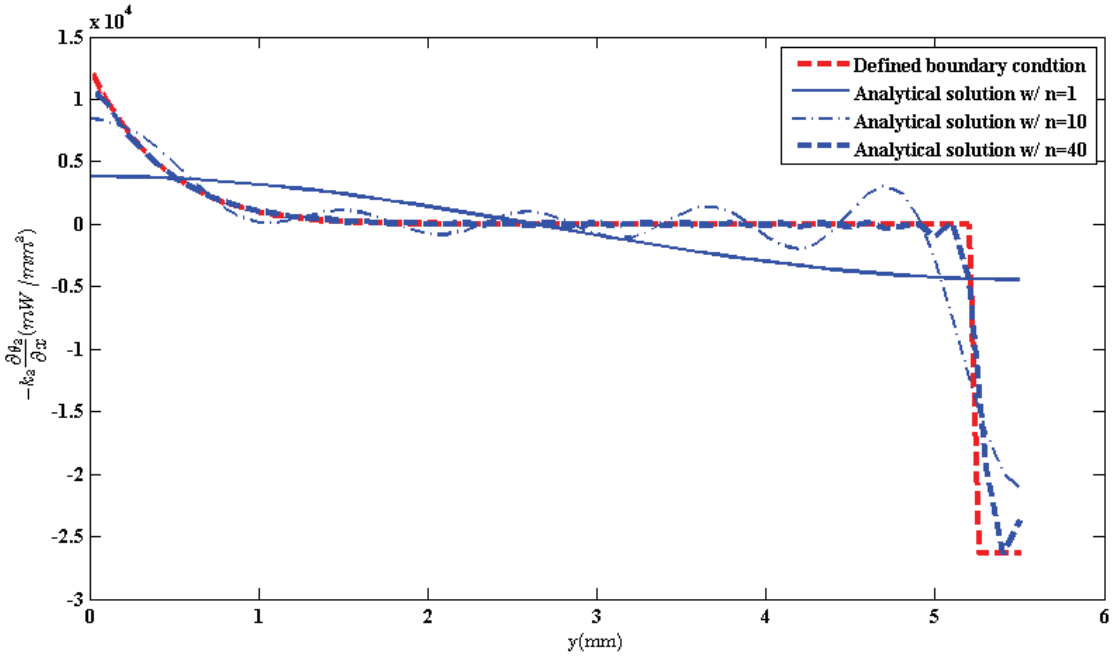

Figure 7.6: Heat flux along the *x*-direction on boundary BC for different numbers of terms.

$\theta_{TC\text{-}V}$ is the predicted relative temperature at TC-V for H_1 = 1, $H_2 = H_{2s}$ and $H_3 = H_{3s}$. Consequently, all the heat flux factors can be determined as follows:

$$H_{1D} = 1 \times \alpha_s = \alpha_s \tag{7.62}$$

$$H_{2D} = \alpha_s H_{2s} \tag{7.63}$$

$$H_{3D} = \alpha_s H_{3s} \tag{7.64}$$

where H_{iD}, i = 1, 2, and 3, are the finally determined factors. The actual values of these factors have been listed in Table 7.3 for the analytical solution.

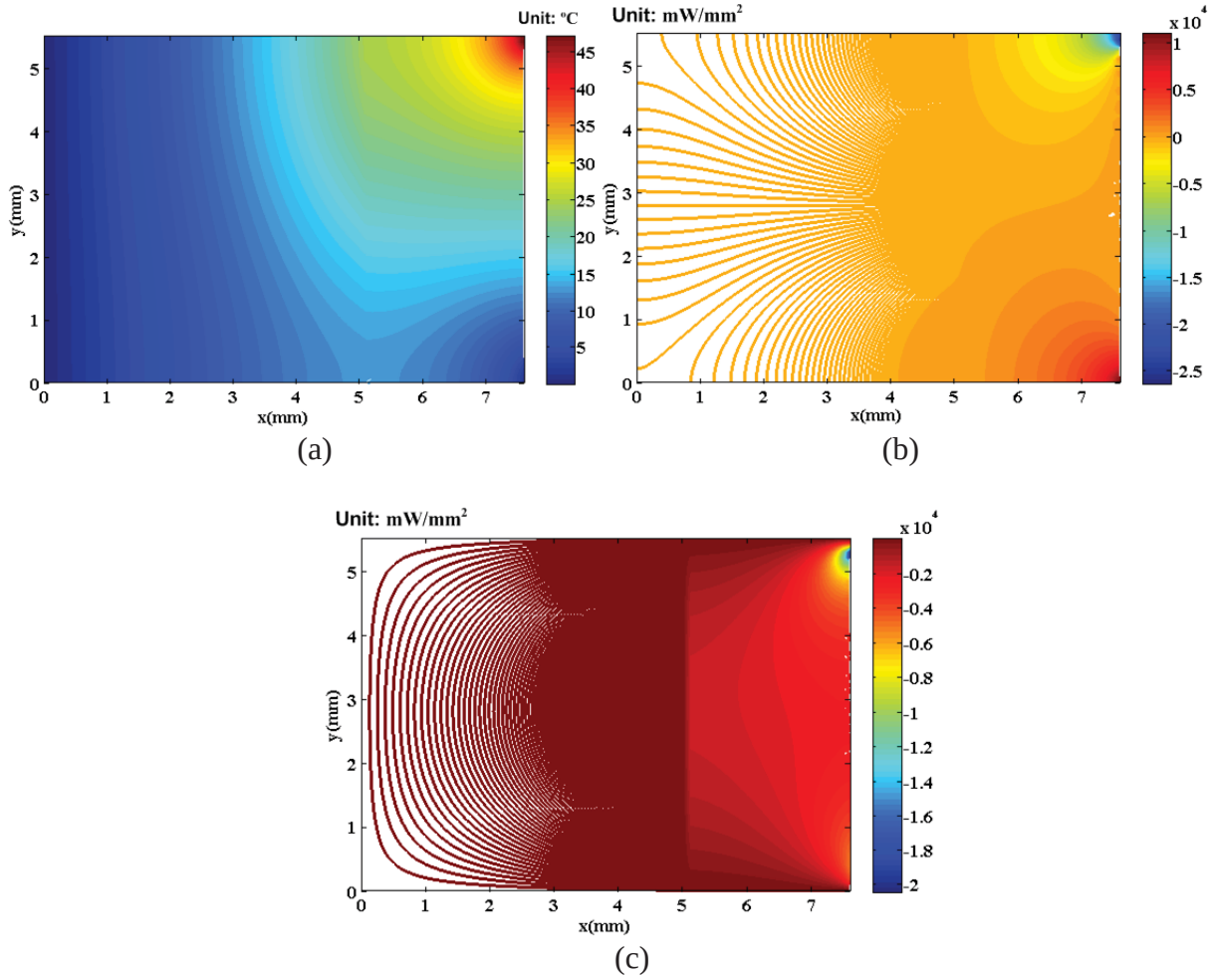

Figure 7.7: Predictions derived by the analytical solution with n = 40: (a) temperature; (b) heat flux along x; (c) heat flux along y.

7.4.2 Results

The temperature and heat flux equations can be fully determined by substituting all the parameters shown in Table 7.3 into Eqs. (7.45-7.54). Since the temperature and heat flux expressions described in Eqs. (7.45-7.50) are all infinite series, these expressions have to be truncated in order to simplify the calculations in MATLAB. The accuracy of the above-derived analytical solution is mainly determined by the number of terms in the expressions of the infinite

series. As shown in Fig. 7.6, convergence of the heat flux on boundary *BC* was obtained by the analytical solution with respect to the number of terms *n*. The larger *n* is, the more accurate the prediction is. The analytical solution converges to the defined boundary condition very quickly. In the current work, *n* was set to 40 in order to achieve a precise enough prediction of temperature and heat flux responses. As shown in Fig. 7.7, the results of thermal responses were derived from the analytical solutions based on an approximation with 40 terms.

7.4.3 Accuracy of the defined boundary value problem

According to the experimental data presented in Section 7.3, besides the temperature at location TC-III which is a pre-defined value according to the prescribed temperature boundary *AO*, the temperature responses at the remaining four thermocouple locations, i.e., TC-I, II, IV and V, need to show a match between the predictions and experimental data by adjusting only the three heat flux factors, i.e., H_1, H_2, and H_3 as mentioned in Section 7.4.1. In other words, the number of factors which are free to be adjusted is not sufficient to easily make the temperature responses at all the sampling locations match the experimental data from the mathematical point of view. The only possibility to make the temperature responses at all the sampling locations match the experimental data is that the above-defined problem and its boundary conditions are close to reality. In this study, H_1, H_2 and H_3 were calibrated based on the temperature responses at TC-II, IV, and V, while the temperature response at TC-I was not included in the calibration procedure. The response at this point can, therefore, be used to validate the model.

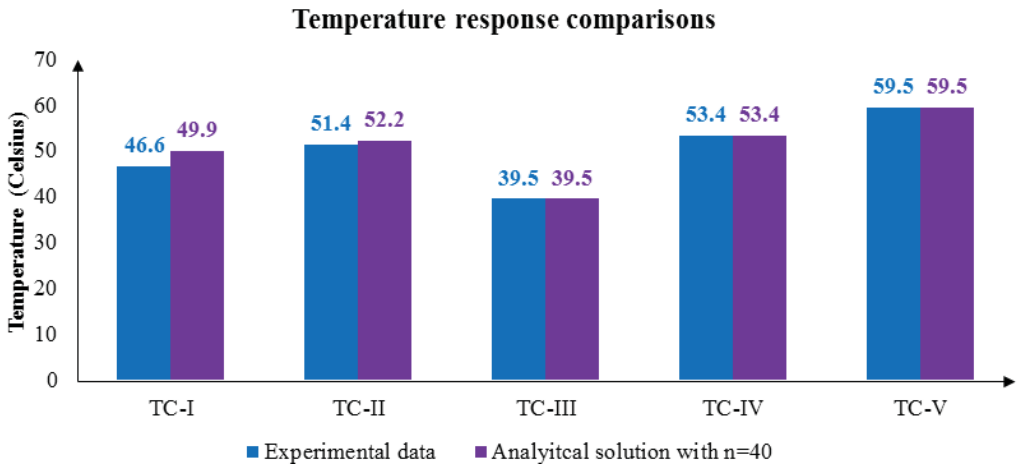

Figure 7.8: Comparison of absolute temperature responses at the five thermocouple locations.

Based on the above-described procedures, the accuracy of the defined boundary value problem was evaluated in comparison to the experimental data in order to determine how accurately the formulated problem can describe realistic rock cutting conditions. The predicted contour of the relative temperature in the PDC cutter with respect to the reference temperature at location TC-III can be easily obtained by the above-derived analytical solution. And then, the absolute temperature response in the cutter can be derived by adding the reference temperature to the relative temperature response. As shown in Fig. 7.8, the absolute temperature responses at different thermocouple locations are compared between the experimental data and analytical solution. As it can be seen, the temperature responses at the five thermocouple locations are in very good agreement with the experimental data and analytical solution. The maximum error, i.e., 7%, occurs at TC-I where the temperature response was not used in the calibration procedure, the error at the other locations is always less than 2%. This close agreement indicates that the formulated heat transfer problem with the defined boundary conditions can quite accurately capture the thermal phenomena involved in 2D rock cutting.

7.4.4 Discussion on the temperature distribution on the rake face

In metal cutting mechanics, the heat transferred into the chip is primarily generated due to plastic deformation. As shown in Fig. 7.9, the chip is considered to heat up first in the primary deformation zone (i.e., shear plane) due to the intense plastic deformation and then is heated up even more in the secondary deformation zone (i.e., rake face area) due to the plastic deformation and sticking-sliding friction. The peak temperature of the tool appears at a locations at a certain distance from the cutting edge (Boothroyd and Knight, 1989). Recently, the temperature responses of PCBN tools at locations very close to the cutting edge (i.e., 75-450 μm from the tool's rake face and 100-500 μm from its flank face) have been successfully measured by using micro thin film thermocouples during machining. The highest temperatures right beneath the rake face were found at locations close to the cutting edge (Werschmoeller et al., 2011). Similarly, by using an infrared system, the peak temperature was found to occur at the cutting edge in micro-end-milling of AL2024-T6 (Yang et al., 2011).

On the other hand, the heat generation and conduction phenomena in rock cutting are quite different from those in metal cutting. The chip will not heat up very much before separating from the virgin rock due to the negligible amount of plastic deformation that is occurring during the brittle cutting mode of rock. Therefore, heat will be generated mainly due to friction. In the tests conducted in this work, the rock failed purely in brittle mode with powder-like chips flowing above the rake face. Since no sticking-sliding friction phenomena were observed in the tests, the only heat source at the rake face of the cutter was assumed to be located very close to the cutting edge. In other words, the heat is assumed to be generated and conducted into the tool in areas of the rake face adjacent to the cutting edge while carried away in areas away from the cutting edge. Therefore,

the peak temperature of the PDC cutter in the model appear at the cutting edge rather than other locations on the rake face that are at a certain distance away from the cutting edge. Similar temperature contours in PDC cutters during rock cutting were also given in a previous finite element study done by Glowka (Glowka, 1989a).

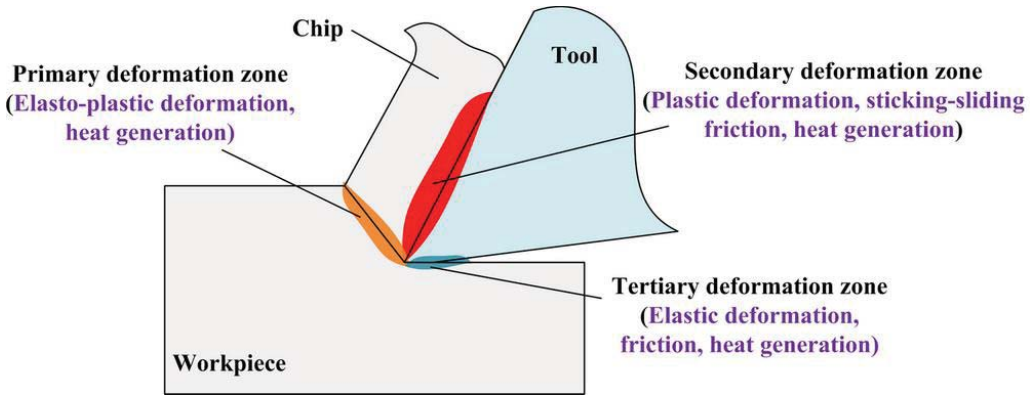

Figure 7.9: Heat generation sources in orthogonal cutting of metal.

The above presented results suggest that more accurate experimental investigations are still needed to obtain more accurate measurements of temperature distributions in PDC cutters during rock cutting. A possible method is to embed micro thin film thermocouple arrays under the rake face extremely close to the cutting edge (~several hundred microns) by using methods similar to those used in hard metal cutting with PCBN tools in the authors' previous work (Li et al., 2013; Werschmoeller et al., 2011), which have been presented in detail in Chapter 2. In addition, the prediction accuracy of the temperature distribution and of the peak temperatures on the rake face can be improved by defining a more realistic heat flux boundary condition along the rake face. According to the above-formulated model, an analytical solution can be derived with an arbitrary heat flux boundary condition along the rake face. Therefore, the model presented in this work can

serve as a foundation for the development of more realistic models based on more accurate experimental data in the future.

7.5 Numerical evaluation of the analytical solution

The problem formulated in Section 7.1 is possible to be accurately solved by the finite element method, as long as the mesh size is small enough. In this section, a finite element model of the above-formulated problem will be formulated and then be used to verify the accuracy of the analytical solution given in Section 7.2.

7.5.1 Finite element formulation

According to the heat transfer problem formulated in Section 7.1, an implicit FEM simulation approach will be formulated by using the commercial code ABAQUS. The conventional units to be used in this study are the same as those used in Chapter 6. As shown in Fig. 7.10, a very thin intermediate layer (i.e., region 3) was introduced between the tungsten carbide stud (i.e., region 1) and the diamond layer (i.e., region 2) with the aim of simulating the thermal contact resistance. The thickness of region 3, t_i, was defined by:

$$t_i = 1\% \times b \tag{7.65}$$

where b is the thickness of the real diamond layer. According to the definition of the thermal contact resistance, one has (Incropera and De Witt, 2011):

$$q_x'' = k_3 \frac{\Delta T}{t_i} = \frac{\Delta T}{R} \tag{7.66}$$

where q_x" is the value of the heat flux along the *x*-direction at the interface *EF*, k_3 is the thermal conductivity in region 3, t_i is the thickness of the very thin region 3, and ΔT is the temperature difference between the two horizontal sides of region 3. Since heat flux cannot be directly defined as zero (i.e., heat insulation) on the boundary in ABAQUS, a very small value of heat flux (i.e., 1e-10) was set at the heat insulted boundaries *AB* and *OC*. The boundary *AO* was assigned a constant temperature, i.e., $\theta = 0$. Based on Eq. (7.6), the boundary *BC* was assigned a constant heat flux Q_1 defined by:

$$Q_1 = -k_2 \left.\frac{\partial \theta_2}{\partial x}\right|_{x=L} = \begin{cases} -k_2 H_1, D - D_c \le y \le D \\ -k_2 H_2 (y - D + D_c)^{H_3}, 0 \le y < D - D_c \end{cases} \tag{7.67}$$

where k_2 is the thermal conductivity in region 2.

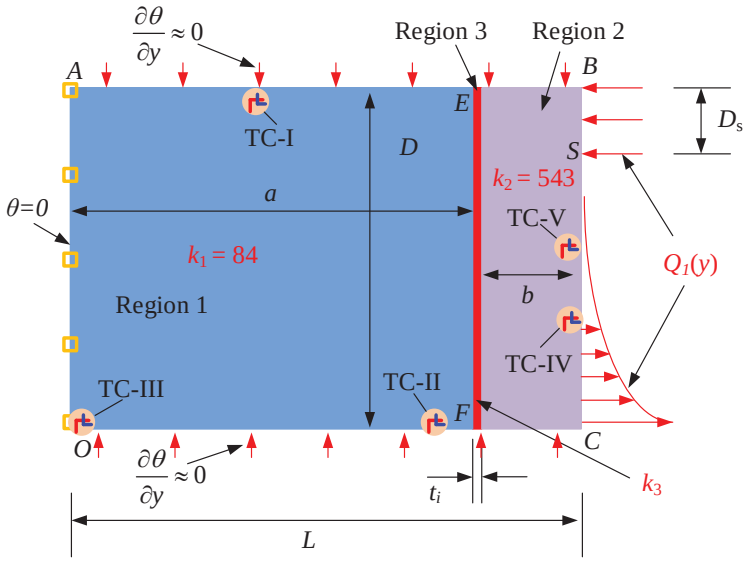

Figure 7.10: Finite element formulation of the heat transfer model.

2D linear quadrilateral solid elements were selected for the solution of this problem. A uniform mesh distribution was assigned to all of the boundaries with an approximate global element size of 0.03 mm. The five temperature sampling locations (i.e., TC-I, II, III, IV, and V) corresponding to the locations of the five thermocouples in the experiments are also shown in Fig. 7.10.

Table 7.4: Parameters for the FE simulation.

Parameters	Symbols	Values
Cutter diameter	D	5.51
Tungsten carbide layer thickness	a	5.08
Diamond layer thickness	b	2.54
Cutter length	L	7.62
Depth of cut	D_c	0.254
Heat fluxes on AB and OC	/	1e-10
Heat flux factor 1	H_1	48.5488
Heat flux factor 2	H_2	-5.15820e-8
Heat flux factor 3	H_3	12
Thermal conductivity of tungsten carbide	k_1	84
Thermal conductivity of polycrystalline diamond	k_2	543
Thermal conductivity in region 3	k_3	50

7.5.2 Numerical verification

Most of the parameters required for the FE model can be determined based on the calibrated parameters listed in Table 7.3. According to the FE formulation, the rest of the parameters can be easily determined as follows: b was determined based on Eq. (7.65) while k_3 can be calculated based on Eq. (7.66). All the relevant parameters required in the simulation are shown in Table 7.4. Figure 7.11 shows the temperature and heat flux contours in the PDC cutter given by the FE model which are actually in good agreement with the experimental results illustrated in Fig. 7.7.

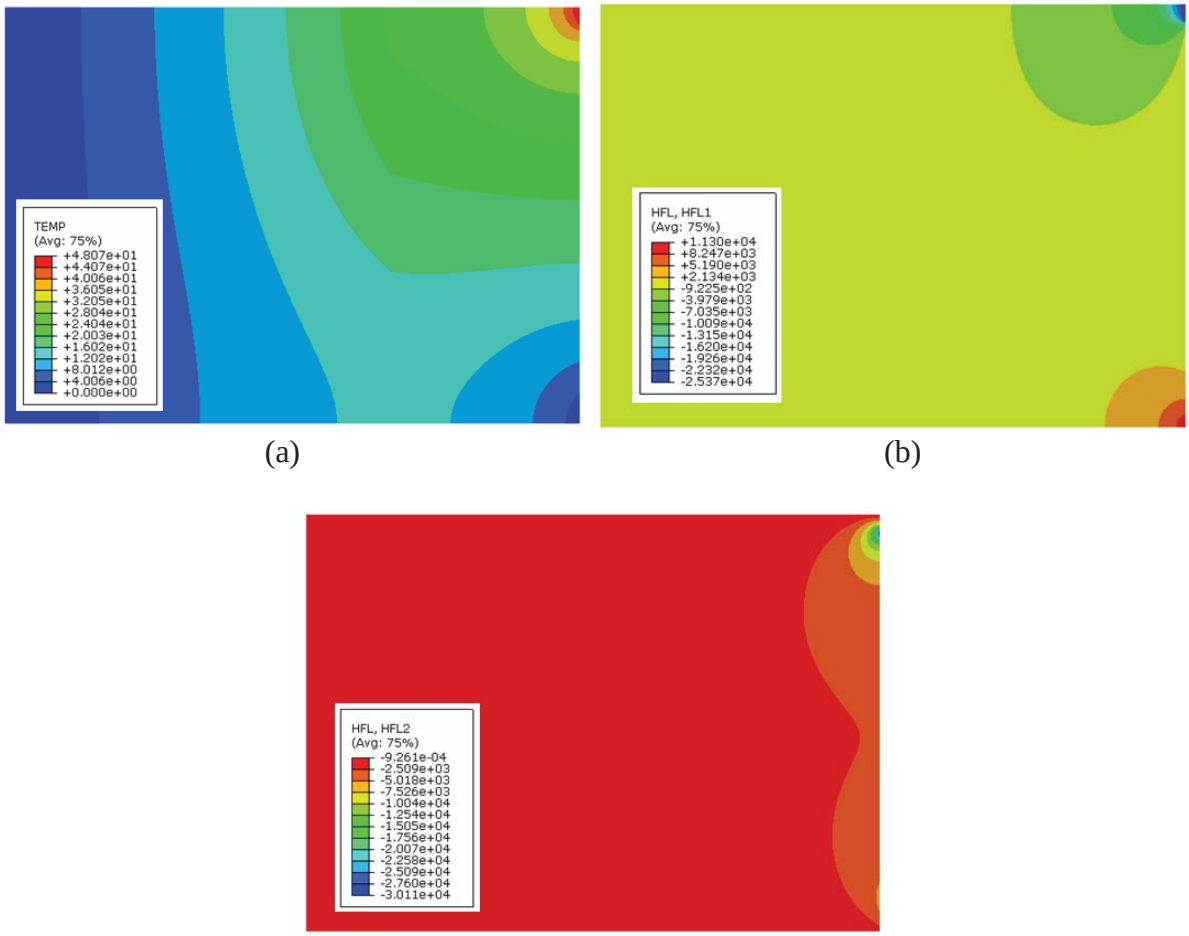

(a) (b)

(c)

Figure 7.11: Predictions derived by the FE model: (a) temperature; (b) heat flux along *x*; (c) heat flux along *y*.

7.6 Conclusions

This chapter deals with the theoretical study of the mechanism of thermal phenomena in PDC cutters during rock cutting processes. The formulated heat transfer problem, the derived analytical solution, the designed rock face turning tests, and the numerical verification expose the intrinsic mechanisms at the cutter and rock interface. The main conclusions are given as follows:

(1) A two-dimensional mixed boundary value problem for the heat transfer in a PDC cutter was formulated for rock cutting under two-dimensional steady state conditions. The Laplace's equation was exploited to govern the thermal response, while mixed boundary conditions, i.e., prescribed temperature and prescribed heat flux boundary conditions, were proposed to specify the problem based on experimental conditions and reasonable assumptions.

(2) An analytical solution in the form of infinite series was derived based on the method of separation of variables. Several significant process parameters were defined to specify the physical properties of the cutter and of the boundary conditions in the formulated problem. In practice, the expressions for the temperature and heat flux responses were truncated by limiting the number of term in the infinite series to 40 in order to balance the prediction accuracy and calculation speed.

(3) Multiple K-type thermocouples were attached to the PDC cutter at different locations to measure the thermal responses during rock cutting tests. Repeated tests were performed to reduce the influence of noise and accurately capture the temperature responses of the cutter. Closer locations to the rock-cutter interface, i.e., the cutting edge, were found to result in higher temperatures.

(4) All the process parameters for the analytical solution were calibrated and determined to achieve the best match between the predictions and the experimental data. The required material parameters for the analytical solution were found from the literature, while the boundary conditions were evaluated based on experimental data.

(5) The formulated problem was found to accurately capture the temperature responses at different locations on the PDC cutter during experimental conditions, based on the comparison between the analytical solutions and experimental data. Therefore the proposed governing equation with defined boundary conditions appears a promising method to expose the intrinsic mechanisms of the thermal phenomena at the rock-cutter interface during rock cutting.

(6) A two-dimensional finite element model was built with the boundary conditions identical to the formulated heat transfer problem. The simulation results further verify the accuracy of the analytical solution.

(7) The general form of the formulated problem and its solution is valuable to be exploited as a foundation for the formulation of more realistic problems based on further experimental evidence on the temperature responses at the rock-cutter interface. A new type of micro temperature sensors is currently being developed with the capability of temperature measurements within the PDC in areas adjacent to the cutting edge. Such a capability will enable more accurate evaluations of the formulated problem.

Chapter 8

Tuned Criticality in Rock Shearing

Shearing is the most widely exploited method to fracture and remove rock formations in many man-made rock opening activities. During shearing, rock breaks into chips due to the periodic nucleation, propagation, and coalescence of numerous micro-cracks. The crack interactions along with the rock's complex physical properties lead to extreme challenges in reaching a consensus on the rock's failure behavior in shearing. In this chapter, force-drop events, as a quantitative measure of the global rock breakage occurrence, were recorded and analyzed. A clear power-law distribution with a tunable cut-off between the frequency of the force-drop events and their magnitudes is shown. The obtained results, for the first time, reveal the rock's tuned critical behavior in shearing that is intrinsically similar to its failure behavior widely observed in earthquakes.

The organization of this chapter is as follows: Section 8.1 will give an overview of self-organized critical and tuned critical systems. Section 8.2 will offer evidence of the rock's critical behaviors from the dynamic force responses in rock shearing, followed by a further explanation of the rock's tuned critical behaviors in Section 8.3. Finally, some discussion will be given in Section 8.4.

8.1 Self-organized critical vs. tuned critical

Many complex dynamical systems with extended degrees of freedom and high levels of non-linearity tend to robustly evolve into a certain critical state without fine tuning of control parameters. In other words, these systems are capable of self-organizing into critical structures of states following certain power law spatial and/or temporal correlation functions. This property of dynamical systems is widely referred to as self-organized criticality.

The SOC behavior in dynamic systems was firstly illustrated by Bak et al. in 1987 in explanation of the 1/*f* noise which had been widely observed in nature (Bak et al., 1987). A famous sand pile model was developed in their work. The sand particles were modeled as identical cubes with unit lengths along the *x*-, *y*- and *z*-directions. The toppling of the sand pile was governed by the following algorithm:

Any site with the coordinates (*x*, *y*) satisfying:

$$z(x, y) \geq 4 \tag{8.1}$$

is unstable and can topple by sending one of its particles to each of its 4 adjacent sites, i.e.:

$$z(x, y)_{new} = z(x, y)_{old} - 4 \tag{8.2}$$

$$z(x \pm 1, y)_{new} = z(x \pm 1, y)_{old} + 1 \tag{8.3}$$

$$z(x, y \pm 1)_{new} = z(x, y \pm 1)_{old} + 1 \tag{8.4}$$

The toppling cascades continuously until no site satisfies Eq. (8.1) any more, which was defined as an avalanche event. Figure 8.1 illustrates a schematic of the sand pile model. The affected area of the sand pile and its frequency in the avalanche event was found to follow a power-law

distribution as shown in Fig. 8.2 (a). Similarly, as seen in Fig. 8.2 (b), the time duration of the avalanche events and their frequency also followed a clear power-law distribution.

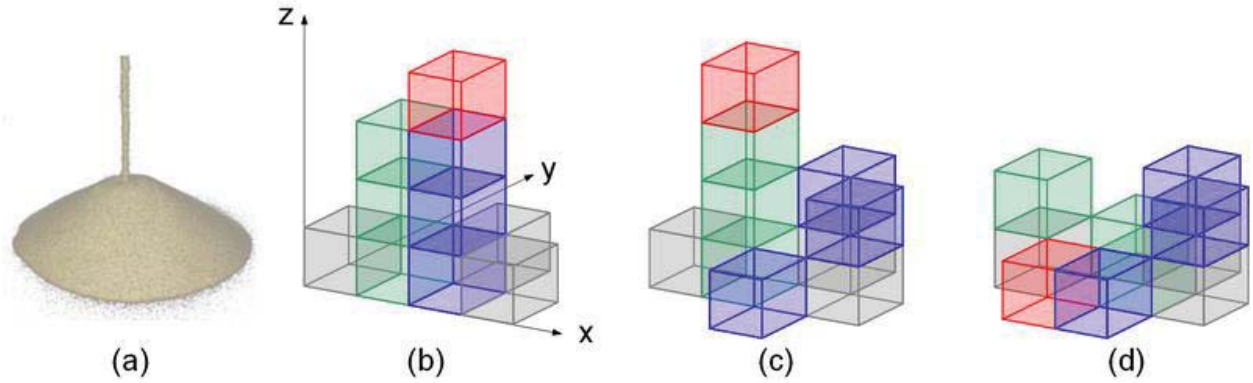

Figure 8.1: Schematic of the sand pile model developed by Bak et al. (Adapted from (Araújo, 2013)): (a) picture of sand pile; (b) one site satisfies the toppling criterion; (c) particles are sent to the adjacent sites triggering the toppling event on the other site; (d) another toppling event is finished.

Since the sand pile model was developed, SOC phenomena have been universally observed in earthquakes (Geller et al., 1997), glacier calving (Åström et al., 2014), forest fires (Malamud et al., 1998), neural networks (Massobrio et al., 2015), crystal plasticity (Dimiduk et al., 2006), brittle fragmentation (Oddershede et al., 1993), intermittent slip failure phenomena (Uhl et al., 2015), micro-fracturing in inhomogeneous materials (Zapperi et al., 1997), etc.

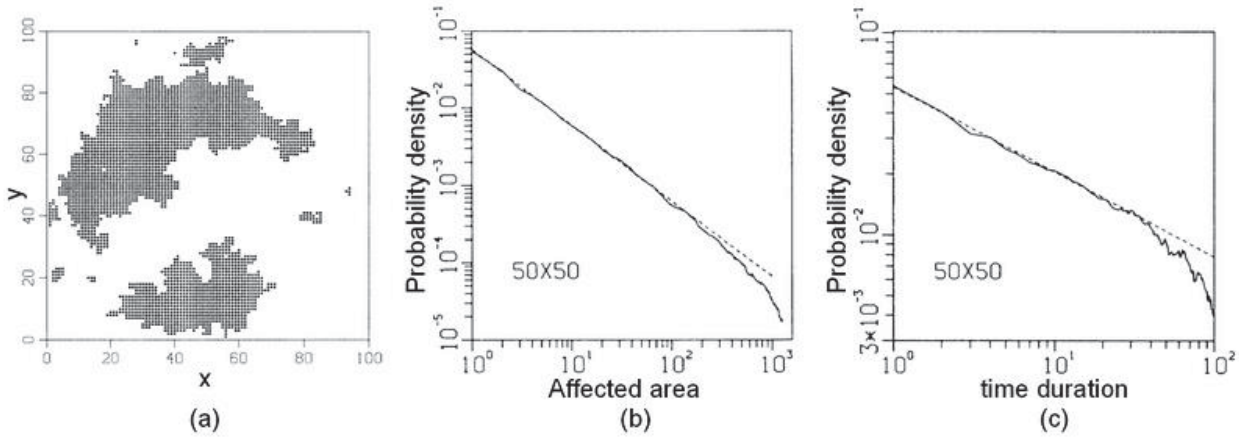

Figure 8.2: Results of the sand pile model: (a) affected area after an avalanche event; (b) distribution of affected area; (c) distribution of time duration. (Adapted from (Bak et al., 1987))

Zapperi et al. developed a numerical model to simulate the formation and propagation of microfractures in inhomogeneous materials subjected to an external elastic stress. The energy emission in avalanches of bond failures in the model was captured and found to follow a power-law distribution as shown in Fig. 8.3, which indicates that SOC phenomena exist in brittle materials' micro-fracturing processes. In addition, nickel microcrystals were also found to behave as a SOC system in the complex dislocation processes by Dimiduk et al. (Dimiduk et al., 2006). They measured the displacement of the microcrystals of pure Ni during compression tests performed with a nano-indenter and found that the slip events and their frequency follow a power-law distribution, as shown in Fig. 8.4. The dislocation motion was concluded to be governed by a scale-free SOC process.

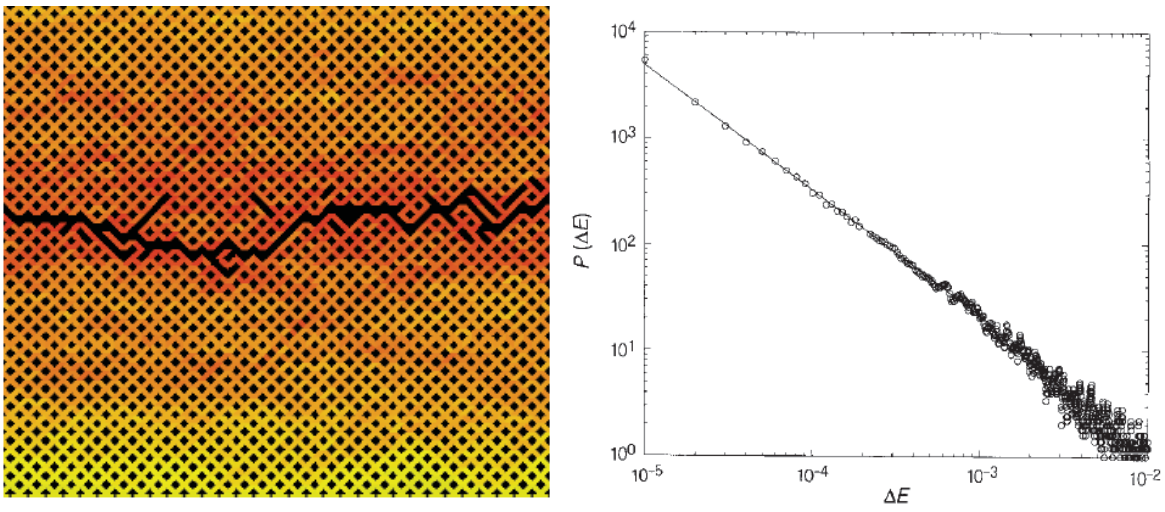

(a) (b)

Figure 8.3: SOC phenomena in micro-fracturing of brittle materials: (a) crack propagation in the numerical model; (b) the distribution of energy emissions. (Zapperi et al., 1997)

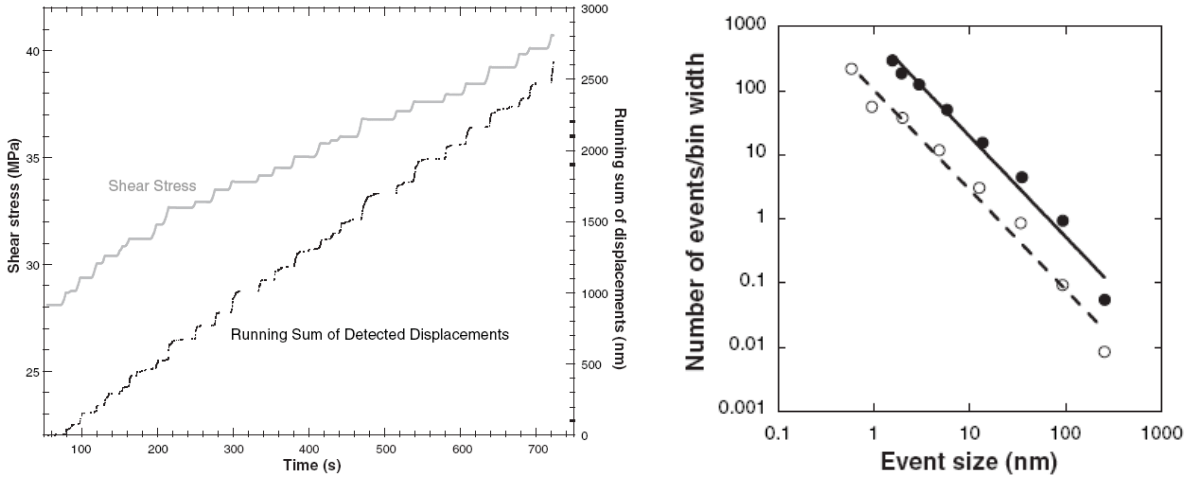

(a) (b)

Figure 8.4: Scale-free intermittent flow in the compression tests of nickel microcrystals: (a) shear and detected displacements vs. time; (b) distribution of slip events. (Dimiduk et al., 2006)

However, many other dynamical systems follow a power-law distribution only in a certain scaling range but exhibit exponential cut-offs at the tail of the distribution. Since cut-offs are usually influenced by loading conditions, these systems are referred to as tuned critical systems. Recently, the distributions of intermittent slips occurring in the deformation of many materials such as bulk metallic glasses (Antonaglia et al., 2014), single crystals (Friedman et al., 2012), granular materials (Dahmen et al., 2011) and even the Earth were found to universally follow a power-law with an exponential cut-off rather than a pure power-law (Uhl et al., 2015). The cut-off changes with the loading conditions indicating that a tuned critical behavior rather than the typical SOC behavior exists in these complex dynamical systems.

8.2 Dynamic force responses in linear rock cutting tests

Although the averaged force responses presented in Chapter 4 exhibit significant behaviors of the rock failure process in linear cutting tests, an understanding of the system's dynamic behavior is still missing. In this section, the dynamic behavior of the system will be exposed by analyzing the force responses in the frequency domain instead of in the time domain.

In a manner similar to the averaging algorithm illustrated in Fig. 4.9, the time-domain cutting force data was sampled, filtered and recorded within a specific sampling period. The sampling rate used in this work is 20 kHz and the low-pass filter's cut-off frequency is 300 Hz. Two examples of the derived time-domain cutting force data can be seen in Fig. 8.5(a) and Fig. 8.6(a) respectively.

The Fast Fourier Transform (FFT) function was exploited for the following frequency analysis of the cutting force signal. Before the FFT, a Hann (or Hanning) window was applied to the time-domain signal to minimize the effect of spectral leakage during the FFT process, i.e.:

$$x_{n-win} = x_n \times w_n \tag{8.5}$$

where x_n is the original time-domain cutting force signal, $x_{n\text{-}win}$ is the force signal after applying a Hann window, and w_n is the Hann window coefficient defined by:

$$w_n = \frac{1}{2}\left(1 - \cos\left(\frac{2\pi n}{N-1}\right)\right) \tag{8.6}$$

where N is the total number of the samples in x_n. After that, the discrete Fourier Transform (DFT) of the cutting force signal after applying the Hann window was derived by the Fast Fourier Transform (FFT) function in the MATLAB programming environment. The formula relating the DFT to the time-domain signal can be given by:

$$X_k = \sum_{n=0}^{N-1} x_{n-win} e^{-i2\pi k \frac{n}{N}} \tag{8.7}$$

where X_k is the DFT of $x_{n\text{-}win}$, and k is an integer ranging from 0 to N-1. The two-sided power spectrum density (PSD) of the signal, i.e., S_{AA} can be then derived by scaling the derived X_k as follows:

$$S_{AA}(k) = \frac{|X_k|^2}{N^2} \cdot \frac{1}{\Delta f \cdot NPBW} \tag{8.8}$$

where *NPBW* is the noise power bandwidth of the Hann window with the value of 1.5, Δf is the frequency resolution defined by:

$$\Delta f = \frac{F_s}{N} \tag{8.9}$$

where F_s is the sampling rate of 20 kHz. In this way, the PSD distribution of the cutting force signal in the frequency domain can be calculated.

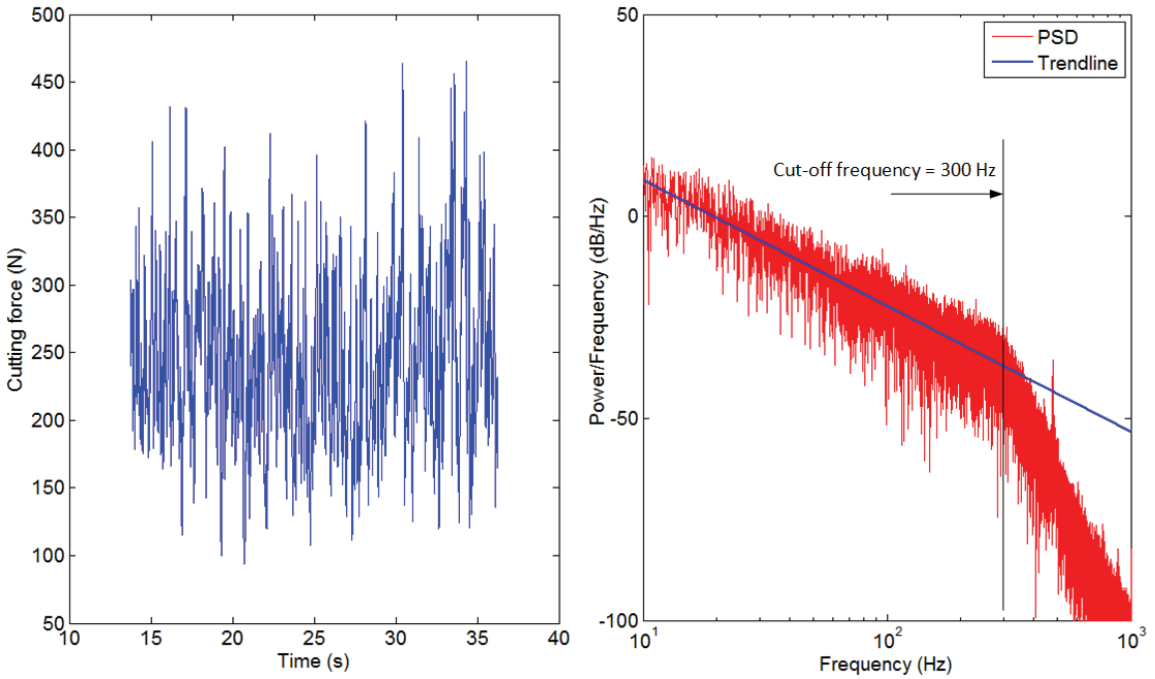

(a) (b)

Figure 8.5: The time-domain cutting force data (a) and its power spectrum density distribution (b) in cutting of Indiana limestone with a 4.2 mm/s cutting speed, a 15° rake angle and a 0.6 mm depth of cut.

According to Fig. 8.5(b) and Fig. 8.6(b), there are no obvious peaks in the PSD distribution. This implies that rock does not break at certain characteristic frequencies. Moreover, the PSD distribution is linearly proportional to the frequency in a log-log space below the cut-off frequency of 300 Hz, i.e.:

$$10\log_{10}\left(S_{AA}(f)\right) = \alpha_0 - \alpha_1 \log_{10} f \tag{8.10}$$

where f is the frequency variable, and α_0 and α_1 are two constants for each given cutting force signal. The form change of Eq. (8.10) gives the power-law distribution of the PSD in the frequency domain, i.e.:

$$S_{AA}(f) \propto \frac{1}{f^{\alpha_1}} \tag{8.11}$$

Based on Eq. (8.11), the cutting signal can be defined as a signal close to $1/f$ noise or pink noise with the definition given in (Halley and Kunin, 1999) regardless of the process parameters and rock types. From the dynamical perspective, the findings indicate that the rock's failure process is essentially near a critical state governed by a certain stochastic mechanism. The theoretical explanation of the above-observed power-law distribution in the dynamic force responses in the frequency domain will be discussed in detail from the physical point view in the next section.

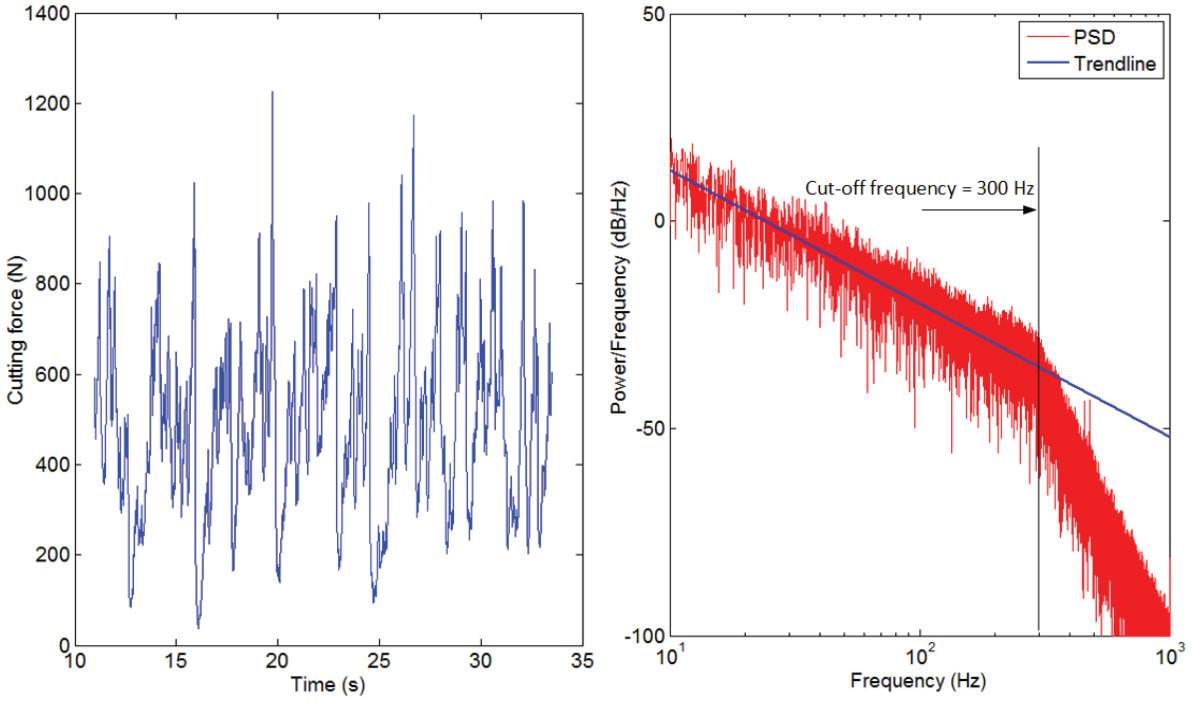

(a) (b)

Figure 8.6: The time-domain cutting force data (a) and its power spectrum density distribution (b) in cutting of Austin chalk with a 4.2 mm/s cutting speed, a 25º rake angle and a 2.4 mm depth of cut.

8.3 Characterization of tuned critical phenomena in rock shearing

In the previous section, the cutting force was found to behave like a $1/f$ noise in the frequency domain. In fact, the $1/f$ noise (also called flicker noise, or pink noise) is not a noise but a reflection of the intrinsic dynamics of dynamical systems at or near a critical state (Bak et al., 1988). Therefore, according to the dynamic force responses, a tuned critical behavior can plausibly exist in rock shearing, i.e., linear rock cutting tests.

In this section, we postulate that rock fails as a dynamical system and attempt to correlate local micro-fractures and global rock breakage in a statistical way, an approach that is generally used in

studying the scaling behaviors of intermittent slips of geological materials or of the Earth under slowly applied loads. In fact, the complex sliding and/or brittle fracture of the Earth's crust along local faults results in global avalanche events, i.e., earthquakes, which are, in principle, quite similar to the aforementioned rock shearing processes. The experimental evidence to be presented below illustrates a scale-free similarity between the rock's failure behavior in nature and those in man-made rock opening practices.

Table 8.1: Loading conditions for the tests.

Test Set	Cutting speed (mm/s)	Depth of cut (mm)	Rake angle (°)	Rock type	Times repeated
1	4.2	0.8	15	Austin chalk	3
2	4.2	2.4	15	Austin chalk	3
3	4.2	0.8	25	Austin chalk	3
4	4.2	2.4	25	Austin chalk	3
5	4.2	0.6	15	Indiana limestone	3
6	4.2	1.4	15	Indiana limestone	3
7	4.2	0.6	25	Indiana limestone	3
8	4.2	1.4	25	Indiana limestone	3

8.3.1 Linear rock cutting tests

The linear rock cutting tests were performed on the LRCT described in Chapter 4. As listed in Table 8.1, eight sets of linear shearing tests were conducted to provide experimental evidence for this work. For each set, three repeated tests were performed to minimize experimental errors. Before each test, the rock block was first clamped by the vice and pre-flattened by the cutter to a certain horizontal level. At the beginning of each test, the cutter was driven along the *z*-direction to achieve a specific depth of cut as shown in Fig. 8.7(a). Then the rock was dragged towards the cutter along the *x*-direction at a constant cutting speed with a user-defined value. The force responses were captured by the dynamometer at a 20 kHz sampling rate, while the chip formation

phenomena were monitored by the high speed camera at a 4,000 fps sampling speed and a 1280x1024 resolution.

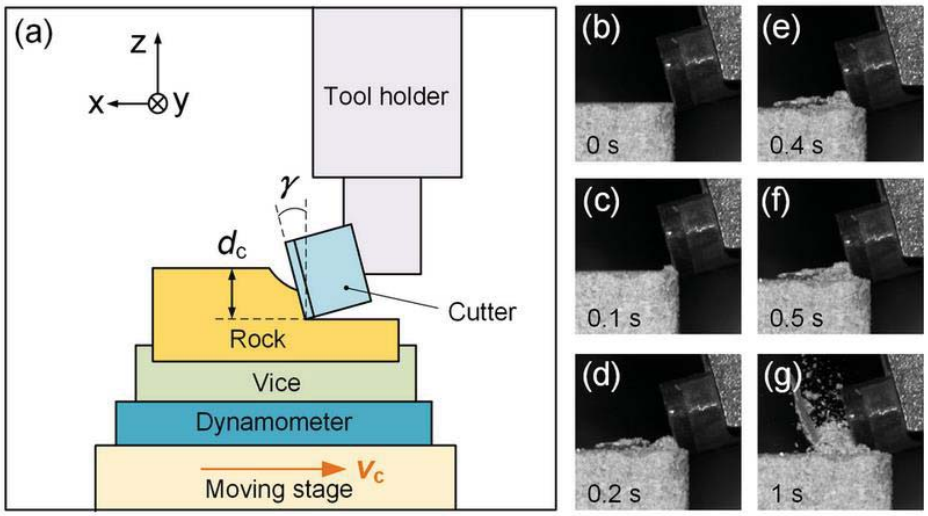

Figure 8.7: Testbed schematic and a detailed example of rock's failure phenomena derived in Indiana limestone cutting with 4.2 mm/s cutting speed, 15° rake angle and 1.4 mm cutting depth.

To further reduce the environmental noise, the force responses were filtered through a digital low-pass filter with a cut-off frequency of 300 Hz. The schematic of the testbed and the rock's failure process recorded by the high speed camera were illustrated in Fig. 8.5. The cutter starts to engage with the rock as seen in Fig. 8.7(b). And then, a small volume of power-like rock chips start to separate from the virgin rock and flow along the cutter's rake face as shown in Fig. 8.7(c). Figures 8.7(d-f) illustrates the continuous formation and accumulation of chips in front of the cutter. Finally, a big chunk-like chip is suddenly formed with many other power-like chips in Fig. 8.7(g).

8.3.2 Characterization of force-drop events

Since the rock is moving along a single direction, i.e., *x*-direction in all the reported tests, the cutting force, F_c, i.e., the force component along the *x*-direction was considered as the exclusive indicator of the total energy input by the cutter during the shearing tests. Therefore, only the response of F_c was monitored and investigated in the reported tests.

As shown in Fig. 8.8, the cutting forces rapidly increase right after each repeated test starts and oscillate randomly along the linear trajectory during the whole shearing process until the end of the test. To keep the sampling conditions consistent, the sampling of the force data starts 4.5 s after the shearing test starts and continues for 22.5 s for all the repeated tests.

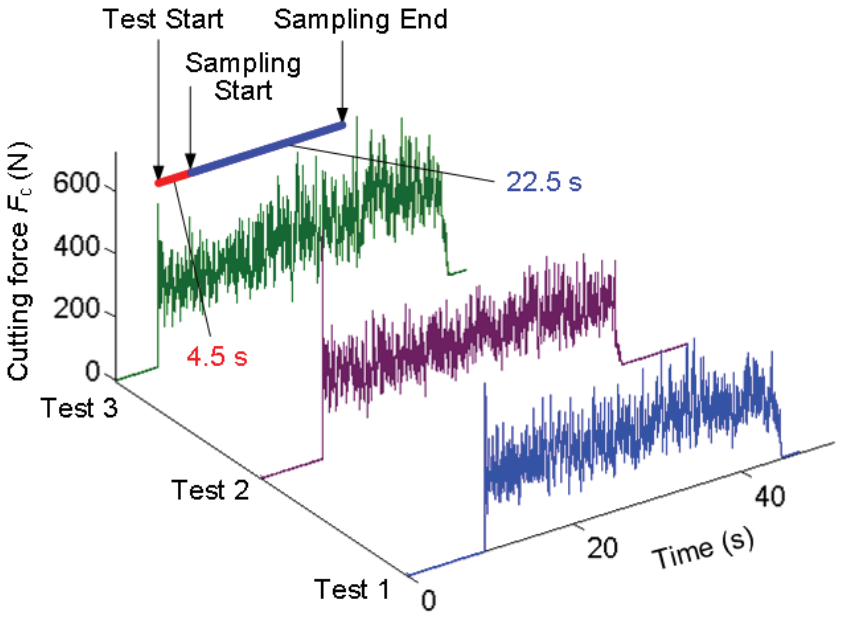

Figure 8.8: Cutting force responses in three repeated tests in shearing Indiana limestone with a 4.2 mm/s cutting speed, a 15° rake angle and a 0.6 mm depth of cut.

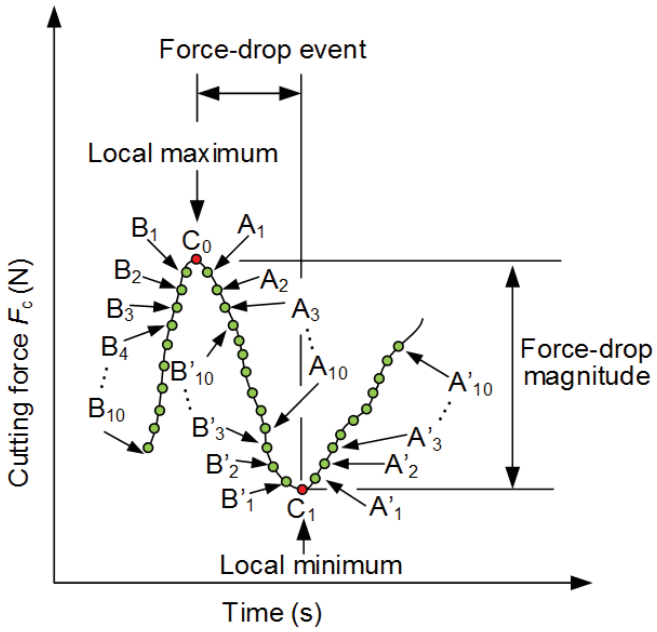

Figure 8.9: Algorithm for the force-drop magnitude calculation.

As defined in Fig. 8.9, a force-drop event starts from a local maximal force to the following local minimal force next to it. We searched and determined all the local maximal and minimal forces from the previously sampled force data by using a MATLAB program. The sampled force data is discrete with a constant time interval of 0.05 ms between two adjacent data points. The fundamental algorithm is to compare the force value at a candidate data point with 20 points in its neighborhood. The program will regard a force value at the candidate data point as a local maximal (or minimal) force if it is larger (or smaller) than those at all the adjacent points. For instance, as shown in Fig. 8.9, C_0, as the candidate point will be compared with 10 points before it (i.e., B_1, B_2, …, B_{10}) and 10 points after it (i.e., A_1, A_2, …, A_{10}). Since the force value at C_0 is higher than at the other 20 points adjacent to it, the force value at C_0 will be considered as a local maximum. Similarly, the force value at C_1 will be recorded as a local minimum which is adjacent to C_0.

Therefore, the force response process from C_0 to C_1 can be defined as a force-drop event. The force-drop magnitude can be calculated by subtracting the force value at C_1 from that at C_0.

8.3.3 Results

The rock's continuous failure in shearing leads to the oscillations in the cutting force F_c, i.e., the force component along the x-direction as seen in Fig. 8.10(a). In fact, a rapid decrease in F_c, i.e., a force-drop event as defined in Fig. 8.10(b), is attributed to a global rock breakage occurrence, as a consequence of the interactions and coalescence of micro-cracks. The magnitude of the force-drop illustrates the level of the corresponding rock breakage event. Thus, force-drop events can be used to quantitatively reflect the rock's failure behavior.

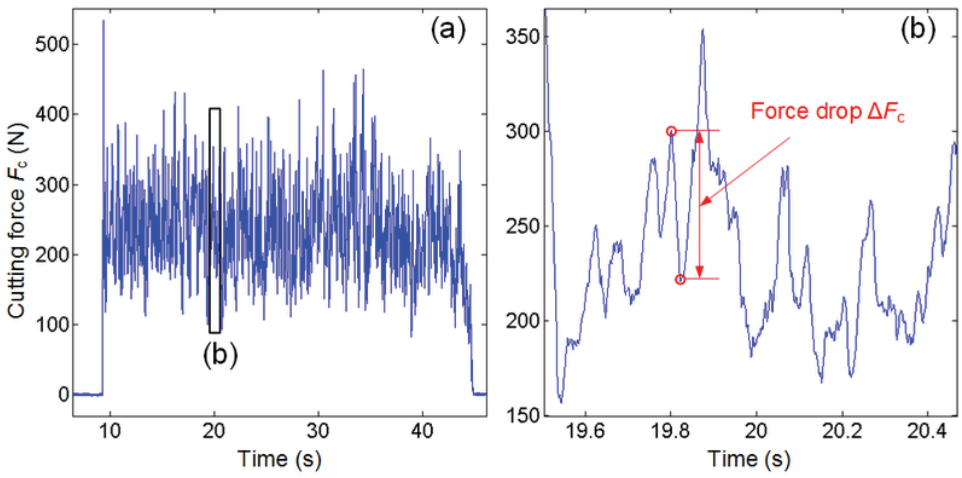

Figure 8.10: Real-time cutting force response and the definition of force-drop events: (a) cutting force F_c obtained in shearing Indiana limestone with v_c = 4.2 mm/s, γ = 15° and d_c = 0.6 mm. A small region of the cutting force response is enlarged in (b).

Since the environmental noise of the dynamometer used is ~ 5 N, the noise threshold of the force-drop events was set to 5 N. For each test set given in Table 8.1, all the force-drop events with a value larger than 5 N are recorded and their magnitudes are sorted into 50 logarithmically spaced bins to estimate their probability distribution (Fig. 8.11). The results show a clear linear trend with a rapid cut-off in the probability distribution of the force-drop events in the log-log space regardless of rock type and loading conditions (i.e., γ and d_c as defined in Fig. 8.7).

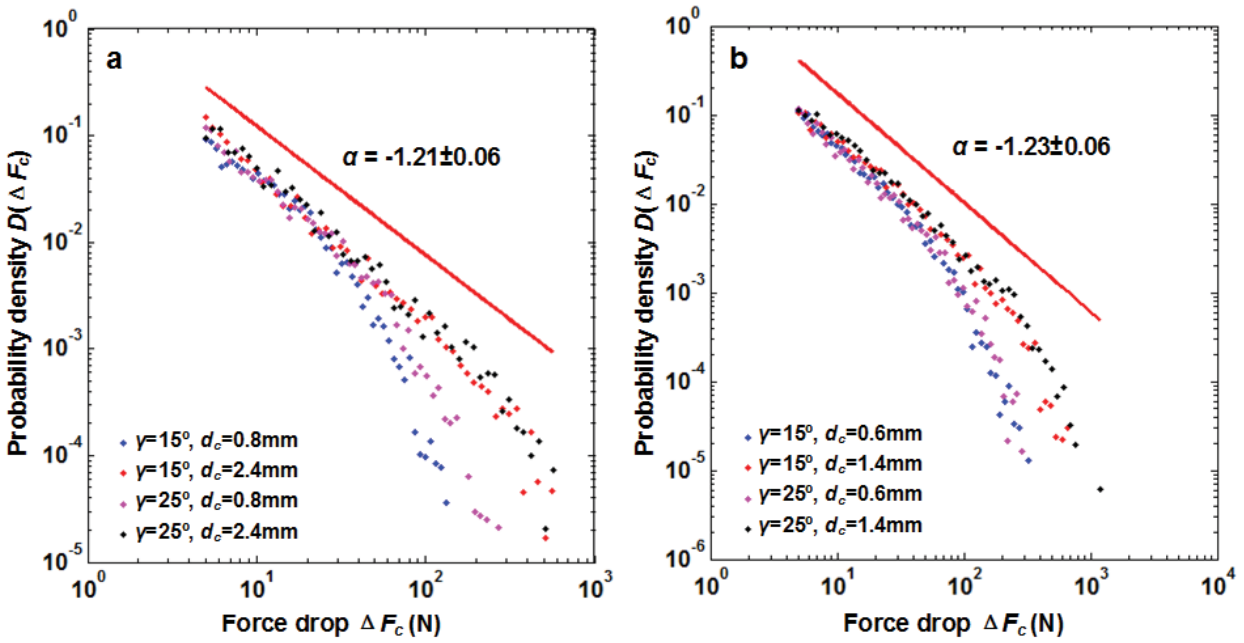

Figure 8.11: Probability density distribution of force-drop events in rock shearing tests: (a) shearing of Austin chalk; (b) shearing of Indiana limestone.

A simple mean field model (Dahmen et al., 2011; Uhl et al., 2015) was adopted to explain and model the rock's tuned critical behavior in shearing. The probability density of the force-drop

events, $D(\Delta F_c)$, can be related to the force-drop magnitude, ΔF_c, with a power-law multiplied by an exponential cut-off, i.e.:

$$D(\Delta F_c) \sim \Delta F_c^{\alpha} e^{-\frac{\Delta F_c}{\beta}} \tag{8.12}$$

where α is the scaling exponent independent of load conditions while β is the cut-off force-drop magnitude dependent on load conditions. The scaling exponent, α, is the slope of the power-law scaling range of $D(\Delta F_c)$ in log-log space. It determines how often large force-drop events may occur in the shearing of rock. The larger α is, the more likely large force-drop events may occur. As shown in Fig. 8.11, α is clearly independent of the loading conditions (γ and d_c) and nearly independent of rock types. β represents the tuned critical behavior of the system. Its value reflects how large the power-law scaling range of $D(\Delta F_c)$ will be. $D(\Delta F_c)$ can approximately follow a power-law ΔF_c^{α} for $\Delta F_c < \beta$ while fall off with an exponential cut-off $e^{-\frac{\Delta F_c}{\beta}}$ for $\Delta F_c > \beta$. The increase of β indicates the extension of the power-law scaling range.

Based on Eq. (8.12), β was determined by fitting all the force-drop data with a pre-determined α (as illustrated in Fig. 8.12) using the non-linear least squares method. β largely increases with the increase of d_c but changes only very slightly with γ. In rock shearing, the increase of d_c leads to more intensive interactions between the micro-cracks in the rock and to the more frequent generation of bigger rock chips. On the other hand, the change of γ has very limited effect on micro-crack interaction intensity. Hence, one can conclude that an increase in micro-crack interaction intensity leads to an increase in the power-law scaling range of $D(\Delta F_c)$.

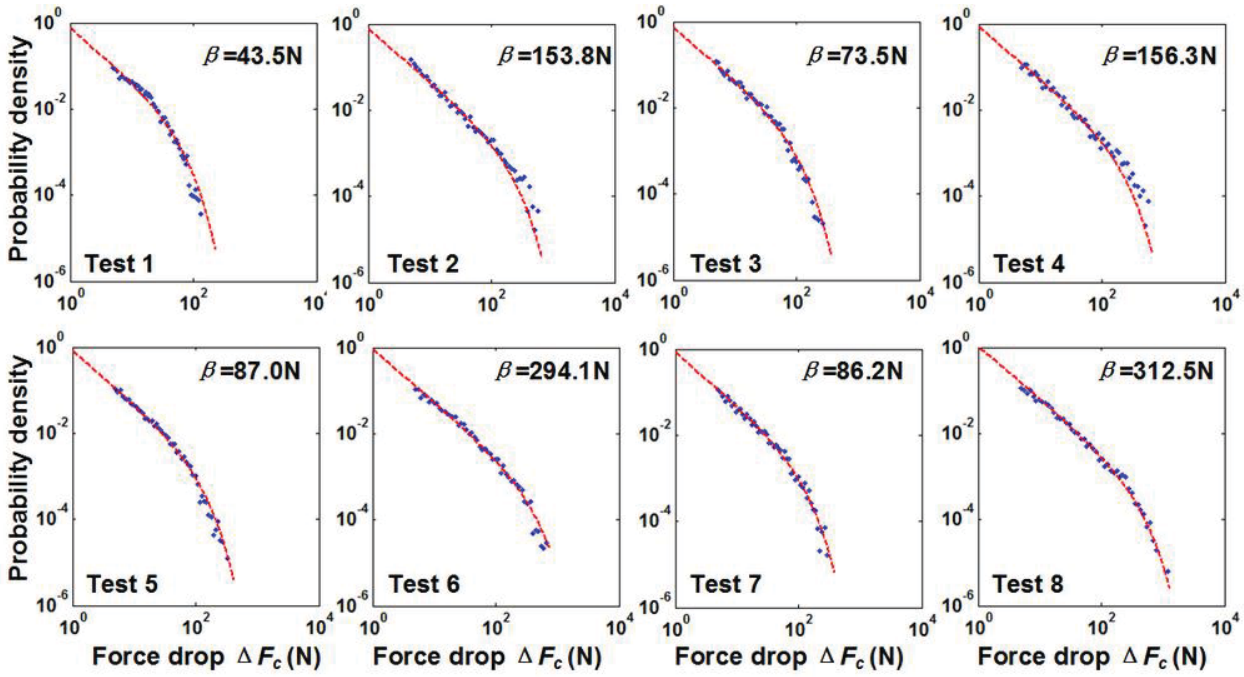

Figure 8.12: Probability density distribution of force-drop events in 8 sets of linear cutting tests.

8.4 Discussions

Since the late 1950s, tremendous efforts have been devoted to obtaining insights into the rock's failure behavior in shearing. Rock is widely believed to fail in two fragmentation modes, i.e., crushing and chipping (Mishnaevsky, 1995). Crushing creates highly fractured small rock fragments in the form of powder-like chips (Fig. 8.13(a)), while chipping initiates and propagates cracks to form big rock fragments, i.e., chunk-like rock chips (Fig. 8.13(c)). Some researchers believe that the crushing and chipping modes work independently (Evans, 1962; Hood and Alehossein, 2000), while others agree that the crushing mode initiates cracks first which then triggers the chipping mode (Guo et al., 1992; Yilmaz et al., 2007). According to fracture mechanics, the chipping and crushing modes have been attributed to different reasons, e.g., tensile

(Liu et al., 2007), shear (Nishimatsu, 1972), or tensile-shear hybrid fractures (Loui and Rao Karanam, 2012).

Recent studies suggest that rock breaks due to the complex interactions of many micro-cracks generated under tensile stresses (Healy et al., 2006; Reches and Lockner, 1994), indicating that the crushing and chipping modes are identical in principle but different only in the geometry of the formed chips as illustrated in Fig. 8.13. However, a scientific consensus on how numerous micro-cracks interact, coalesce and lead to global rock breakage is still missing. In addition, the rock's mechanical properties such as internal friction have also been found to change with loading conditions (Yamashita et al., 2015), which makes the understanding of the failure process even more ambiguous.

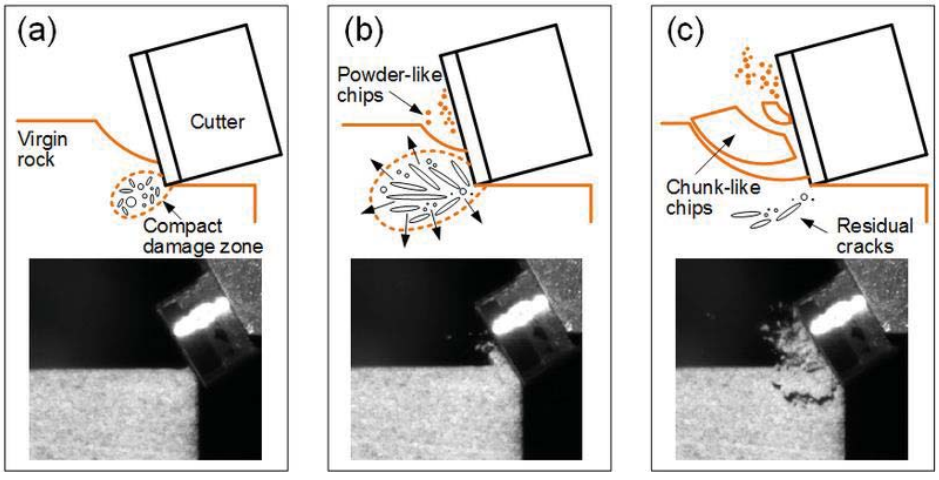

Figure 8.13: Rock failure mechanisms in shearing.

Based on the experimental evidence presented in Section 8.3.3, a new explanation of the rock's failure process in shearing can be drawn from the perspective of dynamical systems. During rock

shearing, the interactions and coalescence of numerous cracks lead to the rock's highly nonlinear failure behavior and to the large number of degrees of freedom of the rock system. Moreover, the crack propagation speed in the rock can reach up to ~ 10^3 m/s while the cutting speed in the reported tests is ~ 10^{-3} m/s, which provides a sufficiently long time to allow the complex dynamical system of the rock, consisting of many micro- and macro-cracks, to evolve into a critical or near critical state. In other words, each force-drop event can be considered to be independent of the other force-drop events. The power-law scaling range of the force-drop distributions at small force-drop sizes indicates that rock behaves in a near critical way, which is similar to the rock's stick-slip behavior observed in earthquakes. In earthquakes, the sliding of the Earth's crust drives the propagation and coalescence of the faults to evolve into a critical state. Similarly, the shearing motion in the reported tests provides the driving force for the nucleation, propagation and coalescence of micro-cracks. The tuned critical phenomena observed in both the reported tests and in earthquakes indicate that the rock's failure behaviors follow a power-law with a tunable cut-off that changes with the loading conditions in both nature and man-made opening activities.

Chapter 9

Summary and Future Directions

This chapter summarizes the findings and ideas presented in this work. The major conclusions and contributions of this dissertation will be given in Section 9.1, followed by a brief discussion on the future directions for research on rock cutting mechanics/process optimization in Section 9.2.

9.1 Summary

Shearing is regarded as one of the most efficient and widely used mechanisms in rock fragmentation practices. Polycrystalline diamond compact (PDC) cutters, as a major shearing tool, have been widely applied in oil and gas drilling processes. The understanding of the complex interactions along with the mechanical/thermal/dynamical responses occurring at the rock and cutter interfaces is essential for the advancement of future drilling technologies, yet, these interactions are still not fully understood. This thesis presents a comprehensive study of the rock-cutter interactions during rock shearing mainly performed with a single PDC cutter, aiming to obtain in-depth insights into the rock cutting mechanics. The obtained knowledge can also be applied to the shearing processes conducted by other cutting tools.

The major contributions of this dissertation are summarized as follows:

(1) Two rock cutting testbeds, namely rock face turning testbed (RFTT) and linear rock cutting testbed (LRCT) have been developed to achieve rotational and simplified linear cutting motions between the rock and a single PDC cutter respectively under well-controlled

laboratory conditions. The RFTT has been utilized to study the mechanical and thermal responses at the tool-cutter interfaces during rotational cutting motions using a 3-component piezoelectric force sensor, five K-type thermocouples, and a tri-axial piezoelectric accelerometer for force, temperature and acceleration measurements respectively. To gain an intrinsic understanding of the process, simple linear cutting was achieved on the LRCT. The LRCT is capable of force and vibration measurements using a 3-component piezoelectric force dynamometer and three unidirectional accelerometers. Moreover, a high speed camera was configured to visually capture the chip formation phenomena at the rock-cutter interface so as to provide essential experimental evidences for the subsequent explanations of rock failure behaviors in cutting.

(2) A full-factorial design of experiments was conducted on the RFTT to investigate how the process parameters, i.e., rake angle, depth of cut, and feedrate influence the force responses when using PDC cutters in face turning of Indiana limestone. For shallow cuts (i.e., depth of cut < 1 mm), the feedrate and depth of cut have been found to be linearly related to the force responses, while the rake angle exerts a highly non-linear influence on the force responses. Based on the experimental data, a phenomenological force model has been developed to illustrate the force responses in terms of four components: the shearing force used to fracture the rock, the friction force occurring at the cutter's flank face, the ploughing force at the cutting edge, and the lateral force on the lateral surface of the cutter.

(3) To further investigate the cutting mechanics involved at the rock-cutter interface, a comprehensive experimental investigation has been performed on the LRCT. The influences of the depth of cut, rake angle, cutting speed and rock type on chip formation and force

responses were discussed. The chipping failure was intensified with an increase in the depth of cut and the rock's uniaxial compressive strength (UCS), leading to an increase in chip size. The magnitude of the force responses increases with an increase in the depth of cut, rake angle and the rock's UCS, but is independent of the cutting speed except for extremely high values. The relation between force responses and the depth of cut is non-linear for a wide range of depths of cut but can be approximated by a linear trend at shallow cuts.

(4) According to the above-mentioned experimental evidences, a cutting theory has been developed to analytically explain the rock removal mechanisms and the loading force responses in orthogonal cutting of rock. The rock removal mechanisms proposed includes two modes, i.e., crushing and chipping failure modes. Crushed and powdery chips are attributed to the crushing mode while chunk-like chips are formed due to the chipping mode. Rock fails due to compressive failure in the crushing mode, while due to tensile failure in the chipping mode. In comparison with the experimental results, the force model shows the capability of accurately capturing the non-linear relationship between the loading and the depth of cut for a range of rake angles.

(5) A finite element model has been formulated to simulate the chip formation and loading force responses in two-dimensional orthogonal rock cutting. The Drucker-Prager material model was used to define the material properties of the rock, while the cutter was defined as a rigid body. Both chipping and crushing modes have been observed in the simulation, which match the experimental tests very well. The force responses were observed to dramatically oscillate in the simulations. The time-averaged force difference is less than 20% between the simulations and experiments. Furthermore, the model has been extended to a 3D model to

simulate three-dimensional face turning of rock. The simulations qualitatively capture the force responses obtained in the experiments.

(6) The heat transfer phenomenon in the PDC cutter during rock cutting has been investigated. Given the experimental results, an analytical model has been developed to describe how the heat transfers into and out of the PDC cutter. All the process parameters for the analytical solution were calibrated and determined to well predict the temperature responses at different locations on the PDC cutter during rock cutting. In addition, a two-dimensional finite element model was built to verify the accuracy of the analytical solution. The analytical solution is valuable to be exploited as a foundation for the formulation of more realistic problems based on further experimental evidence on the thermal responses at the rock-cutter interface.

(7) The dynamical behavior of the cutting forces in linear rock cutting was investigated in the frequency domain. No clear peaks were found in the power spectral density distributions. The sampled cutting force signals were close to $1/f$ noise by definition, indicating that the rock's failure behaviors may be governed by certain stochastic mechanisms. Based on the experimental results, a new explanation of the rock's failure process in shearing was drawn from the perspective of dynamical systems. The force responses were carefully characterized to present the force-drop events, i.e., the rapid drop in the force magnitude. These force-drop events and their frequency have been found to be related by a clear power-law distribution with an exponential cut-off, indicating that the rock system is a tuned critical system during the cutting process. In other words, during the cutting process, the rock evolves into certain critical states governed by a power-law distribution with a tunable cut-off.

9.2 Future directions

The fundamental understanding of the rock-cutter interactions during intensive cutting processes has been investigated in this work. Future work should focus on three major aspects: (1) development of a thermo-mechanical coupled cutting theory; (2) further validation of the analytical and numerical models using advanced sensing technology; (3) advances in numerical simulations, and (4) pragmatic enhancement of rock cutting processes.

9.2.1 Thermo-mechanical-coupled modeling

The cutting theory developed in Chapter 5 and the temperature response model formulated in Chapter 7 should be combined to comprehensively describe the thermo-mechanical coupled responses at the rock-cutter interface.

In metal cutting processes, heat generation is largely dependent on the plastic deformation of the workpiece in the shear zone, or the primary and the secondary deformation zones on the rake face (Boothroyd and Knight, 1989). However, in rock cutting, plastic deformation is rarely observed which indicates that heat generation is largely due to friction at the rock-insert interfaces. Friction in two zones should be taken into account, i.e., the friction between the chip and the insert at the rake face as the primary friction zone and friction between the rock and the insert at the flank face as the secondary friction zone.

As shown in Fig. 9.1, the heat generated due to friction can be expressed by (Halling, 1976):

$$q_1 = \mu_1 F_R V_{chip} \tag{9.1}$$

$$q_2 = \mu_2 F_0 V_c \tag{9.2}$$

where q_1 is the heat generated at the rake face, q_2 is the heat generated at the flank face, μ_1 is the friction coefficient between the chip and the rake face of the insert, μ_2 is the friction coefficient between the rock and the flank face of the insert, F_R is the normal force exerted at the rake face, F_0 is the initial force exerted at the flank face, V_{chip} is the relative velocity of the chip with respect to the insert along the rake face, and V_c is the relative velocity or the cutting speed of the rock with respect to the insert.

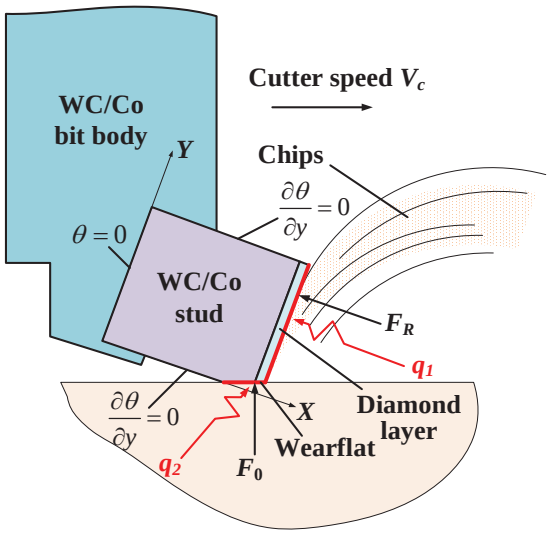

Figure 9.1: Schematic of the thermo-mechanical coupling phenomenon in rock cutting.

The problem of relating the heat transfer model and the force model should be addressed. As a first attempt, the heat generated at the flank face can be ignored. This is the case corresponding to a sharp edge in the absence of a wear-flat. Therefore, the heat transfer model derived in Chapter 7 can be used and q_1 can be assumed to be the total heat generated at the rake face, i.e.:

$$q_1 = \mu_1 R V_{chip} = -k_1 \int_y q(y)dy \tag{9.3}$$

where $q(y)$ is the temperature gradient at the rake face and k_1 is the thermal conductivities of the diamond layer as defined in Chapter 7. μ_1 and V_{chip} can be experimentally determined while F_R can be analytically determined by the force model derived in Chapter 5. Therefore, the heat transfer model is anticipated to be coupled with the force prediction model. After this attempt, a more complex heat generation mechanism should be taken into account, i.e., q_2 should also be added to the boundary condition and more sophisticated expressions for $q(y)$ should be determined and introduced into the thermo-mechanical coupling model as well.

9.2.2 Model validation using micro thin film embedded sensor arrays

As introduced in Chapter 2, micro thin film embedded sensor arrays can realize the measurement of temperature or force responses with a high spatial (50 nm to 50 μm) and high temporal resolution (tens of ns to ms) at and near the insert-rock interface (e.g., within a range of 5 to 50 μm) in bandwidths higher than 100 kHz.

Highly stable and repeatable micro thin film thermocouples (μ-TFTCs) and force sensors (μ TFFSs) are planned to be developed for dynamic and static measurements in various layouts. The sensor materials used must be capable of working under hostile working conditions (high temperature, high strain, thermal shock, thermal fatigue, and mechanical cycling). As an example, a plausible overall sensor layout for an array of μ-TFTCs and a μ-TFFS are shown in Fig. 9.2. A tungsten carbide (WC) piece (layer) will be diffusion bonded to the WC stud to embed and thus protect the thin film connection leads. Initially, eight sensors are being considered close to the cutting edge to be able to measure the temperature field. The theoretical and experimental results from such work could guide the optimal design of sensor layouts.

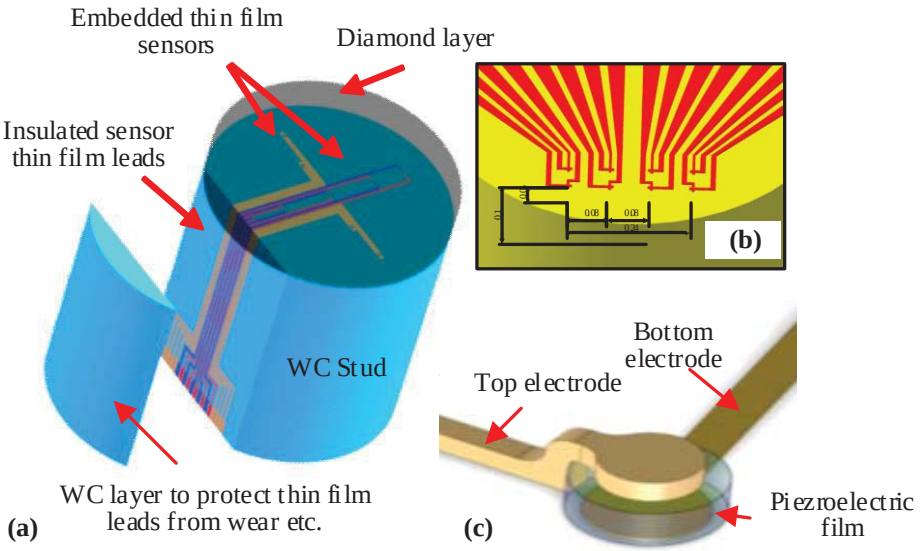

Figure 9.2: Plausible sensor layouts (not to scale): (a) PDC cutter with embedded sensors; (b) enlarged view of the μ-TFTC; (c) enlarged view of the μ-TFFS. (By courtesy of Dr. Xiaochun Li from UCLA)

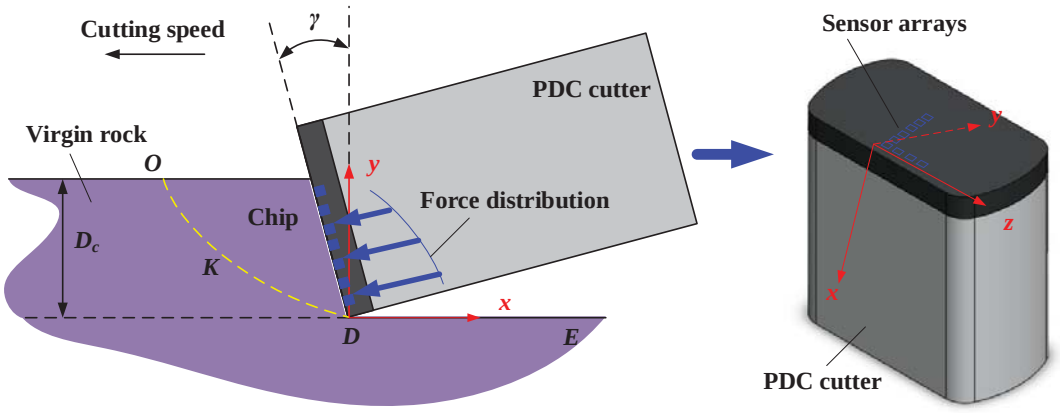

Figure 9.3 Verification of force model using μ-TFFS arrays.

The core capability of the μ-TFES sensor array is to capture in-situ temperature/force/stress at local spots. The array design enables the measurement of temperature and stress distributions in

specific areas on the PDC inserts which is essential to accurately verify thermal/mechanical predictions derived from the proposed models in this work. The experimental verification of models using μ-TFES sensing technique falls into two categories: (1) the verification of the force model as illustrated in Fig. 9.3; and (2) the evaluation of the thermal model as shown in Fig. 9.4.

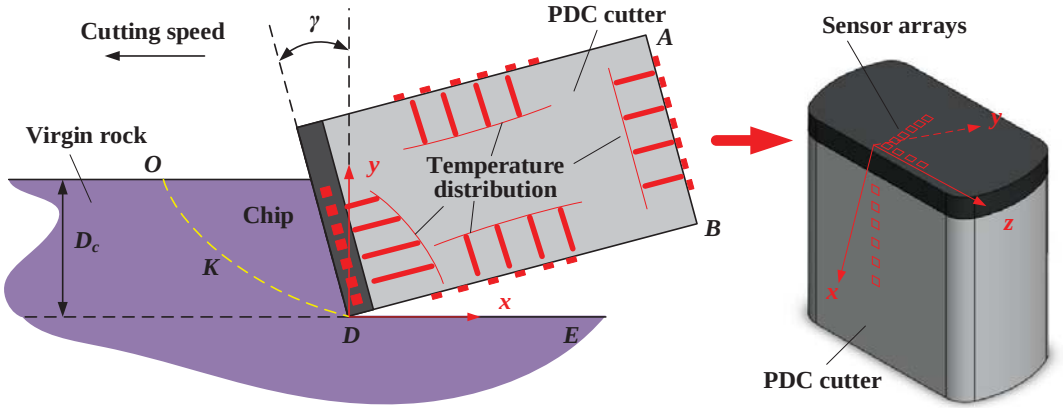

Figure 9.4: Evaluation of thermal model using μ-TFTC arrays.

9.2.3 Advances in numerical modeling

The key to more accurate simulation of rock cutting processes is the utilization of more realistic material models. As shown in Chapter 6, although the simulation provides a qualitative prediction of force responses in rock cutting, the force magnitudes were significantly underestimated in the simulations due to the use of a softer material model as compared to the realistic rock sample. Future work should attempt to model the density and orientation of micro-cracks under the application of varying modes of stresses by using micro-crack based continuum damage models (Shao and Rudnicki, 2000). The occurrence of localization bands should be further extended to model actual rupture as shown in (Rudnicki, 2000). The continuum damage model should be

modified to include a temperature dependent damage evolution and damage based weakening term. Both internal friction and the cutting process should be modeled as sources of heat during the cutting process. The material parameters for this model should be calibrated against the measured profile of cutting forces with time. Moreover, the user-defined material subroutine (VUMAT) should be written for incorporating the above material into finite element simulations. The dynamical force responses from the simulation should be characterized and compared to the experimental results. According to the tuned criticality theory, the distribution of the force-drop events and their frequency obtained from the simulation should be carefully investigated, which is a significant indicator of the prediction accuracy of the cutting dynamics.

9.2.4 Pragmatic enhancement of rock cutting processes

Monitoring and control capabilities are generally highly dependent on sensor response characteristics, size and location. The aforementioned sensor embedding technology is perhaps the closest one that can come to this goal. In future work, sensor arrays should be used to perform a comprehensive performance validation of the sensor bearing PDC cutters in earth strata drilling and formulate real-time process monitoring and adaptive control methods.

Numerous experiments have to be conducted on the developed testbed to test the robustness of the PDC cutters with embedded micro thin film senor arrays. In addition, some other experiments such as impact tests and VTL tests, which are commonly used to test the quality of PDC cutters under industry-accepted testing conditions should also be performed to further evaluate the sensor embedded PDC cutters.

The next step is to develop real-time monitoring and control algorithms for rock cutting processes. Catastrophic failure detection algorithms should be developed to provide alarms related to catastrophic or intolerable events in the process such as cutter breakage, excessive wear, excessive temperature, dramatic force jump, and chatter. Moreover, process control algorithms should be built to offer close-loop feedback to maintain force and/or temperatures at the desired magnitudes by adjusting multiple process parameters such as cutting speed and depth of cut based on the developed theoretical models.

References

Abdelmoneim, M.E., Scrutton, R.F., 1974. Tool edge roundness and stable build-up formation in finish machining. Journal of Engineering for Industry 96, 1258-1267.

Adachi, J.I., Detournay, E., Drescher, A., 1996. Determination of rock strength parameters from cutting tests, 2nd North American Rock Mechanics Symposium. American Rock Mechanics Association, Montreal, Quebec, Canada, pp. 96-1515.

Akbari, B., Butt, S.D., Munaswamy, K., Arvani, F., 2011. Dynamic single PDC cutter rock drilling modeling and simulations focusing on rate of penetration using distinct element method, 45th US Rock Mechanics / Geomechanics Symposium, San Francisco, CA,, pp. 11-379.

Albrecht, P., 1960. New developments in the theory of the metal-utting process: part I. the ploughing process in metal cutting. Journal of Engineering for Industry 82, 348-357.

Aluko, O.B., Seig, D.A., 2000. An experimental investigation of the characteristics of and conditions for brittle fracture in two-dimensional soil cutting. Soil and Tillage Research 57, 143-157.

Amadei, B., Robison, M.J., 1986. Strength of rock in multiaxial loading conditions, The 27th U.S. Symposium on Rock Mechanics (USRMS). American Rock Mechanics Association, Tuscaloosa, AL, pp. 86-0047.

Antonaglia, J., Xie, X., Schwarz, G., Wraith, M., Qiao, J., Zhang, Y., Liaw, P.K., Uhl, J.T., Dahmen, K.A., 2014. Tuned critical avalanche scaling in bulk metallic glasses. Scientific reports 4.

Appl, F.C., Wilson, C.C., Lakshman, I., 1993. Measurement of forces, temperatures and wear of PDC cutters in rock cutting. Wear 169, 9-24.

Araújo, N.A., 2013. Viewpoint: getting out of control. Physics 6, 90.

Åström, J.A., Vallot, D., Schäfer, M., Welty, E.Z., O'Neel, S., Bartholomaus, T., Liu, Y., Riikilä, T., Zwinger, T., Timonen, J., 2014. Termini of calving glaciers as self-organized critical systems. Nature Geoscience 7, 874-878.

Bak, P., Tang, C., Wiesenfeld, K., 1987. Self-organized criticality: An explanation of the 1/f noise. Phys Rev Lett 59, 381.

Bak, P., Tang, C., Wiesenfeld, K., 1988. Self-organized criticality. Phys Rev A 38, 364-374.

Balci, C., 2009. Correlation of rock cutting tests with field performance of a TBM in a highly fractured rock formation: A case study in Kozyatagi-Kadikoy metro tunnel, Turkey. Tunnelling and Underground Space Technology 24, 423-435.

Balci, C., Bilgin, N., 2007. Correlative study of linear small and full-scale rock cutting tests to select mechanized excavation machines. International Journal of Rock Mechanics and Mining Sciences 44, 468-476.

Bazant, Z., Xi, Y., Reid, S., 1991. Statistical size effect in quasi-brittle structures: I. Is Weibull theory applicable? Journal of Engineering Mechanics 117, 2609-2622.

Bazant, Z.P., Xi, Y., 1991. Statistical size effect in quasi-brittle structures: II. Nonlocal theory. Journal of Engineering Mechanics 117, 2623-2640.

Bellin, F., Dourfaye, A., King, W., Thigpen, M., 2010. The current state of PDC bit technology. World Oil 231, 41-46, 53-58, 67-71.

Belytschko, T., Liu, W.K., Moran, B., 2000. Nonlinera finite elements for continua and structures. John Wiley & Sons Ltd.

Beuershausen, C.C., 2004. Multi-aggressiveness cutting face on PDC cutters and method of drilling subterranean formations. Baker Hughes Incorporated, Houston, TX, US.

Bilgesu, I., Sunal, O., Tulu, I.B., Heasley, K.A., 2008. Modeling rock and drill cutter behavior, The 42nd U.S. Rock Mechanics Symposium (USRMS). American Rock Mechanics Association, San Francisco, CA, pp. 08-342.

Block, G., Jin, H., 2009. Role of failure mode on rock cutting dynamics, SPE Annual Technical Conference and Exhibition. Society of Petroleum Engineers New Orleans, Louisiana, pp. 124870-MS.

Boothroyd, G., Knight, W.A., 1989. Fundamentals of machining and machine tools. Marcel Dekker Inc., New York.

Bourgoyne, A.T., Millheim, K.K., Chenevert, M.E., Young, F.S., 1986. Applied Drilling Engineering. Society of Petroleum Engineers.

Brett, J.F., Warren, T.M., Behr, S.M., 1990. Bit whirl - a new theory of PDC bit failure. SPE Drilling Engineering 5, 275-281.

Bruton, G., Crockett, R., Taylor, M., DenBoer, D., Lund, J., Fleming, C., Ford, R., Garcia, G., White, A., 2014. PDC bit technology for the 21st century. Oilfield Review 26.

Byrne, G., Dornfeld, D., Inasaki, I., Ketteler, G., König, W., Teti, R., 1995. Tool condition monitoring (TCM) - The status of research and industrial application. CIRP Annals - Manufacturing Technology 44, 541-567.

Cai, M., Kaiser, P.K., Morioka, H., Minami, M., Maejima, T., Tasaka, Y., Kurose, H., 2007. FLAC/PFC coupled numerical simulation of AE in large-scale underground excavations. International Journal of Rock Mechanics and Mining Sciences 44, 550-564.

Carslaw, H., Jaeger, J., 1959. Conduction of Heat in Solids. The Clarendon Press, Oxford.

Che, D., Ehmann, K., 2013. Polycrystalline diamond turning of rock, ASME 2013 International Manufacturing Science and Engineering Conference, Madison, Wisconsin, USA, pp. MSEC2013-1127.

Che, D., Ehmann, K., 2014. Experimental study of force responses in polycrystalline diamond face turning of rock. International Journal of Rock Mechanics and Mining Sciences 72, 80-91.

Che, D., Ehmann, K., Cao, J., 2015a. Analytical modeling of heat transfer in polycrystalline diamond compact cutters in rock turning processes. Journal of Manufacturing Science and Engineering 137, 031005.

Che, D., Han, P., Guo, P., Ehmann, K., 2012a. Issues in polycrystalline diamond compact cutter-rock interaction from a metal machining point of view - part I: temperature, stresses, and forces. Journal of Manufacturing Science and Engineering 134, 064001.

Che, D., Han, P., Guo, P., Ehmann, K., 2012b. Issues in polycrystalline diamond compact cutter-rock interaction from a metal machining point of view - part II: bit performance and rock cutting mechanics. Journal of Manufacturing Science and Engineering 134, 064002.

Che, D., Han, P., Peng, B., Ehmann, K.F., 2014a. Finite element study on chip formation and force response in two-dimensional orthogonal cutting of rock, ASME 2014 International Manufacturing Science and Engineering Conference, pp. MSEC2014-3952.

Che, D., Saxena, I., Han, P., Guo, P., Ehmann, K.F., 2014b. Machining of carbon fiber reinforced plastics/polymers: a literature review. Journal of Manufacturing Science and Engineering 136, 034001.

Che, D., Smith, J., Ehmann, K., 2014c. Heat transfer in polycrystalline diamond compact cutters in rock turning, 2014 International Symposium on Flexible Automation, Awaji-Island, Hyogo, pp. ISFA2014-2036L.

Che, D., Smith, J., Ehmann, K., 2015b. Finite element study of the cutting mechanics of the three dimensional rock turning process, ASME 2015 International Manufacturing Sciencen and Engineering Conference. ASME, Charlotte, North Carolina, USA, pp. MSEC2015-9249.

Cheatham, J.J.B., Daniels, W.H., 1979. A study of factors influencing the drillability of shales: single-cutter experiments with STRATAPAX drill blanks. Journal of Energy Resources Technology 101, 189-195.

Clayton, R., Chen, S., Lefort, G., 2005. New bit design, cutter technology extend PDC applications to hard rock drilling. SPE/IADC Drilling Conference, 91840-MS.

Cools, P.M.C.B.M., 1993. Temperature measurements upon the chisel surface during rock cutting. International Journal of Rock Mechanics and Mining Sciences & Geomechanics Abstracts 30, 25-35.

Copur, H., 2010. Linear stone cutting tests with chisel tools for identification of cutting principles and predicting performance of chain saw machines. International Journal of Rock Mechanics and Mining Sciences 47, 104-120.

Coudyzer, C., Richard, T., 2005. Influence of the back and side rake angles in rock cutting, AADE 2005 National Technical Conference and Exhibition, Wyndam Greenspoint, Houston, Texas, April 5-7, 2005., pp. AADE-05-NTCE-75.

Crow, S.C., 1973. A theory of hydraulic rock cutting. International Journal of Rock Mechanics and Mining Sciences & Geomechanics Abstracts 10, 567-584.

Dahmen, K.A., Ben-Zion, Y., Uhl, J.T., 2011. A simple analytic theory for the statistics of avalanches in sheared granular materials. Nat Phys 7, 554-557.

Detournay, E., Atkinson, C., 2000. Influence of pore pressure on the drilling response in low-permeability shear-dilatant rocks. International Journal of Rock Mechanics and Mining Sciences 37, 1091-1101.

Detournay, E., Defourny, P., 1992. A phenomenological model for the drilling action of drag bits. International Journal of Rock Mechanics and Mining Sciences & Geomechanics Abstracts 29, 13-23.

Detournay, E., Richard, T., Shepherd, M., 2008. Drilling response of drag bits: theory and experiment. International Journal of Rock Mechanics and Mining Sciences 45, 1347-1360.

Dimiduk, D.M., Woodward, C., LeSar, R., Uchic, M.D., 2006. Scale-free intermittent flow in crystal plasticity. Science 312, 1188-1190.

Durrand, C.J., Skeem, M.R., Crockett, R.B., Hall, D.R., Super-hard, thick, shaped PDC cutters for hard rock drilling: development and test results, 35th Workshop on Geothermal Reservoir Engineering, Stanford, California.

Eberhardt, E., Stead, D., Stimpson, B., 1999. Quantifying progressive pre-peak brittle fracture damage in rock during uniaxial compression. International Journal of Rock Mechanics and Mining Sciences 36, 361-380.

Evans, I., 1962. A theory of the basic mechanics of coal ploughing, Proceedings of the international symposium on mining research. Univ. of Missouri at Rolla, Pergamon Press, pp. 761-798.

Evans, I., 1965. The force required to cut coal with blunt wedges. International Journal of Rock Mechanics and Mining Sciences & Geomechanics Abstracts 2, 1-12.

Evans, I., 1984. A theory of the cutting force for point-attack picks. Geotechnical and Geological Engineering 2, 63-71.

Fairhurst, C., Lacabanne, W.D., 1956. Some principles and developments in hard rock drilling techniques, 6th Annual Drilling and Blasing Symposium, University of Minnesota, pp. 15-25.

Fairhurst, C., Lacabanne, W.D., 1957. Hard rock drilling techniques. Mine and Quarry Engineering 23, 157-161.

Feenstra, R., 1988. Status of polycrystalline-diamond-compact bits: part 1 - development Journal of Petroleum Technology 40, 675-684.

Finger, J.T., Glowka, D.A., 1989. PDC bit research at Sandia National Laboratories, Sandia report. Sandia National Laboratories.

Franca, L.F.P., 2011. A bit–rock interaction model for rotary–percussive drilling. International Journal of Rock Mechanics and Mining Sciences 48, 827-835.

Freeman, M.A., Shen, Y., Zhang, Y., 2012. Single PDC cutter studies of fluid heat transfer and cutter thermal mortality in drilling fluid, 2012 AADE National Technical Conference and Exhibition, Houston, Texas, pp. AADE-12-FTCE-38.

Freudenthal, A.M., 1968. Statistical approach to brittle fracture, Fracture. Academic Press, New York, pp. 592-618.

Friedman, N., Jennings, A.T., Tsekenis, G., Kim, J.-Y., Tao, M., Uhl, J.T., Greer, J.R., Dahmen, K.A., 2012. Statistics of dislocation slip avalanches in nanosized single crystals show tuned critical behavior predicted by a simple mean field model. Phys Rev Lett 109, 095507.

Geller, R.J., Jackson, D.D., Kagan, Y.Y., Mulargia, F., 1997. Enhanced: earthquakes cannot be predicted. Science 275, 1616-1620.

Geoffroy, H., Minh, D.N., 1997. Study on interaction between rocks and worn PDC'S cutter. International Journal of Rock Mechanics and Mining Sciences 34, 95.e91-95.e15.

GEOL615, 2009. Some useful numbers on the engineering properties of materials (geologic and otherwise), Stanford Unviersity.

Gerbaud, L., Menand, S., Sellami, H., 2006. PDC bits: all comes from the cutter rock interaction, IADC/SPE Drilling Conference, Miami, Florida, U.S.A., p. 98988.

Glowka, D.A., 1986. The use of single-cutter data in the analysis of PDC bit designs, Society of Petroleum Engineers Annual Technical Conference and Exhibition, New Orleans, LA, USA.

Glowka, D.A., 1987. Development of a method for predicting the performance and wear of PDC (polycrystalline diamond compact) drill bits. Sandia National Laboratories.

Glowka, D.A., 1989a. The thermal response of rock to friction in the drag cutting process. Journal of Structural Geology 11, 919-931.

Glowka, D.A., 1989b. Use of single-cutter data in the analysis of PDC bit designs: part 1 - development of a PDC cutting force model. Journal of Petroleum Technology 41, 797-799, 844-849.

Glowka, D.A., Stone, C.M., 1985. Thermal response of polycrystalline diamond compact cutters under simulated downhole conditions SPE Journal 25, 143-156.

Goktan, R., Yilmaz, N.G., 2005. A new methodology for the analysis of the relationship between rock brittleness index and drag pick cutting efficiency. Journal - South African Institute of Mining and Metallurgy 105, 727.

Goodman, R.E., 1989. Introduction to Rock Mechanics, 2nd ed. John Wiley & Sons, Inc.

Goodrich, R., 1956. High pressure rotary drilling machines. Bull 94.

Guo, H., Aziz, N.I., Schmidt, L.C., 1990. Linear elastic crack tip modelling by the displacement discontinuity method. Engineering Fracture Mechanics 36, 933-943.

Guo, H., Aziz, N.I., Schmidt, L.C., 1992. Rock cutting study using linear elastic fracture mechanics. Engineering Fracture Mechanics 41, 771-778.

Guo, H., Aziz, N.I., Schmidt, L.C., 1993. Rock fracture-toughness determination by the Brazilian test. Engineering Geology 33, 177-188.

Guyer, R.A., McCall, K.R., Van Den Abeele, K., 1998. Slow elastic dynamics in a resonant bar of rock. Geophys. Res. Lett. 25, 1585-1588.

Haji-Sheikh, A., Beck, J., Agonafer, D., 2003. Steady-state heat conduction in multi-layer bodies. International Journal of Heat and Mass Transfer 46, 2363-2379.

Haji-Sheikh, A., Beck, J.V., 2002. Temperature solution in multi-dimensional multi-layer bodies. International Journal of Heat and Mass Transfer 45, 1865-1877.

Hallbauer, D.K., Wagner, H., Cook, N.G.W., 1973. Some observations concerning the microscopic and mechanical behaviour of quartzite specimens in stiff, triaxial compression tests. International Journal of Rock Mechanics and Mining Sciences & Geomechanics Abstracts 10, 713-726.

Halley, J.M., Kunin, W.E., 1999. Extinction risk and the 1/f family of noise models. Theor Popul Biol 56, 215-230.

Halling, J., 1976. Introduction to Tribology. Wykeham Publications.

Hamade, R.F., Manthri, S.P., Pusavec, F., Zacny, K.A., Taylor, L.A., Dillon Jr, O.W., Rouch, K.E., Jawahir, I.S., 2010. Compact core drilling in basalt rock using PCD tool inserts: Wear characteristics and cutting forces. Journal of Materials Processing Technology 210, 1326-1339.

Hardy, H.R., 1971. Application of acoustic emission techniques to rock mechanics research. Pennsylvania State Univ., University Park.

Harrell, J.W., Dubinsky, V., Leggett, J., 1997. Closed loop drilling system, In: Organization, W.I.P. (Ed.), E21B 44/00 ed.

Healy, D., Jones, R.R., Holdsworth, R.E., 2006. Three-dimensional brittle shear fracturing by tensile crack interaction. Nature 439, 64-67.

Henneuse, H., 1992. Surface detection of vibrations and drilling optimization: field experience, SPE/IADC Drilling Conference. Society of Petroleum Engineers New Orleans, Louisiana, pp. 23888-MS.

Hibbs, L.E., Flom, D.G., 1978. Diamond compact cutter studies for geothermal bit design. Journal of Pressure Vessel Technology 100, 406-416.

Hill, J.R., 2015. Indiana limestone.

Hood, M., Alehossein, H., 2000. A development in rock cutting technology. International Journal of Rock Mechanics and Mining Sciences 37, 297-305.

Huang, H., Detournay, E., Bellier, B., 1999. Discrete element modeling of rock cutting, Vail Rocks 1999, The 37th U.S. Symposium on Rock Mechanics (USRMS). American Rock Mechanics Association, Vail, CO, pp. 99-0123.

Huang, H., Lecampion, B., Detournay, E., 2013. Discrete element modeling of tool-rock interaction I: rock cutting. International Journal for Numerical and Analytical Methods in Geomechanics 37, 1913-1929.

Hurt, K.G., Evans, I., 1981. Point attach tools: an evaluation of function and use for rock cutting. Mining engineer : Incorporating the Transactions of the Institution of Mining Engineers. 140, 673-675.

Hustrulid, W.A., Fairhurst, C., 1972. A theoretical and experimental study of the percussive drilling of rock Part IV—application of the model to actual percussion drilling. International Journal of Rock Mechanics and Mining Sciences & Geomechanics Abstracts 9, 431-442.

Hutchinson, M., Dubinsky, V., Henneuse, H., 1995. An MWD downhole assistant driller, SPE Annual Technical Conference and Exhibition, 22-25 October 1995, Dallas, Texas, pp. 30523-MS.

Incropera, F.P., De Witt, D.P., 2011. Introduction to Heat Transfer, 6th ed. John Wiley & Sons Inc., New York.

Jaeger, J.C., 1942. Moving sources of heat and the temperature of sliding contacts. J. and Proc. Roy. Soc. New South Wales 76, 202.

Jaeger, J.C., Hoskins, E.R., 1966. Rock failure under the confined Brazilian test. J. Geophys. Res. 71, 2651-2659.

Jaime, M.C., Gamwo, I.K., Lyons, D.K., Lin, J.S., 2010. Finite element modeling of rock cutting, 44th US Rock Mechanics Symposium and 5th U.S.-Canada Rock Mechanics Symposium. American Rock Mechanics Association, Salt Lake City, UT, pp. 10-231.

Johnson, P.A., Rasolofosaon, P., Zinszner, B., 1993. Measurement of nonlinear elastic response in rock by the resonant bar method, p. Medium: ED; Size: Pages: (7 p).

Kadiu, M., 1994. A new approach for simulation of the rock cutting process, In: Nelson, P.P., Laubach, S.E. (Eds.), Rock mechanics models and measurements : challenges from industry.

Rotterdam ; Brookfield, VT : A.A. Balkema North American Rock Mechanics Symposium (1st : 1994 : University of Texas at Austin), pp. 343-350.

Kaitkay, P., Lei, S., 2005. Experimental study of rock cutting under external hydrostatic pressure. Journal of Materials Processing Technology 159, 206-213.

Kerr, C.J., 1988. PDC drill bit design and field application evolution. Journal of Petroleum Technology 40, 327-332.

KocurekIndustries, 2015. Rock products.

Kou, S.Q., Liu, H.Y., Lindqvist, P.A., Tang, C.A., 2004. Rock fragmentation mechanisms induced by a drill bit. International Journal of Rock Mechanics and Mining Sciences 41, 460.

Leach, S.J., Walker, G.L., Smith, A.V., Farmer, I.W., Taylor, G., 1966. Some aspects of rock cutting by high speed water jets [and Discussion]. Philosophical Transactions of the Royal Society of London. Series A, Mathematical and Physical Sciences 260, 295-310.

Lee, D.-H., Juang, C.H., Chen, J.-W., Lin, H.-M., Shieh, W.-H., 1999. Stress paths and mechanical behavior of a sandstone in hollow cylinder tests. International Journal of Rock Mechanics and Mining Sciences 36, 857-870.

Lenoir, N., Bornert, M., Desrues, J., Bésuelle, P., Viggiani, G., 2007. Volumetric digital image correlation applied to X-ray microtomography images from triaxial compression tests on argillaceous rock. Strain 43, 193-205.

Leseultre, A., Lamine, E., Jonsson, A., 1998. An instrumented bit: a necessary step to the intelligent BHA, IADC/SPE Drilling Conference, 3-6 March 1998, Dallas, Texas, pp. 39341-MS.

Li, H., Butt, S., Munaswamy, K., Arvani, F., 2010. Experimental investigation of bit vibration on rotary drilling penetration rate, 44th US Rock Mechanics Symposium and 5th U.S.-Canada Rock Mechanics Symposium, Salt Lake City, UT June 27–30, 2010, pp. 10-426.

Li, L., Li, B., Li, X., Ehmann, K.F., 2012. Experimental investigation of hard turning mechanisms by PCBN tooling embedded micro thin film thermocouples, ASME International Manufacturing Science and Engineering Conference, Notre Dame, Indiana, USA.

Li, L., Li, B., Li, X., Ehmann, K.F., 2013. Experimental investigation of hard turning mechanisms by PCBN tooling embedded micro thin film thermocouples. Journal of Manufacturing Science and Engineering 135, 041012-041012.

Li, X.B., Summers, D.A., Rupert, G., Santi, P., 2001. Experimental investigation on the breakage of hard rock by the PDC cutters with combined action modes. Tunnelling and Underground Space Technology 16, 107-114.

Lin, J., 1995. Inverse estimation of the tool-work interface temperature in end milling. International Journal of Machine Tools and Manufacture 35, 751-760.

Liu, H., 2002. Numerical modelling of the rock fracture process under mechanical loading, Civil and Mining Engineering. Lulea University of Technology.

Liu, H.Y., Kou, S.Q., Lindqvist, P.A., 2002a. Numerical simulation of the fracture process in cutting heterogeneous brittle material. International Journal for Numerical and Analytical Methods in Geomechanics 26, 1253-1278.

Liu, H.Y., Kou, S.Q., Lindqvist, P.A., Tang, C.A., 2002b. Numerical simulation of the rock fragmentation process induced by indenters. International Journal of Rock Mechanics and Mining Sciences 39, 491-505.

Liu, K., Li, X.P., Liang, S.Y., 2007. The mechanism of ductile chip formation in cutting of brittle materials. The International Journal of Advanced Manufacturing Technology 33, 875-884.

Liu, S.-y., Du, C.-l., Cui, X.-x., 2009a. Research on the cutting force of a pick. Mining Science and Technology (China) 19, 514-517.

Liu, S.-y., Du, C.-l., Cui, X.-x., Cheng, X., 2009b. Model test of the cutting properties of a shearer drum. Mining Science and Technology (China) 19, 74-78.

Liu, X., DeVor, R.E., Kapoor, S.G., Ehmann, K.F., 2004. The mechanics of machining at the microscale: assessment of the current state of the science. Journal of Manufacturing Science and Engineering 126, 666-678.

Lockner, D., 1993. The role of acoustic emission in the study of rock fracture. International Journal of Rock Mechanics and Mining Sciences & Geomechanics Abstracts 30, 883-899.

Loui, J., Rao Karanam, U.M., 2012. Numerical studies on chip formation in drag-pick cutting of rocks. Geotechnical and Geological Engineering 30, 145-161.

Loui, J.P., Karanam, U.M.R., 2005. Heat transfer simulation in drag–pick cutting of rocks. Tunnelling and Underground Space Technology 20, 263-270.

Lucet, N., Rasolofosaon, P.N.J., Zinszner, B., 1991. Sonic properties of rocks under confining pressure using the resonant bar technique. The Journal of the Acoustical Society of America 89, 980-990.

Malamud, B.D., Morein, G., Turcotte, D.L., 1998. Forest fires: an example of self-organized critical behavior. Science 281, 1840-1842.

Martin, J.A., Fowell, R.J., 1997. Factors governing the onset of severe drag tool wear in rock cutting. International Journal of Rock Mechanics and Mining Sciences 34, 59-69.

Massobrio, P., Pasquale, V., Martinoia, S., 2015. Self-organized criticality in cortical assemblies occurs in concurrent scale-free and small-world networks. Scientific reports 5.

Maurer, W.C., 1966. The state of rock mechanics knowledge in drilling, The 8th U.S. Symposium on Rock Mechanics (USRMS). American Rock Mechanics Association, Minneapolis, MN, pp. 66-0355.

Menand, S., Gerbaud, L., 2005. PDC bit technology improvements increase efficiency, bit life. Drilling Contractor Official Magazine March/April, 52-54.

Mendoza, J.A., Gamwo, I.K., Zhang, W., Lin, J.S., 2010. Discrete element modeling of rock cutting using crushable particles, 44th U.S. Rock Mechanics Symposium and 5th U.S.-Canada Rock Mechanics Symposium. American Rock Mechanics Association, Salt Lake City, Utah, pp. 10-232.

Mendoza, J.A., Gamwo, I.K., Zhang, W., Lin, J.S., 2011. Considerations for discrete modeling of rock cutting, 45th U.S. Rock Mechanics / Geomechanics Symposium. American Rock Mechanics Association, San Francisco, California, pp. 11-210.

Merchant, M.E., 1944. Basic mechanics of the metal-cutting process. Journal of Applied Mechanics 11, 168-175.

Merchant, M.E., 1945. Mechanics of the metal cutting process. I. Orthogonal cutting and a type 2 chip. Journal of Applied Physics 16, 267-275.

Miller, S., Florence, A., 1991. Laboratory particle velocity experiments on Indiana limestone and Sierra White granite. DTIC Document.

Mishnaevsky, L.L., 1994. Investigation of the cutting of brittle materials. International Journal of Machine Tools and Manufacture 34, 499-505.

Mishnaevsky, L.L., 1995. Physical mechanisms of hard rock fragmentation under mechanical loading: A review. International Journal of Rock Mechanics and Mining Sciences & Geomechanics Abstracts 32, 763-766.

Nara, Y., Kaneko, K., 2005. Study of subcritical crack growth in andesite using the Double Torsion test. International Journal of Rock Mechanics and Mining Sciences 42, 521-530.

Nishimatsu, Y., 1972. The mechanics of rock cutting. International Journal of Rock Mechanics and Mining Sciences 9, 261-270.

Nishimatsu, Y., 1993. Theories of rock cutting, In: Hudson, J.A. (Ed.), Comprehensive Rock Engineering : Principles, Practice & Projects. Oxford ; New York : Pergamon Press

Oddershede, L., Dimon, P., Bohr, J., 1993. Self-organized criticality in fragmenting. Phys Rev Lett 71, 3107.

Offenbacher, L.A., McDermaid, J.D., Patterson, C.R., 1983. PDC bits find applications in Oklahoma drilling, IADC/SPE Drilling Conference. Society of Petroleum Engineers, New Orleans, Louisiana, pp. 11389-MS.

Ohbuchi, Y., Obikawa, T., 2003. Finite element modeling of chip formation in the domain of negative rake angle cutting. Journal of Engineering Materials and Technology 125, 324-332.

Ortega, A., Glowka, D.A., 1984. Frictional heating and convective cooling of polycrystalline diamond drag tools during rock cutting. SPE Journal 24, 121-128.

Paterson, M.S., Olgaard, D.L., 2000. Rock deformation tests to large shear strains in torsion. Journal of Structural Geology 22, 1341-1358.

Prins, O.D., 1971. The influence of wear on the temperature distribution. CIRP Annals 19, 579-584.

Qinsen, Y., Shuren, S., 1994. A soil-tool interaction model for bulldozer blades. Journal of Terramechanics 31, 55-65.

Quickelberghe, F.V., Dagrain, F., Tshibangu, J., Richard, T., 2006. A new procedure to analyse the wear of cutting elements, Eurock 2006: Multiphysics Coupling and Long Term Behaviour in Rock Mechanics. Taylor & Francis, pp. 609-615.

Rafatian, N., Miska, S., III, L.W.L., Ahmed, R., Yu, M., Takach, N., 2010. Experimental study of MSE of a single PDC cutter interacting with rock under simulated pressurized conditions. SPE Drilling & Completion 25, 10-18.

Rånman, K.E., 1985. A model describing rock cutting with conical picks. Rock Mechanics and Rock Engineering 18, 131-140.

Rao, K.U.M., Bhatnagar, A., Misra, B., 2002. Laboratory investigations on rotary diamond drilling. Geotechnical & Geological Engineering 20, 1-16.

Rao, M.V.M.S., Ramana, Y.V., 1992. A study of progressive failure of rock under cyclic loading by ultrasonic and AE monitoring techniques. Rock Mechanics and Rock Engineering 25, 237-251.

Reches, Z.e., Lockner, D.A., 1994. Nucleation and growth of faults in brittle rocks. Journal of Geophysical Research: Solid Earth (1978–2012) 99, 18159-18173.

Resende, L., Martin, J.B., 1985. Formulation of Drucker-Prager cap model. Journal of Engineering Mechanics 111, 855-881.

Richard, T., 1999. Determination of Rock Strength from Cutting Tests. University of Minnesota.

Richard, T., Dagrain, F., Poyol, E., Detournay, E., 2012. Rock strength determination from scratch tests. Engineering Geology 147–148, 91-100.

Rojek, J., Oñate, E., Labra, C., Kargl, H., 2011. Discrete element modelling of rock cutting particle-based methods, In: Oñate, E., Owen, R. (Eds.). Springer Netherlands, pp. 247-267.

Rudnicki, J.W., 2000. Geomechanics. International Journal of Solids and Structures 37, 349-358.

Santarelli, F.J., Brown, E.T., 1989. Failure of three sedimentary rocks in triaxial and hollow cylinder compression tests. International Journal of Rock Mechanics and Mining Sciences & Geomechanics Abstracts 26, 401-413.

Santos, S.I.d., Casanova, C.A.M., Teixeira, C.R., Balzaretti, N.M., Jornada, J.A.H.d., 2004. Evaluation of the adhesion strength of diamond films brazed on K-10 type hard metal. Materials Research 7, 293-297.

Saouma, V.E., Kleinosky, M.-J., 1984. Finite element simulation of rock cutting: A fracture mechanics approach, The 25th U.S. Symposium on Rock Mechanics (USRMS). American Rock Mechanics Association, Evanston, IL, pp. 84-0792.

Scheidegger, A., 1982. Principles of Geodynamics. Springer-Verlag.

Shao, J.F., Rudnicki, J.W., 2000. A microcrack-based continuous damage model for brittle geomaterials. Mechanics of Materials 32, 607-619.

Shaw, M.C., 1993. Some observations concerning the mechanics of cutting and grinding. Applied Mechanics Reviews 46, 74-79.

Shaw, M.C., 2005. Metal Cutting Principles, Second edition ed. Oxford University Press, Oxford New York.

Simon, R., 1963. Energy balance in rock drilling. SPE Journal 3, 298-306.

Stephenson, D.A., 1993. Tool-work thermocouple temperature measurements - theory and implementation issues. Journal of Engineering for Industry 115, 432-437.

Su, O., Ali Akcin, N., 2011. Numerical simulation of rock cutting using the discrete element method. International Journal of Rock Mechanics and Mining Sciences 48, 434-442.

Sulem, J., Vardoulakis, I., 1990. Bifurcation analysis of the triaxial test on rock specimens. A theoretical model for shape and size effect. Acta Mechanica 83, 195-212.

Sullivan, E.C., Theodore Edward Zaleski, J., Schmidt, S.R., Nguyen, D.Q., Zadrapa, G.R., Lin, C., 2003. Method and apparatus for monitoring and recording of the operating condition of a downhole drill bit during drilling operations. Baker Hughes Incorporated.

Teale, R., 1965. The concept of specific energy in rock drilling. International Journal of Rock Mechanics and Mining Sciences & Geomechanics Abstracts 2, 57-73.

Thill, R.E., Bur, T.R., 1969. An automated ultrasonic pulse measurement system. Geophysics 34, 101-105.

Tiryaki, B., Dikmen, A.C., 2006. Effects of rock properties on specific cutting energy in linear cutting of sandstones by picks. Rock Mechanics and Rock Engineering 39, 89-120.

Tsuji, T., Nakagawa, Y., Matsumoto, N., Kadono, Y., Takayama, T., Tanaka, T., 2012. 3-D DEM simulation of cohesive soil-pushing behavior by bulldozer blade. Journal of Terramechanics 49, 37-47.

Tulu, I.B., Heasley, K.A., 2009. Calibration of 3D cutter-rock model with single cutter tests, 43rd U.S. Rock Mechanics Symposium & 4th U.S. - Canada Rock Mechanics Symposium. American Rock Mechanics Association, Asheville, North Carolina, pp. 09-160.

Ueda, T., Hosokawa, A., Yamamoto, A., 1985. Studies on temperature of abrasive grains in grinding - application of infrared radiation pyrometer. Journal of Engineering for Industry 107, 127-133.

Uhl, J.T., Pathak, S., Schorlemmer, D., Liu, X., Swindeman, R., Brinkman, B.A.W., LeBlanc, M., Tsekenis, G., Friedman, N., Behringer, R., Denisov, D., Schall, P., Gu, X., Wright, W.J., Hufnagel, T., Jennings, A., Greer, J.R., Liaw, P.K., Becker, T., Dresen, G., Dahmen, K.A., 2015. Universal quake statistics: from compressed nanocrystals to earthquakes. Scientific Reports 5, 16493.

Verhoef, P.N.W., Ockeloen, J.J., 1996. The significance of rock ductility for mechanical rock cutting. Rock Mechanics Tools and Techniques 1, 709-716.

Waldorf, D.J., 2006. A simplified model for ploughing forces in turning. Journal of Manufacturing Processes 8, 76-82.

Waldorf, D.J., DeVor, R.E., Kapoor, S.G., 1998. A slip-line field for ploughing during orthogonal cutting. Journal of Manufacturing Science and Engineering 120, 693-699.

Warren, T.M., 1994. PDC bits: what's needed to meet tomorrow's challenge, University of Tulsa Centennial Petroleum Engineering Symposium. Society of Petroleum Engineers, Tulsa, Oklahoma, pp. 27978-MS.

Warren, T.M., Sinor, A., 1989. Drag bit performance modeling. SPE Drilling Engineering 4, 119-127.

Wawersik, W.R., Fairhurst, C., 1970. A study of brittle rock fracture in laboratory compression experiments. International Journal of Rock Mechanics and Mining Sciences & Geomechanics Abstracts 7, 561-575.

Weibull, W., 1939. A statistical theory of the strength of materials. The Royal Swedish Institute for Engineering Research.

Werschmoeller, D., Ehmann, K., Li, X., 2011. Tool embedded thin film microsensors for monitoring thermal phenomena at tool-workpiece interface during machining. Journal of Manufacturing Science and Engineering 133, 021007.

Werschmoeller, D., Li, X., 2011. Measurement of tool internal temperatures in the tool–chip contact region by embedded micro thin film thermocouples. Journal of Manufacturing Processes 13, 147-152.

Wilson, C., Vorono, O.A., 2003. Diamond turning of granite. Key Engineering Material 250, 138-146.

Wilt, T., Chowdhury, A., 2011. Response of reinforced concrete structures to aircraft crash impact. Center for Nuclear Waste Regulatory Analyses in Southwest Research Institute, San Antonio, Texas.

Wise, J.L., Raymond, D.W., Cooley, C.H., Bertagnolli, K., 2002. Effects of design and processing parameters on performance of PDC drag cutters for hard-rock drilling. Transactions- Geothermal Resources Counicl, 201-206.

Withjack, E.M., 1988. Computed tomography for rock-property determination and fluid-flow visualization. SPE Formation Evaluation 3, 696-704.

Xu, X.P., Huang, H., 2003. Thermal study on rock grinding, part 1: temperature measurement. Key Engineering Material 250, 147-154.

Xue, J., Xia, Y., Ji, Z., Zhou, X., 2009. Soft rock cutting mechanics model of TBM cutter and experimental research, In: Xie, M., Xiong, Y., Xiong, C., Liu, H., Hu, Z. (Eds.), Intelligent Robotics and Applications. Springer Berlin Heidelberg, pp. 383-391.

Yamashita, F., Fukuyama, E., Mizoguchi, K., Takizawa, S., Xu, S., Kawakata, H., 2015. Scale dependence of rock friction at high work rate. Nature 528, 254-257.

Yan, W., 1997. Single PDC cutter force modeling for hard rock cutting, Petroleum and Natural Gas Engineering. New Mexico Institute of Mining and Technology Socorro, New Mexico.

Yang, K., Liang, Y.-c., Zheng, K.-n., Bai, Q.-s., Chen, W.-q., 2011. Tool edge radius effect on cutting temperature in micro-end-milling process. The International Journal of Advanced Manufacturing Technology 52, 905-912.

Yilmaz, N.G., Yurdakul, M., Goktan, R., 2007. Prediction of radial bit cutting force in high-strength rocks using multiple linear regression analysis. International Journal of Rock Mechanics and Mining Sciences 44, 962-970.

Yu, B., 2005. Numerical simulation of continuous miner rock cutting process. West Virginia University.

Zaleski, T.E., Schmidt, S.R., 1998. Method and apparatus for monitoring and recording of operating conditions of a downhole drill bit during drilling operations. Baker Hughes Incorporated, United States.

Zapperi, S., Vespignani, A., Stanley, H.E., 1997. Plasticity and avalanche behaviour in microfracturing phenomena. Nature 388, 658-660.

Zeuch, D., Finger, J., 1985. Rock breakage mechanisms with a PDC cutter, SPE Annual Technical Conference and Exhibition. Society of Petroleum Engineers.

Zhang, Z.X., Kou, S.Q., Tan, X.C., Lindqvist, P.A., 2003. In-situ measurements of cutter forces on boring machine at Äspö hard rock laboratory part I. Laboratory calibration and in-situ measurements. Rock Mechanics and Rock Engineering 36, 39-61.

Zijsling, D.H., 1984. Analysis of temperature distribution and performance of polycrystalline diamond compact bits under field drilling conditions, SPE Annual Technical Conference and Exhibition. Society of Petroleum Engineers, Houston, Texas, pp. 13260-MS.

Zijsling, D.H., 1987. Single cutter testing - a key for PDC bit development, Offshore Europe. Society of Petroleum Engineers Aberdeen, United Kingdom, pp. 16529-MS.

Appendix A: Experimental Results

Table A1: Process parameters and force responses for the 7x3x3 full factorial design of experiments in face turning of rock.

	Test No.	Rake angle (°)	Feedrate (mm/rev)	Depth of cut (mm)	Average cutting force (N)	Average thrust force (N)	Average feed force (N)	Average nominal thrust force (N)
Set 1	1	10	0.16	0.254	8.50	10.27	2.68	10.62
	2	10	0.4	0.254	14.00	15.76	5.84	16.81
	3	10	0.8	0.254	22.56	23.56	12.03	26.46
	4	10	0.16	0.508	11.47	11.91	2.96	12.28
	5	10	0.4	0.508	18.26	17.78	6.09	18.79
	6	10	0.8	0.508	30.46	26.73	13.40	29.90
	7	10	0.16	1.016	16.72	16.49	3.13	16.78
	8	10	0.4	1.016	25.79	23.65	6.95	24.65
	9	10	0.8	1.016	43.37	36.05	15.81	39.36
Set 2	10	12	0.16	0.254	7.87	8.78	2.27	9.07
	11	12	0.4	0.254	13.24	14.07	5.27	15.03
	12	12	0.8	0.254	21.28	20.83	10.93	23.52
	13	12	0.16	0.508	10.93	10.63	2.41	10.90
	14	12	0.4	0.508	18.09	16.83	5.67	17.75
	15	12	0.8	0.508	30.07	25.33	12.46	28.23
	16	12	0.16	1.016	16.90	15.84	2.86	16.10
	17	12	0.4	1.016	25.91	22.89	6.50	23.79
	18	12	0.8	1.016	44.56	36.05	15.40	39.20
Set 3	19	15	0.16	0.254	7.49	8.22	2.07	8.47
	20	15	0.4	0.254	13.41	13.79	4.97	14.66
	21	15	0.8	0.254	22.30	21.60	11.60	24.52
	22	15	0.16	0.508	11.38	11.04	2.65	11.35
	23	15	0.4	0.508	18.50	17.01	5.53	17.89
	24	15	0.8	0.508	30.62	25.59	12.79	28.61
	25	15	0.16	1.016	16.22	15.21	2.66	15.44
	26	15	0.4	1.016	27.22	23.97	6.60	24.86
	27	15	0.8	1.016	45.92	37.17	16.22	40.56
Set 4	28	17	0.16	0.254	7.85	8.36	1.76	8.55
	29	17	0.4	0.254	13.96	14.13	4.72	14.89
	30	17	0.8	0.254	22.57	20.79	10.27	23.19
	31	17	0.16	0.508	12.70	12.50	2.47	12.74
	32	17	0.4	0.508	19.88	18.09	5.36	18.87
	33	17	0.8	0.508	33.14	27.21	12.52	29.95

	34	17	0.16	1.016	18.54	17.43	2.76	17.64
	35	17	0.4	1.016	28.55	25.08	6.33	25.87
	36	17	0.8	1.016	48.82	39.62	15.99	42.73
Set 5	37	20	0.16	0.254	9.44	10.28	1.90	10.45
	38	20	0.4	0.254	14.77	15.52	4.37	16.13
	39	20	0.8	0.254	23.59	22.75	9.70	24.73
	40	20	0.16	0.508	12.30	12.21	1.62	12.31
	41	20	0.4	0.508	20.54	19.03	4.53	19.56
	42	20	0.8	0.508	33.56	28.11	10.96	30.17
	43	20	0.16	1.016	18.22	16.96	2.15	17.10
	44	20	0.4	1.016	29.17	25.38	5.59	25.98
	45	20	0.8	1.016	48.77	39.46	14.10	41.90
Set 6	46	22	0.16	0.254	8.53	9.20	1.73	9.36
	47	22	0.4	0.254	14.98	15.15	4.53	15.81
	48	22	0.8	0.254	24.36	22.60	10.14	24.77
	49	22	0.16	0.508	13.33	13.19	2.45	13.42
	50	22	0.4	0.508	20.97	19.40	5.18	20.08
	51	22	0.8	0.508	35.93	30.44	12.71	32.98
	52	22	0.16	1.016	19.77	18.93	2.71	19.13
	53	22	0.4	1.016	31.39	28.29	6.42	29.01
	54	22	0.8	1.016	54.02	45.44	16.73	48.42
Set 7	55	25	0.16	0.254	8.81	10.51	2.10	10.72
	56	25	0.4	0.254	15.52	17.38	5.36	18.19
	57	25	0.8	0.254	25.83	26.19	11.52	28.61
	58	25	0.16	0.508	14.12	15.10	3.04	15.40
	59	25	0.4	0.508	22.70	22.28	6.19	23.13
	60	25	0.8	0.508	39.96	35.87	14.80	38.80
	61	25	0.16	1.016	20.69	21.17	3.36	21.43
	62	25	0.4	1.016	33.42	31.74	7.61	32.64
	63	25	0.8	1.016	64.29	56.53	21.11	60.34

Table A2: Process parameters and corresponding force responses for the cutting theory evaluations.

Test No.	Rake angle (°)	Depth of cut (mm)	Average cutting force (N)	Average thrust force (N)	Average side force (N)	Predicted cutting force (N)	Predicted thrust force (N)	Cutting force prediction error (%)	Thrust force prediction error (%)
1	10	0.2	83.08	61.94	-0.06	77.80	44.99	6	27
2	10	0.2	80.64	61.57	-5.37	77.80	44.99	4	27
3	10	0.2	72.49	53.27	-0.49	77.80	44.99	7	16
4	10	0.4	162.72	113.83	0.48	148.15	85.67	9	25
5	10	0.4	158.14	109.86	-0.49	148.15	85.67	6	22
6	10	0.4	151.58	102.61	-1.83	148.15	85.67	2	17
7	10	0.6	219.03	141.86	1.56	211.70	122.42	3	14
8	10	0.6	217.49	143.39	-1.47	211.70	122.42	3	15
9	10	0.6	217.02	145.43	-2.05	211.70	122.42	2	16
10	10	0.8	265.19	166.72	0.90	269.11	155.62	1	7
11	10	0.8	272.71	175.97	-1.67	269.11	155.62	1	12
12	10	0.8	259.74	165.02	-2.94	269.11	155.62	4	6
13	10	1	299.76	182.36	1.56	321.02	185.64	7	2
14	10	1	317.28	198.98	0.43	321.02	185.64	1	7
15	10	1	317.33	196.66	-2.32	321.02	185.64	1	6
16	10	1.2	336.33	203.65	0.36	368.02	212.82	9	5
17	10	1.2	358.21	219.98	-0.61	368.02	212.82	3	3
18	10	1.2	363.48	225.44	-5.63	368.02	212.82	1	6
19	10	1.4	405.79	247.58	-1.25	410.67	237.48	1	4
20	10	1.4	411.00	248.89	1.27	410.67	237.48	0	5
21	10	1.4	454.36	285.99	-0.91	410.67	237.48	10	17
22	10	1.6	428.18	259.22	1.89	449.51	259.95	5	0
23	10	1.6	450.22	275.51	-2.59	449.51	259.95	0	6
24	10	1.6	468.33	285.17	3.61	449.51	259.95	4	9
25	10	1.8	467.22	279.96	4.04	485.02	280.48	4	0
26	10	1.8	463.06	279.14	-0.14	485.02	280.48	5	0
27	10	1.8	445.33	263.60	-3.63	485.02	280.48	9	6
28	10	2	483.24	286.04	0.66	517.63	299.33	7	5
29	10	2	484.57	287.55	2.48	517.63	299.33	7	4
30	10	2	510.99	300.48	-0.98	517.63	299.33	1	0
31	10	2.4	605.40	377.26	2.42	575.70	332.92	5	12
32	10	2.4	632.51	381.87	10.29	575.70	332.92	9	13
33	10	2.4	558.52	333.43	-2.03	575.70	332.92	3	0
34	10	2.8	670.45	395.73	-0.27	626.51	362.30	7	8
35	10	2.8	594.71	367.41	-1.60	626.51	362.30	5	1
36	10	2.8	690.65	406.98	7.07	626.51	362.30	9	11
37	10	3	658.31	398.35	3.20	649.92	375.84	1	6
38	10	3	645.94	386.56	4.46	649.92	375.84	1	3
39	10	3	656.86	387.68	1.85	649.92	375.84	1	3

40	20	0.2	135.96	105.57	-2.33	113.96	77.73	16	26
41	20	0.2	111.26	84.12	-2.86	113.96	77.73	2	8
42	20	0.2	110.79	82.15	1.96	113.96	77.73	3	5
43	20	0.4	250.07	186.91	-1.44	221.59	151.15	11	19
44	20	0.4	226.86	165.23	0.44	221.59	151.15	2	9
45	20	0.4	226.32	165.08	-2.12	221.59	151.15	2	8
46	20	0.6	351.66	255.92	-6.46	322.68	220.10	8	14
47	20	0.6	334.03	241.17	-2.78	322.68	220.10	3	9
48	20	0.6	341.34	247.22	-4.06	322.68	220.10	5	11
49	20	0.8	430.02	312.97	-5.85	417.14	284.53	3	9
50	20	0.8	396.23	281.76	-1.85	417.14	284.53	5	1
51	20	0.8	413.76	296.31	-7.09	417.14	284.53	1	4
52	20	1	496.44	356.43	-7.45	505.05	344.49	2	3
53	20	1	481.71	341.29	1.04	505.05	344.49	5	1
54	20	1	487.51	345.64	-3.82	505.05	344.49	4	0
55	20	1.2	598.92	429.59	-13.52	586.56	400.10	2	7
56	20	1.2	533.40	376.23	-1.33	586.56	400.10	10	6
57	20	1.2	582.13	414.01	-9.03	586.56	400.10	1	3
58	20	1.4	654.88	471.68	-13.57	661.93	451.51	1	4
59	20	1.4	618.13	437.43	-4.34	661.93	451.51	7	3
60	20	1.4	644.52	454.32	-0.39	661.93	451.51	3	1
61	20	1.6	695.40	502.36	-11.37	731.47	498.94	5	1
62	20	1.6	690.31	483.26	-0.16	731.47	498.94	6	3
63	20	1.6	656.44	460.45	2.43	731.47	498.94	11	8
64	20	1.8	797.58	569.10	-8.22	795.52	542.63	0	5
65	20	1.8	757.44	537.99	-2.71	795.52	542.63	5	1
66	20	1.8	804.86	566.53	-6.13	795.52	542.63	1	4
67	20	2	861.33	625.22	-16.20	854.46	582.83	1	7
68	20	2	790.79	556.60	1.49	854.46	582.83	8	5
69	20	2	749.20	535.57	3.79	854.46	582.83	14	9
70	20	2.4	1109.94	795.27	-30.78	958.58	653.85	14	18
71	20	2.4	956.47	672.38	-30.74	958.58	653.85	0	3
72	20	2.4	946.48	664.46	-10.97	958.58	653.85	1	2
73	20	2.8	982.15	675.65	-28.50	1046.92	714.11	7	6
74	20	2.8	1094.33	752.44	-25.32	1046.92	714.11	4	5
75	20	2.8	1167.77	825.26	-3.17	1046.92	714.11	10	13
76	20	3	1081.51	760.18	-11.98	1086.11	740.84	0	3
77	20	3	1179.45	829.53	11.67	1086.11	740.84	8	11
78	20	3	1163.67	804.72	11.24	1086.11	740.84	7	8
79	30	0.2	117.59	91.51	1.65	131.65	104.93	12	15
80	30	0.2	118.30	90.13	0.91	131.65	104.93	11	16
81	30	0.2	127.75	99.56	2.04	131.65	104.93	3	5
82	30	0.4	285.27	222.76	-2.37	262.28	209.05	8	6
83	30	0.4	273.03	210.83	-1.30	262.28	209.05	4	1

84	30	0.4	294.48	228.99	2.83	262.28	209.05	11	9
85	30	0.6	421.75	334.35	-5.00	390.24	311.03	7	7
86	30	0.6	388.97	297.13	0.17	390.24	311.03	0	5
87	30	0.6	390.19	302.01	2.57	390.24	311.03	0	3
88	30	0.8	535.14	418.83	1.48	514.04	409.70	4	2
89	30	0.8	497.26	385.23	-1.39	514.04	409.70	3	6
90	30	0.8	509.55	395.05	6.75	514.04	409.70	1	4
91	30	1	619.86	476.40	-3.38	632.44	504.07	2	6
92	30	1	635.49	500.46	-0.81	632.44	504.07	0	1
93	30	1	610.05	468.49	4.90	632.44	504.07	4	8
94	30	1.2	730.58	574.93	-2.05	744.49	593.38	2	3
95	30	1.2	748.93	583.90	0.52	744.49	593.38	1	2
96	30	1.2	738.28	572.92	7.95	744.49	593.38	1	4
97	30	1.4	842.86	673.49	6.08	849.51	677.09	1	1
98	30	1.4	782.21	612.12	-3.98	849.51	677.09	9	11
99	30	1.4	793.16	616.30	9.43	849.51	677.09	7	10
100	30	1.6	833.33	655.15	-1.92	947.10	754.87	14	15
101	30	1.6	866.54	668.23	-14.70	947.10	754.87	9	13
102	30	1.6	873.52	675.68	1.80	947.10	754.87	8	12
103	30	1.8	1123.71	880.01	4.28	1037.10	826.60	8	6
104	30	1.8	1039.00	812.28	-9.99	1037.10	826.60	0	2
105	30	1.8	947.29	725.45	16.55	1037.10	826.60	9	14
106	30	2	1104.37	889.00	9.38	1119.56	892.33	1	0
107	30	2	1050.24	817.28	-13.24	1119.56	892.33	7	9
108	30	2	1026.40	799.86	8.85	1119.56	892.33	9	12
109	30	2.4	1288.37	1015.05	-6.11	1262.96	1006.62	2	1
110	30	2.4	1387.82	1083.89	-20.72	1262.96	1006.62	9	7
111	30	2.4	1314.65	1028.24	15.52	1262.96	1006.62	4	2
112	30	2.8	1217.76	941.20	-2.22	1380.53	1100.33	13	17
113	30	2.8	1362.21	1084.69	-53.24	1380.53	1100.33	1	1
114	30	2.8	1290.86	999.24	9.02	1380.53	1100.33	7	10
115	30	3	1740.73	1384.76	13.95	1430.96	1140.52	18	18
116	30	3	1596.21	1257.56	-44.73	1430.96	1140.52	10	9
117	30	3	1578.68	1251.20	-13.17	1430.96	1140.52	9	9